

OPTICAL SIGNAL PROCESSING USING NONLINEAR PERIODIC
STRUCTURES

by

Lukasz Brzozowski

A thesis submitted in conformity with the requirements
for the degree of Doctor of Philosophy
Graduate Department of Electrical and Computer Engineering
University of Toronto

Copyright © 2003 by Lukasz Brzozowski

Abstract

Optical Signal Processing using Nonlinear Periodic Structures

Lukasz Brzozowski

Doctor of Philosophy

Graduate Department of Electrical and Computer Engineering

University of Toronto

2003

This work advances the field of optical signal processing using nonlinear periodic structures. A novel approach to all-optical signal processing using nonlinear periodic structures is proposed. The nonlinear response of various materials is measured, and nonlinear periodic structures are fabricated and characterized.

This work presents an analytical and numerical study of a stable all-optical limiter that clamps the output level below a design-specific limiting intensity. The introduction of disorder is predicted through theory to result in widening of the nonlinear stopband, localization of light, and formation of stationary gap solitons. It is shown through development and solution of a model that the incorporation of a built-in linear out-of-phase grating into the index-matched limiting structures can enable signal processing functions of hard-limiting, analog-to-digital conversion, and logic gating. A comprehensive theory of intensity-domain optical stability in nonlinear periodic structures is derived and conditions for multistability are presented. The propagation of pulses in the structures proposed is analyzed and effects of pulse intensity limiting and pulse compression are predicted.

The resonant, ultrafast, and thermal nonlinear properties of inorganic crystalline semiconductor, organic, and nanocrystal materials are examined while seeking to maximize the strength of the refractive nonlinear response and associated figures of merit. Nonlinear index changes of record magnitude of -0.14 with figures of merit of 1.38 are

found for InAlGaAs/InGaAs semiconductor multi-quantum-wells under the illumination at a wavelength of $1.5 \mu\text{m}$ and a fluence of $116 \mu\text{J}/\text{cm}^2$. Resonant nonlinear response is demonstrated in strongly-confined semiconductor PbS nanocrystals in the spectral region of 1150 to 1600 nm.

Nonlinear periodic signal processing elements are designed, fabricated, and analyzed. One dimensional semiconductor elements are shown to yield fluence-dependent transfer characteristics due to the interplay of the nonlinear Bragg refraction and nonlinear absorption. A photonic stopband is experimentally demonstrated to emerge in the vicinity of the wavelength of $1.5 \mu\text{m}$ at fluences below $320 \mu\text{J}/\text{cm}^2$. Three-dimensional organic colloidal crystals are proven to exhibit a nonlinear shift in the position of the photonic stopband and a decrease in the reflectivity in the 530 to 570 nm spectral region.

The theoretical and experimental accomplishments of this work expand the field of stable and multistable optical signal processing functionality of nonlinear periodic structures; and map out future directions for enhancing the functional diversity and performance of elements required for optical networks.

Acknowledgements

First and foremost I acknowledge my supervisor Professor Edward H. Sargent. I thank him for his vision, guidance, involvement, motivation, availability, help and generous support.

I thank Professor Eugenia Kumacheva and Chantal Pacquet for friendly, exciting collaboration, as well as for their help in preparation of organic materials and devices.

I thank Anthony SpringThorpe and Marcius Extavour of Nortel Networks for rapid fabrication of high quality semiconductor samples and devices.

I thank Professor Dmitry Pelinovsky for help in theoretical work. I thank Winnie Ye for friendship and fruitful work on numerical simulations.

I thank Margaret Hines and Larissa Levina for synthesizing nanocrystal materials.

I thank Professor Peter Smith, Professor Stewart Aitchison, David Cooper, and Kenton White for exciting conversation about nonlinear optics and for useful advice.

I thank members of the Organic and Polymer Optoelectronics Laboratory Wilfred Lam, Iraklis Nikolakakos, Daniel-Steve Fournier, Vlad Sukhovatkin, and Fumyo Yoshino for help in the experimental work.

I thank all the members of my research group, particularly Mathieu Allard, Andrew Stok, Emanuel Istrate, Erik Johnson, Yuankun Lin, Qiyang Chen, Ludmila Bakoueva, Dayane Ban, Sergei Musikhin, and Marian Tzolov for creating the most friendly, empathic, helpful and stimulating environment.

I am deeply indebted to my wife Miriam Brzozowski for her love and emotional support. I also thank my parents Anna Brzozowska and Andrzej Brzozowski.

I acknowledge National Sciences and Engineering Research Council of Canada, Nortel Networks, and University of Toronto for financial support during various stages of my doctoral studies.

Contents

| | | |
|----------|---|-----------|
| 1 | Switching in Photonic Networks - The Need ... | 1 |
| 1.1 | Signal Processing in Optical Networks | 1 |
| 1.2 | Current Optical Signal Processing Technologies | 3 |
| 1.3 | Optical Signal Processing using Nonlinear Optics | 3 |
| 1.4 | This Work - A Novel Approach to Optical Signal Processing | 5 |
| 1.5 | Organization of Thesis | 6 |
| 2 | Definitions of Concepts | 11 |
| 2.1 | Illumination-Dependent Refractive Index | 11 |
| 2.1.1 | Ultrafast Response | 12 |
| 2.1.2 | Ultrafast Nonlinear Material Figures of Merit | 14 |
| 2.1.3 | Resonant Response | 16 |
| 2.1.4 | Resonant Nonlinear Material Figures of Merit | 17 |
| 2.2 | Periodic Structures | 18 |
| 2.2.1 | Bragg Gratings | 18 |
| 2.2.2 | Nonlinear Periodic Structures | 19 |
| 2.3 | Conclusions | 21 |
| 3 | Literature Survey | 23 |
| 3.1 | Nonlinear Materials | 23 |
| 3.1.1 | Bulk and MQW Inorganic Crystalline Semiconductors | 23 |

| | | |
|----------|---|-----------|
| 3.1.2 | Organic Materials | 33 |
| 3.1.3 | Nanocrystals | 34 |
| 3.1.4 | Other Nonlinear Materials | 38 |
| 3.2 | Nonlinear Periodic Structures | 39 |
| 3.2.1 | Steady-State Response of Nonlinear Optical Elements | 39 |
| 3.2.2 | Propagation of Solitons in Nonlinear Periodic Structures | 42 |
| 3.2.3 | Shifting the Stopband | 44 |
| 3.3 | Conclusions from Literature Survey | 46 |
| 3.3.1 | Summary of Published Results | 46 |
| 3.3.2 | The Need for Additional Research | 48 |
| 4 | Coupled Mode Theory of Nonlinear Periodic Structures | 51 |
| 4.1 | Representation of the Refractive Index Profile | 52 |
| 4.2 | General Coupled Mode Equations for Nonlinear | 55 |
| 4.3 | Nonlinear Coupled Mode Equations for Incoherent Light | 58 |
| 4.3.1 | Assumptions | 58 |
| 4.3.2 | Couple Mode Equations for Incoherent Light | 59 |
| 4.3.3 | Coupled Mode Equations for Incoherent Light, Matched Linear Indices and Opposite Kerr Coefficients | 60 |
| 4.3.4 | Coupled Mode Theory for Weakly Disordered Structures | 60 |
| 4.3.5 | Transfer Matrix Formalism for Nonlinear System | 61 |
| 4.4 | Conclusions | 63 |
| 5 | Theory of Steady-State Optical Limiting and Switching | 65 |
| 5.1 | Structure and Modelling Approach | 66 |
| 5.2 | Theory of All-Optical Limiting | 67 |
| 5.2.1 | Analytical Solutions | 67 |
| 5.2.2 | Numerical Analysis | 69 |

| | | |
|----------|---|------------|
| 5.3 | Theory of Optical Switching with Stable Nonlinear ... | 75 |
| 5.3.1 | Optical Switching | 75 |
| 5.3.2 | Logic OR Gating | 80 |
| 5.4 | Nonlinear Figures of Merit for Periodic Structures | 81 |
| 5.5 | Conclusions | 82 |
| 6 | Theory of Broadband Limiting with .. | 83 |
| 6.1 | Spectral Analysis | 83 |
| 6.2 | Analysis of Intensity Transmittance | 89 |
| 6.3 | Localization of Light | 92 |
| 6.4 | Conclusions | 96 |
| 7 | Theory of Optical Signal Processing with Out-... | 97 |
| 7.1 | Structure and Modelling Approach | 98 |
| 7.2 | Basic Stability Condition | 98 |
| 7.3 | S-shape Transfer Characteristics | 101 |
| 7.4 | Analog-to-digital converter | 105 |
| 7.5 | Logic Gates | 107 |
| 7.6 | Sensitivity of Transfer Curves to Fabrication Errors and Absorption | 109 |
| 7.7 | Conclusions | 110 |
| 8 | Theory of Intensity-Domain Optical Stability ... | 111 |
| 8.1 | Incoherent Light | 112 |
| 8.1.1 | Transmittance expressions | 112 |
| 8.1.2 | Multistable Regime | 115 |
| 8.1.3 | Stable Regime | 115 |
| 8.2 | Coherent Light | 118 |
| 8.2.1 | Balanced Nonlinearity Management: $n_{nl} = 0$ | 119 |
| 8.2.2 | Unbalanced Nonlinearity Management: $n_{nl} \neq 0$ | 122 |

| | | |
|-----------|--|------------|
| 8.3 | Conclusions | 123 |
| 9 | Theory of Pulse Shaping and Compression ... | 125 |
| 9.1 | Case I: $n_{0k}=0$ | 126 |
| 9.2 | Case II: $n_{0k} < 0$ | 131 |
| 9.3 | Conclusions | 135 |
| 10 | Experimental Assessment of the Applicability ... | 137 |
| 10.1 | Experimental Apparatus | 139 |
| 10.1.1 | Laser Systems and Spectrophotometer | 139 |
| 10.1.2 | Z-scan Technique | 142 |
| 10.2 | Non-resonant Response of Nonlinear Materials | 152 |
| 10.2.1 | Non-resonant Nonlinear Response of Azobenzene Dye Disperse Red | 1152 |
| 10.2.2 | Non-resonant Nonlinear Response of MEH-PPV/PMMA | 155 |
| 10.2.3 | Thermal Response of Organic Nonlinear Materials | 159 |
| 10.3 | Resonant Nonlinearities | 160 |
| 10.3.1 | Bandedge Saturation of Absorption in GaAs/AlGaAs Multi-Quantum- Wells | 161 |
| 10.3.2 | Resonant Nonlinear Properties of InGaAs/InAlGaAs Multi-Quantum- Wells | 167 |
| 10.3.3 | Resonant Nonlinear Response of PbS nanocrystals | 175 |
| 10.3.4 | Resonant Nonlinear Response of DR1 | 187 |
| 10.4 | Conclusions | 188 |
| 11 | Measurement of the Transfer Characteristics ... | 191 |
| 11.1 | Experiments | 192 |
| 11.1.1 | Devices | 192 |
| 11.1.2 | Linear Optical Properties | 196 |
| 11.1.3 | Experimental Apparatus | 198 |

| | | |
|-----------|---|------------|
| 11.2 | Results and Discussion | 199 |
| 11.2.1 | Nonlinear Response of Sample A | 199 |
| 11.2.2 | Nonlinear Response of Optical Element B | 202 |
| 11.2.3 | Nonlinear Response of Optical Element C | 205 |
| 11.3 | Analysis of Experimental Results Using | 209 |
| 11.4 | Conclusions | 212 |
| 12 | Summary, Original Contributions, Future Prospects | 215 |
| 12.1 | Perspective and Approach Taken During this Work | 215 |
| 12.2 | Original Contributions of this Work | 216 |
| 12.2.1 | Theoretical Contributions | 216 |
| 12.2.2 | Experimental Contributions | 218 |
| 12.3 | Future Prospects | 219 |
| 12.3.1 | Further Search for Suitable Nonlinear Materials | 219 |
| 12.3.2 | Incorporation of Nonlinear Materials into Periodic Structures | 221 |
| 12.3.3 | Extension of Theoretical Models | 225 |
| 12.4 | Final Comments | 225 |
| | Bibliography | 226 |

List of Figures

| | | |
|-----|---|----|
| 2.1 | Schematic of a linear Bragg grating with period Λ : n_{01} and n_{02} are the linear refractive indices of the two adjacent layers. | 18 |
| 2.2 | Response of a periodic structure in which one set of layers experiences positive refractive nonlinearity. The Bragg frequency ω_0 shifts to lower frequencies ω'_0 and ω''_0 and the size of the bandgap $\Delta\omega_{gap}$ increases with increasing level of illumination. | 20 |
| 3.1 | Trends in the nonlinear response of bulk semiconductors. | 25 |
| 3.2 | Results of the pump-probe measurements illustrating the time-resolved change in transmission for He-InGaAsP samples with different Be doping concentrations. This figure was reproduced from Ref. [37]. | 27 |
| 3.3 | Spectra of GaAs/AlGaAs MQWs of three different well widths, measured at various incident intensities by pulsed pump at 1.52 eV: (a) absorption coefficient, α , (b) the change in the real part of the refractive index, Δn . This figure was reproduced from Ref. [38]. | 30 |
| 3.4 | Data of scaled n_2 measured at 1.06 μm for various bulk inorganic crystalline semiconductors. This figure was reproduced from Ref. [29]. | 33 |
| 3.5 | Typical trends in the nonlinear response of organic materials with one absorption resonance. | 35 |
| 3.6 | Trends in the picosecond nonlinear response of inorganic semiconductor nanocrystals. | 36 |

| | | |
|-----|---|----|
| 3.7 | The transmitted versus incident intensity characteristic of a bistable optical element exhibiting a hysteresis characteristic. | 40 |
| 4.1 | Schematic of a nonlinear periodic structure with period Λ . n_{01} and n_{02} are the linear refractive indices, and n_{nl1} and n_{nl2} are the Kerr coefficients of the adjacent layers. | 52 |
| 4.2 | Profile of the linear parts of refractive index n_{ln} and Kerr coefficients n_{nl} of a nonlinear periodic structure along the propagation direction z | 53 |
| 4.3 | Nonlinear periodic structure where layer thicknesses deviate randomly from their quarter-wave value. | 61 |
| 5.1 | Profile of linear refractive indices and Kerr coefficients of the limiting device. The refractive indices of the two adjacent layers are $n_{01} + n_{nl1}I$ and $n_{02} + n_{nl2}I$, where $n_{01} = n_{02}$ and $n_{nl1} = -n_{nl2}$ | 66 |
| 5.2 | Transmitted intensity as a function of incident intensity for limiting structures with $ n_{nl} = 0.01$ for various numbers of layers. | 69 |
| 5.3 | The transmitted intensity as a function of incident intensity on a semi-log plot for limiting structures with $ n_{nl} = 0.01$ for different numbers of layers. | 70 |
| 5.4 | The effective indices of refraction across the structure of 300 layers with $ n_{nl} = 0.01$ and matched linear indices of $n_{ln} = 1.5$. This plot demonstrates the decay of the intensity across the structure. | 71 |
| 5.5 | The evolution of the transmittance spectra with increasing number of layers for structures with $n_{nl} = \pm 0.01$. The nonlinear behaviour of the limiter is responsible for the formation of a stopband at the desired frequency. | 72 |
| 5.6 | The evolution of the transmittance spectra as a function of increased incident intensity for the structure made of 300 layers with $n_{nl} = \pm 0.01$. As the incident intensity is increased the stopband becomes deeper and wider. | 73 |

| | | |
|------|--|----|
| 5.7 | The limiting intensities as a function of the number of layers for $ n_{nl} = 0.005, 0.01, \text{ and } 0.02$. The values obtained from numerical calculations shown on the plot as squares, triangles and diamonds follow exactly the curves predicted by the analytical model. | 74 |
| 5.8 | Demonstration of the switching capability. The figure shows the transmittance of the signal beam as a function of the frequency of the pump beam. The structures analyzed have refractive indices as in Figure 5.2. The signal beam is on resonance $\lambda_0 = 2\Lambda n_{nl}$ and has a constant intensity of 0.1. The frequency of the pump beam is varied from $0.93\omega_0$ to $1.06\omega_0$. The number of layers is kept constant at 100 and the intensity of the pump beam takes values of 1, 2, and 4. | 76 |
| 5.9 | Transmittance spectrum of the probe beam for the structure analyzed in Figure 5.8. Pump beam intensity is kept constant at 1 and number of layers is varied (100, 300, and 500). | 77 |
| 5.10 | Evolution of the pump beam intensity across a 100-layer structure for pump frequencies of $0.83\omega_0, 0.97\omega_0, \text{ and } \omega_0$ | 78 |
| 5.11 | Transmittance of a signal beam as a function of the pump beam intensity. The frequency of the probe beam is fixed at the Bragg resonance, while the frequency of the pump beam takes values of $(0.83\omega_0, 0.97\omega_0, \text{ and } \omega_0)$ | 79 |
| 5.12 | An OR gate realized using limiting and switching structures proposed. | 80 |
| 6.1 | Influence of the increased layer thickness randomization on the nonlinear transmittance spectra. | 85 |
| 6.2 | A combined system consisting of broadband optical limiters with inserted optical isolators. Decoupling among the constituent limiters eliminates transmittance maxima within the effective stopband. | 86 |
| 6.3 | Combining randomized units in series eliminates transmittance maxima, deepens and widens the effective stopband. | 87 |

| | | |
|------|--|-----|
| 6.4 | A comparison of the transmission spectra for a single perfectly periodic 1000-layer structure (the thin line) versus 5 combined randomized 200-layer units (the thick line). | 88 |
| 6.5 | Transmitted versus incident intensity for various degrees of randomness at various trials. | 89 |
| 6.6 | The transmitted vs. the incident intensity for light at frequencies inside the broadened stopband of a 10% randomized 100-layer structure. | 90 |
| 6.7 | Transmittance versus incident intensity. Comparison between ordered and 10% randomized 100-layer structures at two frequencies. | 91 |
| 6.8 | Evolution of the intensity of the forward propagating wave across a 100-layer structure. Impact of the increasing level of randomness for the incident intensity of 2 is shown. | 92 |
| 6.9 | The localization of light within a 30% randomized structure. The figure shows the impact of increasing incident intensity. | 93 |
| 6.10 | The intensity of the forward-propagating wave across the structure in the transmitting and limiting regimes. | 94 |
| 6.11 | The intensity of the forward-propagating wave across a structure consisting of five randomized 500-layer units. The inset shows the transmittance spectra for structures with one and five units. | 95 |
| 7.1 | Profile of linear refractive indices and Kerr coefficients of a nonlinear periodic structure in the out-of-phase configuration. The refractive indices of two adjacent layers are $n_{01} + n_{nl1}I$ and $n_{02} + n_{nl2}I$, where $n_{01} < n_{02}$ and $n_{nl1} = -n_{nl2} > 0$ | 99 |
| 7.2 | The transmitted intensity for the structures with an out-of-phase effective refractive index profile for various numbers of layers ($N = 100, 400, 1000$). The structures have linear refractive indices of $n_{01}=1.5$ and $n_{02}=1.52$ and Kerr coefficients of $n_{nl1}=0.01$ and $n_{nl2}=-0.01$ | 101 |

| | | |
|------|--|-----|
| 7.3 | Local effective refractive index and the intensity across a 1000-layer structure with material parameters as in Figure 7.2 for various values of incident intensity. The total refractive index is given on the left vertical axis and the local intensity is given on the right axis. | 102 |
| 7.4 | The idealized transmitted intensity for out-of-phase nonlinear periodic structures with different material parameters. | 104 |
| 7.5 | All-optical hard limiter. Arranging the proposed structures in series results in an increasingly steep transition in the transfer characteristics. The inset shows how the response of hard-limiter is modified with an increasing number of units. | 105 |
| 7.6 | All-optical analog-to-digital converter. In the example considered, an analog input of 5 is transformed to a digital word (0101). | 106 |
| 7.7 | OR and AND gates. For two input beams A and B , the transmitted intensity of the hard limiter biased at $a = 1$ implements the OR function while the reflected beam implements the AND operation. | 107 |
| 7.8 | Ideal transmission characteristics of the out-of-phase nonlinear balanced structure with material parameter $a = 2$. The transfer curve enables OR logic operation. | 108 |
| 7.9 | Ideal reflection characteristics of the out-of-phase nonlinear balanced structure with material parameter $a = 2$. This transfer curve enables logic AND and inversion logic operations. | 108 |
| 7.10 | Transmitted intensity as a function of incident intensity for the structure with the same parameters as in Figure 7.3. The thicknesses of layers were allowed to vary 0, 5, and 10% from their quarter-wave value. The effect of the linear absorption on the transmittance is also shown. | 109 |
| 8.1 | The multistable and stable regimes of nonlinear periodic structures illuminated with light at the frequency of Bragg resonance. | 114 |

| | | |
|-----|---|-----|
| 8.2 | The normalized limiting value of the output power I_{lim}/I_0 as a function of the inverse variance of the nonlinear index Γ at $k\Lambda = \pi$ | 116 |
| 8.3 | The limiting transmitted power I_{lim} as a function of the spectral position of the illumination to spatial period ratio $\lambda/(\Lambda n_0)$ | 117 |
| 8.4 | Balanced nonlinearity management with a linear built-in grating, where $n_{nl} = 0$, $n_{2k} = 1$. Horizontal lines show the limiting intensity I_{lim} , while the dotted line displays the regime of complete transparency: $I_{out} = I_{in}$. An out-of-phase ($n_{0k} = -0.02$) grating increases I_{lim} while an in-phase grating ($n_{0k} = 0.02$) decreases it. | 120 |
| 8.5 | Transfer characteristics of nonlinear periodic structures with unbalanced nonlinearity. The threshold between limiting regime and multistability is $n_{nl} = 4/3$ | 122 |
| 9.1 | Pulse energy transmittance as a function of the pulse width for a fixed peak pulse intensity of $I_{peak} = 0.01 n_2 $ | 127 |
| 9.2 | Temporal intensity profiles of input and output pulses after transmission through a 360-period long device for input pulse widths of: (a) $240 \frac{\Lambda}{c}$ and (b) $570 \frac{\Lambda}{c}$ | 128 |
| 9.3 | Heuristic analysis of pulse shaping in a 360-period long nonlinear grating. The time-dependent instantaneous transmittance is attributed to contributions from the forward- and backward-propagating electric fields for an input pulse widths of: (a) $240 \frac{\Lambda}{c}$ and (b) $570 \frac{\Lambda}{c}$ | 130 |
| 9.4 | (a) Peak transmitted intensity versus peak incident intensity of $240 \frac{\Lambda}{c}$ -long pulses for devices that are 140, 360, and 580-periods long (b) Corresponding reflected peak intensity as a function of peak incident intensity. | 132 |
| 9.5 | Output temporal response of the device with length $L = 140 \Lambda$, 360Λ , 420Λ , 720Λ , 1440Λ , and 2160Λ , for a fixed input pulse with $I_{peak} = I_{closing}$ and $FWHM = 240 \frac{\Lambda}{c}$ | 133 |

| | | |
|------|---|-----|
| 9.6 | Output transmitted pulse shapes when for incident pulses with peak intensity of: (a) $I_{peak} = 0.5I_{closing}$ and (b) $I_{peak} = 1.5I_{closing}$. The width of the pulse is $FWHM = 240\frac{\text{\AA}}{c}$ and the device length is equal to 360 Bragg periods. | 134 |
| 10.1 | General layout of the first laser system used: 1. VITESSE seed laser [$\lambda=800$ nm, rep. rate = 80 MHz, $\tau = 30$ fs, power = 300 mW]; 2. YLF pump laser [$\lambda=533$ nm, rep. rate = 1 kHz, $\tau = 150$ ns, power = 12-16 W]; 3. TITAN amplifier [$\lambda=800$ nm, rep. rate = 1 kHz, $\tau = 1.7$ ps, power = 2.0 W]; 4. TOPAS OPA [280 nm < λ < 2600 nm, rep. rate = 1 kHz, $\tau = 1.2$ ps, 8 mW < power < 430 mW]. | 140 |
| 10.2 | Picture of the OPA laser system at installation. The numbers 1 to 4 in the figures correspond to the system components as explained in the caption of Figure 10.1. | 141 |
| 10.3 | Schematic illustration of a z-scan experimental setup used in this work. Diagram taken from Ref. [151]. | 143 |
| 10.4 | Ideal normalized closed-aperture z-scan trace for the sample with a negative refractive nonlinearity. | 144 |
| 10.5 | Ideal normalized open-aperture z-scan trace for the sample exhibiting saturation of absorption. | 145 |
| 10.6 | Normalized closed-aperture z-scan trace showing a negative nonlinear thermal response of CS ₂ at a repetition rate of 76 MHz. The line corresponds to the nonlinear refraction fit. | 150 |
| 10.7 | Normalized closed-aperture z-scan trace showing ultrafast positive index change of CS ₂ at a repetition rate of 5 kHz. | 151 |
| 10.8 | The molecular structure of pseudo-stilbene type azobenzene molecule: the azo group, two benzene rings, donor and acceptor groups. | 153 |

| | | |
|-------|---|-----|
| 10.9 | Absorption spectra of Azobenzene Dye Disperse Red 1. The absorption peaks at 490 nm. | 153 |
| 10.10 | Results from the measurement of nonlinear properties at a laser wavelength of 760 nm of the solution of azobenzene dye Disperse Red 1 in THF at concentrations of 2%, 5%, and 10%. a) Kerr coefficients; b) two-photon absorption coefficients; c) W figure of merit; d) $1/T$ figure of merit. . . . | 154 |
| 10.11 | Linear absorption spectra of pure PMMA (dotted line) and MEH-PPV/PMMA composite (solid line). | 156 |
| 10.12 | Normalized open-aperture z-scan transmittances traces of MEH-PPV/PMMA (circle) and pure PMMA (triangle) film samples using 100 femtosecond pulses at $\lambda=840$ nm. The solid line is a theoretical fit to the open-aperture trace of MEH-PPV/PMMA. | 157 |
| 10.13 | Normalized closed-aperture z-scan transmittance trace of MEH-PPV/PMMA composite. The solid line is a theoretical fitting. | 158 |
| 10.14 | Thermal nonlinear index change of solid samples of DR1/PMMA and MePh as a function of intensity. | 159 |
| 10.15 | Cross-section of the GaAs/AlGaAs MQWs sample analyzed. Sixty-one 10 nm GaAs wells and sixty 21 nm $\text{Al}_{0.28}\text{Ga}_{0.72}\text{As}$ barriers were grown on on Si-doped 001 GaAs 3" substrate. | 162 |
| 10.16 | Photoluminescence intensity of the $\text{Al}_{0.28}\text{Ga}_{0.72}\text{As}/\text{GaAs}$ MQWs sample. | 163 |
| 10.17 | Absorption spectrum of the GaAs/ $\text{Al}_{0.28}\text{Ga}_{0.72}\text{As}$ MQWs sample. | 164 |
| 10.18 | Change in the absorption in the bandedge region of GaAs/AlGaAs MQWs samples at wavelengths of 785, 800, 820, 844, 848, 855, and 874 nm. . . . | 165 |
| 10.19 | Saturation fluences of the GaAs/AlGaAs MQWs sample. | 166 |
| 10.20 | Cross-section of sample. One hundred and twenty-one 10 nm $\text{In}_{0.530}\text{Al}_{0.141}\text{Ga}_{0.329}\text{As}$ barriers and one hundred and twenty 5 nm $\text{In}_{0.530}\text{Ga}_{0.47}\text{As}$ wells were grown on on S-doped 001 InP " substrate. | 168 |

| | | |
|-------|--|-----|
| 10.21 | Photoluminescence spectra of the $\text{In}_{0.530}\text{Al}_{0.141}\text{Ga}_{0.329}\text{As}/\text{In}_{0.530}\text{Ga}_{0.47}\text{As}$ sample. | 169 |
| 10.22 | Linear absorption spectra of the $\text{In}_{0.530}\text{Al}_{0.141}\text{Ga}_{0.329}\text{As}/\text{In}_{0.530}\text{Ga}_{0.47}\text{As}$ sample. | 170 |
| 10.23 | Saturation of absorption in $\text{In}_{0.530}\text{Al}_{0.141}\text{Ga}_{0.329}\text{As}/\text{In}_{0.530}\text{Ga}_{0.470}\text{As}$ MQWs at room temperature in the spectral range 1480–1550 nm at fluences of $46 \mu\text{J}/\text{cm}^2$, $69 \mu\text{J}/\text{cm}^2$, $92 \mu\text{J}/\text{cm}^2$, and $116 \mu\text{J}/\text{cm}^2$ | 171 |
| 10.24 | Nonlinear index change in the $\text{In}_{0.530}\text{Al}_{0.141}\text{Ga}_{0.329}\text{As}/\text{In}_{0.530}\text{Ga}_{0.470}\text{As}$ MQWs at the same experimental conditions as in Figure 10.23. | 172 |
| 10.25 | Figures of merit under the same experimental conditions as in Figures 10.23 and 10.24. | 173 |
| 10.26 | The linear absorption spectra of toluene, THF, chloroform, cyclohexane in the 1300 – 1580 nm spectral range. | 176 |
| 10.27 | The third order nonlinear Kerr coefficients of the compounds of Figure 10.26. The measurements were taken using picosecond pulses with intensity of $75 \text{ GW}/\text{cm}^2$ | 177 |
| 10.28 | The nonlinear absorption coefficients under the same conditions as in Figure 10.28. | 178 |
| 10.29 | The saturation of absorption in the $5.5 \pm 0.5 \text{ nm}$ PbS nanocrystals in the wavelength range from 1150 to 1550 nm at fluences of $1 \text{ mJ}/\text{cm}^2$, $2 \text{ mJ}/\text{cm}^2$ and $3 \text{ mJ}/\text{cm}^2$ | 180 |
| 10.30 | Nonlinear index change of PbS nanocrystals under the same conditions as in Figure 10.29. The inset compares the linear absorption spectrum with spectral position of the refractive index change measured at a fluence of $3 \text{ mJ}/\text{cm}^2$ | 181 |

| | | |
|-------|--|-----|
| 10.31 | Nonlinear figures of merit (FOM) of PbS nanocrystals under the same conditions as in Figures 10.29 and 10.30. The inset displays the figures of merit recorded at a fluence of 3 mJ/cm^2 vs. the linear absorption spectrum. | 183 |
| 10.32 | Linear absorption spectra of the 22 mg/mL PbS nanocrystals in chloroform solution for the samples with mean diameters of $4.8 \pm 0.5 \text{ nm}$, $5.5 \pm 0.5 \text{ nm}$, and $5.8 \pm 0.5 \text{ nm}$. | 184 |
| 10.33 | Nonlinear index change for the same samples as in Figure 10.32 as measured at a fluence of 3 mJ/cm^2 . | 185 |
| 10.34 | Nonlinear figures for merit of the three nanocrystal samples studied under the same conditions as in Figure 10.33. | 186 |
| 10.35 | Trans-cis photoisomerization. Following resonant absorption, the azobenzene molecule changes its configuration, resulting in a decreased dipole moment. | 187 |
| 11.1 | The cross-section of the analyzed MQWs sample A. A is made out of one hundred and twenty-one 10 nm $\text{In}_{0.530}\text{Al}_{0.141}\text{Ga}_{0.329}\text{As}$ barriers and one hundred and twenty 5 nm $\text{In}_{0.530}\text{Ga}_{0.47}\text{As}$ wells. | 193 |
| 11.2 | The cross-section of optical element B. B is made out of MQWs type 1 and MQWs type 2. | 194 |
| 11.3 | The cross-section of optical element C. C is made out of MQWs type 1 and MQWs type 3. | 195 |
| 11.4 | The photoluminescence spectra of semiconductor samples A, B, and C. | 196 |
| 11.5 | The linear transmittance spectra of semiconductor samples A, B, and C. | 197 |
| 11.6 | The experimental set up used in the nonlinear transmittance and reflectance measurement. | 198 |
| 11.7 | The change in the absolute transmittance of sample A in the spectral range 1300 nm to 1600 nm, at incident powers of $0.3 \mu\text{W}$, $1 \mu\text{W}$, $3\mu\text{W}$, $10 \mu\text{W}$, $30 \mu\text{W}$, and $100 \mu\text{W}$. | 200 |

| | | |
|-------|---|-----|
| 11.8 | The change in absolute reflectance of sample A under the same conditions as in 11.7. | 201 |
| 11.9 | The nonlinear transmittance response of the optical element B under the same conditions as in Figure 11.7. | 202 |
| 11.10 | The nonlinear reflectance response of the optical element B under the same conditions as in Figure 11.7. | 203 |
| 11.11 | The nonlinear transmittance response of the optical element C under the same conditions as in Figure 11.7. | 205 |
| 11.12 | The nonlinear reflectance response of the optical element C under the same conditions as in Figure 11.7. | 206 |
| 11.13 | The nonlinear changes in the relative transmittance in A, B, and C. | 207 |
| 11.14 | The nonlinear changes in the relative reflectance in A, B, and C. | 208 |
| 11.15 | Simulated results of a change in the absolute transmittance and reflectance of a sample of uniform nonlinear absorbing material. | 210 |
| 11.16 | Simulated results of a change in the absolute transmittance and reflectance of a sample with a pop-up Bragg grating. | 211 |
| 12.1 | Differential nonlinear reflectance from colloidal crystal 1 compared to its initial reflectance. | 222 |
| 12.2 | Nonlinear reflectance from colloidal crystal 2. The inset demonstrates how the reflectance at 570 nm decreases with increasing incident power | 224 |

Chapter 1

Switching in Photonic Networks - The Need for Agile Solutions

1.1 Signal Processing in Optical Networks

Networking applications such as data browsing, large file transfer, multimedia-on-demand, and videoconferencing require high quality transfer of data streams of different lengths and initial formats.

Optical fiber provides a suitable medium in which it is possible to reach tremendous transmission rates over long distances [1]. The maximum information carrying capacity was estimated to be around 100 THz [2]. Very high data rates can be achieved using a combination of wavelength- and time-division multiplexing techniques (WDM and TDM). WDM involves sending many signals in parallel at closely spaced wavelengths along the same fiber, while TDM allows close spacing in time of bits in a single channel.

While there exist means to produce, transfer, and detect information at a very high bandwidth, there is a need for more agility in photonic networks.

The agility of present-day optical networks is limited by the electronic nature of a very important function: the processing of data signals. Signal processing is responsible

for switching and routing traffic, establishing links, restoring broken links, testing, and managing the network.

At present, important and functionally complex signal processing operations of switching and routing are carried out electronically. Electronic signal processing imposes two significant limitations on the functionality of optical networks: cost and opacity.

Today, signal switching and routing requires converting the optical information into electrical signals, processing in the electronic domain, and converting back to the optical domain before retransmission. Such an operation requires detection, retiming, reshaping, and regeneration at each switching and routing point. This necessitates complex and expensive electronic and electro-optical hardware at each routing and switching node.

The use of electronic signal processing places strict requirements on the format of data streams transferred and processed, thus making the signal processing opaque. Repetition rates of optical signals, power levels, and packet lengths have to be standardized before they can be processed electronically.

In addition, since modern electronics can process information at repetition rates far below the fundamental limits of the optical transmission, electronics imposes limits on the ultimate transmission rate of a network.

The ability to perform signal processing operations entirely within the optical domain would eliminate the requirement of optical-electrical-optical conversions, while providing the agility and speed inherent to optical elements. Provisioning of services with a vast diversity of rates and duration of connections could be enabled. All-optical switching solutions would be transparent to bit rate and protocols. The speed of electronic devices would no longer limit network throughput: optical signal processing, in contrast with electronics, may provide ultrafast subpicosecond switching times [3].

1.2 Current Optical Signal Processing Technologies

Currently commercially implemented all-optical devices and elements do not perform complex self-processing of signals [4, 5].

Interferometric arrayed waveguide gratings and fiber Bragg grating passband filters are used to multiplex, demultiplex, and drop WDM signals. Micro-Opto-Mechanical-Sensors are made out of movable microscopic mirrors that steer light beams between desired input and output ports in one, two, or three-dimensions. Optomechanical switches are made out of movable waveguides. Electro-optical and thermo-optical interferometric signal processing elements rely on changing the index of refraction by exploiting either electro-optical or thermo-optical properties of the waveguide materials. Bubble- and liquid crystal-based signal processing technologies rely on directing the light from input to output ports through the externally controlled matrix. Apart from the electro-optical devices, the technologies discussed above are characterized by slow switching speeds.

1.3 Optical Signal Processing using Nonlinear Optics

In contrast to the optical signal processing solutions discussed in the previous section, nonlinear optics can potentially support transparent and fast self-processing of signals.

A variety of nonlinear optical signal processing functions can be realized with similar fundamental building blocks [6–8]. Nonlinear optical elements and devices can be either integrated in photonic circuits [9] or used in a free-standing configuration [10]. Nonlinear optics can enable signal processing without the requirement of external electrical, mechanical, or thermal control [11]. The response time of properly designed nonlinear optical devices is limited fundamentally only by the nonlinear response time of the constituent materials [3, 12–14].

Photons do not interact with each other *in vacuo*. In order to perform nonlinear optical signal processing operation the properties of a medium through which the light travels must be modified by the light itself. Optical signals then propagate differently as a result of their influence on the medium.

Nonlinear optical signal processing elements utilize the illumination-dependent real and imaginary parts of the index of refraction [11]. Depending on the material and spectral position, the refractive index and absorption of a given nonlinear material can either increase or decrease with increasing illumination.

A wide range of broadband and wavelength-selective nonlinear optical signal processing devices has been proposed and demonstrated.

The most commonly studied nonlinear optical switching elements are nonlinear Fabry-Perot interferometers, nonlinear Mach-Zehnder modulators, nonlinear directional couplers, optical limiters, and nonlinear periodic structures.

A nonlinear Fabry-Perot interferometer consists of two mirrors separated by a nonlinear material. As the refractive index of the nonlinear material changes with an increased level of illumination, the effective path length of the resonator is altered. A nonlinear Fabry-Perot interferometer can be tuned out of, or into, its transmission resonance. When illuminated with the continuous-wave light, a nonlinear Fabry-Perot interferometer can exhibit optical bistability. Optical bistability is a phenomenon in which the instantaneous transmittance of the device depends both on the level of incident illumination and on the prior transmittance of the device. Such an element enables all-optical memory.

In a nonlinear Mach-Zehnder modulator and a nonlinear directional coupler, a part of the waveguide is made out of a nonlinear material. Changing the intensity of the incident light changes the effective path length experienced by the light. This, in turn, through phase interference, results in an illumination-dependent transmittance in a Mach Zehnder modulator, and an illumination-dependent coupling in a nonlinear directional coupler.

A number of techniques use nonlinear properties of materials to obtain power limiting, and associated with it, on-off switching. Such devices are based on total internal reflection [15], self-focusing [16], self-defocusing, two photon absorption [17], or photorefractive beam fanning [18].

Nonlinear periodic structures combine the phenomena of nonlinear index change and distributed Bragg reflection. The intensity-dependent transmission and reflection properties of nonlinear periodic structures can be harnessed to yield various signal processing functions. Prior to this work it has been demonstrated that nonlinear periodic structures can support optical switching, optical bistability, and solitonic propagation of pulses. Nonlinear periodic structures offer many structural and material degrees of freedom allowing modification of the general character and specifics of their optical response.

1.4 This Work - A Novel Approach to Optical Signal Processing

This work will argue that nonlinear periodic structures can enable transparent signal processing in photonic networks, and therefore increase the agility of the transfer of information.

The most important problems with the state of research on nonlinear periodic structures prior to this work were identified as:

- A lack of a comprehensive theory describing the response of the nonlinear periodic devices capable of supporting diversified signal processing functions.
- Insufficient information and understanding about nonlinear properties of materials capable of exhibiting large refractive index changes with good figures of merit.
- A small number of successful experimental demonstrations of optical signal processing using large-index change nonlinear periodic structures.

In this work these issues are addressed by:

- Developing the theory of optically stable nonlinear periodic structures. Through development and solution of a model, it will be shown that this previously unexplored branch of intensity-domain response of nonlinear periodic structures can be used to obtain a variety of all-optical signal processing functions. An in-depth analysis of nonlinear periodic all-optical limiters, switches, hard-limiters, analog-to-digital converters, and a complete set of logic gates will be presented.
- Examining nonlinear properties of various inorganic crystalline semiconductors, organic materials, and semiconductor quantum dots. This will be carried out with an emphasis on simultaneously maximizing the strength of the nonlinear response and the associated figures of merit in the telecommunication and visible spectral regions.
- Fabricating novel nonlinear periodic signal processing elements. One- and three-dimensional optical elements will be shown to yield promising intensity-dependent transfer characteristics due to the interplay of Bragg periodicity, nonlinear absorption, and nonlinear refraction.

1.5 Organization of Thesis

The thesis is organized as follows:

Chapter 2 *Definitions of Concepts* establishes a background for this work. The phenomenon of illumination-dependent refractive index will be explained in terms of the theory of nonlinear material polarization. The concept of figures of merit will be used to describe what constitutes a good nonlinear material. The idea of a Bragg resonance will be introduced and it will be shown that nonlinearity and periodicity can be combined to yield an illumination-dependent nonlinear periodic structure.

Chapter 3 *Literature Survey* will outline the significant prior developments in research fields related to this work. Refractive and absorptive nonlinearities measured in bulk semiconductors, semiconductor multi-quantum-wells, semiconductor nanocrystals, and organic materials will be summarized. It will be shown how the field of optical signal processing using nonlinear periodic structures has evolved. The major results to date, and important gaps in understanding, will be identified.

The nonlinear periodic structures analyzed in the remaining chapters of this work will be introduced in chapter 4 *Coupled Mode Theory of Nonlinear Periodic Structures*. This chapter will establish the theoretical framework for the analytical and numerical work presented in the ensuing chapters.

Chapter 5 *Theory of Steady-State Optical Limiting and Switching* will analyze limiting and switching with balanced nonlinear periodic structures. The analytical solutions that predict clamping of the transmitted intensity below a well-defined limiting intensity threshold will be derived. These derivations will be followed by the comprehensive numerical analysis of optical limiting and single- and double-beam switching.

Broadband optical limiting will be discussed in chapter 6 *Theory of Broadband Limiting with Slightly-Disordered Nonlinear Periodic Structures*. The introduction of limited disorder will be shown to increase the effective operational bandwidth of the limiting nonlinear periodic structures. The formation of stationary gap solitons and localization of light in weakly disordered structures will be demonstrated numerically.

In chapter 7 *Theory of Optical Signal Processing with Out-of-Phase Balanced Nonlinear Periodic Structures* the theory from chapter 5 will be extended to introduce more complex all-optical signal processing functions. These functions will be enabled by structural modification of the limiting devices introduced in chapters 5 and 6. It will be shown through development and solution of a model that the introduction of a weak built-in linear grating into index-matched limiting structures enables all-optical hard-limiting, analog-to-digital conversion, and logic gating.

Chapter 8 *Theory of Intensity-Domain Optical Stability of Transfer Functions of Nonlinear Periodic Structures* will present a comprehensive analytical and numerical study of steady-state intensity-domain optical stability and multistability in nonlinear periodic structures. Regimes in which periodic structures exhibit stable or multistable intensity-domain optical response will be quantified in terms of material and structural parameters.

The time-dependent response of the devices proposed will be discussed in chapter 9 *Theory of Pulse Shaping and Compression in Balanced Nonlinear Periodic Structures*. The propagation of ultrashort pulses in gratings with balanced nonlinearity will be simulated for the cases of: no built-in linear grating, and an out-of-phase built-in linear grating. Pulse intensity limiting and pulse envelope compression will be predicted from numerical simulations.

Chapter 10 *Experimental Assessment of the Applicability of Specific Nonlinear Optical Materials to Nonlinear Periodic Devices* will present the linear and nonlinear properties of materials characterized throughout this work. It will summarize and discuss the results of the illumination-dependent refraction and absorption in inorganic crystalline semiconductors, semiconductor nanocrystals, and organic materials. The results will be contextualized with respect to their applicability to optical signal processing using nonlinear optics in general, and using nonlinear periodic structures in particular. The characterization of the nonlinear properties will investigate which materials should be implemented into the nonlinear periodic structures studied in the ensuing chapters.

Chapter 11 *Measurement of the Transfer Characteristics of Nonlinear Semiconductor Bragg Gratings* will discuss the design, fabrication and characterization of one-dimensional semiconductor periodic structures. Based on the nonlinear transmission and reflection experiments, various aspects of the response of the elements studied will be attributed to nonlinear absorption or nonlinear refraction. Evidence of the emergence of an intensity-dependent Bragg grating will be presented.

This work will be summarized and contextualized in chapter 12 *Summary, Origin-*

nal Contributions, Future Prospects. It will be demonstrated that the research presented herein has exploited various branches of optical signal processing using nonlinear periodic structures. The concluding chapter will also present preliminary results of the measurements of the nonlinear response of an organic periodic structure – a nonlinear three-dimensional colloidal crystal. Experimental observation of an illumination-dependent shift of the stopband position and a decrease in the reflectivity will be presented. Promising avenues for future investigations based on this work will be presented and discussed.

Chapter 2

Definitions of Concepts

This chapter will introduce the most important concepts used in this work. The phenomena of the ultrafast and resonant nonlinear index of refraction and Bragg scattering will be explained. The combination of nonlinearity and periodicity will be shown to yield optical signal processing functionality. The discussion presented in this chapter will lay the foundations for the literature review presented in the next chapter and for the research results reported in the rest of this thesis.

2.1 Illumination-Dependent Refractive Index

In a nonlinear optical medium intense light alters the real and imaginary components of the refractive index. The nonlinear response of the real part of refractive index modifies the phase of propagating light while the imaginary part describes the change in absorption.

This section will present the formalism used to describe how light affects the ultrafast and the resonant changes in nonlinear refractive index. The ultrafast nonlinear index changes take place in the spectral region where the material is nonabsorbing, while the resonant nonlinear index changes take place in the absorbing spectral region. Comprehensive descriptions of the nonlinear optical response can be found in the references [19–24].

2.1.1 Ultrafast Response

Ultrafast nonlinear response is characterized by the instantaneous response, weak nonlinear index changes, and weak nonlinear absorption. The formalism that describes the ultrafast changes in the real and imaginary parts of the refractive index can be derived from the theory of nonlinear polarization.

Polarization $\vec{P}(r, \omega)$ of a material in a presence of an electric field $\vec{E}(r, \omega)$ at a frequency ω is defined as

$$\vec{P}(r, \omega) = \epsilon_0 \chi(\omega) \vec{E}(r, \omega) \quad (2.1)$$

where ϵ_0 is the permittivity of free space and $\chi(\omega)$ is the dielectric susceptibility tensor. $\chi(\omega)$ is related to the index of refraction $n(\omega)$ by

$$\chi(\omega) = n^2(\omega) - 1. \quad (2.2)$$

In a nonlinear material $\chi(\omega)$ is not constant with electric field and the influence of $\vec{E}(r, \omega)$ on $\vec{P}(r, \omega)$ is not linear. In this case it is customary to expand $\vec{P}(r, \omega)$ in a power series of $\vec{E}(r, \omega)$

$$\begin{aligned} \vec{P}(r, \omega) = & \epsilon_0 \chi^{(1)}(\omega) \vec{E}(r, \omega) + \epsilon_0 [\chi_{ijk}^{(2)}(\omega) \vec{E}_j(r, \omega) \vec{E}_k(r, \omega) \\ & + 3\chi_{ijkl}^{(3)}(\omega) \vec{E}_j(r, \omega) \vec{E}_k(r, \omega) \vec{E}_l(r, \omega) \\ & + \textit{higher order terms}], \end{aligned} \quad (2.3)$$

where $\chi^{(1)}$ is the linear susceptibility, while $\chi^{(2)}$ and $\chi^{(3)}$ are the coefficients of the second- and third-order nonlinear susceptibility.

In all known materials the higher order components of the effective nonlinear susceptibility tensor $\chi(\omega)$ yield smaller contributions to the effective polarization than the preceding terms of the same parity. On the other hand, in the presence of high electric field the terms designated as the *higher order terms* in Eq. (2.3) (i.e. terms proportional to the powers of $\vec{E}(r, \omega)$ higher than 4), can be larger than the first three terms. However, the assumption of moderate intensities and the aim to illustrate the concept of nonlinear

refractive index justifies retaining of only first three terms of Eq. (2.3) in the derivation that follows.

This work will concentrate on the nonlinear effects in which intense light changes the refractive index. Under such conditions there are no DC or low-frequency electro-optic effects present and the second term in Eq. (2.3) can be neglected. $\vec{P}(r, \omega)$ reduces to

$$\begin{aligned}\vec{P}(r, \omega) &= \epsilon_0[\chi^{(1)}(\omega) + 3\chi^{(3)}(\omega)\vec{E}(r, \omega)\vec{E}(r, \omega)]\vec{E}(r, \omega) \\ &= \epsilon_0 \left[\chi^{(1)}(\omega) + \frac{6\chi^{(3)}(\omega)I}{\epsilon_0 n_0 c} \right] \vec{E}(r, \omega),\end{aligned}\tag{2.4}$$

where I is the local intensity

$$I = \frac{\epsilon_0}{2} n_0 c |E(\omega)|^2,\tag{2.5}$$

and c is the speed of light in vacuum.

The first term in Eq. (2.4) represents the linear contribution to the polarization and the second term represents the nonlinear, intensity-dependent part. This intensity-dependent part gives rise to the nonlinear index of refraction fundamental to this work.

To obtain the direct expression for the nonlinear refractive index the effective susceptibility from Eq. (2.4) is substituted into Eq. (2.2).

$$n^2 = 1 + \chi^{(1)} + \frac{6\chi^{(3)}(\omega)I}{\epsilon_0 n_0 c}\tag{2.6}$$

In order to relate directly this nonlinear part of polarization to the intensity-dependent part of refractive index — a macroscopic measurable quantity — the effective index of refraction is expressed as

$$n = n_0 + n_2 I.\tag{2.7}$$

Taking a square of Eq. (2.7) and neglecting the terms proportional to I^2 under the assumption of weak relative nonlinearity ($n_2^2 I^2 \ll n_0 n_2 I \ll n_0^2$) gives

$$n^2 = n_0^2 + 2n_0 n_2 I.\tag{2.8}$$

Equating Eq. (2.6) and Eq. (2.8) gives an expression for n_2

$$n_2 = \frac{3\chi^{(3)}}{\epsilon_0 n_0^2 c}, \quad (2.9)$$

where all the factors are in SI units.

In general, n_2 can have real (Re) and imaginary (Im) parts with n_{2Re} responsible for the nonlinear refraction and n_{2Im} responsible for the nonlinear absorption or gain. There are many conventions used to express the real and imaginary parts of the nonlinear refractive index. The approach used by researchers must be always determined prior to the comparison of the absolute numbers. However, in general it is safe to write

$$n_{2Re} = \frac{K}{n_0^2} Re[\chi^{(3)}] \quad (2.10)$$

and

$$n_{2Im} = \frac{K}{n_0^2} Im[\chi^{(3)}], \quad (2.11)$$

where constant K depends on the convention and units used [24].

In the rest of the work n_2 will be used to express the real part of ultrafast nonlinear index of refraction, i.e. n_2 will be as used in Eq. (2.10).

In order to account for the imaginary component of the ultrafast nonlinear response in a commonly used way the following relationship is defined

$$\alpha = \alpha_0 + \beta I. \quad (2.12)$$

Eq. (2.12) expresses total absorption (α) in terms of its linear (α_0) and nonlinear (βI) contribution. β is the measurable, macroscopic quantity that will be used throughout this work to quantify the effects of ultrafast imaginary nonlinear response, i.e. a two photon absorption.

2.1.2 Ultrafast Nonlinear Material Figures of Merit

A nonlinear material useful in a nonlinear optical signal processing device must simultaneously satisfy the following conditions:

- The excitation time of the nonlinear effect must be less than the pulse width.
- The sum of the excitation and the relaxation times must be shorter than the pulse spacing.

In addition, an ultrafast nonlinear material must satisfy the following requirements:

- The effect of linear absorption must be weak compared to the effect of nonlinear refraction. Stegeman quantifies this condition in terms of the unitless figure of merit W [14]

$$W = \frac{|\Delta n|}{\alpha_0 \lambda} > 1, \quad (2.13)$$

where Δn is the induced change in the real part of the refractive index, α_0 is the linear absorption (expressed in units of inverse length) and λ is the wavelength of light (units of length). To facilitate consistent comparison between different nonlinear materials, Δn in Eq. (2.13) was assumed to be evaluated as the intensity approaches the saturation intensity, at which the rate of change of the refractive index drops noticeably below a linear dependence on intensity [14]. In general Eq. (2.13) can be used to quantify the nonlinear quality of a given material at any intensity, not only at the saturation.

- The effect of two-photon absorption must be weak compared to the effect of nonlinear refraction. This condition is quantified using the figure of merit T [14]

$$T = \frac{\beta_2 \lambda}{n_2} < 1, \quad (2.14)$$

where β is the two-photon absorption coefficient from Eq. (2.12) (expressed in units of length/power).

Conditions (2.13) and (2.14) can be combined in terms of a single figure of merit F

$$F = \frac{|\Delta n|}{\alpha_{eff} \lambda} > 1, \quad (2.15)$$

where α_{eff} is the effective absorption experienced by the sample at a given intensity. F can be used to quantify the quality of materials for signal processing with respect to nonlinear processes of any order rather than with respect to only third-order processes as in (2.14).

Condition (2.15) ensures that the nonlinear phase shift $\Delta\phi^{NL} = 2\pi\Delta nL/\lambda$, where L is the length of the material, reaches 2π before the intensity decays to $1/e$ of its input value as a result of the effective absorption. Phase shifts between 0.5π and 3.5π are required for most optical switching devices [14].

2.1.3 Resonant Response

The resonant response of a nonlinear material is the dominant nonlinear effect in the absorbing spectral region. A different formalism than that presented in section 2.1.1 is used to describe the resonant changes in the real and imaginary parts of the refractive index.

Illumination with light which is resonant with the material results in the direct absorption of the incoming photons, generating excited states and giving rise to a decrease in the effective absorption. If the relaxation time of the excited states is longer than the length of the pulse, the resonant effect is proportional to the fluence, rather than to the intensity of the incident ultrafast pulse. This saturation of absorption is described by the following expression for the effective absorption α_{eff} [25]

$$\alpha_{eff} = \frac{\alpha_0}{1 + \frac{P}{P_{sat}}}. \quad (2.16)$$

where $P = \int_0^t I(t')dt'$ is the incident fluence and P_{sat} is the saturation fluence at which the effective absorption decreases to a half of its initial value. P accounts for the cumulative (up to the duration of the pulse) character of the resonant nonlinear response.

The saturation of absorption is accompanied by a change in the real part of the

refractive index [25]

$$\Delta n = \frac{n'_2 P}{1 + \frac{P}{P_{sat}}}. \quad (2.17)$$

n'_2 describes the strength of the real part of the resonant nonlinear refractive index.

In this work, nonresonant and resonant phenomena are considered. The parameters n_2 and β from 2.1.1 are used to quantify the ultrafast response and Δn and $\Delta\alpha$ from section 2.1.2 are used to describe the resonant response.

2.1.4 Resonant Nonlinear Material Figures of Merit

Figures of merit for the non-resonant response have been defined in section 1.1.3. This section will introduce resonant figures of merit that account for the nonlinear phase shift that accumulates over the duration of a pulse.

For illustrative purposes, first order approximations to Eqs. (2.16) and (2.17) of the form $\Delta n(t) = \int_0^t n'_2 I(t') dt'$ and $\alpha_{eff}(t) = \alpha_0$ are considered under the assumption $P \ll P_{sat}$. A resonant nonlinear material is assumed to be illuminated with a square pulse of the form:

$$I(t) = \begin{cases} I_0, & \text{if } 0 < t < \tau_p \\ 0, & \text{if } t > \tau_p. \end{cases} \quad (2.18)$$

In analogy to Eq. (2.15) a time-averaged nonlinear figure of merit is defined for the resonant response

$$\langle F \rangle = \frac{|\langle \Delta n \rangle|}{\langle \alpha \rangle \lambda}. \quad (2.19)$$

The time-averaged nonlinear index change is

$$\langle \Delta n \rangle = \frac{1}{\tau_p} \int_0^{\tau_p} \left[\int_0^t n'_2 I(t') dt' \right] dt = \frac{n'_2 P_{total}}{2} = \frac{|\Delta n_{peak}^{ultrafast}|}{2}, \quad (2.20)$$

where P_{total} is the total fluence of the pulse $P_{total} = \int_0^{\tau_p} I(t') dt' = I_0 \tau_p$. The time-averaged absorption is $\langle \alpha \rangle = \alpha_0$. For the case considered, the figure of merit (2.19) becomes:

$$\langle F \rangle = \frac{|\Delta n_{peak}|}{2\alpha_0 \lambda}, \quad (2.21)$$

which is half of the ultrafast figure of merit. For simplicity, Eq. (2.15) will be used throughout the thesis for both resonant and ultrafast response. The figure of merit specific to the devices introduced in this work will be derived in chapter 5.

2.2 Periodic Structures

2.2.1 Bragg Gratings

Figure (2.1) illustrates an optical Bragg periodic structure. It is made out of two materials with generally different linear refractive indices n_{01} and n_{02} .

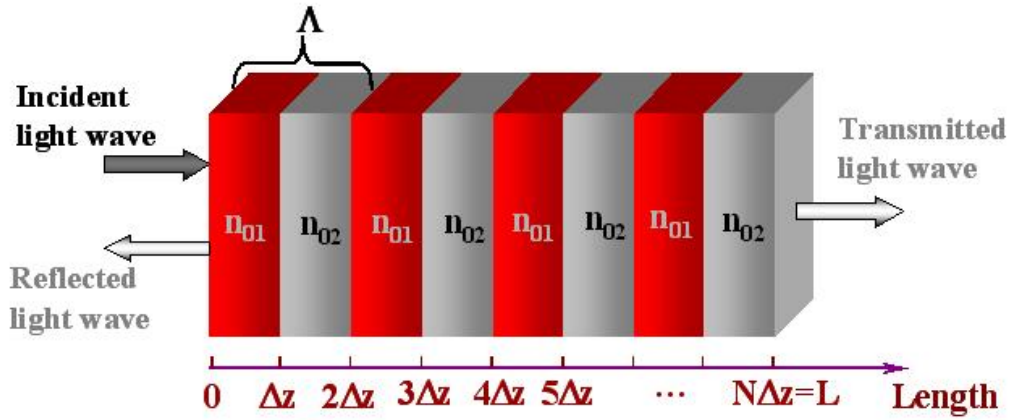


Figure 2.1: Schematic of a linear Bragg grating with period Λ : n_{01} and n_{02} are the linear refractive indices of the two adjacent layers.

The refractive indices n_{01} and n_{02} and corresponding layer thicknesses t_1 and t_2 are chosen in such a way that the period of the grating defined as $\Lambda = t_1 + t_2$ satisfies the condition of a *Bragg Resonance* [26]

$$\lambda_0 = 2\bar{n}\Lambda. \quad (2.22)$$

where \bar{n} is the average refractive index. λ_0 is the center wavelength of the stopband $\Delta\lambda$. Stopband $\Delta\lambda$ contains waves undergoing multiple coherent reflections from successive

grating periods resulting in a net reflection. The width of the *stopband* $\Delta\lambda$ is defined as

$$\Delta\lambda_{gap} \cong \frac{2}{\pi} \frac{\Delta n}{\bar{n}} \lambda_0, \quad (2.23)$$

where Δn is the difference in the refractive indices of the alternating materials. For a light within the spectral range $\Delta\lambda$, the amplitude of the forward-going wave decreases as its energy is transferred to the contradirectional wave, resulting in a reflection.

Structures that are periodic in two or three dimensions also exhibit Bragg scattering [27]. Such multidimensional periodic structures show strong coherent refractive effects over a wider angular range than observed in one-dimensional periodic structures, providing additional degrees of freedom to the design and operation of periodic optical elements.

2.2.2 Nonlinear Periodic Structures

In a periodic structure in which at least one set of layers is made out of materials exhibiting Kerr nonlinearity, the transmittance and reflectance near the Bragg resonance depend on the strength of illumination.

In the case of nonlinear periodic structures, the centre frequency of the photonic stopband ω_0 and the spectral width and depth of the stopband $\Delta\omega_{gap}$ are not fixed but are a function of the intensity I :

$$\omega_0 = \frac{\pi c}{\bar{n}(I)\Lambda}, \quad \Delta\omega_{gap} \cong \frac{2}{\pi} \frac{|\Delta n(I)|}{\bar{n}(I)}. \quad (2.24)$$

This behaviour is illustrated in Figure 2.2. If one of the constituent materials exhibits positive nonlinear index change, the stopband centered initially at ω_0 widens and moves towards lower frequencies with increasing level of illumination.

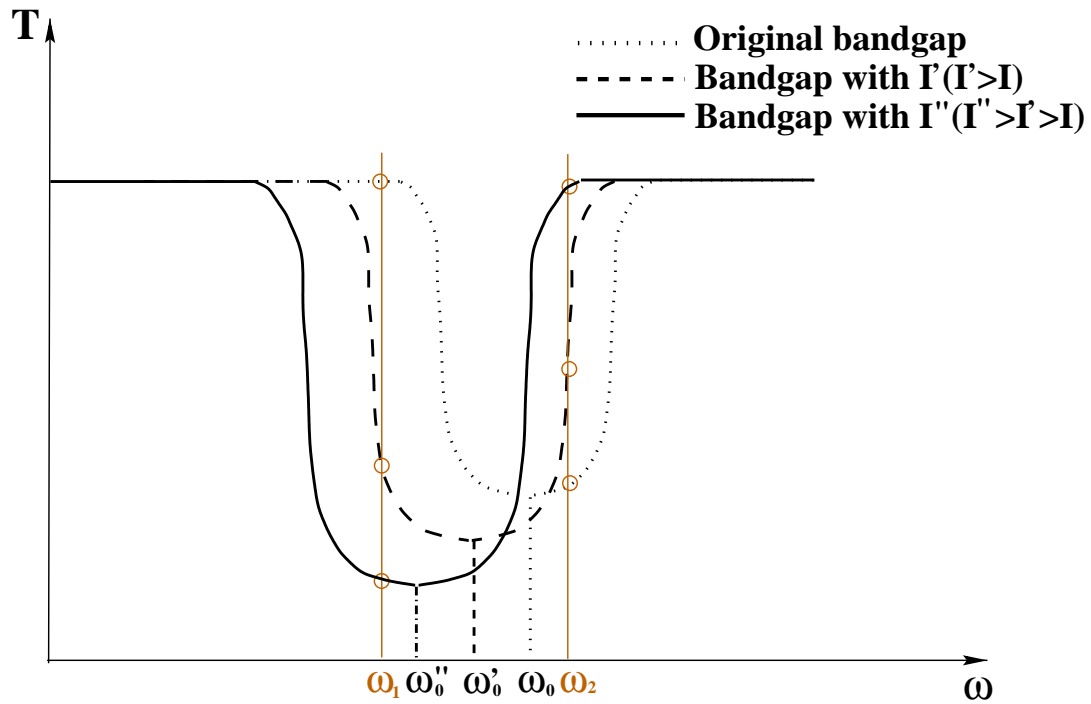


Figure 2.2: Response of a periodic structure in which one set of layers experiences positive refractive nonlinearity. The Bragg frequency ω_0 shifts to lower frequencies ω'_0 and ω''_0 and the size of the bandgap $\Delta\omega_{gap}$ increases with increasing level of illumination.

2.3 Conclusions

This chapter introduced the fundamental concepts central to the understanding of this thesis. Expressions for the real and imaginary parts of the ultrafast and resonant nonlinear refractive index were defined together with the pertinent material figures of merit. It was shown that the nonlinear response of periodic structures can yield illumination-dependent transfer characteristics.

Chapter 3

Literature Survey

The preceding chapters established the motivation and framework of this work. The present chapter discusses how the research on refractive nonlinear materials relevant to this work and nonlinear periodic structures has evolved, what has been discovered, and what remains to be accomplished.

3.1 Nonlinear Materials

3.1.1 Bulk and MQW Inorganic Crystalline Semiconductors

The illumination-dependent refractive and absorptive nonlinear properties of inorganic crystalline semiconductors have been studied comprehensively. Since semiconductors are at the heart of the electronics industry, semiconductor micro- and nanofabrication techniques are well established. This enables the preparation of high-quality nonlinear samples and devices. The ability to change the composition of semiconductor compounds allows the tuning of the electronic bandgap over the visible and infrared spectral ranges. The spectral position of the bandgap, in turn, tunes the nonlinear properties.

The nonlinear response of semiconductors can be divided into two groups: response when illuminated with light at a photon energy above that of the electronic bandgap

of a given semiconductor, and response to light at a photon frequency below that of a bandgap. The former kind is referred to as a resonant nonlinear response and the latter kind is referred to as a non-resonant nonlinear response.

When a semiconductor is illuminated with light at a frequency within the absorbing region, the dominant nonlinear effect relies on the presence of linear absorption. Upon absorption of the incident light, the electrons undergo a transition from the valence band to the conduction band, saturating the absorption. This bandfilling effect is accompanied by a very large change in the real part of the refractive index.

In the spectral region corresponding to the ultrafast response no single-photon absorption takes place. Upon illumination with intense light the electronic clouds of the constituent atoms are distorted, changing the refractive index of the material. Associated with it is a multiphoton absorption process. This takes place when the sum of the photon energies is larger than the bandgap energy. This effect changes the absorption characteristics of the material. Both the real and imaginary parts of ultrafast nonlinear index must change given their connection through the nonlinear Kramers-Kronig relations.

In addition, when subjected to an intense continuous-wave or a high-repetition rate pulsed illumination, the temperature of absorbing materials including semiconductors increases. This in turn changes the refractive index. Thermal effects have relaxation times as long as milliseconds and are not useful in processing trains of closely-spaced pulses.

Figure 3.1 shows typical trends in the non-thermal nonlinear response of bulk inorganic crystalline semiconductor material under picosecond, low-repetition rate illumination.

Resonant Nonlinearities

The two most important characteristics of resonant nonlinear response are saturation of absorption and large nonlinear index change [28–30]. The relaxation times of resonant

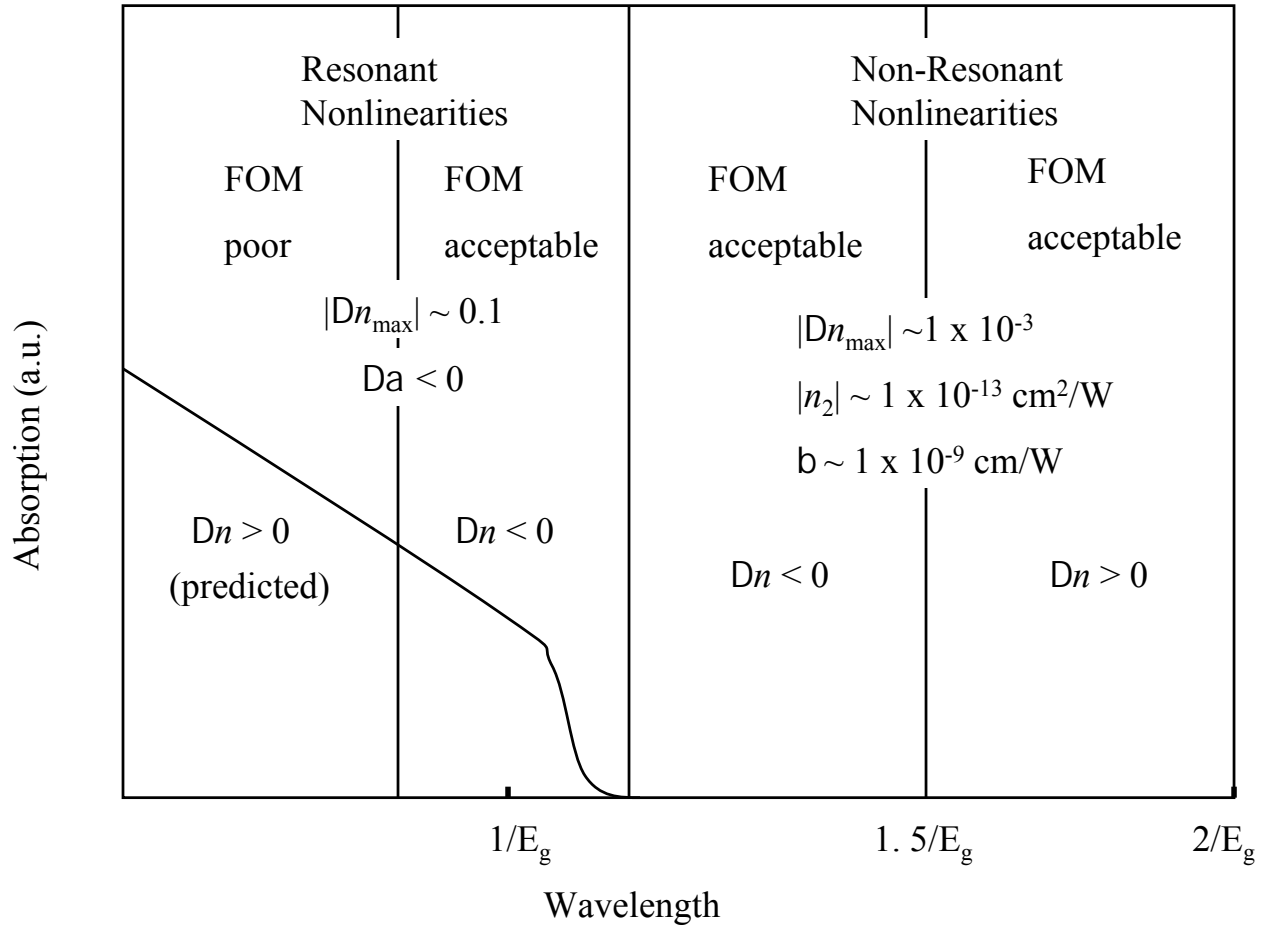


Figure 3.1: Trends in the nonlinear response of bulk semiconductors.

nonlinear effects in semiconductors are not instantaneous. As long as the duration of the incident pulse is shorter than the relaxation time of the material, the magnitude of a nonlinear resonant response is proportional to the fluence, rather than to the intensity of the incident pulse. The relatively long relaxation time of nonlinear effects in bulk and MQW inorganic crystalline semiconductors (from 100s of picoseconds to 10s of nanoseconds) is often used as an argument against using resonant nonlinearities. However, established techniques such as low-temperature growth and doping can reduce the relaxation time down to tens of picosecond [31, 32].

The phenomenon of saturation of absorption translates into absorption that decreases

with increasing incident fluence. This phenomenon will be observed in many of the material systems studied in this work.

Resonant figures of merit of semiconductors are acceptable near the bandedge and become worse at lower wavelengths. Such a behaviour is due to a stronger, lower-threshold saturation of absorption around the bandedge.

Nonlinear index change is negative around the bandedge and has been predicted to be positive at wavelengths lower than corresponding to the first heavy hole and light hole excitonic peaks [33].

Decreasing Relaxation Times of Resonant Nonlinearities in Bulk Semiconductors

In 1991 Gupta *et al.* measured the time of nonlinear response GaAs grown at low temperatures (LT-GaAs) [34]. Changes in reflectivity were monitored during a pump-probe experiment at 620 nm. Relaxation times of several 2 μm thick samples grown at temperatures ranging between 190°C and 400°C were measured. A decrease in the decay time to 0.4 ps was recorded with decreasing growth temperatures. This short relaxation time is drastically lower than the typical value of nanoseconds for unannealed GaAs [34].

In 1993 Harmon *et al.* studied the dependence of the nonlinear relaxation time in LT-GaAs on annealing temperatures. A decrease in the relaxation time down to subpicosecond values was observed with decreasing annealing temperatures [35].

In a number of papers published between 1994 and 1998 group of Smith, Othonos, Benjamin, and Loka reported on a series of comprehensive experiments carried out on various MBE-grown LT-GaAs samples. The dependence of the magnitude and the response time of nonlinear effects on the growth and annealing temperatures was studied. Very large negative nonlinear index changes were measured ($\Delta n_{max} = -0.13$) accompanied by a strong saturation of absorption [36]. The relaxation time was measured to decrease to a few picoseconds for samples grown at 500°C [37]. The pump-probe measurements were carried out in the bandedge region at wavelengths ranging from 870 nm to 890 nm. The decreased response time was attributed to fast decay of excited carriers to mid-gap

states. These states are an effect of the LT growth [32].

In the following years another group of researchers studied the strength and dynamics of intensity-dependent response in InGaAsP doped with Be grown with He-plasma-assisted MBE. As illustrated in Figure 3.2, subpicosecond relaxation times were obtained [38]. The rapid decay was explained by a short lifetime of excited states due to the existence of mid-gap He and He-Be trap states. Again, large negative changes in the real part of the refractive index and strong saturation of absorption were observed [31].

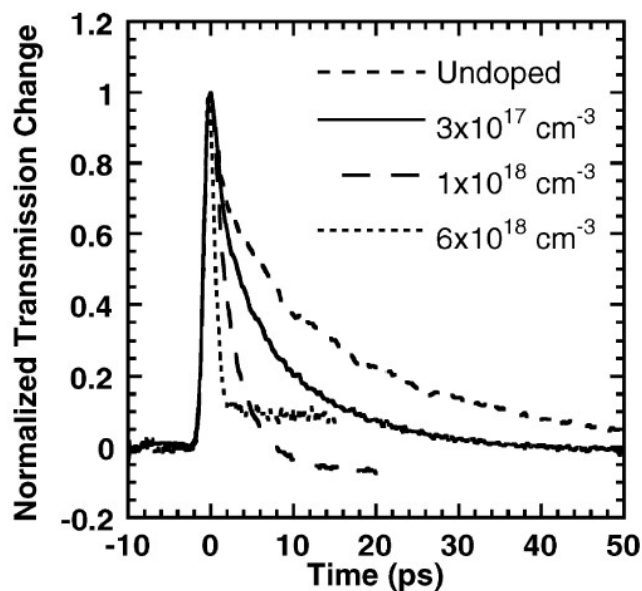


Figure 3.2: Results of the pump-probe measurements illustrating the time-resolved change in transmission for He-InGaAsP samples with different Be doping concentrations. This figure was reproduced from Ref. [37].

Resonant Nonlinearities in Semiconductor Multi-Quantum-Wells

The nonlinear properties of semiconductor multi-quantum-wells (MQWs) are similar to those of bulk semiconductors [30,33,39]. The nonlinear response in MQWs around the bandedge is stronger and begins at lower fluences than in bulk materials. The changes in the real part of refractive associated with the bandedge nonlinear response of semiconductor MQWs will be used in chapters 10 and 11 of this work to trigger the nonlinear

response of a nonlinear superlattice and Bragg periodic structures.

Compared with bulk semiconductors, semiconductor MQWs offer an additional degree of freedom in selecting their nonlinear properties. The effective electronic bandgap of a given semiconductor MQW structure, and hence the dispersion of real and imaginary parts of its linear and nonlinear refractive index, are influenced by two factors: the choice of the compositions of constituent compound and the well-to-barrier thickness ratio.

In 1982 Miller *et al.* reported on the measurements of resonant nonlinear properties of semiconductor MQWs. A very strong absorption saturation was noticed around the first excitonic peak in GaAs/AlGaAs MQWs. Based on these results a large refractive nonlinearity was deduced from the nonlinear Kramers-Kronig relation [40]. A theoretical paper followed explaining the dynamics of transient excitonic nonlinearities [41]. A 20 ns excited carrier relaxation time was predicted.

In 1986 Lee *et al.* measured the nonlinear saturation of absorption of bulk GaAs and 29.9 nm GaAs/AlGaAs wells grown by molecular beam epitaxy. The measurement was performed using a monochromatic pump and a broadband probe over a 40 nm spectral range near the MQW bandedge. Using the nonlinear Kramers-Kronig relation, large index changes of both signs were predicted. In MQWs, absorptive and refractive nonlinearities were enhanced compared to bulk GaAs. Index changes ranging from $\Delta n = -0.06$ to $\Delta n = 0.03$ were predicted in the samples analyzed [42].

This report was followed in 1988 by a study of nonlinearities around the bandedge by the same group [30]. The response of bulk GaAs was compared with that of three sets of GaAs/AlGaAs MQWs, with well thicknesses of 7.6 nm, 15.2 nm and 29.9 nm. Again, a strong saturation of absorption was measured and nonlinear index changes of both signs were predicted from the nonlinear Kramers-Kronig relation [43]. The magnitude of the change in the real part of the refractive index was predicted to increase with decreasing well size. The sign of the refractive nonlinearity changed at wavelengths slightly shorter

than that corresponding to the first excitonic peak [30].

From 1988 on, many results of research on nonlinear properties of GaAs/AlGaAs MQWs were reported by Elsa Garmire *et al.* In a series of papers, the saturation of absorption was studied in GaAs/AlGaAs MQWs grown by metalorganic chemical vapor deposition epitaxy. The nonlinear Kramers-Kronig relation was used to predict the associated change in the real part of the refractive index. Figure 3.3 shows the predicted enhancement of nonlinearity with decreased well size and change of sign near the excitonic peak. Attempts were made to use the illumination-dependent shift of Fabry-Perot fringes to estimate directly the negative nonlinear index change along the bandedge. However, this approach was admitted to yield significant errors, with the Fabry-Perot technique sometimes giving a value of Δn at twice the magnitude predicted from the Kramers-Kronig relation [33].

In 1987 Fox *et al.* reported nonlinear measurements around the bandedge of bulk GaInAs [44] and GaInAs/InP MQWs near the wavelength of $1.6 \mu\text{m}$ [45]. Full saturation of absorption was observed. The nonlinear index changes deduced from the nonlinear Kramers-Kronig relation were slightly larger than that observed in GaAs [25].

In 1996 Judawlikis *et al.* reported the decreased nonlinear relaxation time in LT-grown Be-doped InGaAs/InAlAs MQWs. Nonlinear relaxation times of a few tens of picoseconds were observed in a pump-probe experiment near the bandedge. The nonlinear change in the real part of the refractive index was not reported [46].

A different approach to decrease the response times of bandedge nonlinearities of semiconductor MQWs was taken by groups of White, Sibbet, and Adams. An electric current was applied to active InGaAsP/InP waveguides and the nonlinear optical response under electrical bias was studied. It was found that under a forward bias the refractive nonlinear response was quenched. Under a reverse bias the nonlinear response was slightly reduced, but the initially long recovery time was reduced to 50 ps [47] and 18 ps in subsequent experiments [48]. Further, it was found that when the waveguide was

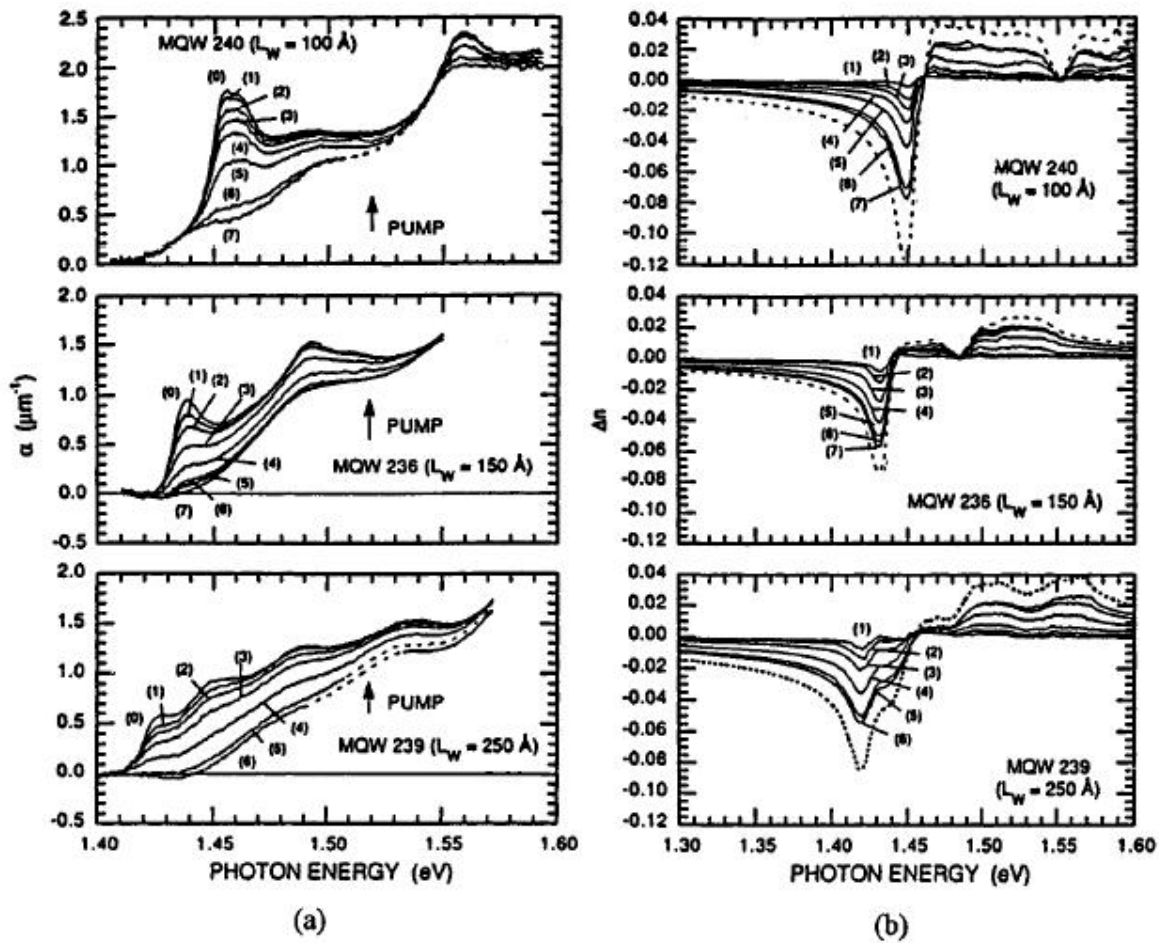


Figure 3.3: Spectra of GaAs/AlGaAs MQWs of three different well widths, measured at various incident intensities by pulsed pump at 1.52 eV: (a) absorption coefficient, α , (b) the change in the real part of the refractive index, Δn . This figure was reproduced from Ref. [38].

biased at transparency, the nonlinear coefficients of the semiconductor MQW waveguides were $n_2=4\times 10^{-11}$ cm²/W and $\beta=4\times 10^{-9}$ cm/W, giving a combined figure of merit of $F = 7$ [49]. In all measurements the negative nonlinear index changes were measured to have magnitude smaller than $|\Delta n| < 0.001$ [50].

Non-Resonant Nonlinearities

Non-resonant nonlinearities are not triggered by direct electronic transitions due to single-photons. Much weaker effects of distortion of electronic clouds and multi-photon absorption are responsible for non-resonant nonlinear response. Maximum non-resonant nonlinear index changes are of the order $|\Delta n_{max}| \sim 1 \times 10^{-3}$. Since in certain spectral regions a typical non-resonant Kerr coefficient is $n_2 \sim 1 \times 10^{-13} \text{ cm}^2/\text{W}$, linear absorption is around 5 cm^{-1} , and the corresponding two photon absorption coefficient is $\beta \sim 1 \times 10^{-9} \text{ cm/W}$, the figures of merit associated with non-resonant semiconductor nonlinearities can be acceptable.

The biggest advantage of non-resonant semiconductor nonlinearities is their sub-picosecond response time. The sum of rise and relaxation times of non-resonant non-linearity has been argued to be comparable to the orbital period of an electron in its motion about the nucleus, estimated to be around 10^{-16} s [19].

Depending on the spectral region, bulk and MQW inorganic crystalline semiconductors may exhibit either positive or negative refractive non-resonant nonlinearities. Under illumination with sub-nanosecond pulses at low repetition rates, the nonlinear index change is negative for wavelengths up to $1.5 \frac{ch}{E_g}$, where $\frac{ch}{E_g}$ is the wavelength corresponding to the bandgap, and h is Planck's constant. Δn is positive for wavelengths longer than $\frac{1.5ch}{E_g}$ [29, 51]. In MQWs the spectral position of the sign change in Δn depends on the nanostructure of MQWs [52]. In 1993 Shaw and Jaros predicted through theory the dispersion of refractive nonlinearity in semiconductor MQWs and superlattices. They found that in MQWs the proximity of the spectral position of the Δn sign change to the bandedge increases with increasing quantum confinement [52].

Under non-resonant illumination with pulses longer than one nanosecond, there is no sign change in the refractive nonlinearity. The negative nonlinearity originating from two photon absorption-induced free-carrier-effects is much stronger than any positive third-order refractive effects at moderate and high intensities for $\frac{hc}{E_g} < \lambda < \frac{2hc}{E_g}$. Consequently,

the measured Δn is always negative in this spectral range [53].

Since the experimental part of this thesis does not deal with non-resonant nonlinear response, the discussion that ensues will be brief and restricted to describing major developments in predicting and measuring trends in the below-the-bandgap nonlinear response. In particular, the following discussion will describe the evidence for the existence of both positive and negative refractive nonlinearities with acceptable figures of merit.

The group of Sheik-Bahae and Van Stryland has authored several reports on predicting the spectral dependence of non-resonant nonlinearities in semiconductors. In 1985 Van Stryland *et al.* predicted trends in the absorptive ultrafast nonlinear response of semiconductors. An equation for the below-the-bandgap two photon absorption was derived and compared with experimental values. Dispersion of two photon absorption is expected to mimic the dispersion of linear absorption; i.e. two photon absorption is strong and relatively flat from bandgap to almost half-bandgap, at which point it goes to zero. Good agreement was obtained between experiment and theory for photon energies not in the vicinity of the bandgap, with two photon absorption coefficients of various semiconductors ranging from $\beta=3\times 10^{-9}$ cm/W to $\beta=25\times 10^{-9}$ cm/W [28].

In the ensuing years the same research group reported the theory describing the spectral dependence of the real part of the ultrafast nonlinearity and compared it with experiments. The results are shown in Figure 3.4. The magnitude of n_2 is largest near the photon energy corresponding to half of the bandgap. Since for wavelengths longer than corresponding to half bandgap two-photon-absorption vanishes, large figures of merit can be expected in these spectral region. In addition, n_2 was predicted to be positive for wavelengths longer than that corresponding to $0.75 E_g$, and negative between $0.75 E_g$ and E_g [29, 54]. A large discrepancy between theoretical and experimental results was observed near the bandgap where the theory drastically underestimated the strength of refractive nonlinearity.

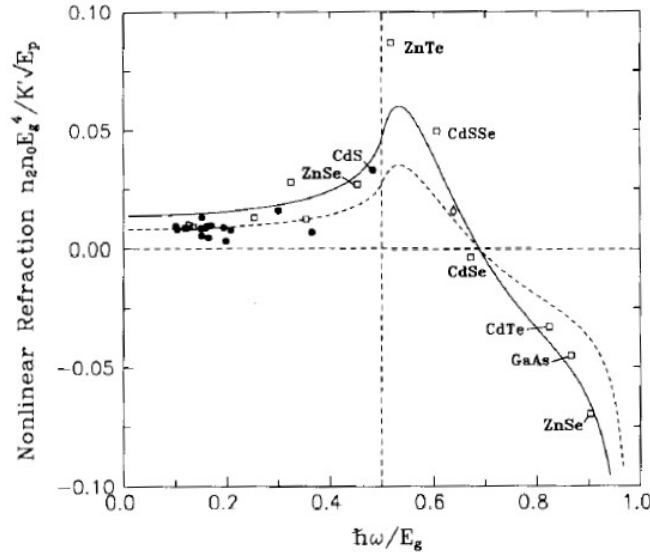


Figure 3.4: Data of scaled n_2 measured at $1.06 \mu\text{m}$ for various bulk inorganic crystalline semiconductors. This figure was reproduced from Ref. [29].

3.1.2 Organic Materials

Organic materials constitute another class of promising nonlinear materials. Organic materials exhibit significant nonlinearities across the visible and infrared spectral regions [55]. They are readily processable into thin-film waveguide structures [23, 56] and in general do not rely on a high degree of perfection in ordering or purity to manifest their desired properties. The molecules which make up organic materials provide a tremendous range of structural, conformational, and orientational degrees of freedom for exploration with the aid of novel synthetic chemistry. This permits flexible modification and optimization of linear and nonlinear properties [23].

As in the case with semiconductor nonlinearities, the nonlinear response of organic materials can be divided into resonant and non-resonant, occurring in the absorbing and transparent regions, respectively. The resonant nonlinearities are a result of a single-photon absorption, while the non-resonant nonlinearities arise as a result of perturbations of electronic clouds and multi-photon absorption.

Depending on the structure of constituent molecules, organic materials may exhibit many absorption resonances and hence many spectral areas of different strength and sign of nonlinear response. Phenomena such as molecular reorientation and photoisomerization, which are often found in organic materials, make the picture even more complex.

Nonlinear organic dyes are one class of organic materials that has been studied comprehensively. Among nonlinear dyes, azobenzenes have received special attention. Azobenzenes have been shown to exhibit large, low-threshold nonlinear index changes as a result of optically-induced structural changes in the middle and near the edge of the absorption resonance [57]. The nonlinear index changes associated with this photochemical phenomenon, called *trans-cis photoisomerization*, will be used in chapter 12 of this work to trigger the nonlinear response of a three-dimensional nonlinear colloidal crystal.

Most nonlinear dyes (among them azobenzenes) have only one absorption resonance, which permits to qualitatively predict their nonlinear response in the visible and near-infrared regions. Figure 3.5 shows the nonlinear response of a typical nonlinear organic material with one absorption resonance.

In general, the figures of merit of organic materials in the absorbing region are poor. However, molecular effects such as *trans-cis* photoisomerization strongly increase the nonlinear index change along the absorption edge. The magnitudes of ultrafast nonlinearities and associated figures of merit of organic materials are comparable to those of inorganic crystalline semiconductors.

3.1.3 Nanocrystals

Nanoscale quantum-confined inorganic crystalline semiconductors represent an interesting group of nonlinear materials [58]. The size of such quantum dots is less than the bulk radii of excitons, holes, and electrons in a given semiconductor. As in the case of semiconductor MQWs, this results in quantum confinement of carriers. In a nanocrystal, this takes place in all three dimensions [59,60]. Quantized energy levels make nanocrystals an

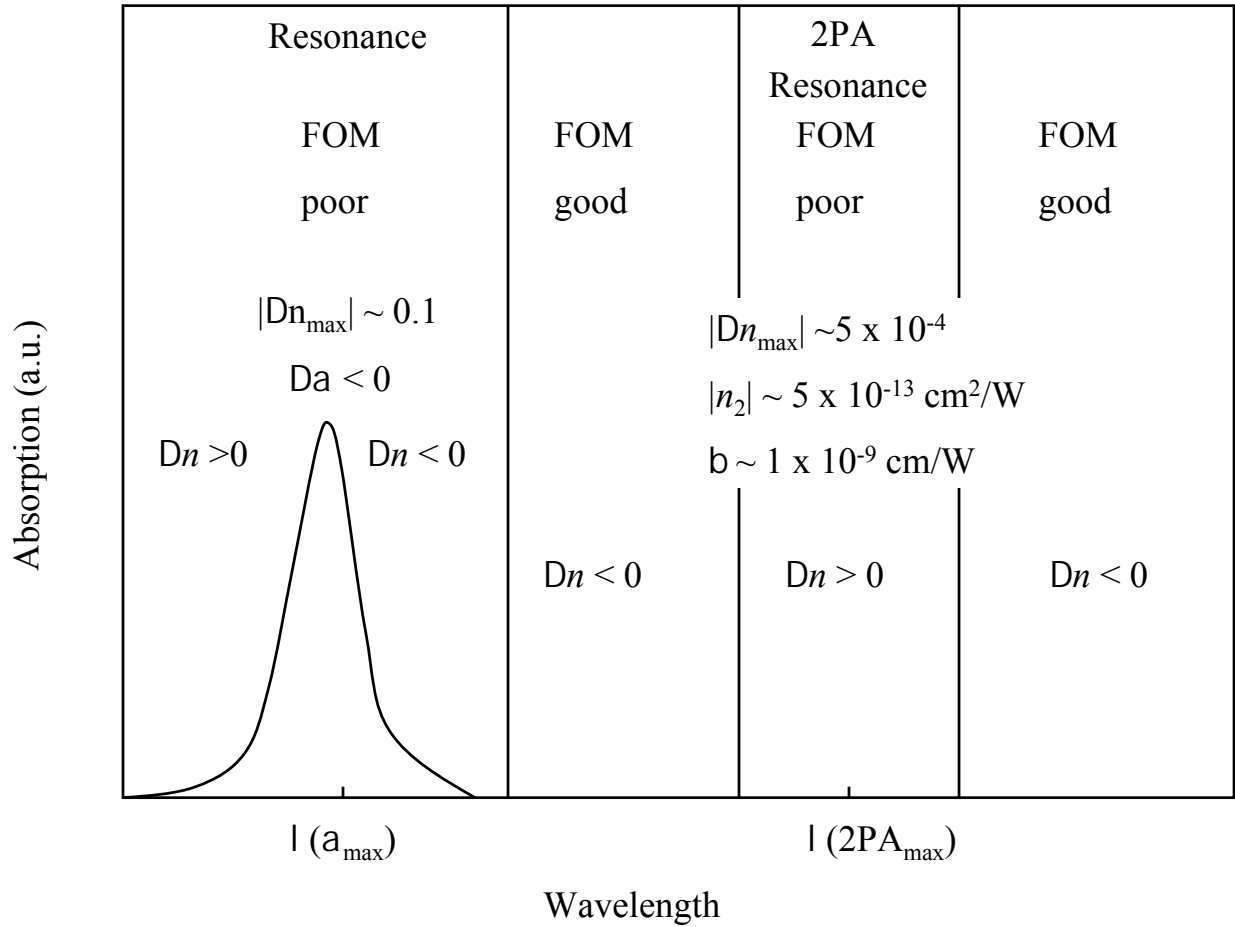


Figure 3.5: Typical trends in the nonlinear response of organic materials with one absorption resonance.

artificial analogue of non-interacting atoms in a gas, raising the possibility of explaining the nonlinear processes by adopting the models of atomic physics.

To allow processability nanocrystals are usually embedded in either solid or liquid optically linear organic or glass hosts. Nanocrystal material systems are thus hybrids of semiconducting and insulating materials and combine interesting properties from both material groups. As in the case of semiconductor MQWs, the composition and size of quantum dots determines the energy of electronic transitions. This allows spectral tunability of absorption features and nonlinear properties over the entire visible and infrared

spectrum. On the other hand, the organic or glass host permits flexible fabrication of samples, waveguides, and other integrated components using polymer photonics technologies [61].

Figure 3.6 shows the properties of a typical resonant and non-resonant nonlinear response of strongly-confined semiconductor nanocrystal composites. The data presented in this figure are based on the published theoretical predictions and experimental reports.

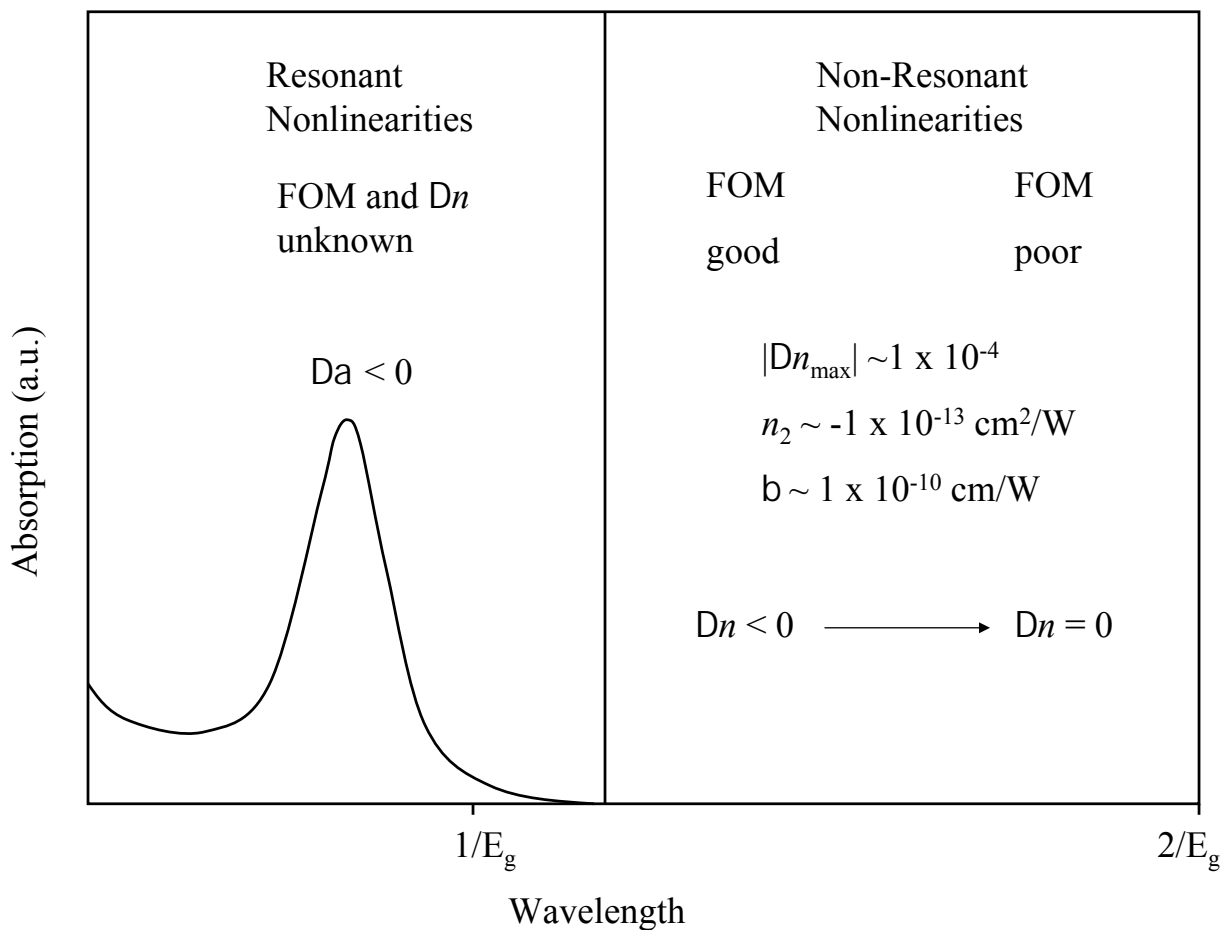


Figure 3.6: Trends in the picosecond nonlinear response of inorganic semiconductor nanocrystals.

The finite number of allowed lower electronic levels leads to more pronounced excitonic features and resonant nonlinearities that take place at lower fluences than in bulk or

MQW semiconductors [62].

Similarly to the nonlinear response of bulk and MQW semiconductors, the resonant nonlinear response of nanocrystals is characterized by the saturation of absorption and the large changes in the real part of the refractive index associated with it.

Saturation of absorption in strongly-confined PbS quantum-dot glasses was measured in the 1.2 μm to 1.3 μm spectral range [63], covering the spectral position of the valley between the first and second excitonic peak in the 6.6 nm diameter sample studied. This material system was used as a passive saturable absorber in the production of 4.6 ps pulses via mode-locking around the wavelength of 1.3 μm [63]. The report was followed by studies of saturation of absorption dynamics in quantum dots of various sizes at a wavelength of 1.3 μm . This wavelength covered spectral regions ranging from first to second electronic transitions depending on the size of a nanocrystal. The saturation energy and nonlinear decay times at a given wavelength were found to decrease with increasing size of nanocrystals [64]. Values for the refractive nonlinearity were not reported.

Lu *et al.* measured the nonlinear refractive properties of strongly-confined PbS nanocrystals of mean diameter 3.3 nm with polymeric coatings in the spectral range 580 nm to 630 nm. This spectral range corresponds to the wavelengths around the first excitonic peak. The degenerate four wave mixing technique was used to measure the nonlinear susceptibility of nanocrystals near the photon energy of the first electronic transition at 595 nm. The values were found to range between $\chi^{(3)} = 1 \times 10^{-6}$ esu and $\chi^{(3)} = 1 \times 10^{-5}$ esu. Combined with the 50 kW/cm² intensity used in the experiment such values of $\chi^{(3)}$ suggest maximum nonlinear index changes of $\Delta n \approx 0.013$. No data on saturation of the absorption were reported.

The non-resonant nonlinear response of nanocrystals shows different dispersion characteristics than that of any other material group. Under illumination with picosecond pulses, the non-resonant nonlinear index change is negative for photon energies between half-bandgap and bandgap, at which point the index change disappears entirely [65].

Such a response is in contrast to the Δn sign change between absorption and two-photon absorption resonances as observed in bulk semiconductors and organic materials. However, similar to the non-resonant response of bulk semiconductors, the sign of the non-resonant nonlinearity depends on the duration of the pulses used to measure the nonlinear effect in some spectral ranges. For pulses shorter than 1 ps the contribution of third-order positive refractive effects is comparable to that of the negative free carrier absorption nonlinearities. Consequently, the measured Δn can be positive [53].

It has been predicted through theory that in the spectral region close to the absorption edge the third-order non-resonant nonlinear refraction effects could be as large as $n_2 \sim 1 \times 10^{-13} \text{ cm}^2/\text{W}$ with nonlinear absorption of $\beta \sim 1 \times 10^{-10} \text{ cm}/\text{W}$ [66]. This would result in a nonlinear figure of merit $T \sim 0.6$. Most of the experimental data suggest that non-resonant n_2 coefficients are in reality at least an order of magnitude smaller [67, 68].

3.1.4 Other Nonlinear Materials

Metallic nanocomposites and cascaded 2nd order materials are two other promising groups of nonlinear materials. Metallo-organic nanocomposites are made out of metallic quantum dots embedded in organic or glass hosts. Resonant nonlinear properties of copper [69] and silver nanoparticles [70, 71] embedded in the glass host were measured using degenerate four wave mixing experiment at visible wavelengths. The nonlinear coefficients and figures of merit of metallic nanocrystals characterized were similar to those of semiconductor nanocrystals and reached a maximum near the plasma-frequency absorption peak.

It has been argued that metallic nanoparticles can potentially exhibit stronger nonlinear effects than other material systems [72]. This is associated with local field effects that enhance nonlinear response of the composite systems if the refractive index of the nonlinear constituent is lower than that of the linear host. Such a scenario can be realized in metallic nanoparticle-glass composites, since around the spectral positions of the

plasma resonance the refractive index of metals can be lower than 1.

Cascaded refractive nonlinear material systems are made out of materials with second order nonlinear properties. An appropriate design results in a net accumulated phase shift for the illumination at a fundamental optical frequency at the end of a cascaded system. Cascaded material system acts as an effective 3rd order nonlinear material [73–75]. However, cascaded materials do not lend themselves naturally to the fabrication of the third order nonlinear Bragg periodic structures considered in this work, since each section of the cascade has to be many wavelengths long in order to accumulate sufficient phase shift.

3.2 Nonlinear Periodic Structures

The remainder of this chapter will discuss published results on nonlinear periodic structures. To date, research on nonlinear periodic structures has concentrated on: steady-state bistable response and the presence of stationary gap solitons; studies of reflection and transmission properties of, and localization of light, in nonlinear partially disordered structures; propagation of Bragg solitons and pulse compression; and several experimental demonstrations of nonlinear stopband shifting.

3.2.1 Steady-State Response of Nonlinear Optical Elements

Bistable Optical Elements and Stationary Gap Solitons

In a bistable nonlinear element the value of transmittance depends on whether the incident intensity is increasing or decreasing, i.e. the transmittance depends on its previous state and the strength of incident illumination. This behaviour is illustrated in Figure 3.7. The hysteresis loop present in the transfer characteristics of bistable elements enables steady-state optical memory operation.

In the late 1970s and early 1980s a number of research groups predicted and demon-

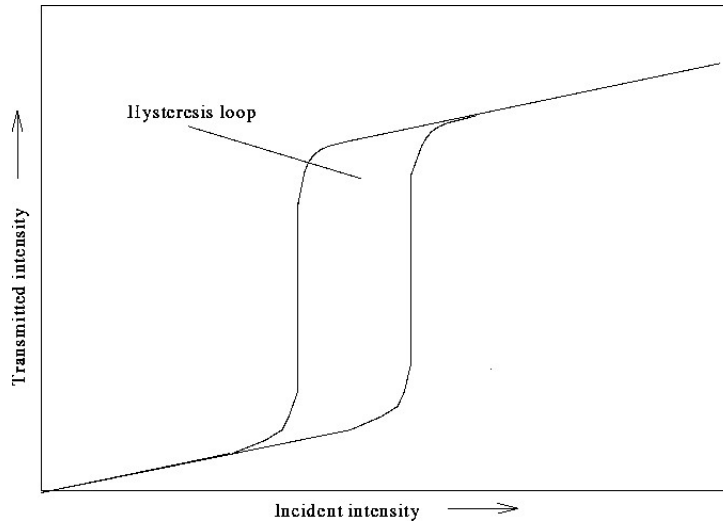


Figure 3.7: The transmitted versus incident intensity characteristic of a bistable optical element exhibiting a hysteresis characteristic.

strated steady-state optical bistability in a nonlinear Fabry-Perot interferometer. In a number of publications the groups of Smith and Gibbs reported bistability in an electro-optically biased crystal in free-space [10, 76] and integrated [9, 77] configurations, determined threshold conditions for bistability in terms of the incident power and strength of the nonlinearity [78], and demonstrated optical bistability in dielectric [79] and semiconductor [78, 80] materials. These achievements were summarized in [81] and a book [82], both written by Gibbs and published in 1985.

In 1979 Winful *et al.* published the theory of bistability in distributed feedback structures. Analytical expressions for the intensity-dependent transmissivity were provided [83]. In the following years additional reports provided analyses of: the effects of linear absorption on the response of nonlinear periodic structure [84], the response of a periodic nonlinear element to non-monochromatic illumination [85], a combined distributed feedback — Fabry-Perot interferometer structure [86], and coupling between various modes in a nonlinear fiber Bragg grating [87].

In 1992 He *et al.* reported experimental demonstration of optical bistability in non-

linear periodic structures. The optical element analyzed consisted of 30 GaAs/AlGaAs Bragg periods. Strong bandedge nonlinearities were used in the spectral region of 875 to 885 nm. A shift in the reflectivity peak with increasing intensity was observed when the sample was illuminated with 10 μ s square pulses [88].

In 1993 Herbert *et al.* experimentally demonstrated bistability and multistability in a colloidal crystal exhibiting electrostrictive nonlinearity illuminated with continuous-wave light at 514.5 nm [89].

In 1996 Li *et al.* discussed the dependence of the strength of bistability on the sign of the real part of nonlinearity. It was concluded that for a positive Kerr nonlinearity the transmission is severely suppressed near the low-energy end of the stopband, while for a negative Kerr nonlinearity the transmittance increases [90].

The field of optical bistability in nonlinear periodic structures was summarized by Lidorikis *et al.* in a paper published in 1997. The strength of the bistable behaviour was analyzed with respect to the spectral position relative to the center of the stopband [91].

Bistable structures in general also support stationary gap solitons. Stationary gap solitons are fully-transmissive continuous-wave states whose electric field envelope distribution within a nonlinear periodic structure resembles the $\text{sech}^2(z)$ shape of a temporal soliton. In a stationary gap soliton the intensity inside the structure is higher than the incident intensity. This is in contrast to the fully-transmissive states at wavelengths that are far from the Bragg resonance in which the intensity distribution is uniform across the structure. Stationary gap solitons arise under monochromatic continuous-wave illumination of a nonlinear periodic structure at a wavelength lying within the initial built-in photonic stopband [92]. Nonlinear refraction changes the position and shape of the stopband. The transmittance of the structure can change from low to high as the stopband is shifted entirely away from the spectral position of the light. The concept of a stationary gap soliton was first introduced in 1987 by Chen and Mills [93] with Mills and Trullinger [94] later analytically predicting the existence of stationary gap solitons.

Disordered Nonlinear Periodic Structures

The optical response of linear and nonlinear disordered structures that are periodic on average preserves in part the scattering properties of perfectly ordered structures, but it exhibits additional effects.

In 1987 John for the first time discussed localization of light in disordered systems that are periodic on average. It was found that when partial disorder breaks the perfect periodicity, light-trapping microcavities are formed [95]. In the ensuing years additional work was reported on partially disordered periodic structures with analysis of: the dependence of the localization length on the degree of disorder [96–98], the localization of light in three-dimensional random dielectric media [99], reflection from disordered point-like scatterers [100], and scattering from randomly-distributed two-dimensional dielectric cylinders within a planar metallic waveguide [101].

Simultaneously with the work on linear partially randomized structures, research was carried out on nonlinear disordered structures. It was found that in partially disordered systems in which at least one material exhibits Kerr nonlinearity, the decay length of intensity increases, with the intensity decreasing closer to $1/x$ than to $1/x^2$ (as in the case of fully-ordered periodic structures) with distance x from its maximum [102, 103]. In 1988 Li *et al.* further analyzed the effects of nonlinearity on transmittance through partially disordered structures. It was found that, depending on the magnitude of the Kerr coefficient, the decay length at any spectral position can vary from $1/x$ to $1/\sqrt{x}$ with stronger nonlinearity increasing the decay length [104].

3.2.2 Propagation of Solitons in Nonlinear Periodic Structures

Investigations of pulse propagation in nonlinear periodic structures have concentrated on Bragg solitons and a pushbroom switching effect.

Bragg solitons are solitary waves: they propagate without changing their shape. In

the case of a nonlinear periodic structures, solitonic propagation occurs due to the balance of the effects of grating dispersion and nonlinear self-phase modulation [105].

In 1985 and 1988 Winful and Sipe [105, 106] and de Sterke and Sipe [107] showed that near the edge of a stopband in a Bragg nonlinear periodic structure, the nonlinear Schrödinger equation can be solved to yield soliton solutions for the propagation of optical pulses.

In 1989 Christodoulides and Joseph [108] and Aceves and Wabnitz [109] analyzed propagation of pulses with carrier frequencies close to the centre of the stopband and with power spectra within the stopband. Since the nonlinear Schrödinger equation assumes weak coupling between counterpropagating modes it cannot be used to describe the scenario in which a significant amount of pulse intensity is continuously transferred back and forth between the counterpropagating modes. Coupled mode theory that allows strong coupling was used to analyze such a system. It was shown that soliton solutions exist and that the velocity of these solitons can vary from 0 to the speed of light. The slower speed of the soliton corresponds to a greater rate of transfer of energy between forward and backward modes during pulse propagation. Because the spectrum of these solitons lies entirely within the stopband, they were later named *gap solitons* [110]. Propagating gap solitons are distinct from stationary gap solitons discussed in preceding subsection of this chapter [93, 94].

The experimental work on propagation of pulses in nonlinear periodic structures includes demonstration of pulse switching and solitonic propagation.

In 1992 Sankey *et al.* [111] reported all-optical pulse switching in a corrugated silicon-on-insulator waveguide. The reflectance experienced by the nanosecond pulses increased with increasing intensity as the stopband shifted to overlap partially with the spectrum of the incident pulse.

Eggleton *et al.* [110] reported direct observation of Bragg soliton propagation in fiber Bragg gratings in 1996 using a Q-switched YLF laser producing 60 and 90 ps pulses at

a wavelength of 1064 nm. Formation of solitons was observed for pulses with spectra overlapping the edge of the linear stopband and for pulses with spectra significantly overlapping the center of the stopband. These experiments verified experimentally the theories from Refs. [105–107] and [108, 109].

The formation of gap solitons was also observed by Miller *et al.* in 1999 in an AlGaAs waveguide [112]. At moderate incident powers, transmission of soliton-shaped pulses was observed for pulses with spectra at the centre of the bandgap at 1.5 μm . For higher powers the solitons split into several shorter pulses [112].

In 1997 Broderick *et al.* demonstrated experimentally pulse switching in a nonlinear fiber Bragg grating using a pushbroom effect at 1.55 μm [113]. A strong pump pulse spectrally detuned a part of the continuous-wave probe out of the stopband. This detuned part of the probe had the time duration comparable to the length of the pump pulse and emerged out of the grating as a new probe pulse. This switching mechanism has not been attributed to the shifting of the built-in stopband but entirely to cross-phase modulation [113].

In a similar experiment in 1997 Broderick *et al.* demonstrated a reflection-based modification of the pushbroom effect [114]. In this experiment the wavelength of a continuous-wave probe was initially outside of the grating stopband. A pulsed pump at a frequency far outside the bandgap was used to shift, through the cross-phase-modulation, the wavelength of probe into the grating stopband, generating a reflected pulse.

3.2.3 Shifting the Stopband

Complementary to work on the steady-state response of nonlinear periodic structures and propagation of solitonic pulses, research was carried out on periodic structures in which the induced nonlinear index change is large, i.e. $\Delta n > 0.01$. The focus of this work was not the demonstration of bistable or solitonic behaviour but rather an observable movement of a photonic stopband.

An experimental demonstration of observable stopband shift in a 30 Bragg period GaAs/AlGaAs stack was reported in 1992 by He *et al.*. 1 μ s square pulses produced by a dye laser at a repetition rate of 10 kHz excited bandedge negative thermal nonlinearities. A 4 nm shift of the center of the stopband was observed at high levels of illumination [88]. Since the duration of the pulses used in the experiment was much greater than the propagation time through the grating, the experiment can be treated as a response to a continuous-wave illumination.

In 1992, Herbert *et al.* reported a power-dependent shift in the stopband of a three-dimensional dye-doped colloidal crystal. A decrease in transmittance through the crystal was observed under continuous-wave illumination of the Ar Ion beam at 514.5 nm [89].

In 1992 Scalora *et al.* published a qualitative discussion of nonlinear stopband dynamics in periodic structures. A scenario was considered in which, depending on the spectral position of the probe beam, a strong pump beam would move the stopband towards or away from the weak probe beam, thereby altering probe transmission [115].

An experimental demonstration of nonlinear stopband shifting using short pulses was reported in 1997 by Pan *et al.* Intensity-dependent coherent scattering from a colloidal crystal infiltrated with optically linear liquid was described. The index of refraction of the liquid was slightly higher than that of the photonic crystal spheres. Under the illumination with 3.5 ns pulses at 514 nm, the negative thermal nonlinearity of the dye-doped spheres increased the contrast of the grating. A maximum increase in the reflectance was estimated at 2 % [116].

A theoretical paper was published in 1999 by Tran in which the nonlinear response of a structure with a very sharp stopband was studied theoretically. The paper discussed optical switching when the frequency of light was aligned with the edge of the stopband and with the maximum of one of the sidelobes in the reflectance spectrum [117].

A novel approach to fabricating nonlinear periodic structures was presented in 2001 and 2002 by a group of researchers from the Naval Research Laboratory [118, 119]. A

sheet made out of two layers of two different polymers, each few tens of nanometers thick, was folded upon itself multiple times to generate a periodic structure of 4096 layers. The layers were not uniform in thickness. This introduced a disorder which resulted in a broadband response. Increasing reflection in the visible region was observed upon steady-state illumination. This was attributed to the nonlinear intensity-dependent refractive index contrast between the two constituent materials [118, 119].

Recently an experimental demonstration of ultrafast stopband shifting was reported by Leonard *et al.* [120]. In a pump-probe experiment with 300 fs pulses at 800 nm, a 20 nm shift of the edge of the stopband towards shorter wavelengths around 1.9 μm was observed in the silicon two-dimensional photonic crystal [120].

3.3 Conclusions from Literature Survey

3.3.1 Summary of Published Results

Following the preceding review, the discussion that ensues will summarize the major conclusions, as well as the missing pieces, of the published literature on nonlinearity and nonlinear periodic structures.

Nonlinear Response of Materials

Bulk and MQW semiconductors have been demonstrated to exhibit low-threshold saturation of absorption near the bandedge. The spectral position of the bandedge can be tuned over the entire visible and near-infrared spectrum. It has been predicted from the nonlinear Kramers-Kronig relation, and has been measured directly in isolated cases, that the bandedge saturation of absorption results in large changes of the real part of the refractive index.

In the regions of transparency, semiconductors exhibit weak nonlinear refractive effects of both signs. The non-resonant effects can be accompanied by two-photon ab-

sorption. Depending on the spectral position, the non-resonant nonlinear response of semiconductors can be characterized by good figures of merit.

Semiconductor nanocrystals also permit spectral tunability of their linear and nonlinear optical properties over the entire visible and near-infrared regions. Semiconductor nanocrystals have been demonstrated to exhibit strong saturation of absorption near the excitonic peak associated with the first allowed electronic transition. The non-resonant nonlinear response of nanocrystals is of a similar magnitude as in bulk and MQW semiconductors.

The figures of merit for organic materials in the absorbing region are in general poor. In the transparent region the Kerr and two-photon absorption coefficients of organic materials are of magnitudes comparable to those of inorganic crystalline semiconductors. The sign of the refractive nonlinearity varies across the spectrum depending on the proximity to various absorption resonances.

Nonlinear Periodic Structures

A large number of nonlinear periodic optical signal processing elements has been proposed and, in some cases, demonstrated experimentally.

Nonlinear periodic systems have been shown to exhibit optical bistability and therefore provide a prospective basis for optical memory. Bistable systems exhibit illumination-dependent spectral movement and change of the shape of photonic stopband and can support stationary gap solitons.

It has been shown that the introduction of a controlled degree of disorder in nonlinear periodic structures results in the formation of light-trapping microcavities. The decay length of intensity in such structures increases with an increasing magnitude of nonlinear coefficients and disorder.

Nonlinear reflection of laser pulses from a fiber Bragg grating has been demonstrated experimentally. The power and spectral content of the reflected pulses was shown to vary

with the level of illumination.

Corrugated waveguides have been shown to support the propagation of solitary pulses whose spectrum lies close to the edge of a photonic stopband and whose spectrum lies within the photonic stopband. These Bragg and gap solitons, respectively, can propagate through a nonlinear periodic grating without spreading temporally by balancing the effects of grating dispersion and self-phase modulation.

A pushbroom effect has been proposed and demonstrated in a fiber Bragg grating. In a pushbroom effect a strong pulsed pump beam tunes the spectral content of a continuous-wave probe either out of or into a stopband.

An illumination-dependent movement of stopband was observed in three-dimensional organic and inorganic semiconductor nonlinear photonic crystals.

3.3.2 The Need for Additional Research

Despite vast accomplishments in the research on nonlinear periodic structures, there are many opportunities to increase their optical signal processing functionality.

A theory on nonlinear periodic structures preceding this work has to be expanded to enable complex signal processing functions. To achieve this, a new approach to signal processing using nonlinear periodic structures is needed. A theory should be derived that describes and summarizes the conditions for intensity-domain optical stability and allows prediction of the transfer characteristics. Analyses of the effect of disorder on the optical signal processing functionality of nonlinear periodic structures need to be carried out.

Although nonlinear properties of many materials systems have been reported, further characterization is needed to assess the applicability of various nonlinear material systems to optical signal processing. In contrast to previously reported measurements carried out at isolated wavelengths, measurements of the refractive and absorptive nonlinear response over wide spectral ranges, which would permit determination of figures of merit need to be carried out. In particular, the refractive and absorptive nonlinear response in

the most promising absorption-edge regions of MQW semiconductors and semiconductor nanocrystals should be examined comprehensively and the applicability of these material systems to optical signal processing should be determined.

New approaches to fabrication of nonlinear periodic structures with increased signal processing functionality should be considered and demonstrated. To facilitate operation and implementation these techniques should aim to exploit large index changes at wavelengths important in telecommunications.

Chapter 4 to 9 will advance the theory of optical signal processing using nonlinear periodic structures. A stable optical response of nonlinear periodic structures will be proposed and theoretically demonstrated to yield an array of simple and complex signal processing functions. The designs of nonlinear periodic devices capable of supporting optical limiting, switching, logic gating, and analog-to-digital conversion will be proposed. The theory of optical stability will be derived and the impact of the disorder on the performance of optically stable nonlinear periodic structures will be studied.

Chapters 10 and 11 constitute the experimental part of this work. Nonlinear properties of a variety of nonlinear materials will be characterized and their applicability to optical signal processing using nonlinear periodic structures will be determined. In particular, the broadband nonlinear response of large index change bandedge nonlinearites in semiconductor MQWs and nanocrystals will be directly measured and their figures of merit will be reported. This work will conclude with the experimental demonstration of the nonlinear response of nonlinear periodic structures.

Chapter 4

Coupled Mode Theory of Nonlinear Periodic Structures

This chapter will present the theoretical formalism that will be used in the ensuing chapters. The theory derived will enable the analysis of new nonlinear periodic devices capable of supporting optical signal processing functions as presented in the ensuing chapters.

Coupled mode theory (CMT) will be derived for the general case of a shallow nonlinear periodic structure under coherent illumination. It will be shown that the general CMT can be applied to the special cases of incoherent radiation and partial disorder. The formalism derived represents a basis for the analysis of the nonlinear periodic structures studied theoretically in chapters 5-9.

An alternative method of analyzing propagation of light through nonlinear periodic structures, the transfer matrix method (TMM), will be presented and compared with CMT. TMM will be selectively used in the following chapters to verify the results of CMT analysis.

4.1 Representation of the Refractive Index Profile

The general refractive index cross-section of the optical elements studied in this work is illustrated in Figure 4.1. The periodic structure consists of two materials with generally different linear and nonlinear indices of refraction.

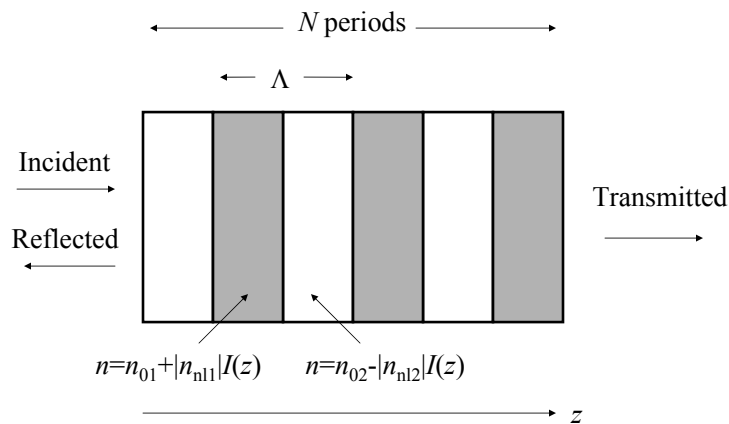


Figure 4.1: Schematic of a nonlinear periodic structure with period Λ . n_{01} and n_{02} are the linear refractive indices, and n_{n1} and n_{n2} are the Kerr coefficients of the adjacent layers.

To derive coupled mode equations the refractive index profile will be expanded in a Fourier series and then substituted into the nonlinear Maxwell wave equation.

The linear parts of the refractive index n_{ln} and Kerr coefficients n_{nl} of the structure shown in Figure 4.1 can be well approximated by the periodic functions $n_{(ln)\Lambda}(z)$ and $n_{(nl)\Lambda}(z)$, respectively. This is illustrated in Figure 4.2.

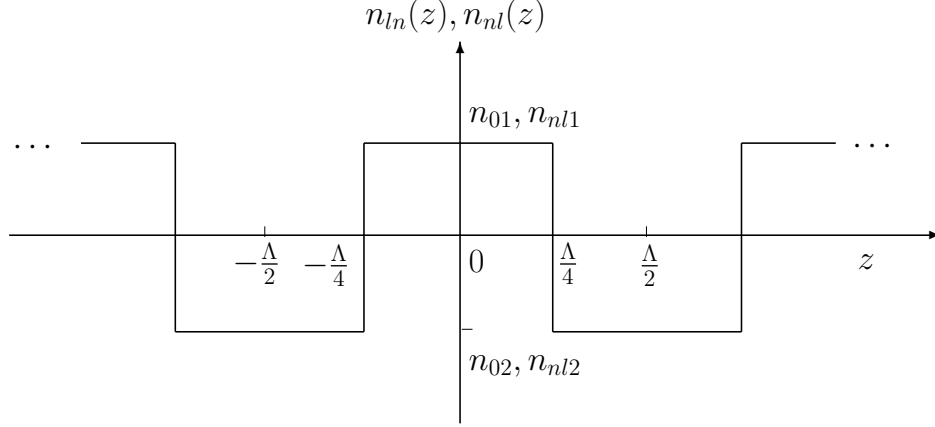


Figure 4.2: Profile of the linear parts of refractive index n_{ln} and Kerr coefficients n_{nl} of a nonlinear periodic structure along the propagation direction z .

The functions $n_{(ln,nl)\Lambda}(z)$ and $n_{(nl)\Lambda}(z)$ may be described over one period as follows:

$$n_{(ln,nl)\Lambda}(z) = \begin{cases} n_{02}, n_{nl2}, & \text{if } -\frac{m\Lambda}{2} < z < -\frac{m\Lambda}{4}; \\ n_{01}, n_{nl1}, & \text{if } -\frac{m\Lambda}{4} < z < \frac{m\Lambda}{4}; \\ n_{02}, n_{nl2}, & \text{if } \frac{m\Lambda}{4} < z < \frac{m\Lambda}{2}; \quad m = 1, 2, \dots \end{cases} \quad (4.1)$$

Using a Fourier series expansion, Eqs. (4.1) can be resolved into an infinite sum of sine and cosine terms:

$$n_{\Lambda}(z) = a_0 + 2 \sum_{n=1}^{\infty} [a_n \cos(2\pi n f_0 z) + b_n \sin(2\pi n f_0 z)], \quad (4.2)$$

where f_0 is the fundamental spatial frequency of the grating, $f_0 = 1/\Lambda$. The coefficients of a_m and b_m represent the amplitudes of even and odd terms, respectively. The quantity $m f_0$ represents the m th harmonic of the fundamental spatial frequency f_0 . The coefficient a_0 is the mean value of the periodic signal $n_{\Lambda}(z)$ over one period. It is calculated according to:

$$a_0 = \frac{1}{\Lambda} \int_{-\Lambda/2}^{\Lambda/2} n_{\Lambda}(z) dz \quad (4.3)$$

Fourier coefficients a_m and b_m are:

$$\begin{aligned} a_m &= \frac{1}{\Lambda} \int_{-\Lambda/2}^{\Lambda/2} n_{\Lambda}(z) \cos(2\pi m f_0 z) dz, & m = 1, 2, 3, \dots \\ b_m &= \frac{1}{\Lambda} \int_{-\Lambda/2}^{\Lambda/2} n_{\Lambda}(z) \sin(2\pi m f_0 z) dz, & m = 1, 2, 3, \dots \end{aligned} \quad (4.4)$$

For an even function such as the one shown in Figure 4.2, $b_m = 0$ and $a_m \neq 0$.

Substituting $\mathbf{n}_{(ln)\Lambda}(\mathbf{z})$ from Eq. (4.1) into Eq. (4.3) gives:

$$\begin{aligned} a_0 &= \frac{1}{\Lambda} \int_{-\Lambda/2}^{\Lambda/2} n_{(ln)\Lambda}(z) dz \\ &= \frac{2}{\Lambda} \left(\int_0^{\Lambda/4} n_{01} dz + \int_{\Lambda/4}^{\Lambda/2} n_{02} dz \right) \\ &= \frac{n_{01} + n_{02}}{2} \end{aligned} \quad (4.5)$$

The Fourier coefficient a_m is evaluated as:

$$\begin{aligned} a_m &= \frac{1}{\Lambda} \int_{-\Lambda/2}^{\Lambda/2} n_{(ln)\Lambda}(z) \cos(2\pi m f_0 z) dz \\ &= \frac{2}{\Lambda} \int_0^{\Lambda/4} n_{01} \cos(2\pi m f_0 z) dz \\ &\quad + \frac{2}{\Lambda} \int_{\Lambda/4}^{\Lambda/2} n_{02} \cos(2\pi m f_0 z) dz \\ &= \begin{cases} 0, & \text{if } m \text{ is even} \\ \frac{1}{\pi m} (n_{01} - n_{02}) \sin\left(\frac{\pi m}{2}\right), & \text{if } m \text{ is odd} \end{cases} \end{aligned} \quad (4.6)$$

Using (4.5) and (4.6), and similar Fourier coefficients for the $\mathbf{n}_{(nl)\Lambda}(\mathbf{z})$, the index of refraction in Eq. (4.2) can be rewritten as:

$$\begin{aligned} n_{\Lambda}(z, |E|^2) &= n_{(ln)\Lambda}(z) + n_{(nl)\Lambda}(z) |E|^2 \\ &= \frac{n_{01} + n_{02}}{2} + \frac{n_{nl1} + n_{nl2}}{2} |E|^2 \\ &\quad + 2 \sum_{m=1, m \text{ odd}}^{\infty} \frac{1}{\pi m} (n_{01} - n_{02} + n_{nl1} |E|^2 - n_{nl2} |E|^2) \sin\left(\frac{\pi m}{2}\right) \cos(2\pi m f_0 z) \end{aligned} \quad (4.7)$$

The reflectance and transmittance of periodic structures display the most interesting features near the Bragg resonance which takes place when the wavelength of light is close

to twice the optical length of the grating period. For wavelengths in the vicinity of the Bragg resonance only the terms with $m=1$ in (4.7) will couple with the terms representing electric field. In this case (4.7) reduces to:

$$n_{\Lambda}(z, |E|^2) \approx \frac{n_{01} + n_{02}}{2} + \frac{n_{nl1} + n_{nl2}}{2} |E|^2 + 2 \left(\frac{n_{01} - n_{02}}{\pi} + \frac{n_{nl1} - n_{nl2}}{\pi} |E|^2 \right) \cos \frac{2\pi z}{\Lambda} \quad (4.8)$$

To simplify the above equation, four new parameters are introduced: average linear index (n_{ln}), linear index difference (n_{0k}), average Kerr coefficient (n_{nl}), and Kerr coefficient difference (n_{2k}):

$$\begin{aligned} n_{ln} &= \frac{n_{01} + n_{02}}{2}, & n_{nl} &= \frac{n_{nl1} + n_{nl2}}{2}, \\ n_{0k} &= \frac{n_{01} - n_{02}}{\pi}, & n_{2k} &= \frac{n_{nl1} - n_{nl2}}{\pi}. \end{aligned} \quad (4.9)$$

Defining the wavenumber of the grating as $k_0 = \frac{2\pi}{\Lambda}$, Eq. (4.8) can be rewritten as:

$$n_{\Lambda}(z, |E|^2) = n_{ln} + n_{nl} |E|^2 + 2n_{0k} \cos k_0 z + 2n_{2k} |E|^2 \cos k_0 z. \quad (4.10)$$

4.2 General Coupled Mode Equations for Nonlinear Periodic Structure

The scalar electromagnetic wave equation states:

$$\frac{\partial^2 E}{\partial z^2} - \frac{\mathbf{n}^2(\mathbf{z}, |E|^2)}{c^2} \frac{\partial^2 E}{\partial t^2} = 0, \quad (4.11)$$

where c is the speed of light and $E(z, t)$ is the electric field expressed as:

$$E(z, t) = A_+(z, t) e^{i(kz - \omega_0 t)} + A_-(z, t) e^{-i(kz + \omega_0 t)}. \quad (4.12)$$

$\omega_0 = ck/|n_{ln}|$ is the center optical frequency and $k = 2\pi|n_{ln}|/\lambda_0$ is the wavenumber of light. A_+ and A_- are the slowly-varying envelopes of amplitudes of the forward- and backward-propagating waves.

The analyses that follow will concentrate on the spectral region that is close to the Bragg resonance, i.e. $\lambda_0 \approx 2n_{ln}\Lambda$ or $k_0 \approx 2k$.

Substituting Eq. (4.12) into first term of Eq. (4.11) and making the slowly-varying envelope approximation gives the following expression for the second order time derivative of the electric field:

$$\begin{aligned} \frac{\partial^2 E}{\partial z^2} &= -k^2 A_+ e^{i(kz-\omega_0 t)} + 2ik \frac{\partial A_+}{\partial z} e^{i(kz-\omega_0 t)} - k^2 A_- e^{-i(kz+\omega_0 t)} \\ &\quad + 2ik \frac{\partial A_-}{\partial z} e^{-i(kz+\omega_0 t)} + \frac{\partial^2 A_+}{\partial z^2} e^{i(kz-\omega_0 t)} + \frac{\partial^2 A_-}{\partial z^2} e^{-i(kz+\omega_0 t)} \\ &\approx \left(-k^2 A_+ + 2ik \frac{\partial A_+}{\partial z} \right) e^{i(kz-\omega_0 t)} + \left(-k^2 A_- - 2ik \frac{\partial A_-}{\partial z} \right) e^{-i(kz+\omega_0 t)}. \end{aligned} \quad (4.13)$$

The second term in Eq. (4.11) becomes:

$$\begin{aligned} \frac{n^2(z, |E|^2)}{c^2} \frac{\partial^2 E}{\partial t^2} &\approx \frac{k}{\omega_0 n_{ln} c} \left[n_{ln}^2 + 2n_{ln} n_{nl} |E|^2 + (2n_{ln} n_{0k} + 2n_{ln} n_{2k} |E|^2) (e^{ik_0 z} + e^{-ik_0 z}) \right] \frac{\partial^2 E}{\partial t^2} \\ &\quad (\text{neglecting all higher terms in } n_{2k}) \\ &= \frac{k}{\omega_0 c} \left[n_{ln} + 2n_{nl} |E|^2 + (2n_{0k} + 2n_{2k} |E|^2) (e^{ik_0 z} + e^{-ik_0 z}) \right] \\ &\quad \cdot \left[-\omega_0 (\omega_0 A_+ + 2i \frac{\partial A_+}{\partial t}) e^{i(kz-\omega_0 t)} - \omega_0 (\omega_0 A_- + 2i \frac{\partial A_-}{\partial t}) e^{-i(kz+\omega_0 t)} \right]. \end{aligned} \quad (4.14)$$

The intensity term $|E|^2$ in Eq. (4.14) is expressed in terms of A_+ and A_- as:

$$|E|^2 = E \cdot E^* = |A_+|^2 + |A_-|^2 + A_+ A_-^* e^{i2kz} + A_+^* A_- e^{-i2kz}. \quad (4.15)$$

Eq. (4.14) then becomes:

$$\begin{aligned} \frac{n^2(z, |E|^2)}{c^2} \frac{\partial^2 E}{\partial t^2} &\approx -\frac{k}{c} \left[n_{ln} \omega_0 A_+ + 2in_{ln} \frac{\partial A_+}{\partial t} + 2n_{0k} \omega_0 A_- e^{i\Delta kz} + 2n_{nl} (|A_+|^2 + |A_-|^2) \omega_0 A_+ \right. \\ &\quad + 2n_{nl} A_+ A_-^* \omega_0 A_- + 2n_{2k} (|A_+|^2 + |A_-|^2) \omega_0 A_- e^{i\Delta kz} + 2n_{2k} A_+^* A_- \omega_0 A_+ e^{i\Delta kz} \\ &\quad + 2n_{2k} A_+ A_-^* \omega_0 A_+ e^{-i\Delta kz} \left. \right] \cdot e^{i(kz-\omega_0 t)} - \frac{k}{c} \left[n_{ln} \omega_0 A_- + 2in_{ln} \frac{\partial A_-}{\partial t} \right. \\ &\quad + 2n_{0k} \omega_0 A_+ e^{-i\Delta kz} + 2n_{nl} (|A_+|^2 + |A_-|^2) \omega_0 A_- + 2n_{nl} A_+^* A_- \omega_0 A_+ \\ &\quad + 2n_{2k} (|A_+|^2 + |A_-|^2) \omega_0 A_+ e^{-i\Delta kz} + 2n_{2k} A_+ A_-^* \omega_0 A_- e^{-i\Delta kz} \\ &\quad \left. + 2n_{2k} A_+^* A_- \omega_0 A_- e^{i\Delta kz} \right] \cdot e^{-i(kz+\omega_0 t)}. \end{aligned} \quad (4.16)$$

where Δk is the detuning, defined as $\Delta k = k_0 - 2k$.

Eq. (4.16) can be decomposed into two equations, one describing the change in A_+ and the second equation describing the change in A_- . Using expansions (4.13) and (4.16) terms proportional to $e^{i(kz-\omega_0t)}$ in Eq. (4.11) can be combined to give:

$$\begin{aligned} & -k^2 A_+ + 2ik \frac{\partial A_+}{\partial z} + \frac{k}{c} [n_{ln} \omega_0 A_+ + 2in_{ln} \frac{\partial A_+}{\partial t} + 2n_{0k} \omega_0 A_- e^{i\Delta kz} \\ & + 2n_{nl} (|A_+|^2 + |A_-|^2) \omega_0 A_+ + 2n_{nl} A_+ A_-^* \omega_0 A_- + 2n_{2k} (|A_+|^2 + |A_-|^2) \omega_0 A_- e^{i\Delta kz} \\ & + 2n_{2k} A_+^* A_- \omega_0 A_+ e^{i\Delta kz} + 2n_{2k} A_+ A_-^* \omega_0 A_+ e^{-i\Delta kz}] = 0. \end{aligned} \quad (4.17)$$

Using product expansions and simplification, (4.17) becomes:

$$\begin{aligned} & i \frac{c}{\omega_0} \frac{\partial A_+}{\partial z} + i \frac{n_{ln}}{\omega_0} \frac{\partial A_+}{\partial t} + n_{0k} A_- e^{i\Delta kz} + n_{nl} (|A_+|^2 + |A_-|^2) A_+ + n_{nl} |A_-|^2 A_+ \\ & + n_{2k} (|A_+|^2 + |A_-|^2) A_- e^{i\Delta kz} + n_{2k} |A_+|^2 A_- e^{i\Delta kz} + n_{2k} A_+^2 A_-^* e^{-i\Delta kz} = 0. \end{aligned} \quad (4.18)$$

Similarly, by grouping all the $e^{-i(kz+\omega_0t)}$ terms the second coupled-mode equation, that describes the evolution of the A_- envelope is obtained:

$$\begin{aligned} & -i \frac{c}{\omega_0} \frac{\partial A_-}{\partial z} + i \frac{n_{ln}}{\omega_0} \frac{\partial A_-}{\partial t} + n_{0k} A_+ e^{-i\Delta kz} + n_{nl} (|A_+|^2 + |A_-|^2) A_- + n_{nl} |A_+|^2 A_- \\ & + n_{2k} (|A_+|^2 + |A_-|^2) A_+ e^{-i\Delta kz} + n_{2k} |A_-|^2 A_+ e^{-i\Delta kz} + n_{2k} A_-^2 A_+^* e^{i\Delta kz} = 0. \end{aligned} \quad (4.19)$$

To simplify further the coupled-mode equations (4.18) and (4.19), the normalized space Z and time T coordinates are introduced: $Z = \omega_0 z / c$ and $T = \omega_0 t / n_{ln}$. This process of parameter normalization ensures that the spatial and time parameters are of the same unit, which facilitates the numerical analysis. After grouping similar terms together the resulting normalized coupled-mode equations are:

$$\begin{aligned} & i \left(\frac{\partial A_+}{\partial Z} + \frac{\partial A_+}{\partial T} \right) + n_{0k} A_- e^{i\Delta kz} + n_{nl} (|A_+|^2 + 2|A_-|^2) A_+ \\ & + n_{2k} [(2|A_+|^2 + |A_-|^2) A_- e^{i\Delta kz} + A_+^2 A_-^* e^{-i\Delta kz}] = 0 \end{aligned} \quad (4.20)$$

and

$$\begin{aligned} & -i \left(\frac{\partial A_-}{\partial Z} - \frac{\partial A_-}{\partial T} \right) + n_{0k} A_+ e^{-i\Delta kz} + n_{nl} (2|A_+|^2 + |A_-|^2) A_- \\ & + n_{2k} [(|A_+|^2 + 2|A_-|^2) A_+ e^{-i\Delta kz} + A_-^2 A_+^* e^{i\Delta kz}] = 0 \end{aligned} \quad (4.21)$$

The coupled mode equations (4.20) and (4.21) describe the evolution of electric field envelopes (forward wave A_+ and backward wave A_-) across a nonlinear periodic structure. They will be used in chapter 8 during the stability analysis, and in chapter 9 to describe the propagation of pulses.

4.3 Nonlinear Coupled Mode Equations for Incoherent Light

In this section Eqs. (4.20) and (4.21) will be simplified and rearranged to account for special cases that will be studied in the chapters that follow.

4.3.1 Assumptions

A continuous-wave illumination is now assumed. To simplify the initial analysis, the radiation is also considered to be incoherent. The first assumption translates into zero $\frac{\partial A_+}{\partial T}$ and $\frac{\partial A_-}{\partial T}$ partial time derivatives. The second assumption means that the cross terms in Eq. (4.15) are zero and that the intensity is defined as:

$$I = |E|^2 = E \cdot E^* = |A_+|^2 + |A_-|^2. \quad (4.22)$$

Because of the simplified expression for intensity (4.22), fewer terms couple in the analysis (4.14) to (4.21). Consequently Eqs. (4.20) and (4.21) will contain fewer terms. As will be demonstrated in chapter 5, for some special cases these simplified coupled mode equations can be solved analytically.

4.3.2 Couple Mode Equations for Incoherent Light

The steady-state coupled mode equations for incoherent light become:

$$i\frac{dA_+}{dZ} + n_{0k}A_-e^{i\Delta kz} + n_{nl}IA_+ + n_{2k}IA_-e^{i\Delta kz} = 0 \quad (4.23)$$

$$-i\frac{dA_-}{dZ} + n_{0k}A_+e^{-i\Delta kz} + n_{nl}IA_- + n_{2k}IA_+e^{-i\Delta kz} = 0. \quad (4.24)$$

If the thicknesses of layers are not equal, the Fourier coefficients from the refractive index expansion (4.1) to (4.10) have to be modified. The total (including linear and nonlinear parts) refractive index is then redefined as:

$$n(z) = n_{ln} + \pi n_{0k}f(z) + n_{nl}I + \pi n_{2k}If(z), \quad (4.25)$$

where $n_{ln} = (n_{01}d_1 + n_{02}d_2)/\Lambda$ and $n_{nl} = (n_{nl1}d_1 + n_{nl2}d_2)/\Lambda$, with d_1 and d_2 being the thicknesses of layers 1 and 2, and Λ is again the period of the grating, $\Lambda = d_1 + d_2$. $f(z)$ is the Fourier expansion of the step function:

$$f(z) = -\sum_{m \neq 0} \exp(im\pi X) \frac{\sin(m\pi X)}{m\pi} \exp\left(i\frac{2m\pi z}{\Lambda}\right) \quad (4.26)$$

with $X = d_1/\Lambda$.

Since layer thicknesses are assumed not to deviate significantly from their quarter-wave value, only the first order terms with $m = 1$ in the Eq. (4.26) couple with the spatial derivatives of A_+ and A_- . The resulting coupled mode equations are:

$$i\frac{dA_+}{dZ} - n_{0k}A_- \exp\left(-i\frac{\pi d_2}{\Lambda}\right) \sin(\pi d_1/\Lambda)e^{i\Delta kz} + n_{nl}IA_+ - n_{2k}IA_- \exp\left(-i\frac{\pi d_1}{\Lambda}\right) \sin(\pi d_2/\Lambda)e^{i\Delta kz} = 0 \quad (4.27)$$

$$-i\frac{dA_-}{dZ} + n_{0k}A_+ \exp\left(i\frac{\pi d_2}{\Lambda}\right) \sin(\pi d_1/\Lambda)e^{-i\Delta kz} + n_{nl}IA_- + n_{2k}IA_+ \exp\left(i\frac{\pi d_1}{\Lambda}\right) \sin(\pi d_2/\Lambda)e^{-i\Delta kz} = 0 \quad (4.28)$$

Eqs. (4.27) and (4.28) describe the propagation of steady-state monochromatic incoherent light in nonlinear periodic structures with, in general, different adjacent layer thicknesses.

These equations will be used in chapter 7 to describe the response of structures that support hard limiting, logic gating, and analog-to-digital conversion in nonlinear periodic structures.

4.3.3 Coupled Mode Equations for Incoherent Light, Matched Linear Indices and Opposite Kerr Coefficients

As will be shown in chapter 5, the important signal processing functions of stable optical limiting and switching require additional constraints on the material parameters. These constraints are: matched linear indices $n_{01} = n_{02}$, Kerr coefficients of opposite sign and equal magnitude $n_{nl1} = -n_{nl2}$, and same layer thicknesses $d_1 = d_2$.

These conditions result in $n_{0k} = 0$ and $n_{nl} = 0$. Eqs. (4.27) and (4.28) simplify to:

$$i \frac{dA_+}{dZ} + n_{2k} I A_- e^{i\Delta kz} = 0 \quad (4.29)$$

$$-i \frac{dA_-}{dZ} + n_{2k} I A_+ e^{-i\Delta kz} = 0 \quad (4.30)$$

4.3.4 Coupled Mode Theory for Weakly Disordered Structures

The introduction of weak disorder in nonlinear periodic structures results in the widening of the effective photonic stopband and, associated with it, broadband limiting. Such structures will be analyzed in chapter 6. Disorder will be introduced by allowing layer thicknesses to deviate randomly from their quarter-wave value over a predefined range. The conditions of matched linear indices and opposite Kerr coefficients still hold. Such a structure is illustrated in Figure 4.3.

The Corresponding CM equations (4.27) and (4.28) become:

$$i \frac{dA_+}{dZ} + f_{nl}^{AC}(z) n_{2k} I A_- e^{ik_0 z} + n_{nl} I A_+ = 0 \quad (4.31)$$

$$-i \frac{dA_-}{dZ} + f_{nl}^{AC}(z) n_{2k} I A_+ e^{-ik_0 z} + n_{nl} I A_- = 0 \quad (4.32)$$

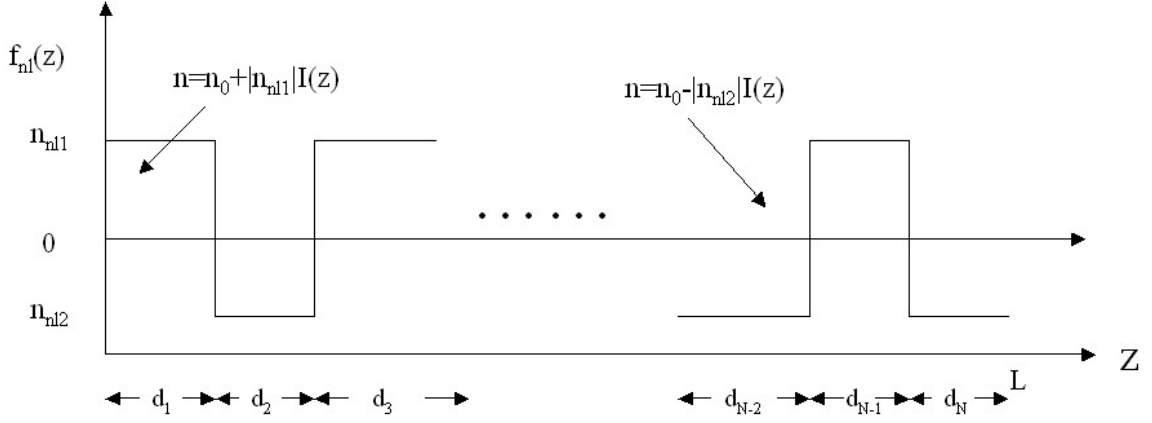


Figure 4.3: Nonlinear periodic structure where layer thicknesses deviate randomly from their quarter-wave value.

where f_{nl}^{AC} is the AC component of the numerical Fourier expansion of the nonlinear index profile f_{nl} at a given position z . n_{nl} is the average Kerr coefficient of the structure with length L , made out of N layers with corresponding n_{nli} Kerr coefficients. n_{nl} is calculated according to:

$$n_{nl} = \frac{1}{L} \sum_{i=1}^N n_{nli} d_i \quad (4.33)$$

Both f_{nl}^{AC} and n_{nl} are calculated separately for each disordered structure analyzed.

4.3.5 Transfer Matrix Formalism for Nonlinear System

An alternative computational technique, the transfer matrix method (TMM), can be used to verify the results of coupled mode computations. Unlike CMT, TMM allows the determination of the transfer characteristics of arbitrary structures, with no restrictions on the periodicity of material coefficients. TMM is only computationally time-efficient for the analysis of steady-state response. Computations using CMT are faster and in some special case CMT equations are integrable.

To permit numerical simulations using TMM, the traditional TMM [121] is modified

to account for the intensity-dependent refractive index. The structure under analysis is first sliced into spatial increments. The natural choice is that each spatial increment corresponds to one layer in a structure consisting of locally homogeneous materials. The relation between the coefficients a of the forward-propagating wave and b of the backward propagating wave in layers j and $j + 1$ is determined by:

$$\begin{pmatrix} a_j \\ b_j \end{pmatrix} = M_{j,j+1} \begin{pmatrix} a_{j+1} \\ b_{j+1} \end{pmatrix}, \quad (4.34)$$

where the matrix $M_{j,j+1}$ that relates a and b coefficients in the adjacent spatial steps, is:

$$M_{j,j+1} = \frac{1}{2} \begin{bmatrix} (1 + k_{j+1}/k_j)e^{ik_{j+1}t_{j+1}} & (1 - k_{j+1}/k_j)e^{-ik_{j+1}t_{j+1}} \\ (1 - k_{j+1}/k_j)e^{ik_{j+1}t_{j+1}} & (1 + k_{j+1}/k_j)e^{-ik_{j+1}t_{j+1}} \end{bmatrix}. \quad (4.35)$$

In Eq. (4.35) t_i are the lengths of the i^{th} spatial step in the numerical computation.

At each step of the computation the wavenumbers k_j in corresponding spatial increments are calculated according to:

$$k_i = \frac{2\pi(n_0 + n_{nl}I)}{\lambda}. \quad (4.36)$$

Using Eqs. (4.34) and (4.35), the coefficients of the forward- and backward-propagating field at the beginning of the structure (a_0 and b_0) can be related to the coefficients at the end of the structure (a_N and b_N) through:

$$\begin{pmatrix} a_0 \\ b_0 \end{pmatrix} = M_{0,1} \times M_{1,2} \times \dots \times M_{N-1,N} \begin{pmatrix} a_N \\ b_N \end{pmatrix}. \quad (4.37)$$

Eq. (4.37) enables calculation of the transfer characteristics of the nonlinear structures.

4.4 Conclusions

This chapter established the general theoretical formalism used throughout this work. The computational techniques of coupled mode theory and transfer matrix were introduced. The general (preexisting) method of CMT was applied to the physical system to be explored in this work.

Chapter 5

Theory of Steady-State Optical Limiting and Switching

This chapter utilizes the formalism derived in chapter 4 to analyze theoretically the response of novel nonlinear periodic elements.

The first section of this chapter analyzes the intensity-dependent optical response of passive optical limiters. The limiters are realized using nonlinear periodic structures that consist of alternating layers of materials possessing matched linear refractive indices and opposite Kerr nonlinearities. The device performance is explored using an analytical model and numerical simulations.

The second part of this chapter is devoted to the analysis of additional optical signal processing functionality of the limiting device proposed. The performance of the resulting optical switches and logic gates is explored for signal and pump beams having the same and different wavelengths.

The material figures of merit pertinent to the limiting and switching elements presented in this chapter are derived and compared with the figures of merit introduced in chapter 2.

5.1 Structure and Modelling Approach

The structures analyzed consist of materials with matched linear indices, $n_{01} = n_{02} = n_0$, Kerr coefficients of opposite sign and equal magnitude, $n_{nl1} = -n_{nl2}$, and the same layer thicknesses, $d_1 = d_2$.

A refractive index profile of such structures is shown in Figure 5.1.

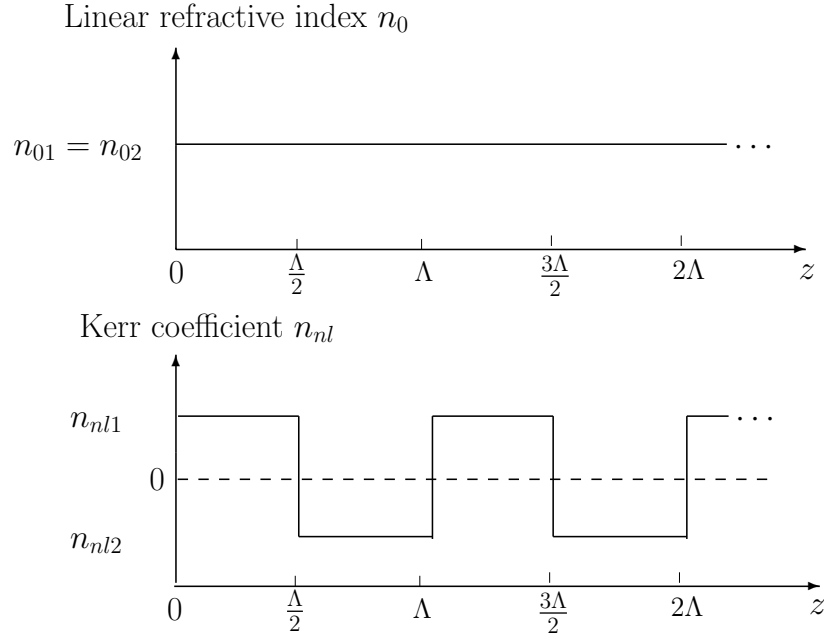


Figure 5.1: Profile of linear refractive indices and Kerr coefficients of the limiting device. The refractive indices of the two adjacent layers are $n_{01} + n_{nl1}I$ and $n_{02} + n_{nl2}I$, where $n_{01} = n_{02}$ and $n_{nl1} = -n_{nl2}$.

The steady-state response of such structures is described by Eqs. (4.29) and (4.30).

In obtaining analytical and numerical solutions, two boundary conditions were specified: $A_-(L) = 0$, which stipulates that no radiation is incident on the structure from the right, and $A_+(L) = A_{+1out} = \sqrt{I_{out}}$, which defines the transmitted intensity. Choosing transmitted rather than incident intensity as a boundary condition allows analytical and numerical study of both stable and multistable response of nonlinear periodic structures.

The results presented in this chapter were selectively verified using TMM (4.34) to

(4.37).

5.2 Theory of All-Optical Limiting

The work presented in this section was published in Refs. [6, 122].

5.2.1 Analytical Solutions

To obtain the analytical solutions for the transfer characteristic of optical elements proposed, Eqs. (4.29) and (4.30) are solved for $A_+(z)$ and $A_-(z)$ at a Bragg resonance ($k_0 = 2k$). The following expression is obtained for the envelope of the forward-propagating wave in terms of the transmitted intensity, $I_{out} = |A_{+out}|^2$:

$$A_+(z) = \sqrt{\frac{1 + 2 \exp\left[\frac{-2\pi i I_{out} n_{2k}(L-z)}{\Lambda n_{ln}}\right] + \exp\left[\frac{-4\pi i I_{out} n_{2k}(L-z)}{\Lambda n_{ln}}\right]}{2 + 2 \exp\left[\frac{-4\pi i I_{out} n_{2k}(L-z)}{\Lambda n_{ln}}\right]}} |A_+(L)| \quad (5.1)$$

Taking the squared modulus of (5.1) yields the expression for the evolution of the intensity of the forward propagating wave across the structure:

$$I(z) = \left| \frac{1 + \cos\left[\frac{2\pi I_{out} n_{2k}(L-z)}{\Lambda n_{ln}}\right]}{2 \cos\left[\frac{2\pi I_{out} n_{2k}(L-z)}{\Lambda n_{ln}}\right]} \right| I_{out} \quad (5.2)$$

Solving expression (5.2) at the beginning of the structure ($z=0$) gives the relation between incident and transmitted intensity:

$$I_{in} = \frac{1}{2} \left| \frac{1}{\cos\left(\frac{4I_{out}}{a}\right)} + 1 \right| I_{out}, \quad (5.3)$$

where $a = \frac{4n_{ln}}{Nn_{2k}\pi}$ and $N = \frac{2L}{\Lambda}$ is the number of layers in the structure.

Expression (5.3) gives I_{in} as a periodic function of I_{out} . Only solutions from the first band of this function ($\frac{4I_{out}}{a}$ ranges from 0 to $\frac{\pi}{2}$) are physically possible – the remaining solutions imply a transmitted intensity larger than the incident intensity. The limiting value of intensity is:

$$I_{limiting} = \frac{n_{ln}}{2Nn_{2k}}. \quad (5.4)$$

The limiting intensity (5.4) is inversely proportional to the product of the number of layers in the structure and the strength of the nonlinear coefficient.

As numerical results will confirm, expression (5.4) gives the highest value of the intensity that can be transmitted by the limiter. The result constitutes an analytical proof of true, or ideal, limiting action: for the nonabsorbing periodic structure with matched linear refractive indices and opposite Kerr coefficients, the transmitted intensity should always lie below a fixed value for an arbitrarily intense incident steady-state illumination.

A figure of merit for the limiters is the dynamic range (DR) [123]. This quantity ($DR = \frac{TL}{TH}$) is defined as the ratio of the low-intensity transmission (TL) to the high-intensity transmission (TH), measured at the highest energies employed [123]. The analytical expressions derived for the structures analyzed predict that the transmission of the proposed structures approaches zero as the incident intensity is sufficiently increased. There is thus no theoretical limit to the DR of the idealized devices proposed, given that the constituent materials exhibit nonlinearity that is fully described by the Eq. (2.7).

5.2.2 Numerical Analysis

The response of the limiting nonlinear distributed feedback structures described above was also studied numerically.

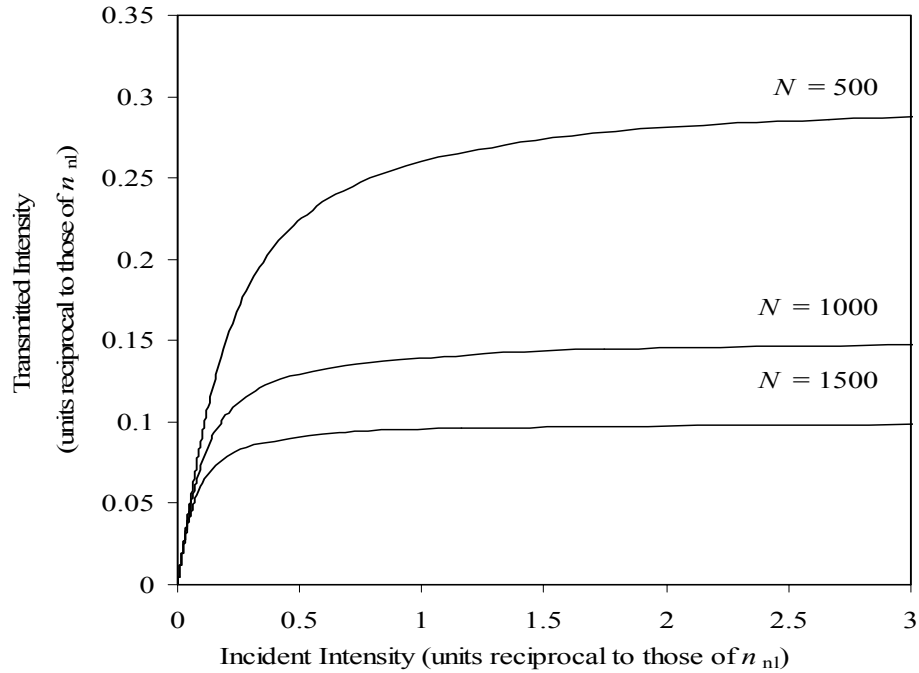


Figure 5.2: Transmitted intensity as a function of incident intensity for limiting structures with $|n_{nl}| = 0.01$ for various numbers of layers.

Figures 5.2 and 5.3 demonstrate the limiting behaviour of the structures proposed on linear and semi-logarithmic plots. The indices of refraction and nonlinear coefficients of the constituent two materials the structures modelled were taken to be $n_{01}=n_{02}=1.5$ and $n_{n1}=-n_{n2}=0.01$, respectively. The normalized incident intensity was increased from 0 to 100. Here and throughout this work normalized intensity is assumed to have units that are reciprocal to those of n_{nl} . The response of the limiter was investigated for various numbers of layers. In all cases the thicknesses of the layers were given the values corresponding to a quarter-wave value at a wavelength λ_0 , $d_1=d_2=\frac{\Lambda}{2}=\frac{\lambda_0}{4n_{01}}$.

Since the structure is considered to be made out of nonabsorbing materials with

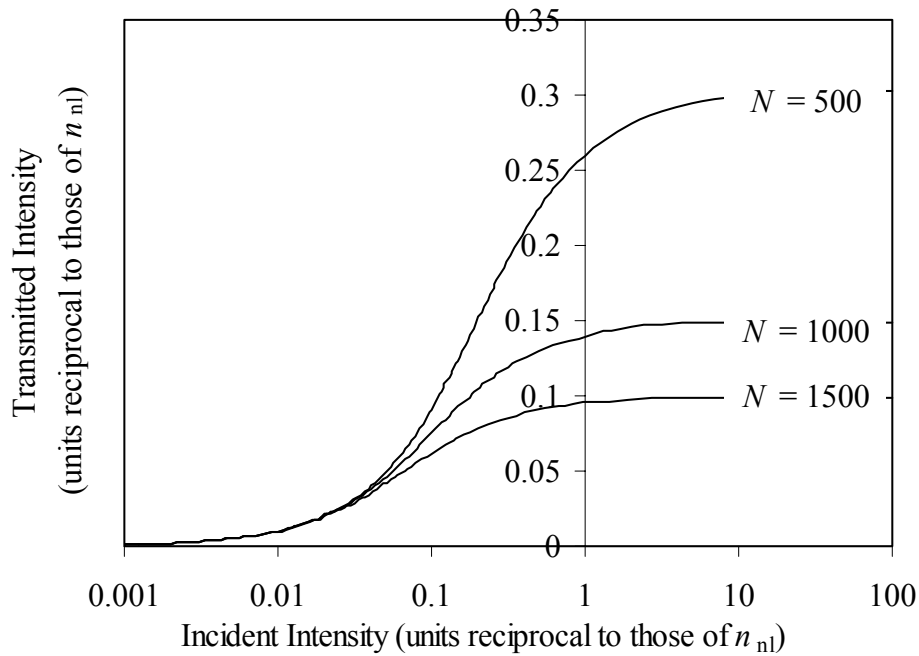


Figure 5.3: The transmitted intensity as a function of incident intensity on a semi-log plot for limiting structures with $|n_{nl}| = 0.01$ for different numbers of layers.

matched linear indices, the Bragg grating is hidden, and the transmitted intensity is equal to the incident intensity for very low incident intensities. Increasing incident intensity causes the effective refractive indices to change, forming a Bragg grating which reflects some of the incident light, leading to the decreased transmitted intensity. As the incident intensity is increased further, the effect of the pop-up nonlinear grating increases. This causes the saturation of transmitted intensity at a given limiting intensity. This last feature is most desired from the optical limiter. As shown in Figures 5.2 and 5.3 the value of the limiting intensity decreases with increasing numbers of layers. Eq. (5.4) proves that nonabsorbing, nonsaturating Kerr-nonlinear structures considered exhibit true steady-state optical limiting for any number of layers.

Since the two materials have opposite Kerr characteristics, the center of the stopband remains fixed at an initial spectral position. Unlike in cases in which only one material

is nonlinearly active, the nonlinear periodic structures considered here are stable in the intensity domain. The feasibility of fabrication of periodic structures made out of many periods will be discussed in the section 12.3.2.

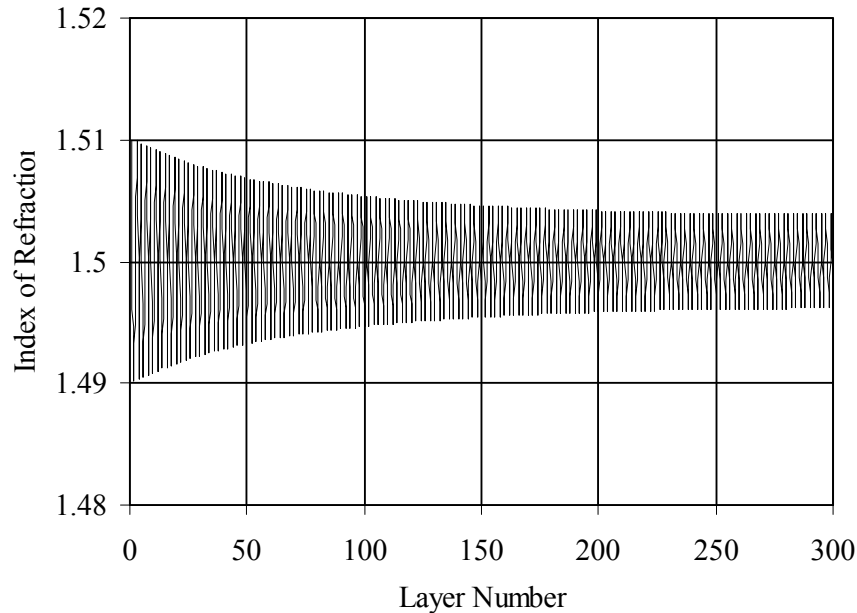


Figure 5.4: The effective indices of refraction across the structure of 300 layers with $|n_{nl}| = 0.01$ and matched linear indices of $n_{ln} = 1.5$. This plot demonstrates the decay of the intensity across the structure.

Figure 5.4 shows the evolution of the effective refractive index across a structure made of 300 layers illuminated by the incident intensity equal to 1. The indices of refraction of materials and the thicknesses of the layers are the same as in Figures 5.2 and 5.3. This plot can be used to track the decay of the intensity as the light penetrates into the limiter. The first few layers experience almost all of the incident intensity, whereas the last ones see only a fraction of it. The index contrast at the beginning of the structure is much greater than at the end. With the increased length of the structure the effective refractive indices of the last layers more closely approach the value of the average index n_0 .

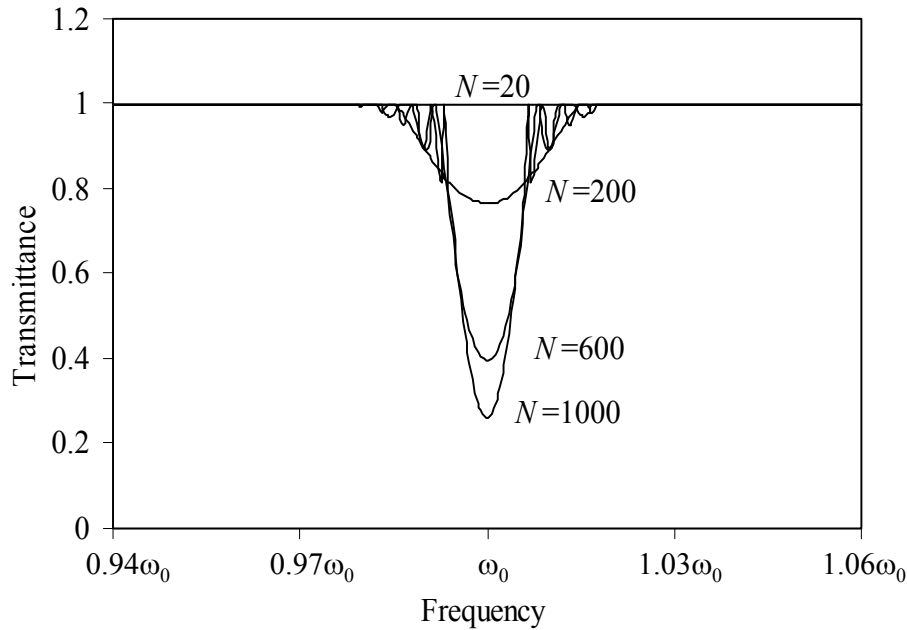


Figure 5.5: The evolution of the transmittance spectra with increasing number of layers for structures with $n_{nl} = \pm 0.01$. The nonlinear behaviour of the limiter is responsible for the formation of a stopband at the desired frequency.

Figures 5.5 and 5.6 display the transmittance spectra of limiters analyzed. Figure 5.5 shows the spectra for the same systems as in Figures 5.2 and 5.3 for various numbers of layers. The nonlinear indices of adjacent layers are matched in magnitude and opposite in sign: the average index does not change with intensity, the Bragg frequency stays fixed, and the device is optically stable within the intensity domain. As the number of the layers in the structure is increased, the stopband becomes deeper and sharper.

Optical bistability occurs if the rate of shift of the photonic stopband with increasing illumination exceeds the rate of growth of its depth at a given spectral position. Since in the limiters analyzed the center position of the stopband stays fixed, bistability is not manifest.

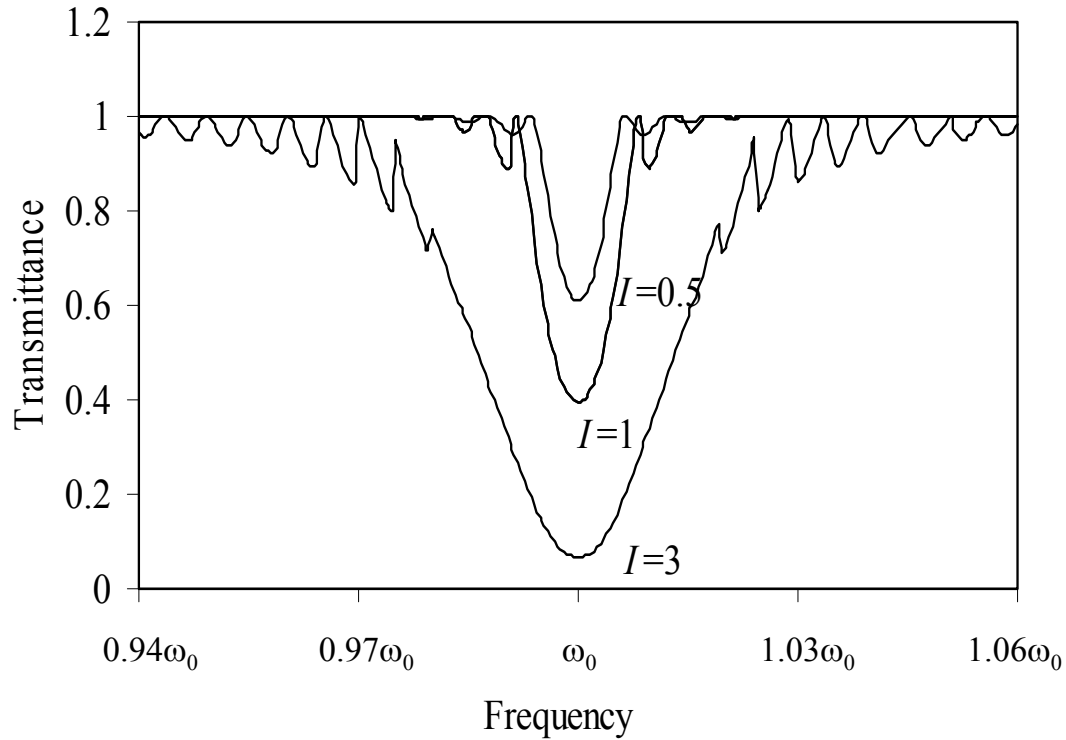


Figure 5.6: The evolution of the transmittance spectra as a function of increased incident intensity for the structure made of 300 layers with $n_{nl} = \pm 0.01$. As the incident intensity is increased the stopband becomes deeper and wider.

Figure 5.6 shows the transmittance spectra for a structure with 300 layers with $n_{nl} = \pm 0.01$ for incident intensities of 0.5, 1, and 3. This plot again illustrates the limiting behaviour. As the strength of the incident intensity is increased, the transmittance decreases and the width of the stopband gets larger. Increasing the incident intensity has the same effect on the transmittance spectrum as increasing the value of n_{nl} since it is the product of these two quantities which changes the effective refractive index.

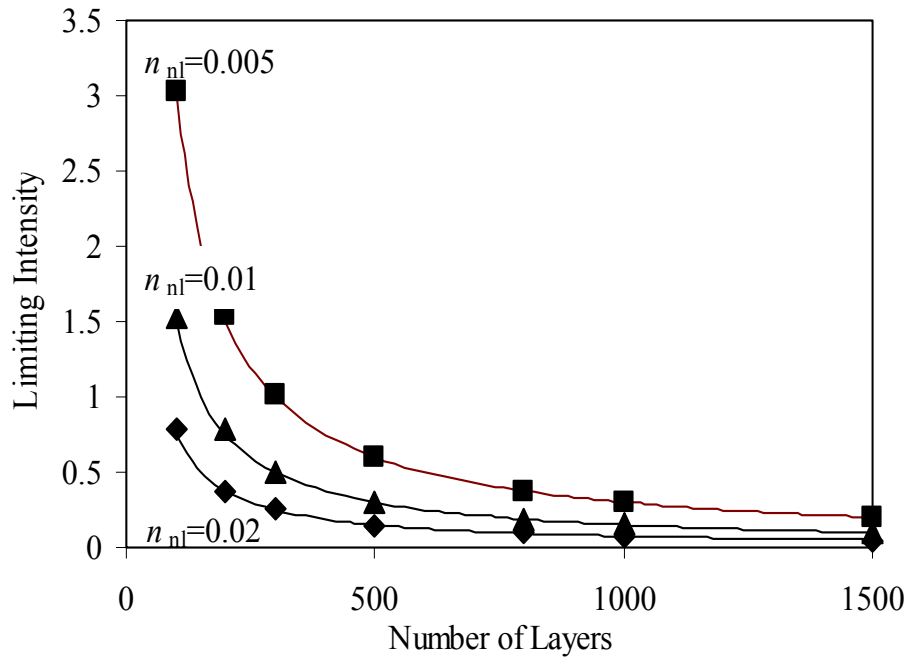


Figure 5.7: The limiting intensities as a function of the number of layers for $|n_{nl}| = 0.005$, 0.01, and 0.02. The values obtained from numerical calculations shown on the plot as squares, triangles and diamonds follow exactly the curves predicted by the analytical model.

Figure 5.7 displays the limiting intensities as a function of the number of layers for structures with $|n_{nl}|$ values of 0.005, 0.01 and 0.02 illuminated using light at the centre of the stopband. The curves obtained from Eq. (5.4) were plotted for the same cases. The points obtained from the numerical simulations appear in the predicted places on these curves. Thus, the highest possible intensity that will be transmitted by a given structure is inversely proportional to the nonlinear strength n_{nl} and number of layers N , but directly proportional to n_0 , the average index of refraction of the two materials used.

5.3 Theory of Optical Switching with Stable Nonlinear Periodic Structures

The work presented in the rest of this chapter was published in Refs. [7] and [124].

This section will discuss how the optical limiters introduced in the previous section can be used as optical switches and OR gates.

5.3.1 Optical Switching

In the optical switch considered, the increasing intensity of the pump beam is used to control the transmittance of a signal beam. In order to distinguish the pump and signal beam at the output of the structure, it may be desirable to use beams at different frequencies. This scenario is analyzed using numerical simulations.

Figures 5.8 and 5.9 show the results of these simulations. In both figures the structures analyzed have refractive indices as in Figure 5.2. The signal beam is on resonance $\lambda_0 = 2\Lambda n_{nl}$ and has a constant intensity of 0.1. The low-intensity signal does not perturb significantly the characteristics of the grating. The frequency of the pump beam is varied from $0.94\omega_0$ to $1.06\omega_0$. In Figure 5.8 the number of layers is kept constant at 100 and the transmittance spectra of signal beam is obtained for pump intensities of 1, 2 and 4. In Figure 5.9 the pump beam intensity is fixed at 1 and the number of layers is varied (100, 300, and 500).

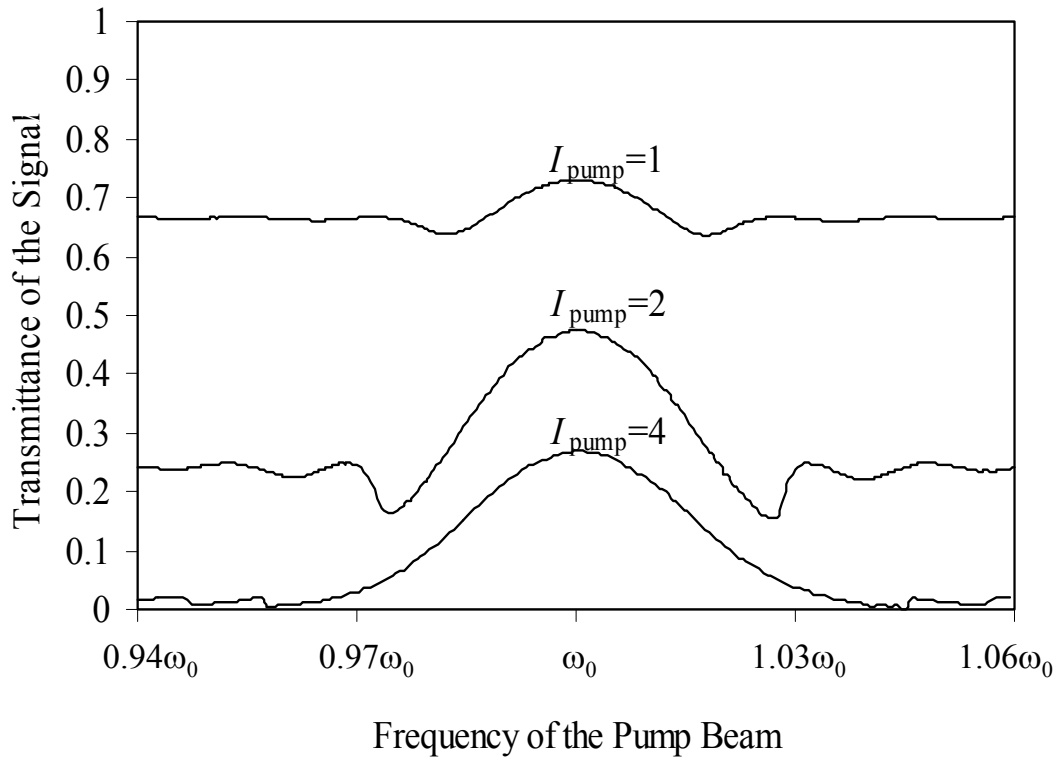


Figure 5.8: Demonstration of the switching capability. The figure shows the transmittance of the signal beam as a function of the frequency of the pump beam. The structures analyzed have refractive indices as in Figure 5.2. The signal beam is on resonance $\lambda_0 = 2\Lambda n_{nl}$ and has a constant intensity of 0.1. The frequency of the pump beam is varied from $0.93\omega_0$ to $1.06\omega_0$. The number of layers is kept constant at 100 and the intensity of the pump beam takes values of 1, 2, and 4.

It is shown in Figures 5.8 and 5.9 that the highest transmittance of the signal beam occurs when the frequency of the pump beam approaches the structural resonance of the periodic medium. As the frequency of the pump beam moves away from the resonance, the transmittance of the signal beam oscillates, eventually saturating far from the Bragg resonance. If the frequency of the pump beam is far away from the Bragg resonance, the transmittance of the pump approaches unity. The intensity of the pump beam is

then constant throughout the structure. A uniform Bragg grating is formed. The signal beam, which is Bragg-resonant with the structure, is substantially reflected.

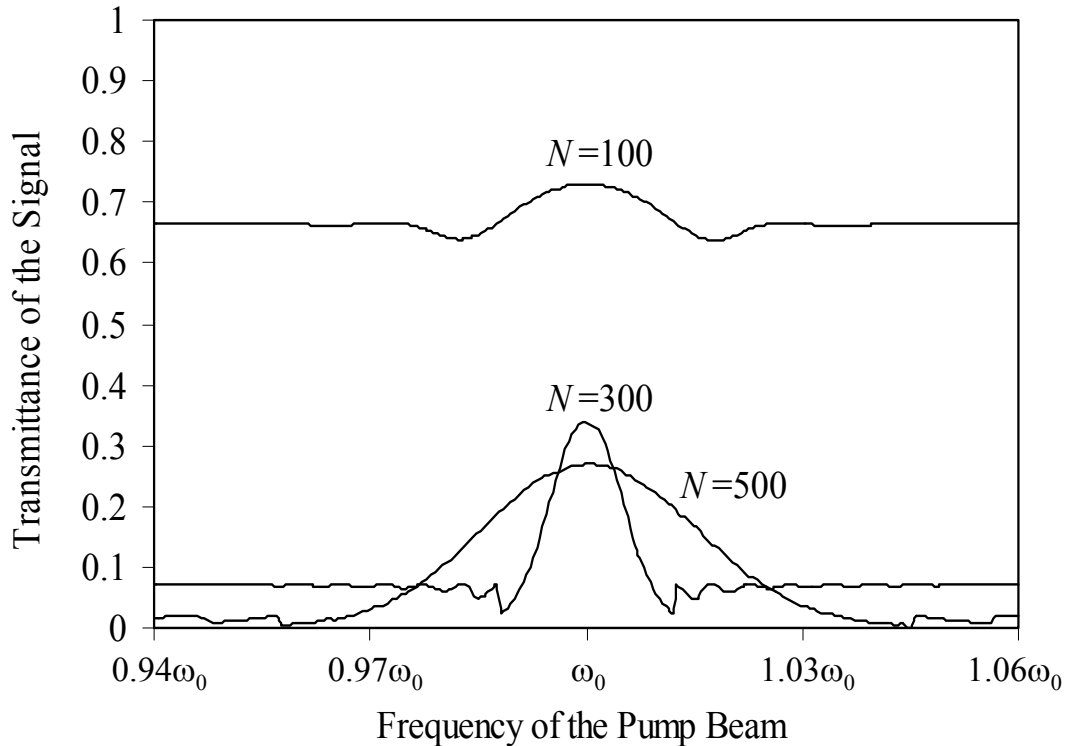


Figure 5.9: Transmittance spectrum of the probe beam for the structure analyzed in Figure 5.8. Pump beam intensity is kept constant at 1 and number of layers is varied (100, 300, and 500).

If, on the other hand, the frequency of the pump beam is close to the Bragg resonance, the intensity of the pump beam decays substantially within the first part of the structure and the refractive indices of only the layers at the beginning of the structure are strongly affected; the signal does not see a strong Bragg grating throughout the entire structure. The lowest value of the transmittance of the signal beam takes place at the first minimum of the transmittance spectra. At this point the intensity of the pump beam inside the structure is higher than the incident intensity. This spatial distribution of intensity

represents a stationary gap soliton that was previously observed in bistable systems.

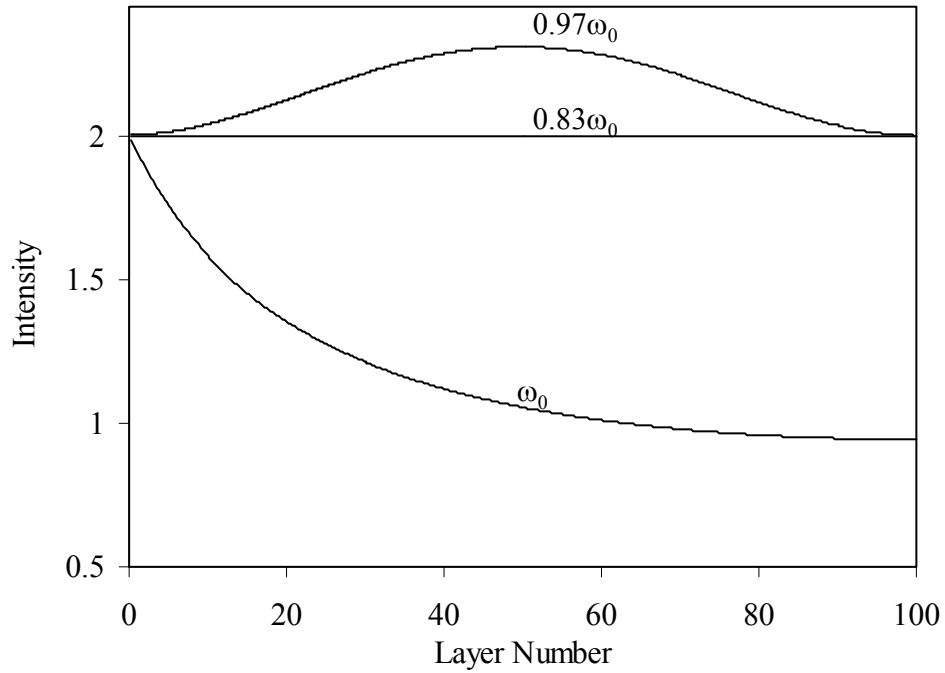


Figure 5.10: Evolution of the pump beam intensity across a 100-layer structure for pump frequencies of $0.83\omega_0$, $0.97\omega_0$, and ω_0 .

Figure 5.10 depicts the evolution of the pump beam intensity across the 100-layer structure for $|n_{nl}| = 0.01$, $n_0 = 1.5$, and $I_{pump} = 2$. The curves presented correspond to the pump beam at frequencies of $0.83\omega_0$ (far from the Bragg resonance), $0.97\omega_0$ (at the first transmittance maximum), and ω_0 (at the Bragg resonance).

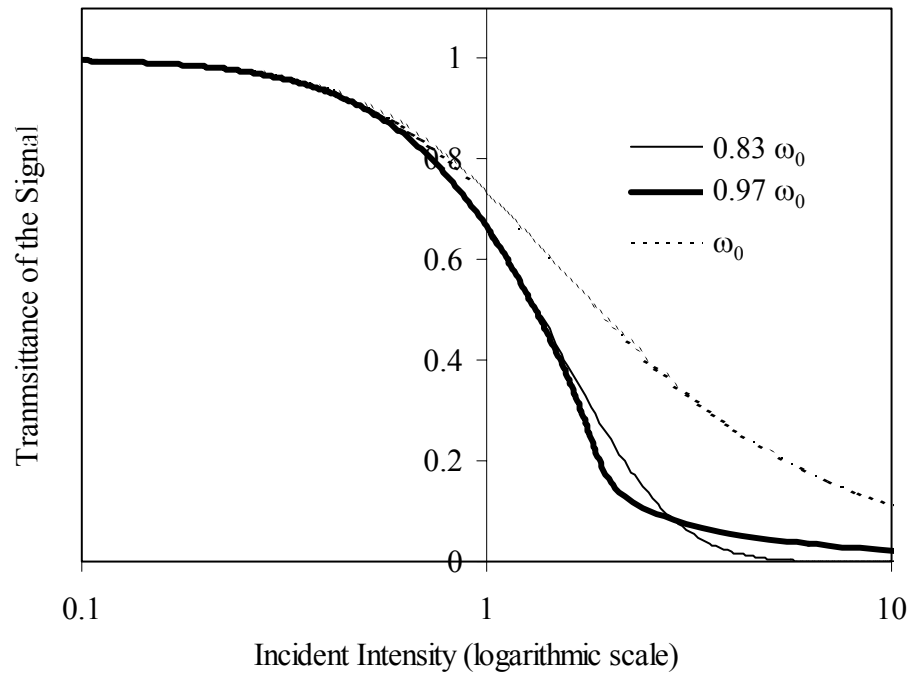


Figure 5.11: Transmittance of a signal beam as a function of the pump beam intensity. The frequency of the probe beam is fixed at the Bragg resonance, while the frequency of the pump beam takes values of $(0.83\omega_0, 0.97\omega_0, \text{ and } \omega_0)$.

Figure 5.11 shows the transmittance of the signal beam as a function of I_{pump} for the same structure as in Figure 5.10 for the same three frequencies of the pump beam. As the pump intensity is increased an effective index grating emerges. The value of the incident intensity at which the probe beam experiences substantial decrease in the transmittance depends on the frequency of the pump beam. For the pump frequencies of $0.83\omega_0$ and $0.97\omega_0$, the onset of probe switching takes place at lower incident intensities than if the frequency of the pump is at the Bragg resonance.

5.3.2 Logic OR Gating

The stable limiting and switching nonlinear periodic structures proposed above may be used as OR gates.

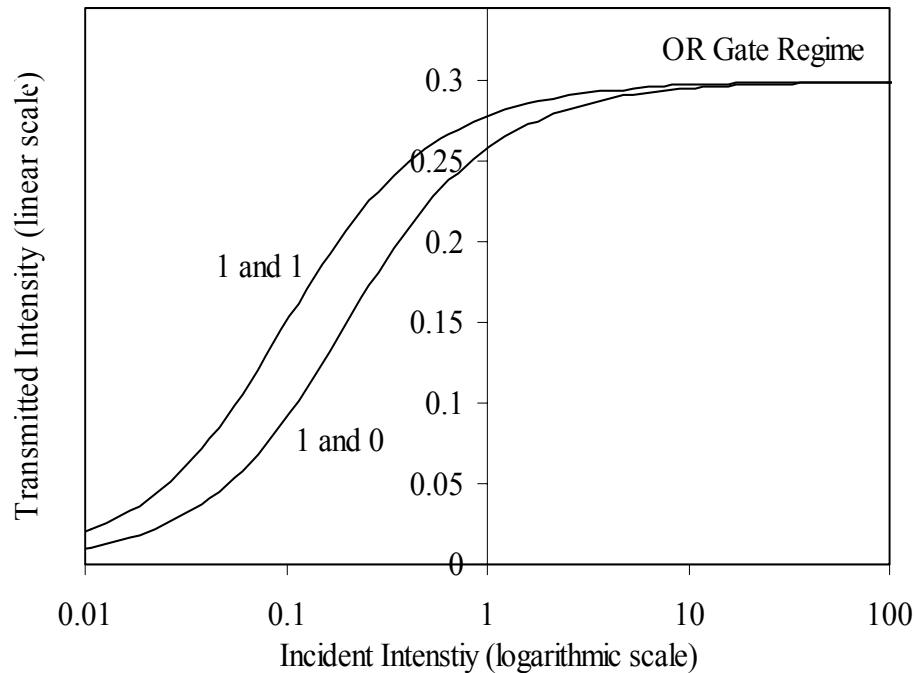


Figure 5.12: An OR gate realized using limiting and switching structures proposed.

If two beams are incident on the balanced structure considered in this chapter, and only one beam is at a sufficiently high intensity, then the net transmitted intensity will approach the limiting value described by Eq. (5.4). This situation corresponds to the input logic state (0,1) or (1,0) and an output of 1. If the intensities of both beams are high (analogous to an input of (1,1)), the transmitted intensity will approach the limiting intensity as well. This OR gate behaviour is illustrated in Figure 5.12.

5.4 Nonlinear Figures of Merit for Periodic Structures

Nonlinear figures of merit have been previously derived by comparing the switching and absorption lengths for a number of nonlinear devices [14]. These devices require figures of merit (2.15) ranging from 0.25 for the conventional distributed feedback grating to 1.75 for the X switch.

In order to quantify the usefulness of a given nonlinear material to optical limiting and switching proposed above, pertinent material figures of merit are derived for this class of devices. Scattering from the nonlinear grating will be a dominant signal processing effect if its characteristic decay length (L_{scatt}) is shorter than the decay length due to effective absorption (L_{alpha})

$$L_{scatt} \approx \frac{\Lambda n_{av}}{|\Delta n|} = \frac{\lambda}{2|\Delta n|} < L_{alpha} = \frac{1}{\alpha_{eff}}. \quad (5.5)$$

In (5.5) n_{av} is the average index of the grating, and Δn is the index contrast originating from the nonlinear effect. Inequality (5.5) is solved to give

$$\frac{2|\Delta n|}{\alpha_{eff}\lambda} > 1. \quad (5.6)$$

Inequality (5.6) has been derived with the assumption that the nonlinear index change is constant across the structure. Since in reality the intensity may decay across the structure, an assumption that the average index change is half of that at the beginning of the structure yields the lower bound for the figure of merit

$$F = \frac{|\Delta n|}{\alpha_{eff}\lambda} > 1. \quad (5.7)$$

Figure of merit (5.7) is the same as Eq. (2.15) that was derived in chapter 2 and is used throughout this thesis.

5.5 Conclusions

This chapter proposed a novel approach to optical signal processing using nonlinear periodic structures — it introduced the notion of stable intensity-domain optical response that supports functional transfer characteristics.

This chapter proposed and analyzed the response of limiters realized using nonabsorbing nonlinear periodic structures with matched linear refractive indices and opposite Kerr coefficients. The nonabsorbing limiters based on Kerr-nonlinearities should exhibit the key properties desired of ideal optical limiters under steady-state illumination: the transmitted intensity is clamped at a certain value. The limiters considered can be designed to clamp transmitted intensity at a specific value due to the relationship derived between the limiting intensity and the parameters of the structure. In the second part of the chapter it was demonstrated through development and solution of a model that the structures proposed can be used as optical switches and OR logic gates.

Chapter 6

Theory of Broadband Limiting with Slightly-Disordered Nonlinear Periodic Structures

It was found in chapter 5 that balanced nonlinear periodic structures with matched linear indices and opposite Kerr coefficients can support optical limiting and switching. This chapter explores the effect of weak disorder on the smoothness of the limiting spectrum and on the strength of the limiting response. This is followed by analyses of the impact of the disorder on the localization of light within nonlinear periodic structures that are periodic on average.

The work presented here was published in Refs. [8, 125].

6.1 Spectral Analysis

As in the previous chapter, the nonabsorbing structures analyzed within the present chapter are assumed to consist of materials with matched linear refractive indices, $n_{01} = n_{02} = n_0$, and Kerr coefficients of opposite sign and equal magnitude $n_{nl1} = -n_{nl2}$.

However, in contrast with the previous chapter, the layer thicknesses are not in general equal $d_1 \neq d_2$. The thickness of the i^{th} layer d_i is allowed to vary uniformly the average quarter-wave value $d_{\lambda/4n_{in}}$ within a specified range δ :

$$d_i = d_{\lambda/4n_{in}} \pm \delta \quad (6.1)$$

Such structures were introduced in Section 4.3.4 and are illustrated in Figure 4.3. The analyses presented in this chapter were performed by solving Eqs. (4.31) and (4.32) numerically.

Figure 6.1 shows the effect of introducing a disorder into the limiting structures proposed in chapter 5. The structures analyzed consist of 1000 layers and have linear index 1.5 and magnitude of Kerr indices $|n_{nl}| = 0.003$. The system was taken to be illuminated with the light at a normalized intensity of 1. The individual layer thicknesses were randomly and uniformly distributed within 1% , 7% and 10% of their quarter wave value at the centre of the stopband ω_0 .

The spectral region on which a given structure acts increases with the degree of disorder. For 1% deviation the transmittance spectrum is very similar to the unperturbed response. For 7% deviation, most of the limiting strength is still concentrated close to the centre of the unperturbed stopband. Increasing the degree of randomness to 10% spreads the effective stopband over a wider spectral range.

Two new features are distinct when the transmittance spectra of the randomized structures is compared with the transmittance spectra of the ordered structures of chapter 5:

- Increased disorder widens the spectral range over which the limiter exhibits nonlinear refraction, but reduces its depth. Randomly varying the layer thickness decreases the availability of wavevectors for which the Bragg condition is satisfied at a given optical frequency close to the center of the original unperturbed stopband, but a larger range of frequencies experiences some degree of backscattering. The strength

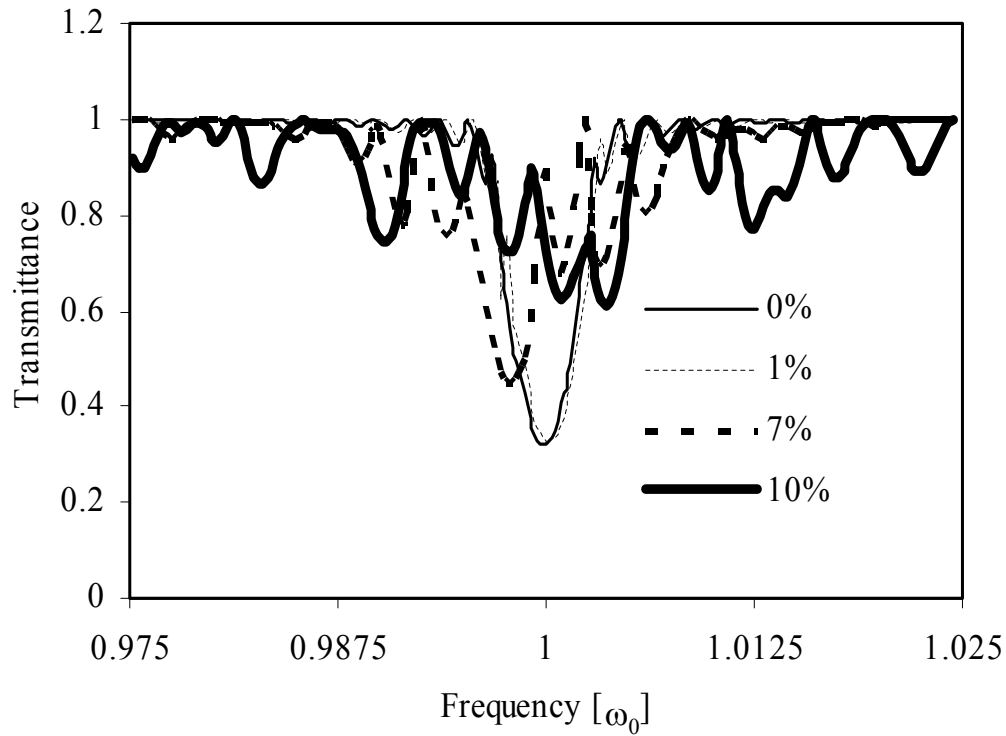


Figure 6.1: Influence of the increased layer thickness randomization on the nonlinear transmittance spectra.

of this backscattering is proportional to the number of coherent scatterers and the proximity of the individual layers to the quarter-wave value at a given optical frequency. A randomized system with a fixed number of layers will therefore have a smaller number of strongly backscattering regions than the fully ordered system.

- The introduction of randomness makes it possible for a particular optical frequency at a specific intensity to see a high transmittance even if it lies within the new, wider effective stopband. For a randomized system there is a possibility of obtaining a phase difference of close to 2π between the incident and reflected waves even for the light at an optical frequency that is close to the center of the unperturbed stopband. In this case, constructive interference between forward- and backward-

propagating waves results in a transmittance spike. Such a behaviour — associated with photonic defect states — is not observed within the stopband of a nonabsorbing ordered structure made up of materials with opposite Kerr coefficients.

The details of the transmittance spectra of structures with randomly-varying layer thicknesses depend on the random thickness fluctuations. It is not sufficient to specify statistical properties of the structure and materials: the details of a given random trial will determine the transmittance spectrum, in particular the location of any transmittance maxima within the stopband.

With the increased degree of randomization the spectral characteristics of individual structures differ from each other more significantly. This fact will be exploited to design a broadband optical limiter with no transmittance maxima within the effective stopband.

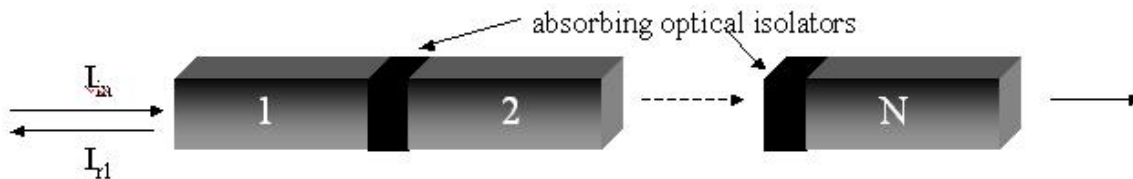


Figure 6.2: A combined system consisting of broadband optical limiters with inserted optical isolators. Decoupling among the constituent limiters eliminates transmittance maxima within the effective stopband.

Figure 6.2 proposes inserting optical isolators between adjacent limiters. These isolators are assumed to absorb only in the reverse (leftward) direction. Because the principle of superposition does not apply to periodic structures — n structures each made up of N layers differ in their response from a single $n \times N$ -layer structure — combining the limiters without eliminating feedback between adjacent structures will not eliminate the occurrence of local transmittance maxima within the stopband of the combined structure. The maxima of the individual units may disappear from the transmittance spectra, but new features originating from the combined periodic structure will appear.

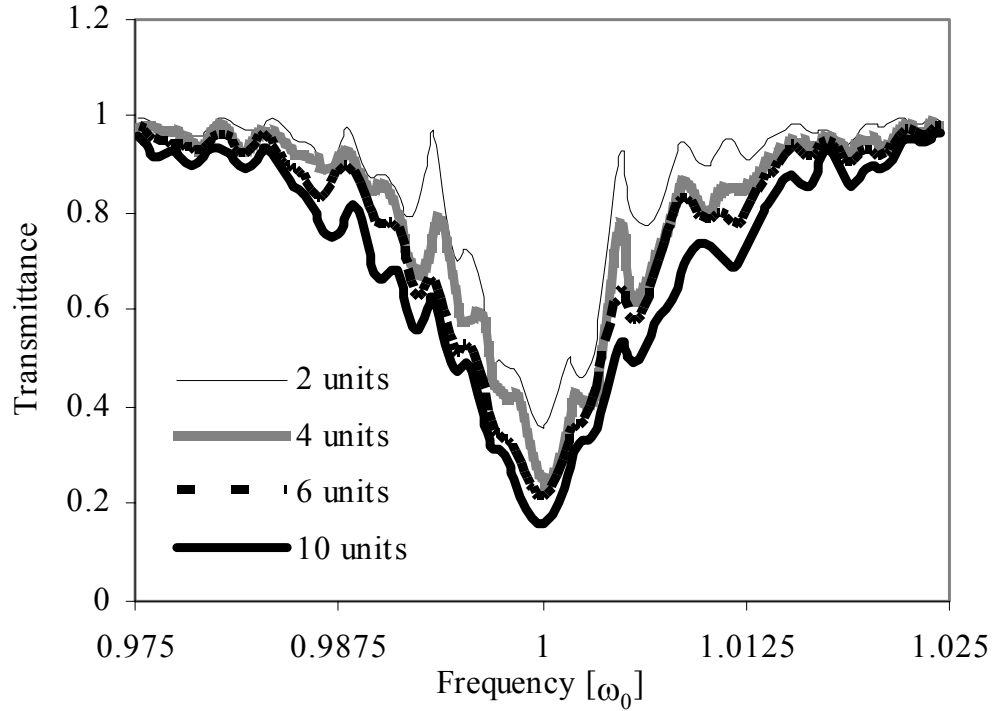


Figure 6.3: Combining randomized units in series eliminates transmittance maxima, deepens and widens the effective stopband.

In Figure 6.3 the transmittance spectra of a limiter made up of increasing numbers of 1000-layer units with 10% randomness, $n_0 = 1.5$, and $|n_{nl}| = 0.002$ is plotted. The structure is assumed to be illuminated with an incident intensity of 3. The 1000-layer units are separated by optical isolators. In the many-unit system with isolators, the transmittance maxima which are present in the shorter systems are eliminated. A wide stopband with no transmittance maxima is formed.

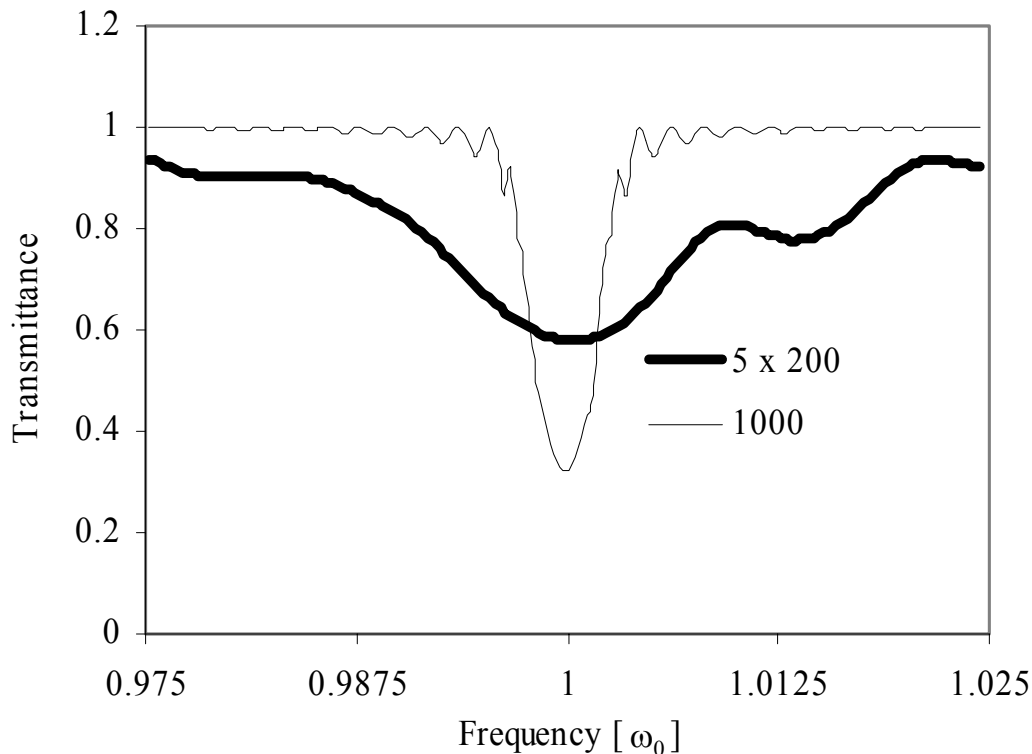


Figure 6.4: A comparison of the transmission spectra for a single perfectly periodic 1000-layer structure (the thin line) versus 5 combined randomized 200-layer units (the thick line).

In Figure 6.4 the transmittance spectra of two 1000-layer structures are compared: a combined system of five units with 200 layers and 7% randomization separated by optical isolators, and a 1000-layer ordered system. The system with isolators acts on a much wider range of optical frequencies.

6.2 Analysis of Intensity Transmittance

It will be now theoretically demonstrated that the randomized systems exhibit true limiting behaviour: the transmitted intensity is clamped below a fixed level at high incident intensities.

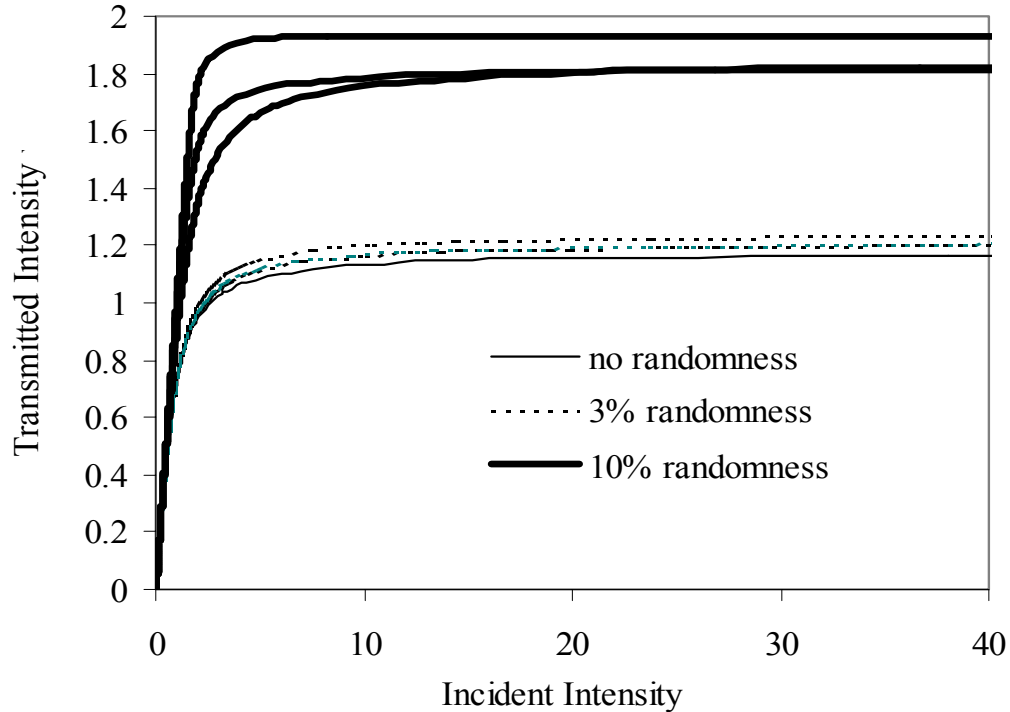


Figure 6.5: Transmitted versus incident intensity for various degrees of randomness at various trials.

Figure 6.5 depicts the transmitted versus incident intensity for a structure of 100 layers with $|n_n| = 0.01$ for various degrees of randomness. The frequency of the optical signal lies at the centre of the ordered stopband. All of the structures exhibit saturation to a limiting intensity. A stronger randomization leads to a higher limiting intensity. However, true limiting behaviour is preserved even in the presence of a high degree of randomness. As it was shown in the previous chapter, the choice of Kerr indices of

opposite sign and comparable magnitude is essential in order to preserve this limiting behaviour. The structure would otherwise exhibit multistability. For a low degree of randomization this behaviour is still preserved in disordered structures.

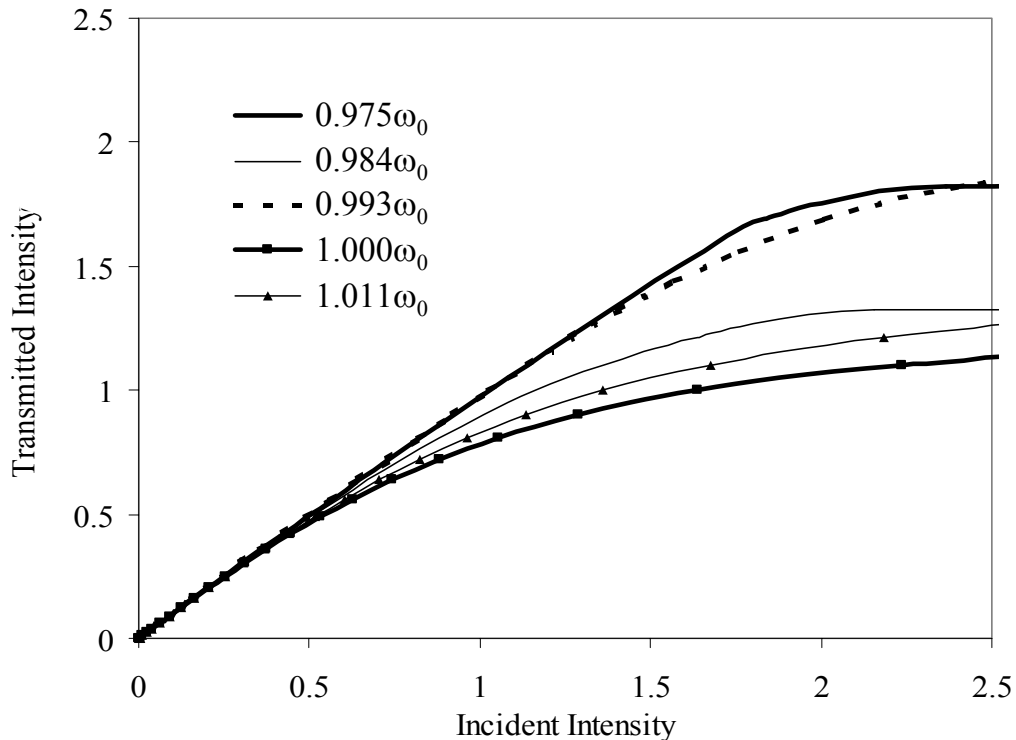


Figure 6.6: The transmitted vs. the incident intensity for light at frequencies inside the broadened stopband of a 10% randomized 100-layer structure.

A broadband optical limiter should display a limiting behaviour over its entire stopband. Since the width of the stopband is proportional to the index contrast, and in the structures analyzed index contrast is proportional to I_{in} , it is necessary to keep the incident intensity constant when comparing broadband characteristics of ordered and randomized structures.

Figure 6.6 displays the transmitted versus incident intensity for a 100-layer structure with $|n_{nl}| = 0.01$ and 10% randomization at various frequencies. Even without elimi-

nating feedback between adjacent nonlinear periodic structures, the combined systems behave like limiters. However, unless the feedback is inhibited there is a possibility that light at particular frequency will experience limiting at a much higher intensity than the rest of the effective stopband ($0.993\omega_0$ in Figure 6.6). This behaviour manifests itself with resonance spikes present in the transmittance spectra for a range of incident intensities. The proposed elimination of backward feedback between adjacent units ensures that the combined structure exhibits limiting behaviour over the entire stopband (i.e. no resonance spikes) also at intermediate intensities.

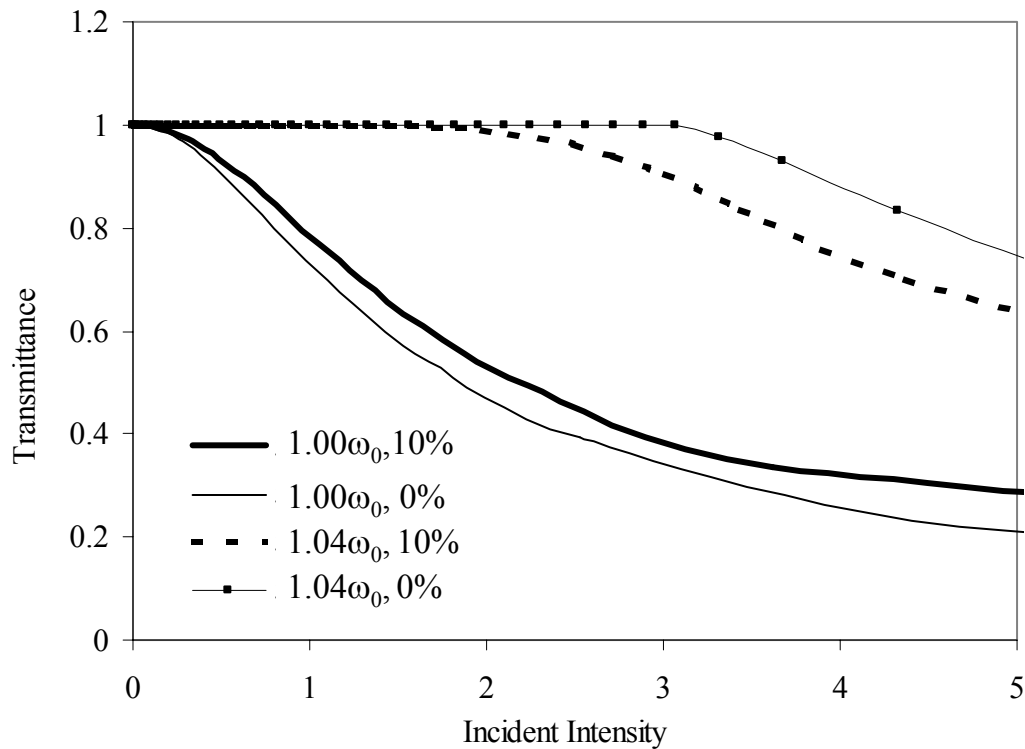


Figure 6.7: Transmittance versus incident intensity. Comparison between ordered and 10% randomized 100-layer structures at two frequencies.

In Figure 6.7 the transmittance ($T = I_{out}/I_{in}$) as a function of incident intensity for the structure of Figure 6.6 and an ordered 100-layer unit is compared. Near ω_0 , ordered

and disordered structures start to display limiting properties at comparable incident intensities. For the off-centre frequencies ($1.04\omega_0$), randomized structures begin to display limiting behaviour at lower intensities. This confirms that at a particular I_{in} the effective broadband stopband is larger for a disordered structure.

6.3 Localization of Light

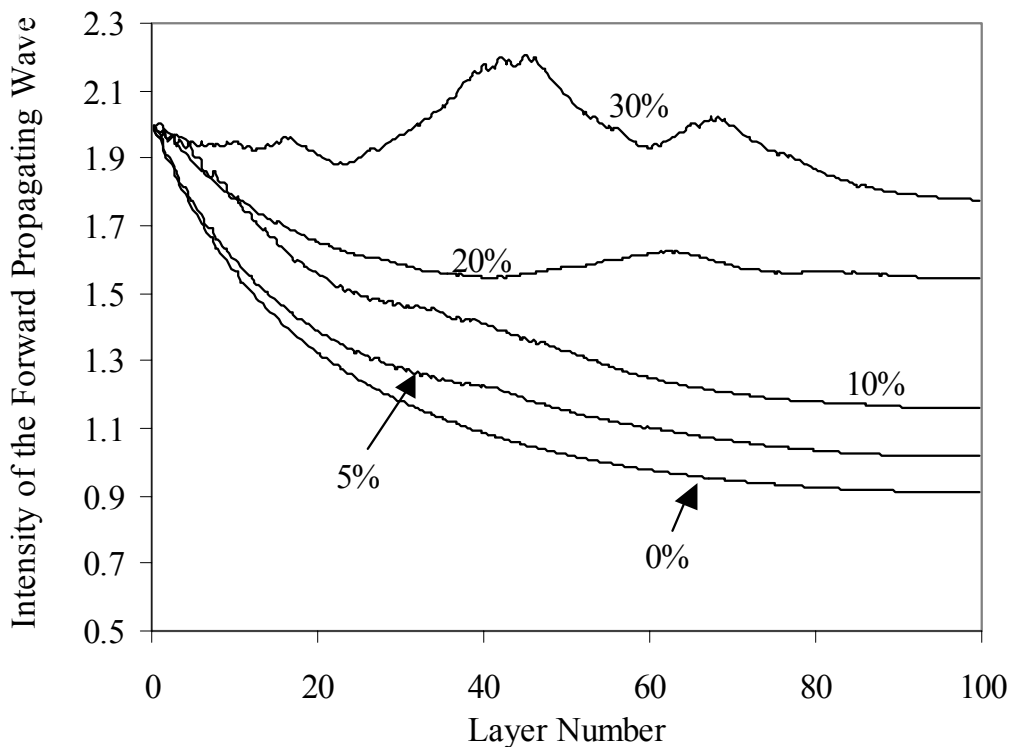


Figure 6.8: Evolution of the intensity of the forward propagating wave across a 100-layer structure. Impact of the increasing level of randomness for the incident intensity of 2 is shown.

Figure 6.8 shows the evolution of intensity associated with the forward-propagating wave across a 100-layer structure with $|n_{nl}| = 0.01$ illuminated with an intensity of 2. These structures employ no isolators. As the degree of randomization is increased,

the forward-propagating wave experiences weaker attenuation — its localization length increases and the limiting strength decreases. For high degrees of disorder (20% and 30%), light exhibits localization within the structure.

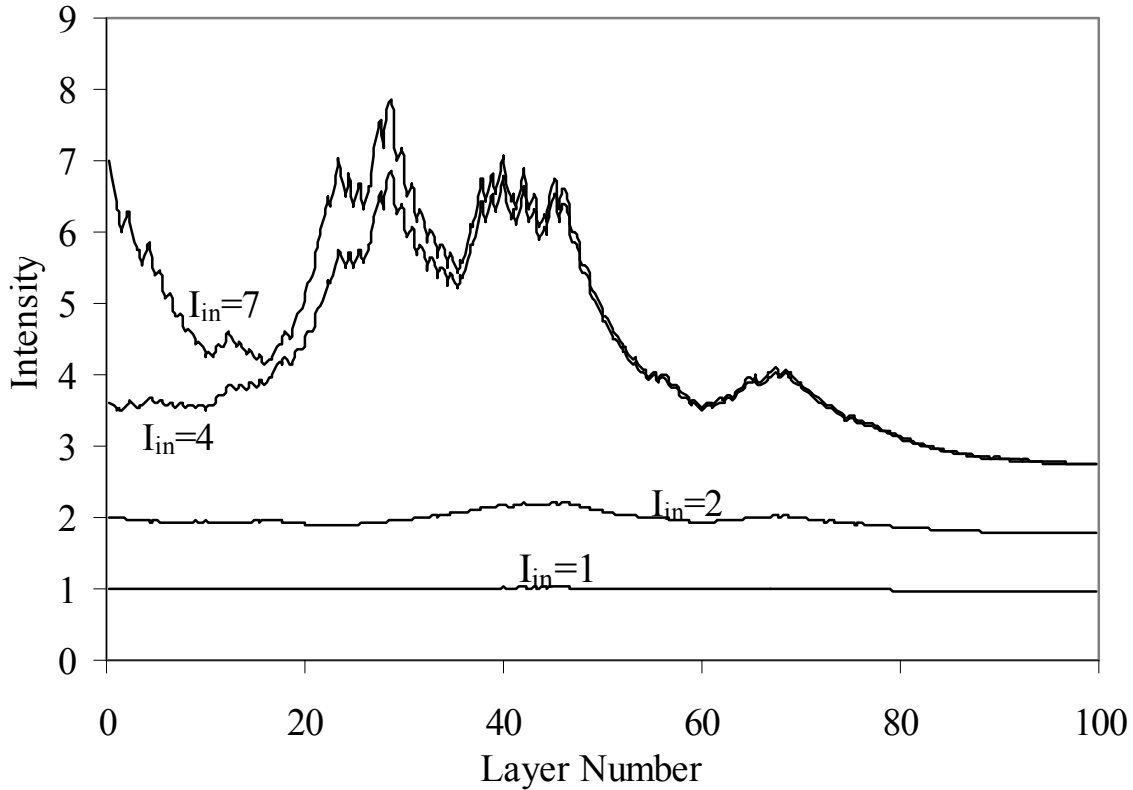


Figure 6.9: The localization of light within a 30% randomized structure. The figure shows the impact of increasing incident intensity.

Figure 6.9 illustrates the localization of light within a 30% randomized structure for various values of incident intensity. As the incident intensity is increased, a nonlinear grating is formed and light becomes trapped within the structure. However, as is evident from the comparison of curves corresponding to $I_{in} = 3.5$ and $I_{in} = 7$, for high incident intensity the transmitted intensity is constant. This confirms the limiting behaviour of nonlinear disordered structures that are periodic on average.

As discussed previously, introducing disorder may result in certain frequencies exhibiting a high transmittance even if these frequencies lie within the stopband of the original, ordered structure. Figures 6.10 and 6.11 show that eliminating feedback between adjacent structures removes a transmittance maximum.

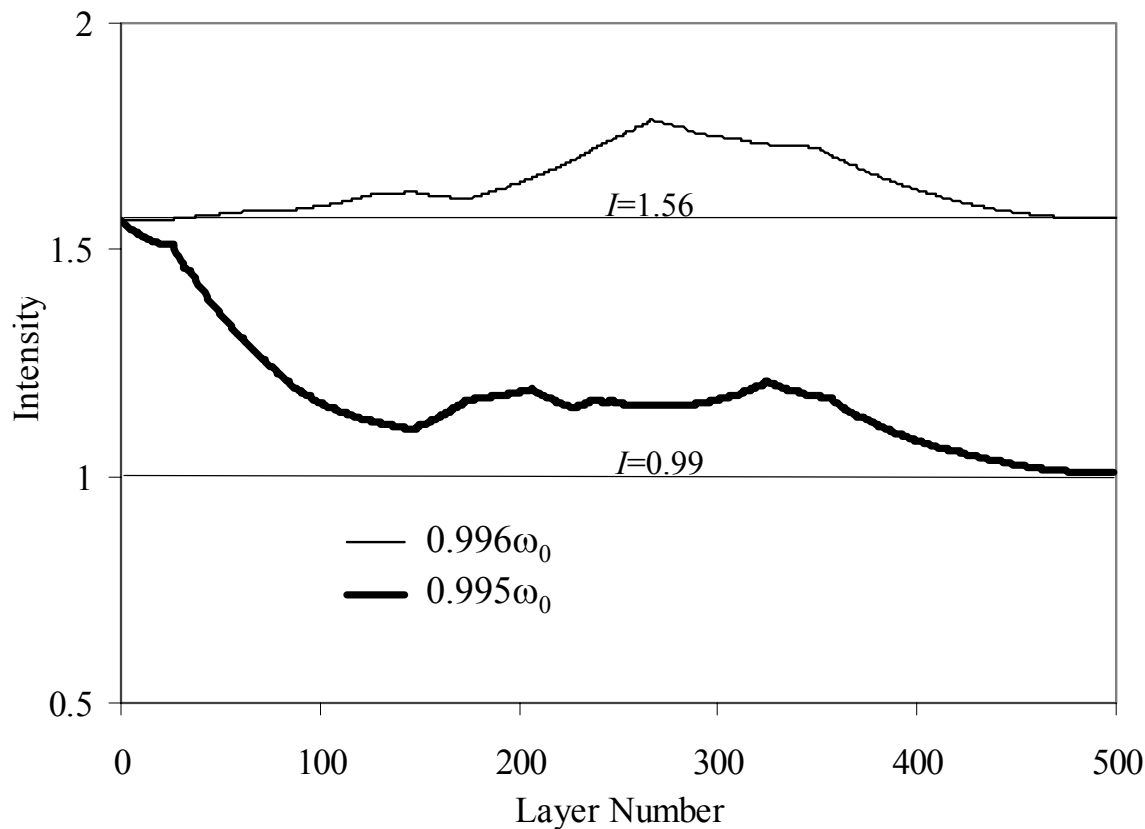


Figure 6.10: The intensity of the forward-propagating wave across the structure in the transmitting and limiting regimes.

Figure 6.10 shows the evolution of the intensity associated with the forward-propagating wave in the limiting and transmitting states. A 500-layer structure with $|n_{nl}| = 0.002$ and 7% randomization is considered to be illuminated with light at $I_{in} = 1.56$ at two frequencies, $0.996\omega_0$ and $0.995\omega_0$. Within the limiting domain ($0.996\omega_0$) the intensity decays across the structure. When the transmittance maximum is reached ($0.995\omega_0$), a

gap soliton is formed.

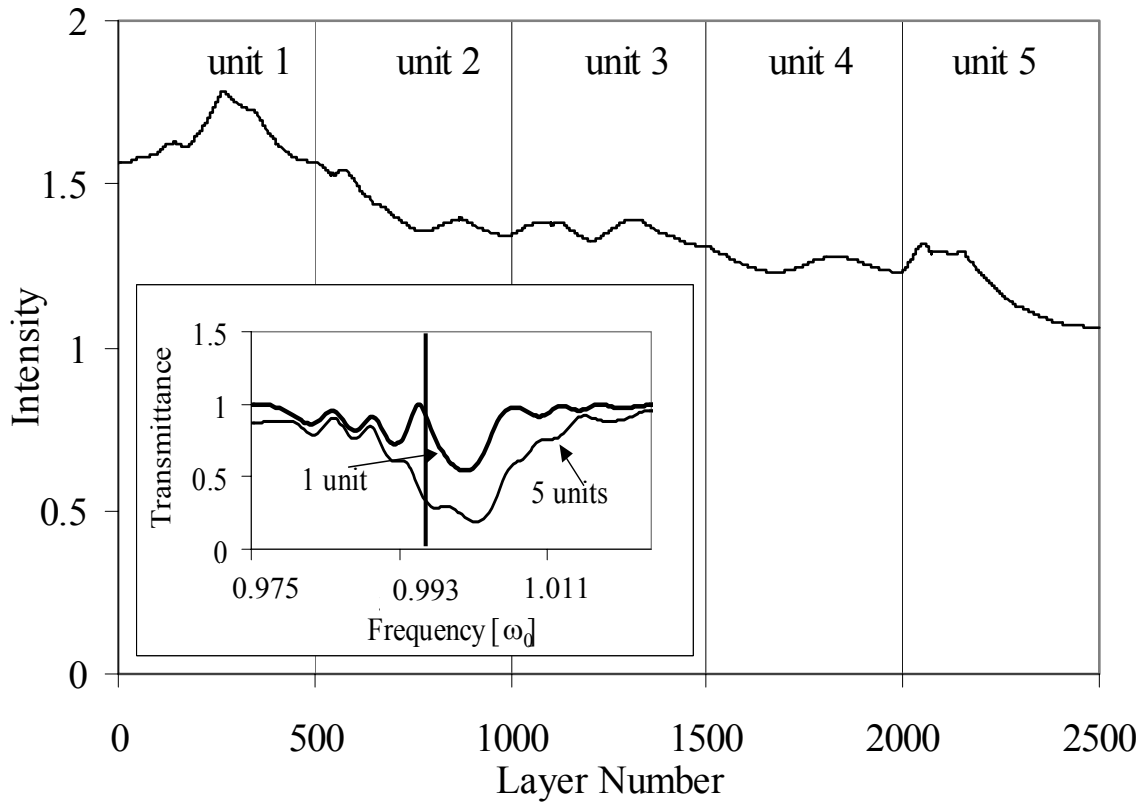


Figure 6.11: The intensity of the forward-propagating wave across a structure consisting of five randomized 500-layer units. The inset shows the transmittance spectra for structures with one and five units.

Figure 6.11 shows the evolution of the intensity of the forward-propagating mode across a structure consisting of five 100-layer units with 7%-randomization separated by isolators. The first unit is identical to that whose response is illustrated in Figure 6.10. The degree of randomization, as well as the structural and material parameters, are the same as in Figure 6.10. For the incident intensity of 1.56 and frequency $0.995\omega_0$, light is fully transmitted by the first periodic unit. On its own, this first segment does not provide limiting, but instead possesses a transmittance spike for this particular choice

of frequency and intensity for the incident wave. However, eliminating feedback in the combined system removes the transmittance maximum.

6.4 Conclusions

This chapter analyzed further the limiting nonabsorbing structures introduced in chapter 5. The limiters were assumed to exhibit a realistic degree of randomness in the layer thicknesses. This enabled additional signal processing function of the broadband optical limiting. It was shown that disordered structures exhibit true optical limiting over a spectral range much greater than the limiting bandwidth of a perfectly periodic nonlinear media. However, the limiting response of the disordered structure at a given optical frequency may be diminished when compared to the response of perfectly periodic structure. The disordered structures exhibit localization of light over a spectral bandwidth related to both the incident intensity and the degree of disorder. A method was proposed to eliminate the spikes in the transmittance spectra of disordered structures by inhibiting the feedback at certain spatial stages within a composite nonlinear periodic structure.

Chapter 7

Theory of Optical Signal Processing with Out-of-Phase Balanced Nonlinear Periodic Structures

Chapters 5 and 6 have explored the limiting and switching capabilities of balanced nonlinear periodic structures. This chapter will modify the limiting structures that have matched linear indices. A structure with a shallow, built-in linear index grating that is out-of-phase with the distribution of Kerr coefficients will be considered. This structure will be shown theoretically to support additional signal processing functions.

The work presented in this chapter was published in Refs. [126–130].

7.1 Structure and Modelling Approach

As in the devices proposed in previous chapters, the structures analyzed in this chapter are assumed to be made out of materials with Kerr coefficients of opposite the sign and equal magnitude ($n_{nl1} = -n_{nl2}$). However, in contrast to the limiting structures of chapters 5 and 6, the linear indices are not matched, ($n_{01} \neq n_{02}$) and layer thicknesses are not in general equal, ($d_1 \neq d_2$).

A new nonlinear periodic system is proposed:

- The structures analyzed herein are assumed to have a shallow built-in linear grating.
- The material with higher linear refractive index has a negative Kerr nonlinearity, while the material with lower linear refractive index has a positive nonlinearity. This structural and material arrangement will be referred to as an *out-of-phase* nonlinear periodic grating.

The profile of an out-of-phase nonlinear periodic structure is shown in Figure 7.1.

The out-of-phase configuration ($n_{0k} < 0, n_{nl} = 0$) results in an effective refractive index grating that, with increasing intensity, first closes and then reopens. The character and optical stability of this response depends on the relative strengths of linear and nonlinear coefficients. Eqs. (4.27) and (4.28) were used to simulate the response of the devices proposed.

7.2 Basic Stability Condition

This section derives the conditions that ensure that the steady-state response of the nonlinear periodic structures with built-in linear index grating is stable in the intensity-domain.

The Bragg condition [121] for a medium with intensity-dependent refractive indices

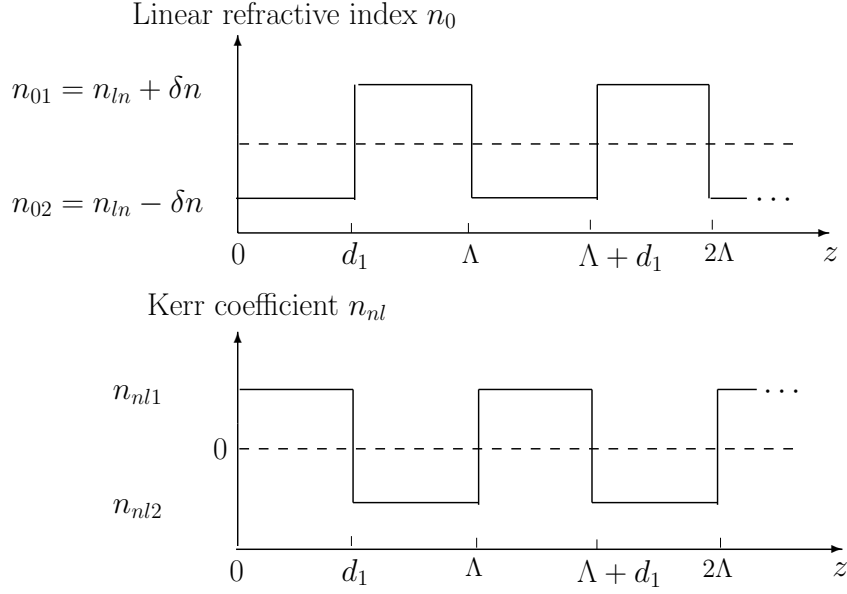


Figure 7.1: Profile of linear refractive indices and Kerr coefficients of a nonlinear periodic structure in the out-of-phase configuration. The refractive indices of two adjacent layers are $n_{01} + n_{nl1}I$ and $n_{02} + n_{nl2}I$, where $n_{01} < n_{02}$ and $n_{nl1} = -n_{nl2} > 0$.

is itself a function of intensity:

$$(n_{01} + n_{nl1}I)d_1 + (n_{02} + n_{nl2}I)d_2 = \frac{\lambda_0}{2} \quad (7.1)$$

The spectral position, λ_0 , of the centre of stopband in a periodic grating is given by Eq. (7.1).

In order to achieve an optically stable device operation in the intensity domain, the spectral position of the centre of stopband should stay fixed. This is expressed in terms of two conditions:

$$\begin{aligned} n_{01}d_1 + n_{02}d_2 &= \frac{\lambda_0}{2} \\ n_{nl1}d_1 + n_{nl2}d_2 &= 0 \end{aligned} \quad (7.2)$$

Conditions (7.2) can be fulfilled only if the Kerr coefficients are of opposite sign. Solving

for d_1 and d_2 gives:

$$\begin{aligned} d_1 &= \frac{\lambda_0}{2 \left(n_{01} - n_{02} \frac{n_{nl1}}{n_{nl2}} \right)} \\ d_2 &= \frac{\lambda_0}{2 \left(n_{02} - n_{01} \frac{n_{nl2}}{n_{nl1}} \right)} \end{aligned} \quad (7.3)$$

Expressions (7.3) specify the thicknesses of layers which, for a given pair of nonlinear materials, ensure the optical stability of system. They fix the center of stopband at λ_0 regardless of the value of incident intensity. The analysis in (7.1) to (7.3) is heuristic. In reality, the intensity will vary from layer to layer, but only slowly between adjacent layers in low-index-contrast structures. Then the approximation is valid in the incoherent case. Results obtained through exact TMM methods confirm that the fulfilment of conditions (7.3) results in a stable optical response.

7.3 S-shape Transfer Characteristics

Figure 7.2 shows the transmitted intensity of the periodic nonlinear medium analyzed as a function of incident intensity for various numbers of layers ($N = 100, 400,$ and 1000). Here and in the rest of this chapter the incident light is assumed to be at a wavelength corresponding to the center of linear stopband, chosen according to Eqs. (7.3).

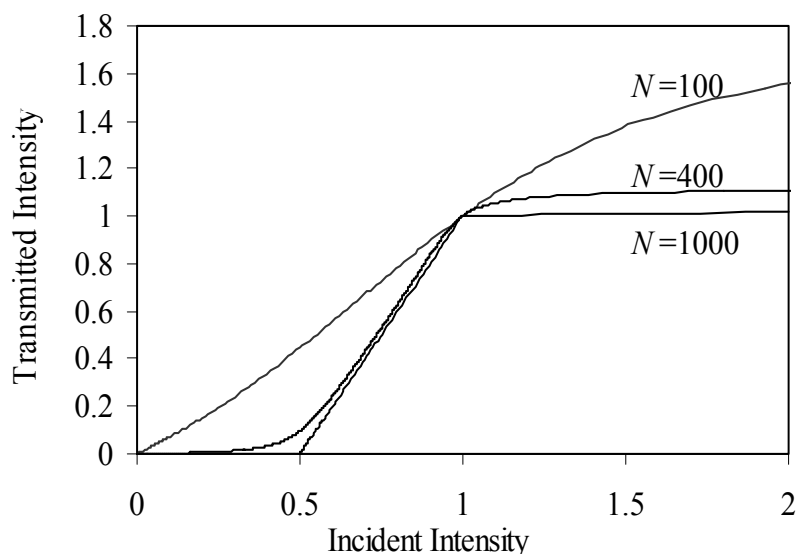


Figure 7.2: The transmitted intensity for the structures with an out-of-phase effective refractive index profile for various numbers of layers ($N = 100, 400, 1000$). The structures have linear refractive indices of $n_{01}=1.5$ and $n_{02}=1.52$ and Kerr coefficients of $n_{nl1}=0.01$ and $n_{nl2}=-0.01$.

The structures analyzed consist of materials with the linear indices of refraction of $n_{01}=1.5$ and $n_{02}=1.52$ and Kerr coefficients of $n_{nl1}=0.01$ and $n_{nl2}=-0.01$. In Figure 7.2 three regimes of operation are observed: at low intensities, the incident signal is resonantly reflected; for intermediate incident intensity, the system goes through a region of constant differential transmittance; for high incident intensity, the transmittance descends back to zero.

Figure 7.3 illustrates the physical mechanisms responsible for this behaviour. The figure shows the evolution of intensity and the intensity-dependent refractive index for various values of I_{in} across a 1000-layer structure with the same material parameters as in Figure 7.2.

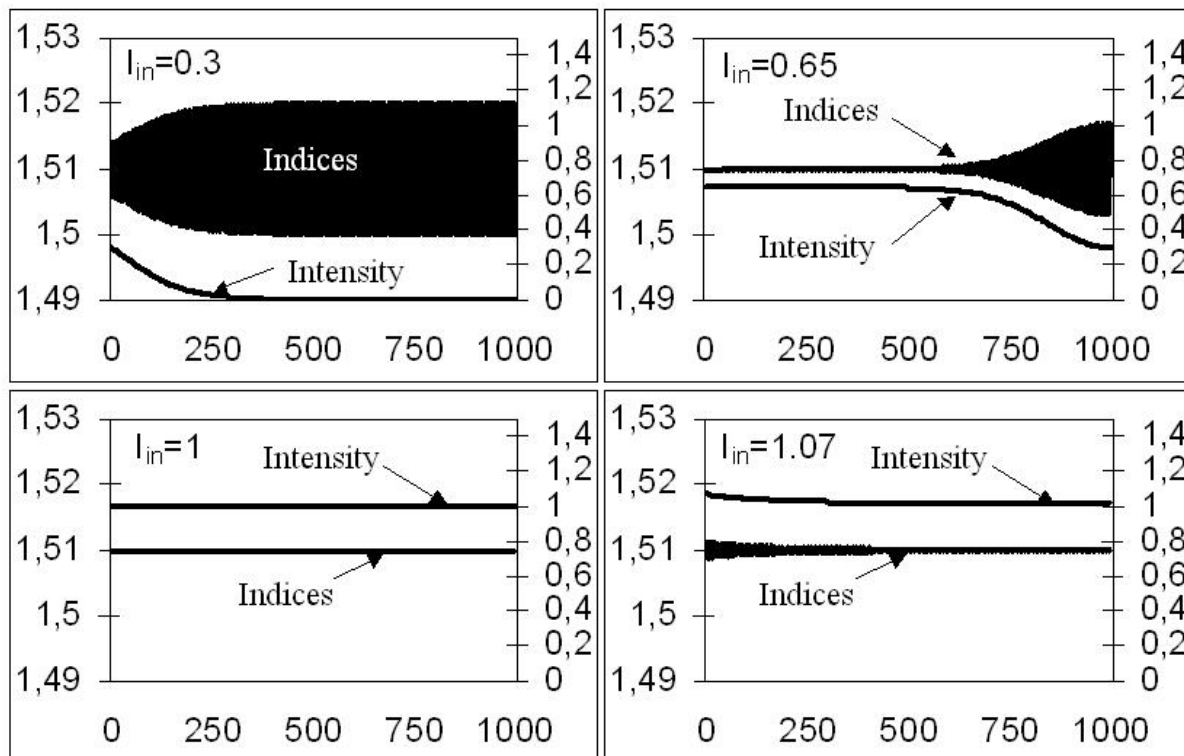


Figure 7.3: Local effective refractive index and the intensity across a 1000-layer structure with material parameters as in Figure 7.2 for various values of incident intensity. The total refractive index is given on the left vertical axis and the local intensity is given on the right axis.

Light with low incident intensity ($I_{in} = 0.3$) is reflected by the built-in linear grating and decays to a negligible value within the first part of the structure. As the intensity is increased beyond $I_{in} = \frac{n_{01} - n_{02}}{2(|n_{n11}| + |n_{n12}|)}$ the nonlinearity modifies substantially the profile of refractive index variation across the structure ($I_{in} = 0.65$). Since the layers with higher linear index have a negative Kerr coefficient, and those with lower n_0 have a positive n_{nl} ,

increasing intensity initially decreases the difference between the total indices of refraction, reducing the net amplitude of the grating. The transmitted intensity is no longer zero. When the incident intensity reaches $I_{in} = \frac{n_{01}-n_{02}}{(|n_{nl1}|+|n_{nl2}|)}$, the grating disappears and the structure assumed is completely transmitting. As the incident intensity is increased further ($I_{in} = 1.07$) the grating (phase-shifted relative to the initial linear grating) forms again, resulting in the limiting behaviour manifested in Figure 7.2. The transmitted intensity is clamped at $\frac{n_{01}-n_{02}}{(|n_{nl1}|+|n_{nl2}|)}$. In order to achieve such sharp characteristics, the structures analyzed need to be at least 1000 layers long.

Figure 7.4 shows the idealized response of structures with strong built-in linear stop-band (large number of layers or high linear index contrast) for different materials (different n_0 and n_{nl}). In order to describe analytically the response of such composite structures, a new parameter a is defined:

$$a = \frac{n_{01} - n_{02}}{|n_{nl1}| + |n_{nl2}|} \quad (7.4)$$

For a given choice of material parameter a , the idealized transmitted intensity I_{out} is related to incident intensity by the approximate relation:

$$I_{out} = \begin{cases} 0, & \text{for } I_{in} < \frac{a}{2}; \\ 2I_{in} - a, & \text{for } \frac{a}{2} < I_{in} < a; \\ a, & \text{for } I_{in} > a; \end{cases} \quad (7.5)$$

As the strength of the linear grating weakens (short structures or low linear index contrast) the transmission characteristics deviate near $I_{in} = \frac{a}{2}$ and $I_{in} = a$ from the values defined by Equation (7.5).

In a hard-limiter the output should be 1 for an input greater than or equal to 1, and 0 otherwise [131, 132]. In Figure 7.5 an all-optical hard limiter with arbitrarily steep transition stages is proposed. N limiters with $a = 1$ are positioned in series, with optical isolators between each pair. These isolators are needed to eliminate a feedback by allowing light to propagate in the forward direction and absorbing reflected light. The

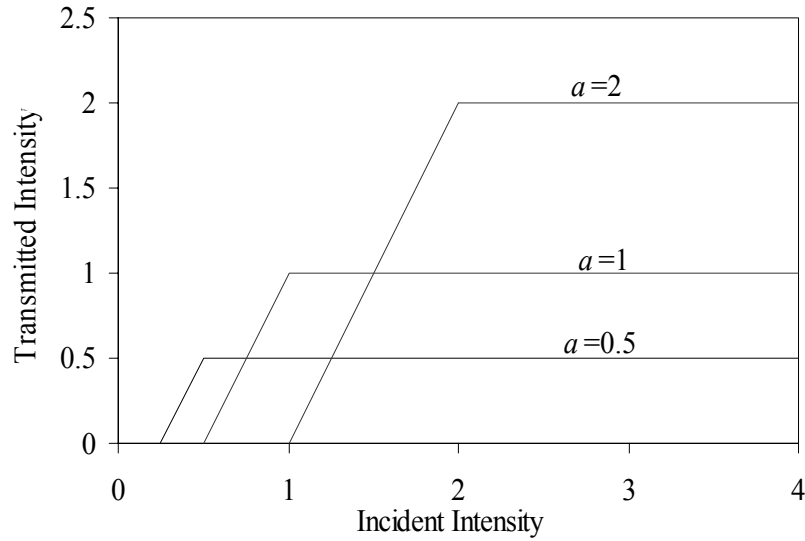


Figure 7.4: The idealized transmitted intensity for out-of-phase nonlinear periodic structures with different material parameters.

first nonlinear grating blocks incident radiation with intensity less than $\frac{a}{2}$. However, the intensity transmitted by the first unit still ranges from 0 to a . This transmitted intensity is then fed into the second unit and again, light with intensity lower than $\frac{a}{2}$ is blocked. Light with intensity lower than $\frac{a}{2}$ seen by the second unit corresponds to light incident on the composite device with intensity larger than $\frac{a}{2}$ and lower than $\frac{3a}{4}$. Generalizing for N units, the following transmission characteristic is obtained:

$$I_{out} = \begin{cases} 0, & \text{for } I_{in} < a \left(1 - \frac{1}{2^N}\right); \\ 2^N I_{in} + a(1 - 2^N), & \text{for } a \left(1 - \frac{1}{2^N}\right) < I_{in} < a; \\ a, & \text{for } I_{in} > a; \end{cases} \quad (7.6)$$

Thus, given a sufficiently large number of units, the proposed non-absorbing, non-saturating, Kerr-nonlinear device will behave as an arbitrarily abrupt all-optical hard limiter. All of the intensities smaller than a will be reflected and all greater or equal to a will be transmitted. The transmitted intensities will clamp at the value of a . Since a

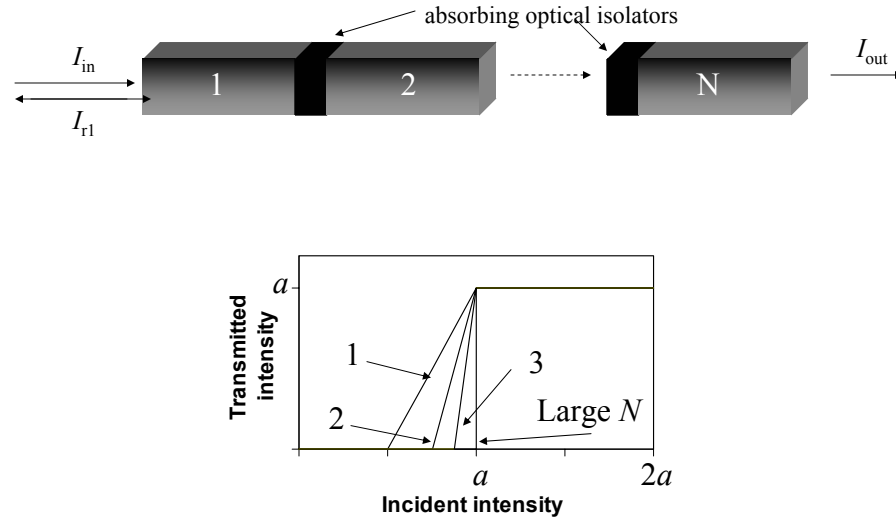


Figure 7.5: All-optical hard limiter. Arranging the proposed structures in series results in an increasingly steep transition in the transfer characteristics. The inset shows how the response of hard-limiter is modified with an increasing number of units.

is determined by linear and nonlinear indices, the choice of material biases the device at the desired value.

7.4 Analog-to-digital converter

Figure 7.6 illustrates a four-bit analog-to-digital converter (A-to-D) utilized using the out-of-phase structures proposed above. This approach is scalable to higher resolutions. The n th additional bit requires $n - 1$ limiters. The total number of limiters for an N -level A-to-D converter is $\frac{N(N-1)}{2}$. The separation of the incident and reflected signals can be performed with nonreciprocal directional couplers or circulators [133, 134].

The analog-to-digital converter illustrated in Figure 7.6 is constructed using limiters

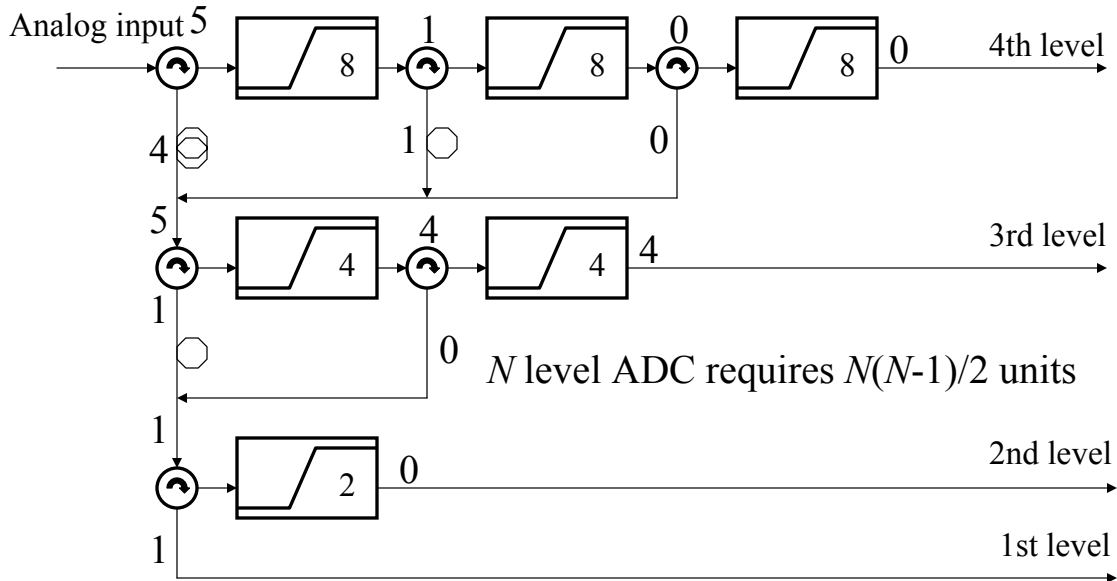


Figure 7.6: All-optical analog-to-digital converter. In the example considered, an analog input of 5 is transformed to a digital word (0101).

biased at values $a=8$, 4, and 2. As an example, the A-to-D conversion of an analog input 5 is illustrated. 5 is fully reflected by the first set of limiters (4th level) giving a transmitted output of 0. In the third level 4 is transmitted and 1 reflected. The output 4 is normalized to yield the second digital output, 1. The reflected 1 is fed into the 2nd level and is completely reflected. The 0 at the output of the 2nd level provides the third digit. The signal 1 reflected from the 2nd level yields the lowest-order digit. Placing delay lines behind second, third and fourth levels ensures that the four digital signals arrive simultaneously at the corresponding receivers. An analog input of 5 is converted to a (0101) digital word in a single byte interval. This approach provides a basis for

all-optical, ultrafast decoding of multilevel intensity signals [135].

7.5 Logic Gates

Figure 7.7 illustrates the use of out-of-phase structures proposed in the construction of OR and AND gates. Separate signals A and B are first combined into a single input. The transmitted intensity is defined as the $O1$ output and the reflected value as the $O2$. The hard limiter is assumed to have $a = 1$. If one of the inputs is 0 and the other 1 , the output at $O1$ is 1 and at $O2$ is 0 . If both A and B inputs have the value of 1 , 1 is transmitted and 1 reflected. Thus, $O1$ yields the result of an OR operation and $O2$ the result of logic AND.

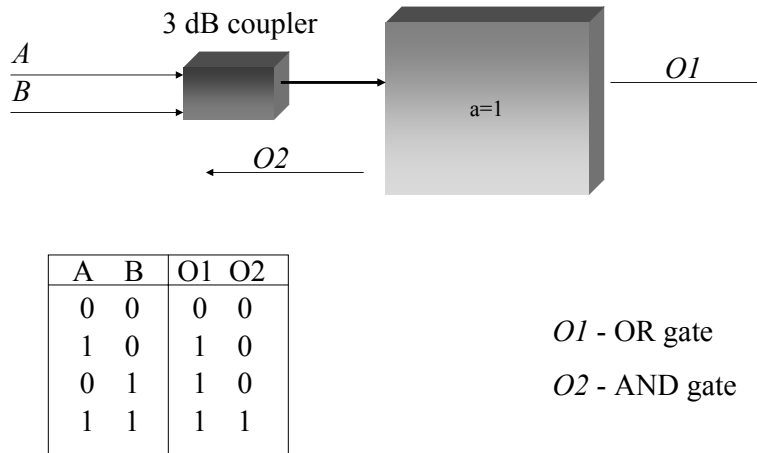


Figure 7.7: OR and AND gates. For two input beams A and B , the transmitted intensity of the hard limiter biased at $a = 1$ implements the OR function while the reflected beam implements the AND operation.

Figures 7.8 and 7.9 show the ideal transmitted and reflected powers of a hard-limiter

biased at $a = 2$. As discussed above, the curve from Figure 7.8 enables the OR operation while the Figure 7.9 curve represents the AND operation. Additionally if the device is externally biased by a pump beam at input power $P_{in} = 1$ then the response curve of Figure 7.9 is shifted towards the left by 1. In such externally-biased configuration the device acts as an inverter over the region $0 < P_{in} < 1$. Since the proposed devices enable the inversion and AND logic operations, a complete set of logic gates can be constructed.

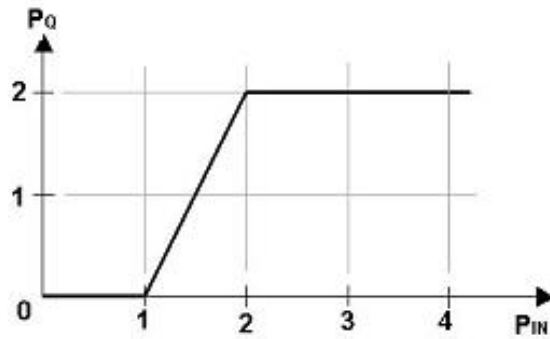


Figure 7.8: Ideal transmission characteristics of the out-of-phase nonlinear balanced structure with material parameter $a = 2$. The transfer curve enables OR logic operation.

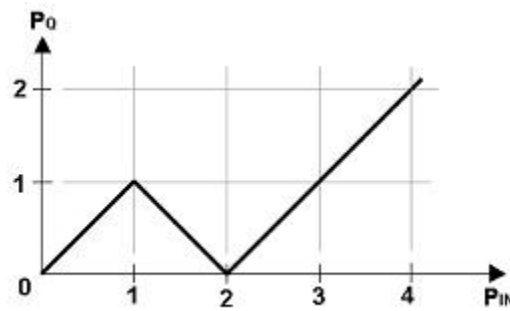


Figure 7.9: Ideal reflection characteristics of the out-of-phase nonlinear balanced structure with material parameter $a = 2$. This transfer curve enables logic AND and inversion logic operations.

7.6 Sensitivity of Transfer Curves to Fabrication Errors and Absorption

This section analyzes the sensitivity of optical elements presented to realistic imperfections incurred during fabrication. The response of structures with built-in random fluctuations in the layer thicknesses is simulated. Keeping all other parameters fixed, the thicknesses of layers are allowed to be distributed uniformly over a predefined range.

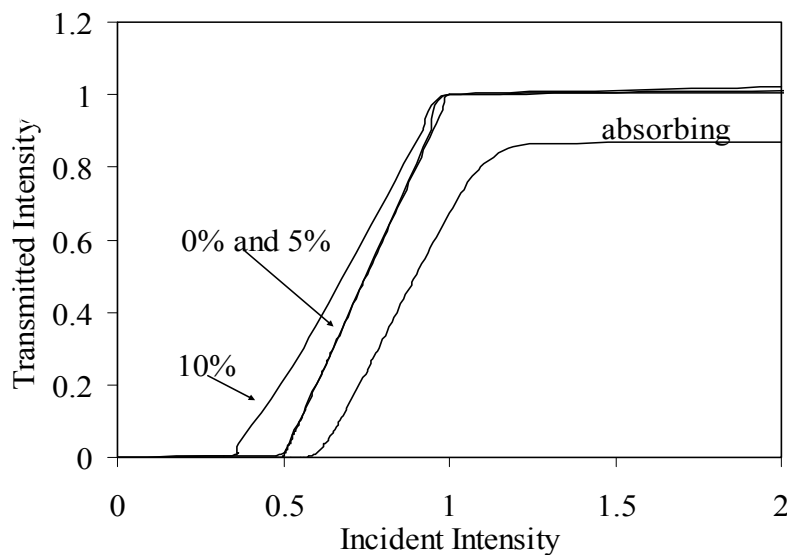


Figure 7.10: Transmitted intensity as a function of incident intensity for the structure with the same parameters as in Figure 7.3. The thicknesses of layers were allowed to vary 0, 5, and 10% from their quarter-wave value. The effect of the linear absorption on the transmittance is also shown.

Figure 7.10 shows the transmitted intensity as a function of incident intensity for the structure with the same average parameters as in Figure 7.7. Layer thicknesses were allowed to vary 5% and 10% from their quarter-wave value. For 5% deviation there is no detectable difference in the responses of the imperfect device and the ideal device. Even in

devices with 10% layer thickness fluctuations the transmitted intensity saturates to some limiting value. The quantitative performance of the device is affected by fabrication errors and realistic absorption of $\alpha = 6 \text{ cm}^{-1}$, but qualitative features of the S-shape transfer characteristics are preserved.

7.7 Conclusions

This chapter showed that the introduction of an out-of-phase linear grating to the limiting structures from chapters 5 and 6 increases their ability to process optical signals by permitting S-shaped transfer characteristics. The performance of all-optical hard limiters was explored through analytical expressions and numerical simulations. The hard limiters proposed could be used in optical A-to-D conversion, or to create a complete set of logic gates. This devices should operate will even with substantial fabrication errors.

The optical elements proposed in chapters 5–7 represent a novel class of all-optical stable signal processing devices. As shown in previous research on the theory of non-linear optical signal processing, building-block functional elements may be combined to implement more complex operations.

Chapter 8

Theory of Intensity-Domain Optical Stability of Transfer Functions of Nonlinear Periodic Structures

Chapters 5, 6, and 7 presented the broad optical signal processing functionality of nonlinear periodic structures that are stable in the intensity domain. This chapter will explore in detail the structural and material conditions for optical intensity-domain stability.

A significant portion of the analytical results presented in this chapter has been derived in collaboration with Professor Dmitry Pelinovsky from McMaster University. The author of this work has posed the problems, defined the structures, and carried out the numerical simulations. Professor Pelinovsky derived the analytical expressions.

The work presented in this chapter was published in [136–138].

8.1 Incoherent Light

The nonlinear periodic structures analyzed in this section are assumed to be made out of material with the same linear coefficients, $n_{01} = n_{02} = n_0$, and the same layer thicknesses, $d_1 = d_2$. No general constraints are placed on the sign and magnitude of Kerr coefficients.

8.1.1 Transmittance expressions

Equations (4.23) and (4.24) are re-written in the following form:

$$i \frac{dA_+}{dz} = k \Delta \bar{n}_{nl} (\kappa A_- e^{-3ik\Lambda/2} - A_+) (|A_+|^2 + |A_-|^2), \quad (8.1)$$

$$i \frac{dA_-}{dz} = k \Delta \bar{n}_{nl} (-\kappa A_+ e^{3ik\Lambda/2} + A_-) (|A_+|^2 + |A_-|^2), \quad (8.2)$$

where $\Delta \bar{n}_{nl} = (n_{nl1} + n_{nl2})/(2n_0)$ is the average normalized nonlinear index and κ is a product of variance of the nonlinear index and the resonance factor:

$$\kappa = \left| \frac{n_{nl1} - n_{nl2}}{n_{nl1} + n_{nl2}} \right| \frac{\sin(k\Lambda/2)}{k\Lambda/2}. \quad (8.3)$$

The nonlinear coupling between forward- and backward-propagating waves is described by the κ terms in Eqs. (8.1) and (8.2). These terms provide stable limiting behaviour for $n_{nl1} = -n_{nl2}$. The other right-hand-side terms in Eqs. (8.1) and (8.2) are associated with the oscillatory multistable behaviour. The transition to multistability takes place when the self-coupling oscillatory terms overwhelm the mutually-coupling κ terms. It will be shown that the threshold condition between these two regimes is given by $\kappa = 1$, i.e. the stable limiting behaviour occurs for:

$$\left| \frac{n_{nl1} - n_{nl2}}{n_{nl1} + n_{nl2}} \right| \frac{\sin(k\Lambda/2)}{k\Lambda/2} \geq 1. \quad (8.4)$$

Under the assumption of nonabsorbing structures, the coupled system (8.1) and (8.2) exhibits conservation of energy flow through the periodic structure:

$$|A_+(z)|^2 - |A_-(z)|^2 = I_{out}, \quad (8.5)$$

Figure 8.1 shows the transmitted versus incident intensity for structures of two different lengths illuminated with light at a Bragg resonance $k\Lambda = \pi$. The nonlinear indices are specified as $n_{nl1} = 0.01$ and $n_{nl2} = 0$ for two solid curves, where $\kappa = 2/\pi$. This is the multistability regime in which the transmitted intensity oscillates between the values determined by minimum and maximum transmittance. The transmittance is defined by:

$$T = 1 - \left| \frac{A_-(0)}{A_+(0)} \right|^2. \quad (8.6)$$

The maximum transmittance appears when $A_-(0) = 0$, so that $T_{max} = 1$. The minimum transmittance is defined by the condition $dA_-(0)/dz = 0$, which translates to $A_-(0) = \kappa A_+(0)e^{3ik\Lambda/2}$ so that $T_{min} = 1 - \kappa^2$.

When $\kappa = 0$, e.g. at $n_{nl1} = n_{nl2}$, the optical structure is homogeneous for all intensities and $I_{out} = I_{in}$. The area between oscillations in the input-output transmission characteristics widens with the increasing values of κ . It is shown in Figure 8.1 that the period of the multistable oscillations (measured in terms of I_{in}) becomes smaller for longer structures (when N grows). As a result, more possible transmission levels are present within a given range of incident intensities.

When κ reaches 1, T_{min} vanishes. This marks the onset of stable optical limiting. In the region $\kappa \geq 1$, the coupling of the two contrapropagating waves dominates over the phase-related oscillations and no multistability takes place. The stable limiting behaviour is shown by a dashed curve in Figure 8.1 for the structure with parameters: $n_{nl1} = 0.015$, $n_{nl2} = -0.005$, when $\kappa = 4/\pi$.

In order to find the limiting value for the transmitted intensity and to characterize the features of the multistability regime, exact solutions to Eqs. (8.1) and (8.2) are obtained. First, the distance z is scaled by $Z = k\Delta\bar{n}_{nl}z$ and the amplitudes $A_{\pm}(z)$ are substituted in the polar form:

$$A_+(Z) = \sqrt{I_{out} + Q}e^{i(\Phi+\Psi)} \quad (8.7)$$

$$A_-(Z) = \sqrt{Q}e^{i(\Phi+3k\Lambda/2)}. \quad (8.8)$$

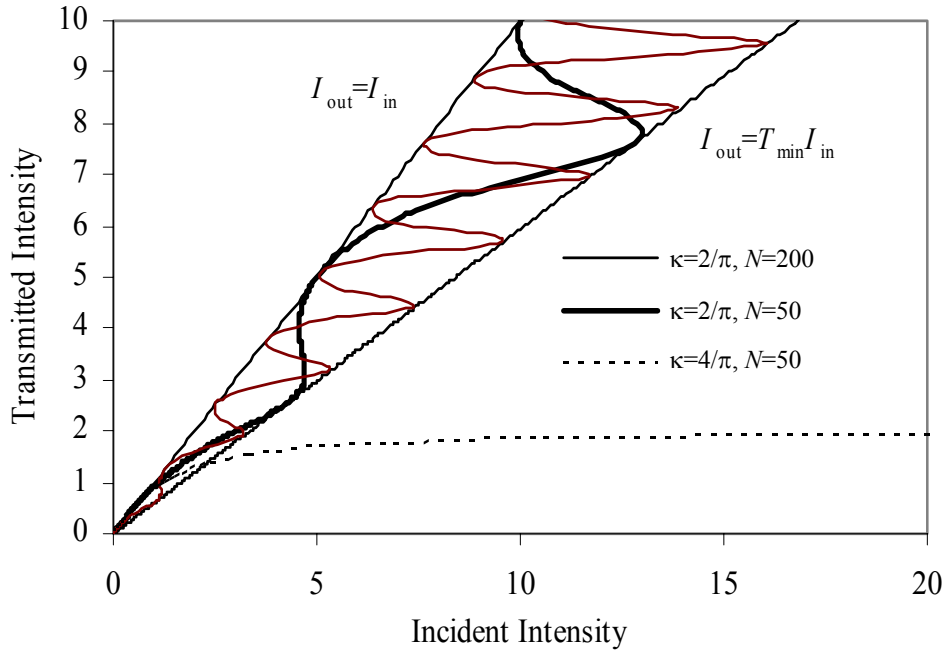


Figure 8.1: The multistable and stable regimes of nonlinear periodic structures illuminated with light at the frequency of Bragg resonance.

Here $Q(Z)$ and $\Phi(Z)$ are the intensity and phase of reflected wave, and $\Psi(Z)$ is the phase mismatch between the incident and reflected waves. The coupled system (8.1) and (8.2) reduces to the following form:

$$\frac{dQ}{dZ} = -2 (I_{out} + 2Q) \sqrt{Q(I_{out} + Q)} \kappa \sin \Psi \quad (8.9)$$

$$\frac{d\Psi}{dZ} = (I_{out} + 2Q) \left[2 - \frac{I_{out} + 2Q}{\sqrt{Q(I_{out} + Q)}} \kappa \cos \Psi \right]. \quad (8.10)$$

The boundary conditions are $Q(L) = 0$ and $\Psi(L) = \pi/2$, where $L = k\Delta\bar{n}_nl$. The latter condition is motivated by a negative slope of $Q(Z)$ near $Z = L$. Subject to this boundary condition, the integral of Eqs. (8.9) and (8.10) is found to be:

$$\kappa |\cos \Psi| = \sqrt{\frac{Q}{I_{out} + Q}}. \quad (8.11)$$

Using relation (8.11) the system (8.9) and (8.10) can be reduced to the single equation:

$$\frac{d\Psi}{dZ} = I_{out} [1 + \kappa^2 \cos^2 \Psi], \quad (8.12)$$

which can be integrated further. The exact solution for $Q(Z)$ follows from (8.11) and (8.12) in the form:

$$Q(Z) = \frac{\kappa^2 I_{out} \sin^2 [\sqrt{1 + \kappa^2 I_{out}}(L - Z)]}{1 + \kappa^2 \cos [2\sqrt{1 + \kappa^2 I_{out}}(L - Z)]}. \quad (8.13)$$

Expression (8.13) describes via (8.7) and (8.8) the evolution of the envelopes of the forward and backward propagating fields in both stable and multistable regimes. The two transmission regimes are separated by the condition $\kappa = 1$.

8.1.2 Multistable Regime

In the multistable regime, $\kappa < 1$, the transmittance T can be found from Eq. (8.6) and (8.13) as:

$$T = \frac{1 + \kappa^2 \cos [2\sqrt{1 + \kappa^2 I_{out}}L]}{1 + \kappa^2 \cos^2 [\sqrt{1 + \kappa^2 I_{out}}L]}. \quad (8.14)$$

The points of maximum transmittance ($T_{max} = 1$, $Q(0) = 0$) are given by the roots

$$I_{out} = I_n = \frac{\pi n}{\sqrt{1 + \kappa^2}L}, \quad n = 0, 1, 2, \dots \quad (8.15)$$

The distribution for the reflected wave $Q(z)$ has exactly n nodes across the optical structure within the parameter range $I_n \leq I_{out} < I_{n+1}$. The points of minimum transmittance ($T_{min} = 1 - \kappa^2$, $dQ(0)/dZ = 0$) are located exactly in the middle of each interval (I_n, I_{n+1}).

8.1.3 Stable Regime

In the stable regime, $\kappa \geq 1$, the distribution of the reflected wave $Q(Z)$ can be found for $I_{out} \leq I_{lim}$, where

$$I_{lim} = \frac{\pi}{4\sqrt{1 + \kappa^2}L} \left[1 + \frac{2}{\pi} \arcsin \left(\frac{1}{\kappa^2} \right) \right]. \quad (8.16)$$

is obtained by setting the denominator of Eq. (8.11) to zero.

At the limiting value, $I_{out} = I_{lim}$, the distribution $Q(Z)$ diverges as $Z \rightarrow 0$ so that $I_{in} \rightarrow \infty$. True optical limiting is therefore achieved: the transmitted intensity is bounded by its limiting value irrespective of the incident power (see the dashed curve at Figure 8.1).

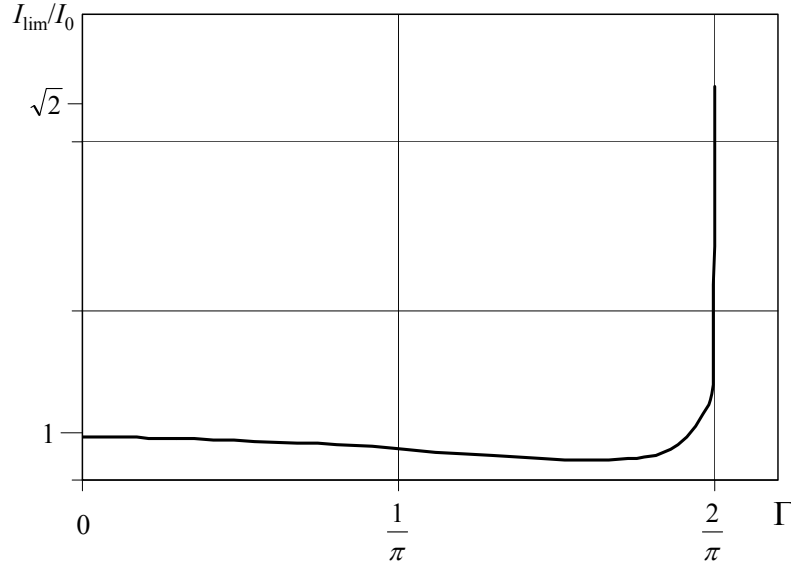


Figure 8.2: The normalized limiting value of the output power I_{lim}/I_0 as a function of the inverse variance of the nonlinear index Γ at $k\Lambda = \pi$.

When $\bar{n}_{nl} \rightarrow 0$, (i.e. when the Kerr coefficients are of equal magnitude and opposite signs), the limiting intensity approaches the asymptotic value:

$$\lim_{\bar{n}_{nl} \rightarrow 0} I_{lim} = \lim_{\bar{\kappa} \rightarrow \infty} I_{lim} = \frac{\pi n_0}{2N|n_{nl1} - n_{nl2}| \sin(k\Lambda/2)}. \quad (8.17)$$

Figure 8.2 shows the normalized limiting intensity (I_{lim}/I_0) as a function of Γ at the exact resonance $k\Lambda = \pi$, where Γ is the inverse variance of the nonlinear index given by

$$\Gamma = \left| \frac{n_{nl1} + n_{nl2}}{n_{nl1} - n_{nl2}} \right|. \quad (8.18)$$

When the inverse variance Γ is small, the normalized limiting intensity is close to but smaller than 1. When Γ approaches the threshold boundary (8.4), which happens when $\Gamma = 2/\pi$ for the exact resonance, the normalized intensity approaches $\sqrt{2}$. Thus, the

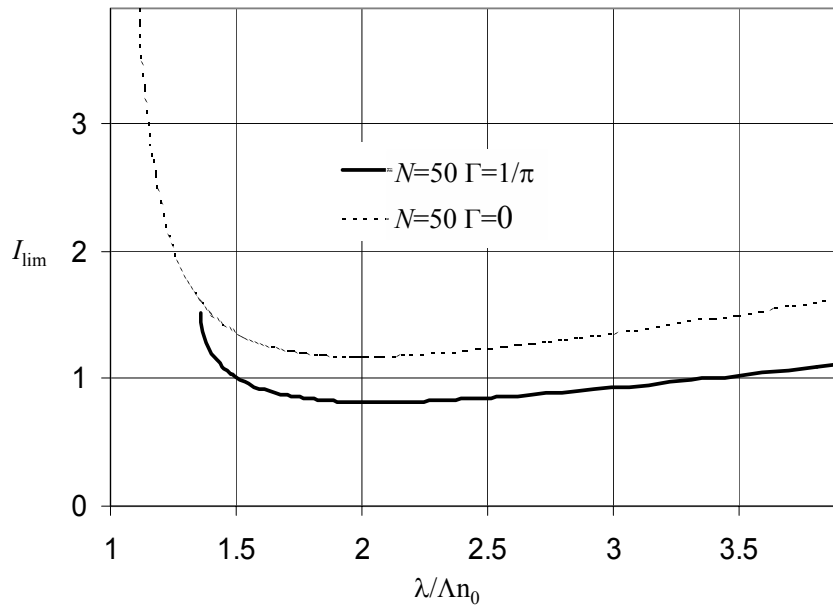


Figure 8.3: The limiting transmitted power I_{lim} as a function of the spectral position of the illumination to spatial period ratio $\lambda/(\Lambda n_0)$.

limiting intensity remains within 40% of its asymptotic value I_0 for any value of the material parameters within the stable regime.

The stable regime is facilitated by close proximity of the spectral position of the incident illumination to the Bragg resonance. When the spectral position of light deviates from the exact Bragg resonance $\lambda_0 = 2\Lambda n_0$, the stable regime breaks down. This feature is illustrated in Figure 8.3 by plotting the limiting transmitted intensity I_{lim} (8.16) versus the wavelength ratio $\lambda/(\Lambda n_0)$ for two values of Γ : $\Gamma = 0$ (a dashed curve) and $\Gamma = 1/\pi$ (a solid curve). The stable behaviour of the nonlinear periodic structure is affected weakly by deviation of the spectral position of the illumination to longer-than-resonance region. Wavelengths shorter than resonance wavelengths quickly undergo transitions to the multistable regime.

8.2 Coherent Light

The assumption of the incoherent illumination makes the analysis presented in chapters 5 to 7 easier. However, in order provide the complete theory of the intensity-domain stability, the case of coherent illumination will be now discussed.

Equations (4.20) and (4.21) describe the response of structures analyzed under coherent illumination. Only the steady-state response ($\partial A_{\pm}/\partial T = 0$) on resonance ($k = 2k_0$) is considered. The governing equations become:

$$\begin{aligned} i\frac{\partial A_+}{\partial Z} + n_{0k}A_- + n_{nl}(|A_+|^2 + 2|A_-|^2)A_+ \\ + n_{2k}[(2|A_+|^2 + |A_-|^2)A_- + A_+^2\bar{A}_-] = 0, \end{aligned} \quad (8.19)$$

$$\begin{aligned} -i\frac{\partial A_-}{\partial Z} + n_{0k}A_+ + n_{nl}(2|A_+|^2 + |A_-|^2)A_- \\ + n_{2k}[(|A_+|^2 + 2|A_-|^2)A_+ + A_-^2\bar{A}_+] = 0, \end{aligned} \quad (8.20)$$

Conservation of energy (8.5) has the same form as in the case of incoherent radiation. Similarly, the boundary conditions are:

$$|A_+(0)|^2 = I_{in}, \quad |A_-(0)|^2 = I_{ref}, \quad |A_+(L)|^2 = I_{out}, \quad |A_-(L)|^2 = 0. \quad (8.21)$$

The system (8.19) and (8.20) is integrable. Eq. (8.5) is used to parameterize the solutions in the polar form:

$$A_+(Z) = \sqrt{I_{out} + Q} e^{i(\Phi - \Psi)}, \quad A_-(Z) = \sqrt{Q} e^{i\Phi} \quad (8.22)$$

The system (8.19) and (8.20) can be reduced in the form (8.22) to the coupled system for $Q(Z)$ and $\Psi(Z)$,

$$\frac{dQ}{dZ} = -2\sqrt{Q(I_{out} + Q)} \sin \Psi [n_{0k} + n_{2k}(I_{out} + 2Q)], \quad (8.23)$$

$$\frac{d\Psi}{dZ} = -3n_{nl}(I_{out} + 2Q) - \frac{\cos \Psi}{\sqrt{Q(I_{out} + Q)}} [n_{0k}(I_{out} + 2Q) + n_{2k}(I_{out}^2 + 8I_{out}Q + 8Q^2)]. \quad (8.24)$$

The boundary conditions (8.21) are satisfied when $Q(Z)$ and $\Psi(Z)$ are connected by the relation,

$$\cos \Psi = \frac{-3n_{nl}\sqrt{Q(I_{out} + Q)}}{2[n_{0k} + n_{2k}(I_{out} + 2Q)]}. \quad (8.25)$$

The coupled system (8.23) and (8.24) can be reduced with the help of Eq. (8.25) to a single equation either for $Q(Z)$ or for $\Psi(Z)$. The outcome of this reduction depends on the parameters n_{nl} , n_{0k} , n_{2k} , and I_{out} of the model. Two different cases will be considered: (i) $n_{nl} = 0$ and (ii) $n_{nl} \neq 0$.

8.2.1 Balanced Nonlinearity Management: $n_{nl} = 0$

When the periodic structure consists of alternating layers with zero net-average Kerr nonlinearity, the Eqs. (8.23) and (8.24) can be solved analytically. In this regime the true all-optical limiting is predicted to be the strongest.

First, the case in which $|n_{0k}| \leq n_{2k}I_{out}$ (i.e. the built-in grating is assumed to be weak compared to the induced nonlinear index change) is considered. Direct integration of Eq. (8.23) for $\Psi(Z) = \pi/2$ produces the explicit solution:

$$Q(Z) = \frac{I_{out}(n_{0k} + n_{2k}I_{out})\sin^2 \theta}{n_{2k}I_{out} \cos 2\theta - n_{0k}}, \quad (8.26)$$

where $\theta = \sqrt{n_{2k}^2 I_{out}^2 - n_{0k}^2}(L - Z)$. It is clear that the solution $Q(Z)$ is monotonically decreasing between $Z = 0$ and $Z = L$ and is defined for $I_{out} \leq I_{lim}$, where I_{lim} is the solution of:

$$-1 \leq \cos \left[2\sqrt{n_{2k}^2 I_{lim}^2 - n_{0k}^2} L \right] = \frac{n_{0k}}{n_{2k}I_{lim}} \leq 1. \quad (8.27)$$

It is obtained when the denominator of Eq. (8.26) vanishes.

I_{lim} is the limiting intensity for the case of the nonlinear periodic structure illuminated with the coherent light. Typical transmission curves for $n_{2k} = 1$ and three different values of n_{0k} are displayed in Figure 8.4. The transmitted intensity I_{out} is a one-to-one function of the incident intensity I_{in} and is bounded by its limiting value I_{lim} (shown in Figure 8.4 using horizontal lines). Equation (8.27) permits to consider the limit in which the linear

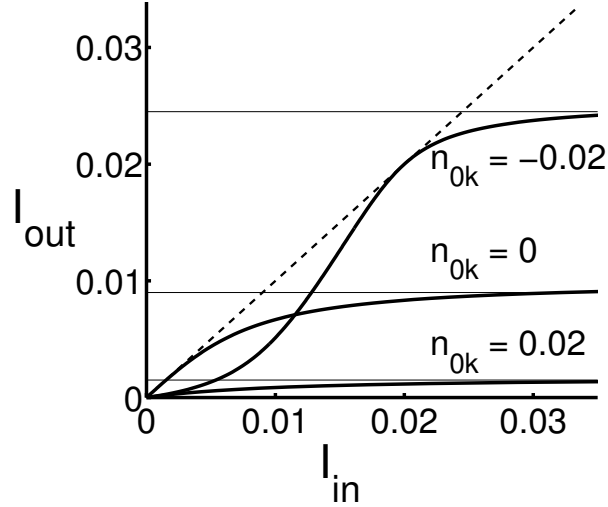


Figure 8.4: Balanced nonlinearity management with a linear built-in grating, where $n_{nl} = 0$, $n_{2k} = 1$. Horizontal lines show the limiting intensity I_{lim} , while the dotted line displays the regime of complete transparency: $I_{out} = I_{in}$. An out-of-phase ($n_{0k} = -0.02$) grating increases I_{lim} while an in-phase grating ($n_{0k} = 0.02$) decreases it.

grating is weak compared to the nonlinearity management i.e. $|n_{0k}| \ll n_{2k}I_{lim}$. In this case, the limiting intensity can be approximated as:

$$I_{lim} = \frac{\pi}{4n_{2k}L} \left[1 - \frac{8n_{0k}L}{\pi^2} \right]. \quad (8.28)$$

It follows from Eq. (8.28) that the limiting value becomes smaller for in-phase gratings when $n_{0k} > 0$ and grows for out-of-phase gratings when $n_{0k} < 0$. No matter how large the mismatch between linear and nonlinear refractive indices is, true all-optical limiting is still achieved for out-of-phase gratings with sufficiently large input intensities. This property is expressed by the estimate on the limiting intensity,

$$I_{lim} \geq \frac{|n_{0k}|}{n_{2k}} \quad \text{for } n_{0k} < 0 \text{ and } n_{nl} = 0 \quad (8.29)$$

The in-phase gratings always support true all-optical limiting with no constraints on the value for the limiting intensity I_{lim} .

The case when $|n_{0k}| > n_{2k}I_{out}$ (i.e. the case when built-in grating is stronger than

the induced grating) is considered next. The solution (8.26) then becomes:

$$Q(Z) = \frac{I_{out}(n_{0k} + n_{2k}I_{out}) \sinh^2 \phi}{n_{0k} - n_{2k}I_{out} \cosh 2\phi}, \quad (8.30)$$

where $\phi = -i\theta = \sqrt{n_{0k}^2 - n_{2k}^2 I_{out}^2} (L - Z)$. The behaviour of the wave profile $Q(Z)$ across the structure is now different depending on the sign of n_{0k} . To obtain the the expression for the limiting intensity, the denominator of Eq. (8.30) is set to 0.

In the case when $n_{0k} > 0$ (in-phase gratings), the following solution is obtained:

$$\cosh \left[2\sqrt{n_{0k}^2 - n_{2k}^2 I_{lim}^2} L \right] = \frac{n_{0k}}{n_{2k} I_{lim}} > 1. \quad (8.31)$$

In contrast, in the case $n_{0k} < 0$ (out-of-phase gratings), the limiting intensity cannot be reached as the constraint $|n_{0k}| > n_{2k} I_{out}$ restricts values of the incident intensity within the range that is insufficient to close the built-in linear grating. However, the constraint of balanced nonlinearity, $n_{nl} = 0$ still ensures that the response of such structures is stable.

8.2.2 Unbalanced Nonlinearity Management: $n_{nl} \neq 0$

When $n_{nl} \neq 0$, the connecting relation (8.25) can still be used to give the exact condition when the limiting behaviour is possible, i.e. when $Q(0) \rightarrow \infty$ for $I_{out} \rightarrow I_{lim}$. Since $|\cos \Psi| \leq 1$, the limiting regime exists when

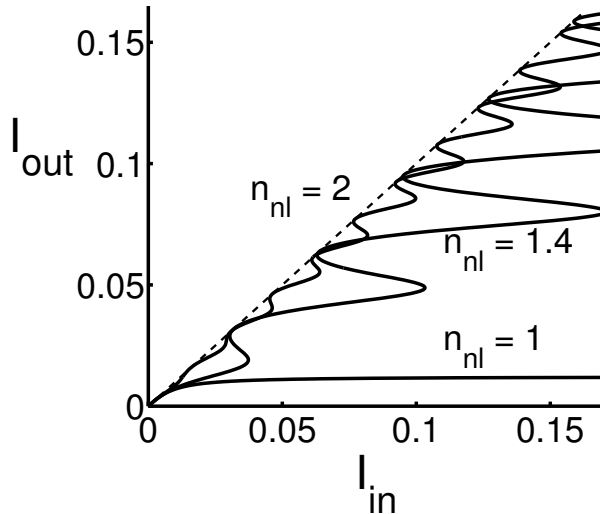


Figure 8.5: Transfer characteristics of nonlinear periodic structures with unbalanced nonlinearity. The threshold between limiting regime and multistability is $n_{nl} = 4/3$.

$$n_{2k} \geq \frac{3|n_{nl}|}{4}. \quad (8.32)$$

In the opposite case, i.e. when $n_{2k} < 3|n_{nl}|/4$, no limiting regime is possible and the system is bistable or multistable. Figure 8.5 shows the dependence $I_{out}(I_{in})$ for $n_{0k} = 0$, $n_{2k} = 1$ and three values of n_{nl} . The value $n_{nl} = 1$ falls within the domain (8.32) and therefore the structure displays the limiting regime. On the other hand, the values $n_{nl} = 1.4$ and $n_{nl} = 2$ are outside of the domain (8.32) and the structure displays multistability which shrinks for strongly unbalanced gratings, i.e. when n_{nl} grows.

8.3 Conclusions

Optical bistability has been previously predicted and demonstrated by other researchers. However, prior to this work, no research has been published that would provide an in-depth analysis of the conditions necessary for optical stability of nonlinear periodic structures capable of supporting optical signal processing functions. In this chapter such conditions were derived. They predict a threshold condition for optical stability in terms of the material parameters and wavelength. This condition defines the regime in which the rate of the shift of the central position of the nonlinear stopband exceeds the rate of the growth of depth of the stopband at a given spectral position which leads to bistability. It was proven that, in the stable regime, nonlinear periodic structures exhibit saturation in the transmitted intensity at the limiting value. It was found that all-optical limiting is best achieved in nonlinear periodic structures when the Kerr nonlinearity is compensated exactly across the alternating layers, i.e. when the net-average nonlinearity is zero and the spectral position of the stopband remains fixed with the increasing level of illumination.

Chapter 9

Theory of Pulse Shaping and Compression in Balanced Nonlinear Periodic Structures

Chapters 5 to 8 dealt comprehensively with the steady-state response of nonabsorbing balanced nonlinear periodic structures. Since realistic optical signal processing would involve mostly pulsed illumination, this chapter will examine the time-dependent response of these structures. Time-domain analyses of non-solitonic pulse propagation through balanced nonlinear periodic structures with and without built-in linear grating will be presented.

Numerical simulations that produced results presented in this chapter were carried out in collaboration with Winnie Ye. The work presented in this chapter was published in Refs. [139–141].

9.1 Case I: $n_{0k}=0$

The structures considered in this section are the same as in chapter 5. They have matched linear indices $n_{ln1} = n_{ln2} = n_{ln}$ and opposite Kerr coefficients $n_{nl1} = -n_{nl2} = n_2$ in the adjacent layers. The coupled-mode system (4.20)–(4.21) was used to simulate the response of such nonlinear periodic structures. Throughout the simulations, the center frequency of the incident pulses was fixed at the Bragg resonance $\omega_0 = \frac{cn_{ln}}{2\Lambda}$. The average index of refraction was taken to be $n_{ln}=1.5$.

The incident pulses were assumed to take the Gaussian form of:

$$I_{in}(T) = I_{peak} e^{-\frac{(T-\mu)^2}{\ln 2\sigma^2}}, \quad (9.1)$$

where I_{peak} is the peak intensity of the pulse, μ is the time-delay of the pulse, and 2σ is the pulse duration as the full width at half maximum (FWHM).

Figure 9.1 depicts the pulse energy transmittance as a function of pulse temporal width for fixed incident intensity of $I_{peak} = 0.01|n_2|$. The graph shows that the limiting behaviour of the device depends on the pulse bandwidth.

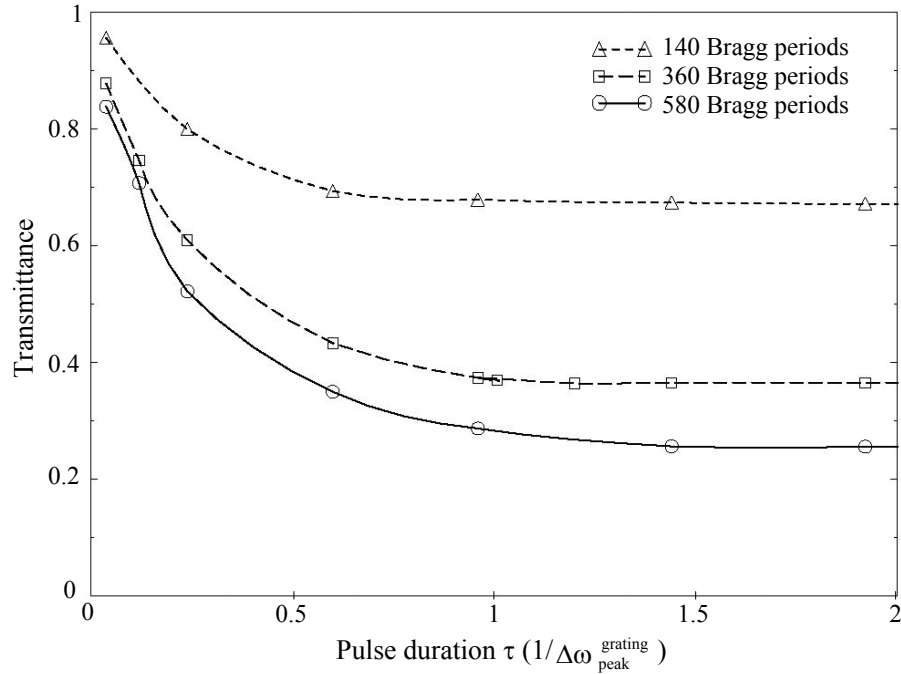
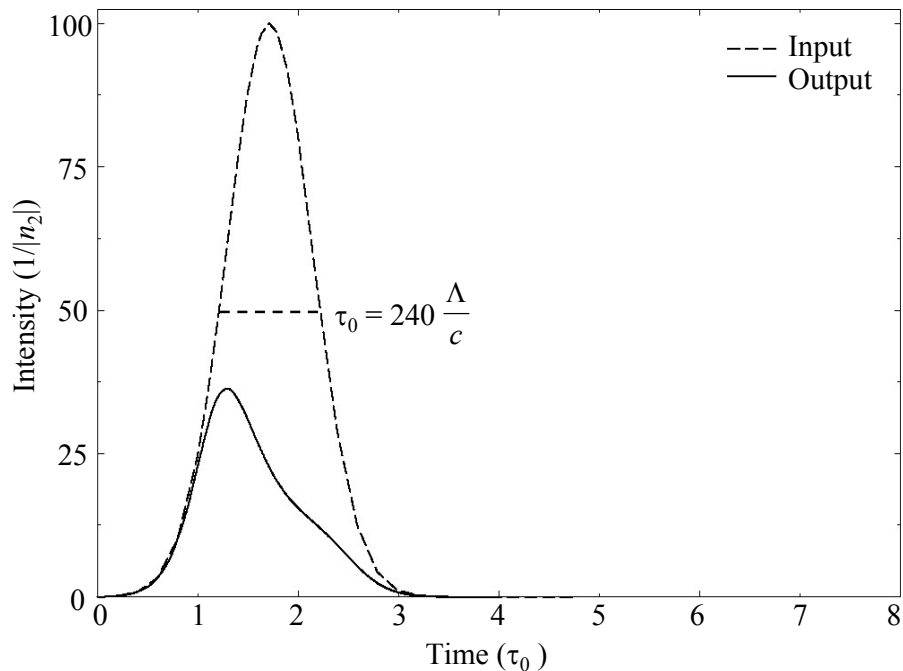


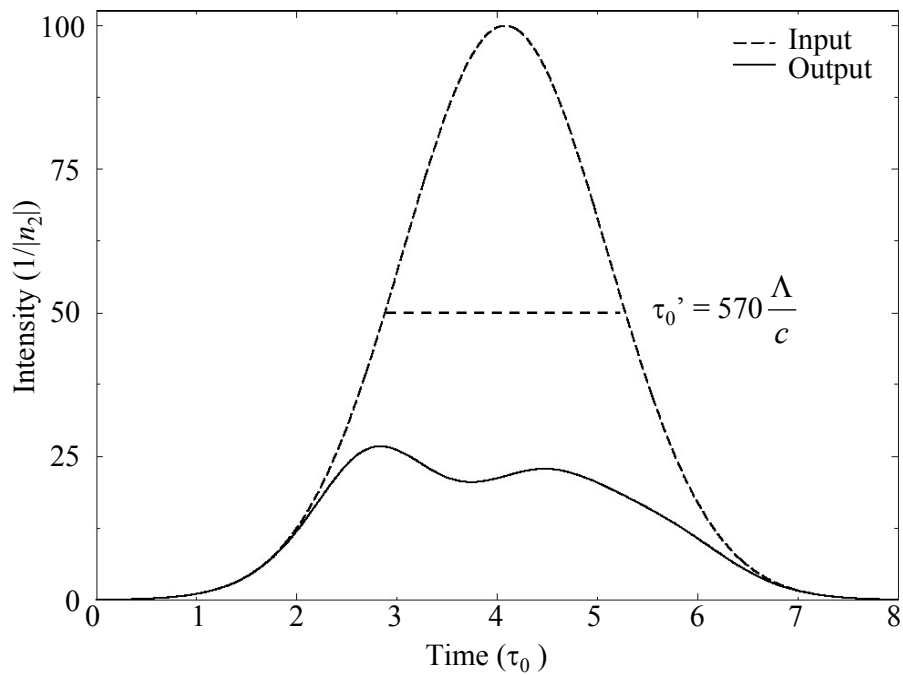
Figure 9.1: Pulse energy transmittance as a function of the pulse width for a fixed peak pulse intensity of $I_{peak} = 0.01|n_2|$.

The long-duration pulses in Figure 9.1 exhibit the desired limiting behaviour because their relatively narrow spectral bandwidth lies entirely within the induced stopband of the nonlinear grating. This leads to bandwidth-independent transmittance. Short-duration pulses, on the other hand, have a spectral bandwidth which exceeds the width of the dynamic stopband, resulting in transmission of the spectral portion of the power which lies outside of the stopband of the device. The transition region between regimes of relative wide and narrow pulse bandwidths is indicated by the knee in the characteristics of Figure 9.1. This occurs when the pulse bandwidth $\Delta\omega_{pulse}$ and the bandwidth of nonlinear grating at the peak pulse intensity $\Delta\omega_{peak}^{grating}$ become comparable:

$$\Delta\omega_{peak}^{grating} = \frac{8|n_{nl}|I_{peak}}{\pi n_{ln}}\omega_0 \approx \Delta\omega_{pulse}. \quad (9.2)$$



(a)



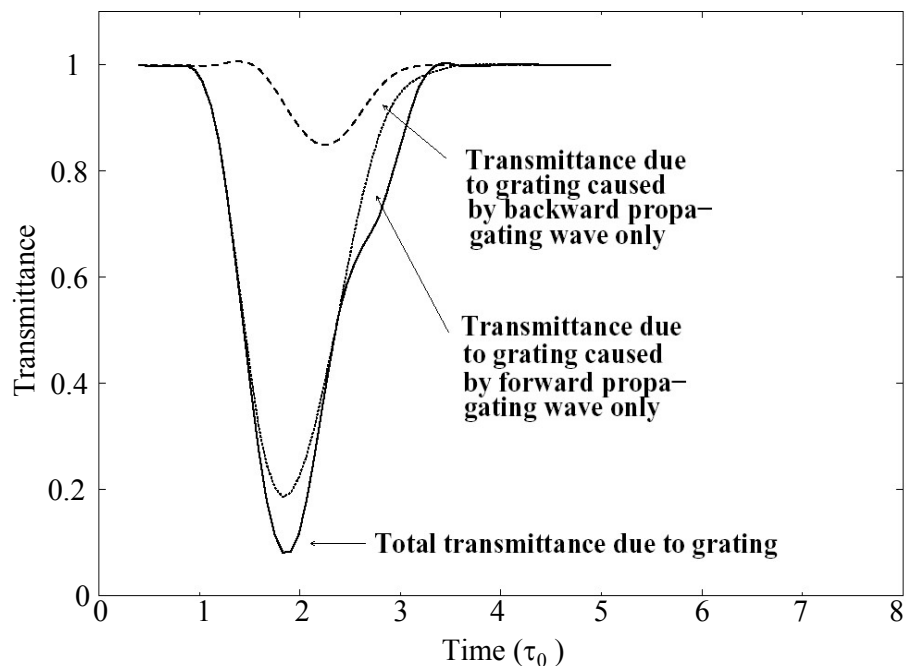
(b)

Figure 9.2: Temporal intensity profiles of input and output pulses after transmission through a 360-period long device for input pulse widths of: (a) $240 \frac{\Lambda}{c}$ and (b) $570 \frac{\Lambda}{c}$.

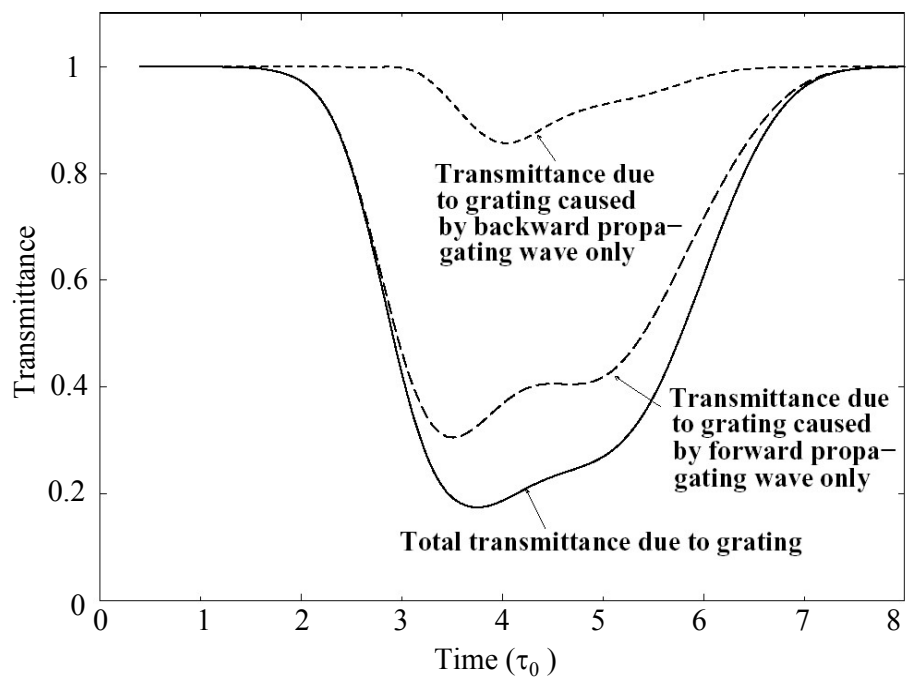
The decay of the pulse amplitude gives an example of the non-solitonic character of propagation. The shape of Gaussian pulses is strongly distorted during propagation. For a fixed pulse peak intensity, the degree of distortion depends on the length of the structure and the length of the pulse. Figures 9.2(a) and 9.2(b) show the transmitted pulse shapes through a 360-period long device for two different temporal widths.

Since the bandwidths of both pulses are narrower than the effective bandwidth of the device, it is justified to study the intensity self-patterning of the pulses while neglecting potential effects of incomplete reflectance across the spectrum. To explain the distortion in transmitted pulses, the time-dependent transmittance of the induced nonlinear grating is calculated and illustrated in Figure 9.3(a) and 9.3(b).

For the shorter pulse length of $240 \frac{\Lambda}{c}$ in Figure 9.3(a), the forward- and backward-propagating waves form their strongest instantaneous gratings at different times. The backward-propagating wave gives rise to an additional delayed echo of the transmitted pulse in the time-dependent transmittance, causing a dip in the transmitted pulse of Figure 9.2(a). When the incident pulse is longer than the device, as in Figure 9.2(b), the strongest instantaneous gratings are formed roughly at the same time period for forward- and backward-propagating waves (Figure 9.3(b)). This results in a more uniform intensity limiting throughout the entire temporal length of the pulse, than in the case of a shorter pulse.



(a)



(b)

Figure 9.3: Heuristic analysis of pulse shaping in a 360-period long nonlinear grating. The time-dependent instantaneous transmittance is attributed to contributions from the forward- and backward-propagating electric fields for an input pulse widths of: (a) $240 \frac{\lambda}{c}$ and (b) $570 \frac{\lambda}{c}$.

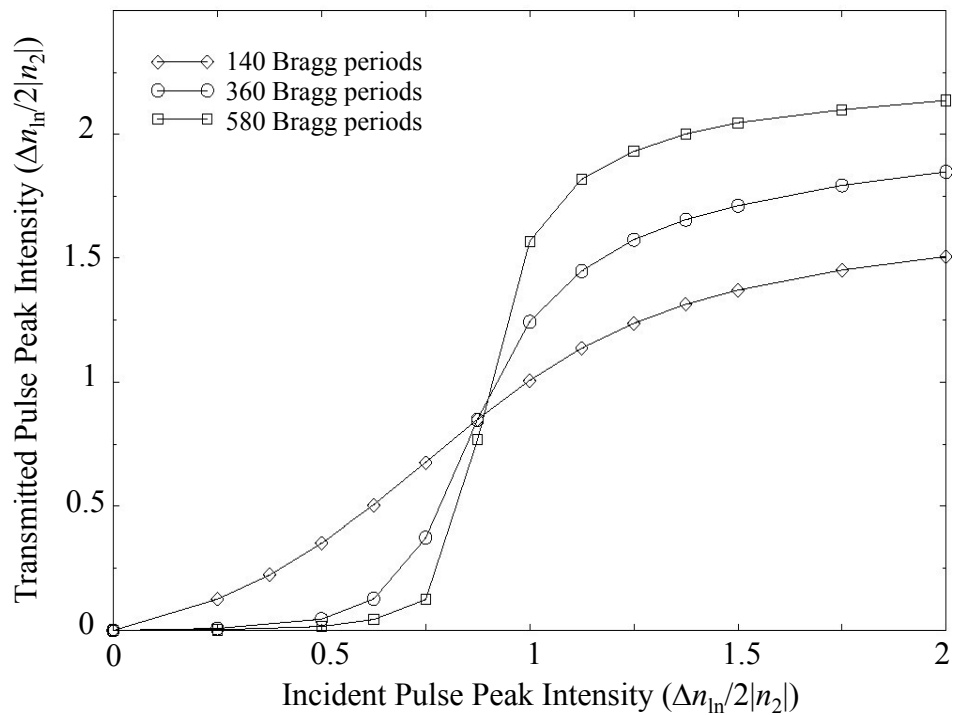
9.2 Case II: $n_{0k} < 0$

This section considers propagation of pulses through the balanced nonlinear periodic structures with a built-in out-of-phase linear grating. It was shown in chapter 7 that under continuous-wave illumination such structures exhibit S- and N- transfer characteristics capable of supporting optical switching, hard-limiting and logic gating. This section will study how the out-of-phase linear grating allows for a dynamic balance of the intensity-induced nonlinear grating as the pulse propagates through the structure.

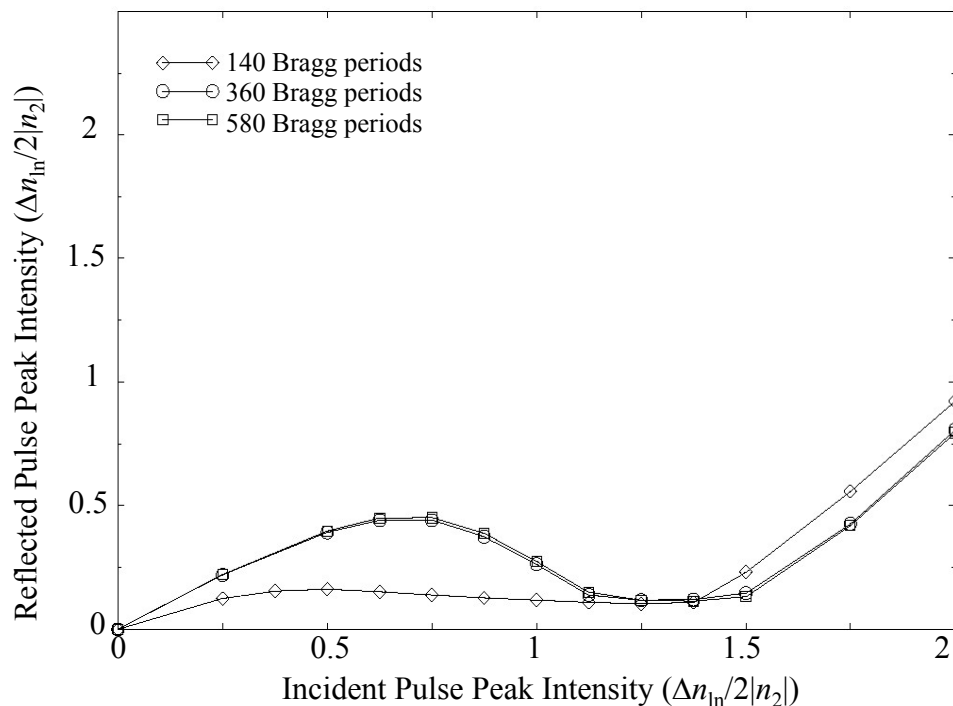
In the following analysis the intensity $I_{cl} = |n_{0k}|/n_{2k}$ will be referred to as the *closing intensity*. The closing intensity causes the nonlinear index change to balance completely with the out-of-phase linear grating. When the balance between linear and nonlinear grating closes the overall grating profile the device is locally transparent for a given section of a pulse.

Figures 9.4(a) and 9.4(b) shown the pulse peak transmitted and reflected intensity versus the pulse peak incident intensity of a $240 \frac{\text{\AA}}{c}$ -long pulse that is assumed to be launched at structures of various lengths with linear built-in out-of-phase gratings of $n_{0k} = -0.01$.

At small incident pulse intensities the linear built-in grating reflects most of the light, resulting in a transmittance close to 0. The transmittance gradually increases as the increasing intensity-induced nonlinear index change offsets the linear grating. The closing and the reopening of the grating are responsible for the S-curve character of the transfer function in Figure 9.4(a). As argued in the steady-state analysis of chapter 7, the S-shape transfer characteristics support logic OR gate operation. The transmittance is at its maximum when the peak intensity of the incident pulse is at the closing intensity. Under these conditions, the pulse regions around the peak of the pulse bleach the grating, permitting the propagation of pulse.



(a)



(b)

Figure 9.4: (a) Peak transmitted intensity versus peak incident intensity of $240 \frac{\Lambda}{c}$ -long pulses for devices that are 140, 360, and 580-periods long (b) Corresponding reflected peak intensity as a function of peak incident intensity.

It is of practical importance to consider the influence of device length on transmitted pulse shapes.

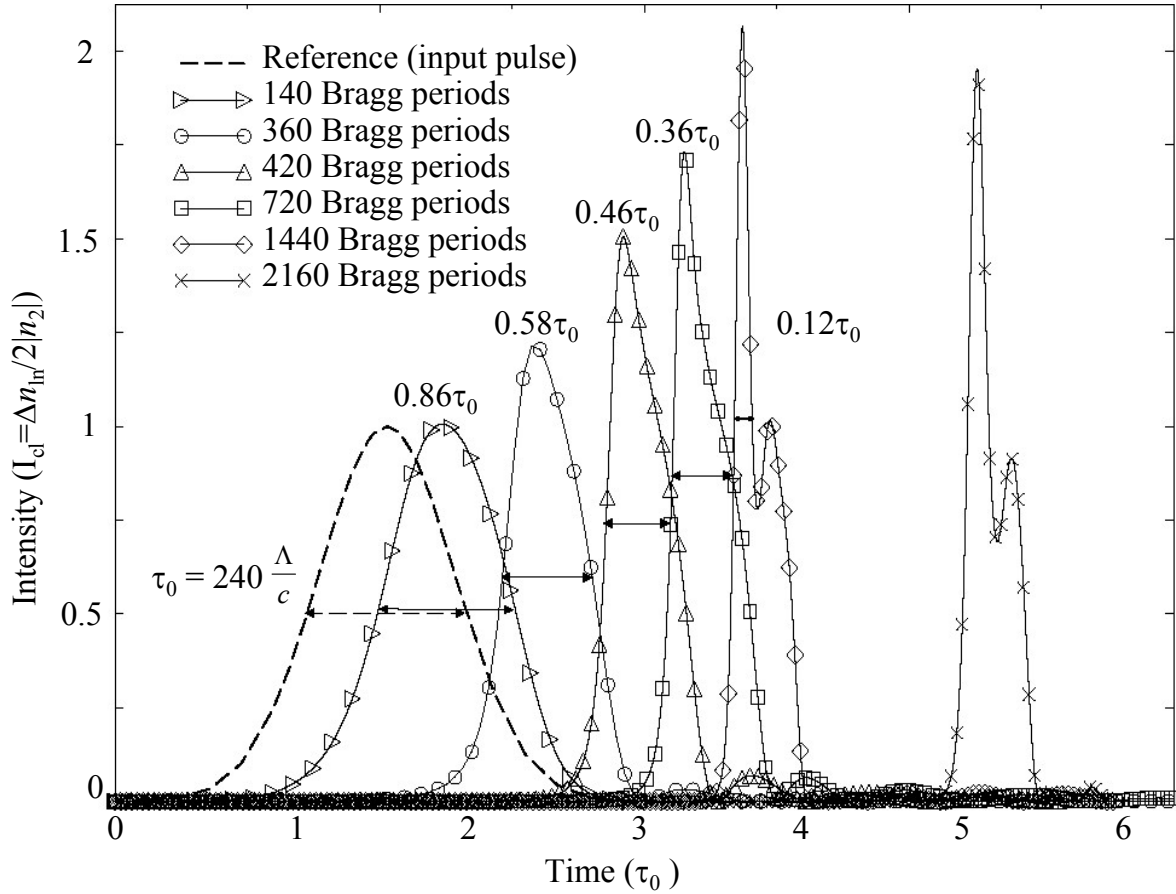
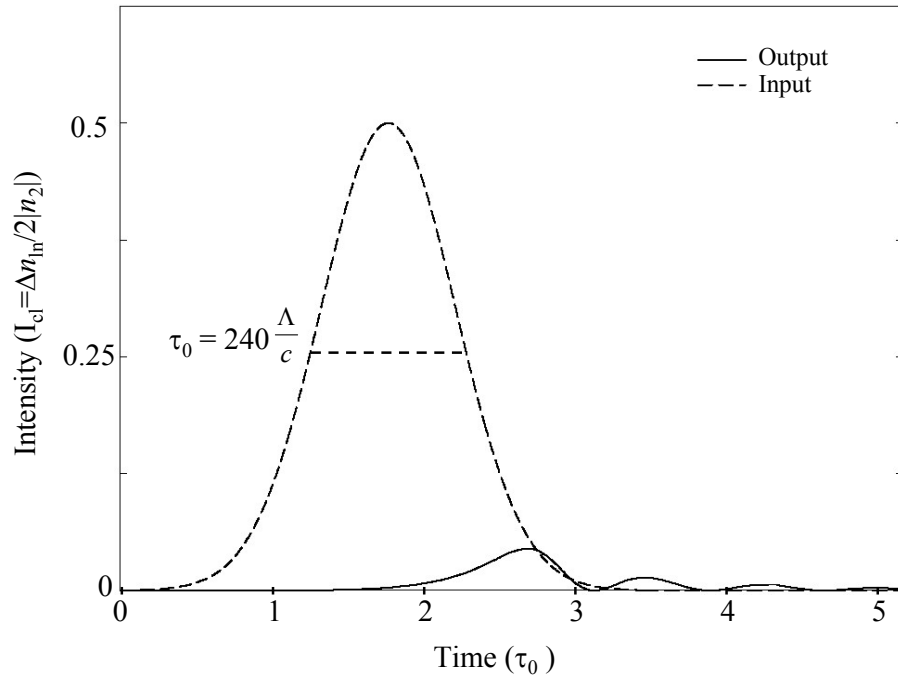
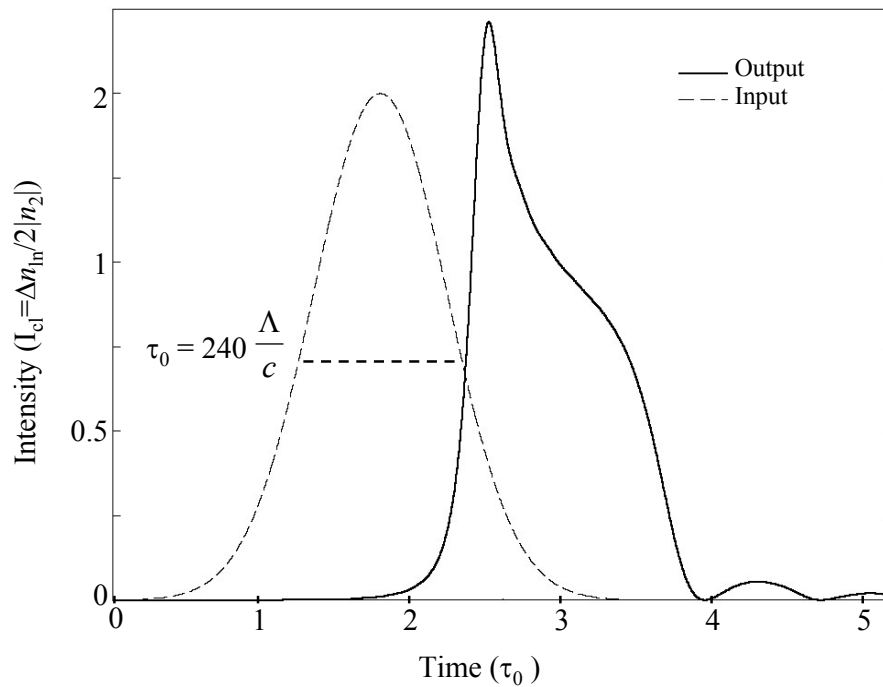


Figure 9.5: Output temporal response of the device with length $L = 140 \Lambda$, 360Λ , 420Λ , 720Λ , 1440Λ , and 2160Λ , for a fixed input pulse with $I_{peak} = I_{closing}$ and $FWHM = 240 \frac{\Lambda}{c}$.

Figure 9.5 shows the transmitted temporal profiles of $240 \frac{\Lambda}{c}$ -long pulses with $I_{peak} = I_{closing}$ assumed to be launched on structures of various widths with the built-in linear grating of $\Delta n_{ln} = -0.01$. The initial stage of pulse compression occurs at distances $L < 700\Lambda$, when the compressed Gaussian pulse preserves a single-peak structure. For longer devices, further peak intensity increase is accompanied by a weak distortion near the edges of the pulse. For devices with $L > 1400\Lambda$ the pulse splits.



(a)



(b)

Figure 9.6: Output transmitted pulse shapes when for incident pulses with peak intensity of: (a) $I_{peak} = 0.5I_{closing}$ and (b) $I_{peak} = 1.5I_{closing}$. The width of the pulse is $FWHM = 240 \frac{\Lambda}{c}$ and the device length is equal to 360 Bragg periods.

The compression effects are best observed when the peak pulse intensity I_{peak} is set to close the grating completely, i.e. $I_{peak} = I_{closing}$. If the intensity-induced nonlinear grating is small compared to the out-of-phase linear grating, the transmittance is expected to be lower due to the reflection by the linear grating. Figure 9.6(a) shows the low transmittance and decay of the pulse with the peak intensity of $I_{peak} = 0.5I_{closing}$. Such a peak intensity gives a maximum nonlinear grating of 0.005, which is lower than the out-of-phase linear grating of $\Delta n_{ln} = 0.01$. In the case of peak incident intensity being larger than the closing intensity (as in Figure 9.6(b) with $I_{peak} = 1.5I_{closing}$), pulse compression will be accompanied by a more severe temporal shape distortion than in the case of $I_{peak} = I_{closing}$. The central part of this pulse with intensity higher than that of $I_{closing}$, i.e. the part of the pulse that creates the effective grating that is out-of-phase with the initial linear grating, is most distorted.

9.3 Conclusions

This chapter examined the time-dependent response of nonabsorbing balanced nonlinear periodic structures whose optical signal processing functionality was introduced in chapters 4-8. It was predicted through theory that the intensity limiting and switching functions of the devices proposed are supported in the case of pulsed illumination under the assumption of instantaneous nonlinear response.

This chapter discussed the propagation of ultrashort pulses in stable systems with no built-in grating, and with a built-in linear grating that is out-of-phase with the distribution of Kerr coefficients. In the absence of the linear grating, the transmittance of pulses with small bandwidth, as compared to the bandwidth of the induced grating, is independent of pulse width and exhibits peak intensity limiting. In the presence of a built-in linear out-of-phase grating, the S -shaped transmittance characteristics and temporal compression effects have been predicted due to the closing and re-opening of the

effective refractive index grating. It was shown that the magnitude of the pulse distortion depends strongly on the length of the device and peak intensity of the pulse.

Chapter 10

Experimental Assessment of the Applicability of Specific Nonlinear Optical Materials to Nonlinear Periodic Devices

The literature review of chapter 3 concluded that the successful potential implementation of nonlinear periodic structures relies on: increasing their optical signal processing functionality; and finding nonlinear materials with good figures of merit that can be incorporated into periodic structures.

Chapters 5 to 9 proposed new methods of optical signal processing using nonlinear periodic structures. By changing the structure and the materials of the optical elements they could limit, switch, perform logic operations or analog-to-digital conversion. This analysis was strengthened by studying the sensitivity of the response of the signal processing elements proposed to weak disorder and to variations in the material parameters.

Chapters 10 and 11 constitute the experimental part of this thesis. They aim to address the additional challenges that inhibit the successful implementation of nonlinear

periodic optical signal processing devices. Following the investigation and evaluation of the nonlinear properties of promising materials in chapter 10, chapter 11 will demonstrate the illumination-dependent response of novel nonlinear periodic structures.

This chapter is organized as follows:

Following the introduction of laser systems and experimental techniques used, this chapter presents the results of the measurements of nonlinear properties of selected nonlinear materials. The survey of materials studied starts with the demonstration of the non-resonant nonlinear response of two organic compounds: DR1 and MEH-PPV. The next section of this chapter presents the results of direct measurements of resonant nonlinear properties of inorganic crystalline semiconductor MQWs and PbS semiconductor nanocrystals. Throughout the search for the appropriate materials it was sought to maximize simultaneously both the magnitude of the nonlinear index change and the figures of merit. The fulfilment of these requirements is fundamental to the applicability of a given material to the large-index change theory proposed in the theoretical part of this work.

The results presented in this chapter were published in Refs. [39, 142–148].

10.1 Experimental Apparatus

This section introduces the equipment and experimental techniques used to characterize the linear and nonlinear properties of materials.

10.1.1 Laser Systems and Spectrophotometer

Two laser systems were used to measure the nonlinear refractive and absorptive properties of the materials. The first laser system was also used to characterize the nonlinear periodic structures described in chapters 11 and 12.

The first laser system is illustrated in Figures 10.1 and 10.2. It is composed of a computer controlled Light Conversion TOPAS optical parametric amplifier (OPA) pumped by a Quantronix Titan regenerative (RGA) and multipass (MPA) amplifier. The Titan amplifier is itself pumped by a Quantronix YLF (modified YAG) pump laser and seeded by a Coherent Verdi diode-pumped Ti-Sapphire laser Vitesse.

The Vitesse seed source produces broadband ultrashort 30 fs pulses at a repetition rate of 80 MHz at a wavelength of 802 nm. The average power of this ultrafast pulse train is 300 mW. The YLF pump laser provides high-energy 150 ns pump pulses at 527 nm at a repetition rate of 1 kHz with an average power of 12–14 W.

Inside the Titan amplifier the seed and pump pulses are combined. First, the 30 fs seed pulses are temporally stretched to 150 ps using a pair of gratings and only a part of the initial bandwidth is selected for amplification. These stretched pulses are then sent to the RGA where they are combined with a part of the YLF pump. The repetition rate of the RGA cavity is controlled by the Pockels cell operating at a YLF repetition rate of 1 kHz. The second stage of amplification takes place in the multipass amplifier. Here the pre-amplified pulses are combined with the rest of the pump light in a Ti:Sapphire crystal. The energy of the pulses coming out of the multipass amplifier is about 2.5 mJ. The last stage of the Titan amplifier is a compressor in which the temporal width of each

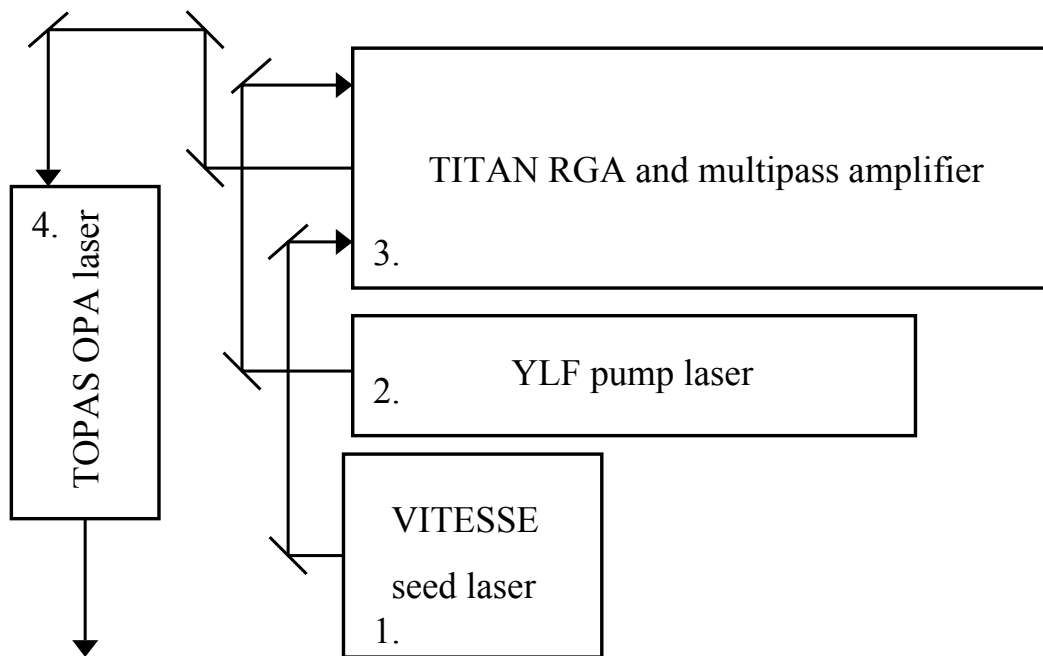


Figure 10.1: General layout of the first laser system used: 1. VITESSE seed laser [$\lambda=800$ nm, rep. rate = 80 MHz, $\tau = 30$ fs, power = 300 mW]; 2. YLF pump laser [$\lambda=533$ nm, rep. rate = 1 kHz, $\tau = 150$ ns, power = 12-16 W]; 3. TITAN amplifier [$\lambda=800$ nm, rep. rate = 1 kHz, $\tau = 1.7$ ps, power = 2.0 W]; 4. TOPAS OPA [280 nm $< \lambda < 2600$ nm, rep. rate = 1 kHz, $\tau = 1.2$ ps, 8 mW $< \text{power} < 430$ mW].

pulse is reduced to 1.2 ps using a pair of gratings. These bandwidth-limited pulses come out at a repetition rate of 1 kHz, have a bandwidth of 0.7 nm, and an average power of 1.8 W.

In the TOPAS OPA various spectral components are produced from the 800 nm laser illumination produced by the Titan. First, a superfluorescence is generated inside the TOPAS in a BBO crystal. Using a diffraction grating, and by phase matching angle of the nonlinear crystal, a parametric conversion (signal and idler beams) is achieved from

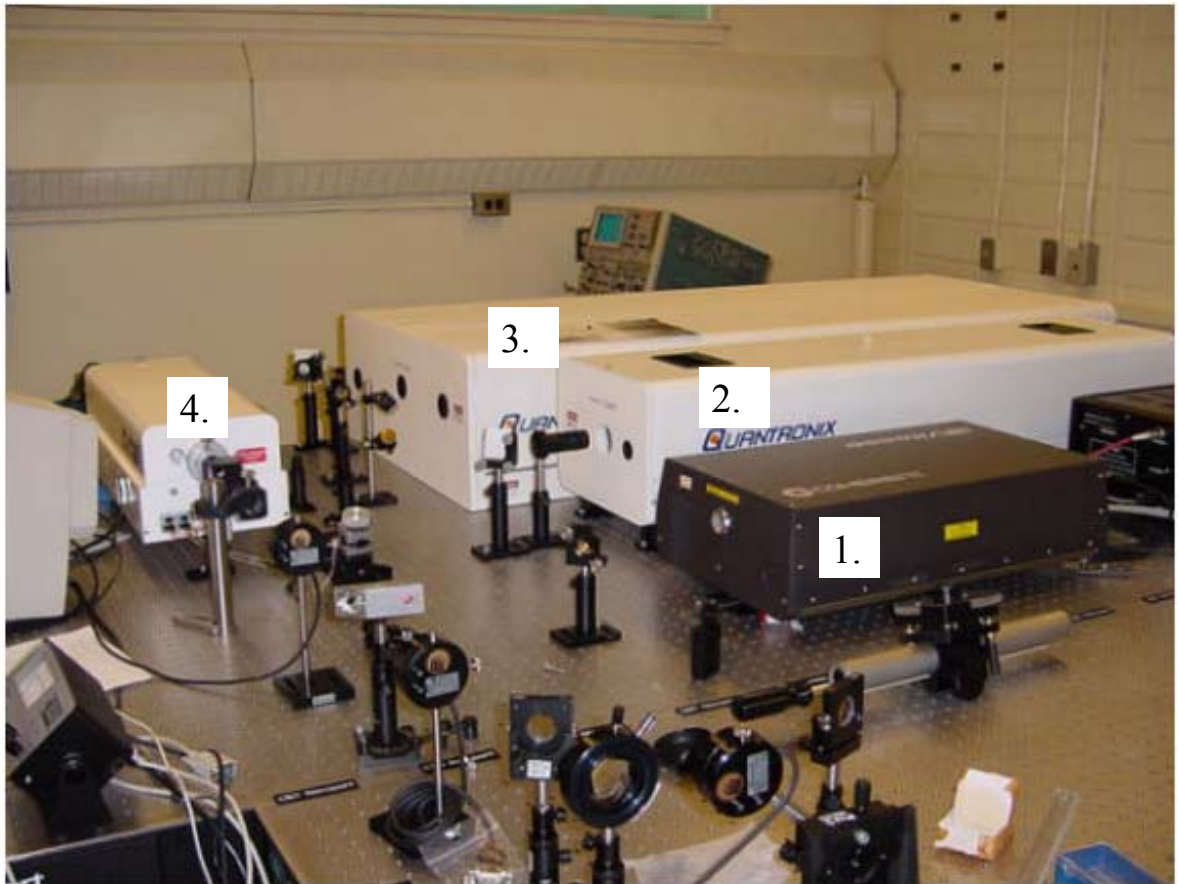


Figure 10.2: Picture of the OPA laser system at installation. The numbers 1 to 4 in the figures correspond to the system components as explained in the caption of Figure 10.1.

the Titan pump light. By using a variety of crystals and nonlinear mixing techniques, light at wavelengths ranging from 280 nm to 2.6 μm can then be generated from the signal and idler beams. The average output power of the TOPAS varies from 8 mW to 400 mW depending on the wavelength range. The pulse width ranges from 0.9 to 2 ps also depending on the wavelength.

The second laser system used in the measurements of nonlinear properties of materials presented in this chapter was a Coherent Mira Ti:Sapphire laser pumped by an Innova 300 laser. The Innova 300 is an Ar-Ion tube source producing multi-line continuous-wave illumination in the vicinity of a wavelength of 510 nm at an average power of up to 8

W. The mode-locked Mira laser produces 150 fs pulses tunable from 780 nm to 900 nm at a repetition rate of 76 MHz. The average power from the Mira ranges from 100 to 300 mW. In order to eliminate the heating effects, the effective repetition rate of the pulse train produced by the second laser system was often reduced to 5 kHz with an electro-optic Pockels cell switch. Pockels cell is made out of two crossed polarizers that block incident illumination in the absence of high voltage bias. In the presence of high voltage, the polarization of the incident light is rotated within the crystal, allowing full transmittance.

The measurements of linear transmittance and absorbance were carried out with a Cary 500 spectrophotometer that allows spectral tunability in the 300 nm to 2.9 μm spectral range.

10.1.2 Z-scan Technique

Experimental Set Up

Measurements of nonlinear properties of materials were performed with a single-beam z-scan experiment [149, 150]. Z-scan technique allows determination of both real and imaginary parts of the nonlinear response. A layout of the z-scan experiment used in this work is shown in Figure 10.3 [151].

Following parametric amplification in the TOPAS, filters and wavelength separators were used to single out the desired wavelength. Two crossed polarizers with an inserted half-waveplate controlled the beam intensity. The laser beam was focused and the transmittance through the sample was recorded as the position of the sample was varied relative to the focal length of the lens. A reference beam detector was used to monitor the fluctuations in the power of the incident laser beam. Z-scan was performed in two configurations: with and without an aperture on the detector. Measurement with an aperture in place allowed the determination of the sign and magnitude of the Kerr

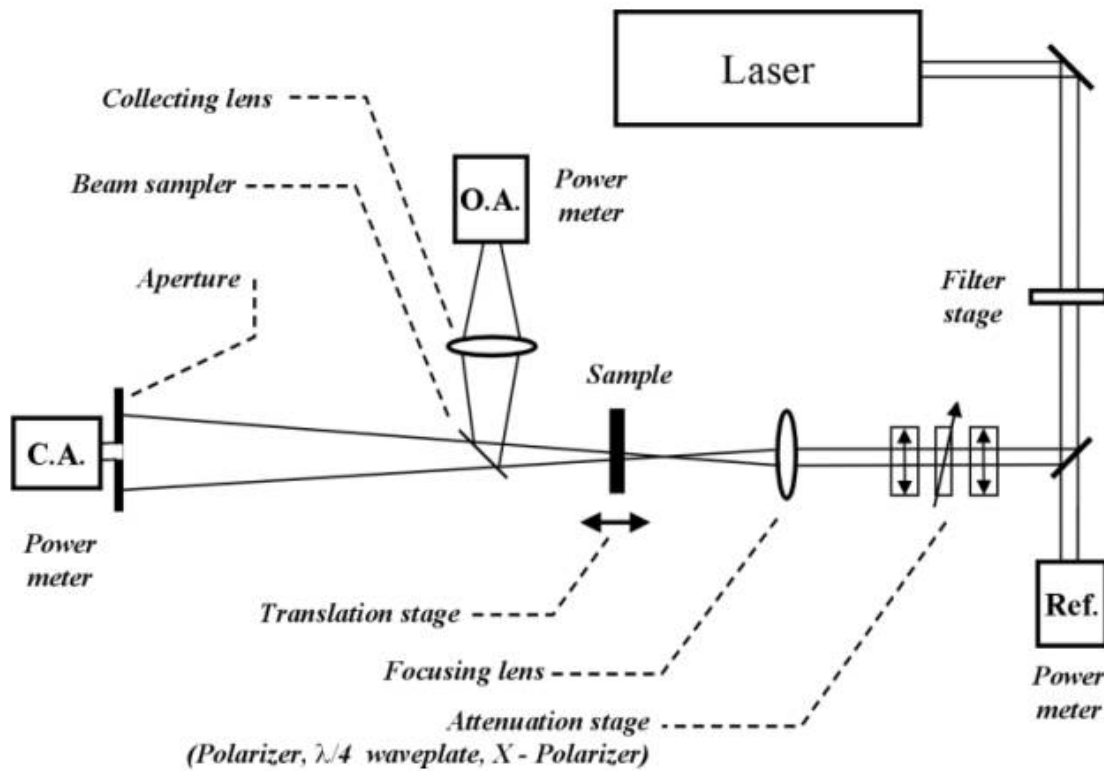


Figure 10.3: Schematic illustration of a z-scan experimental setup used in this work. Diagram taken from Ref. [151].

coefficient, while measurement with no aperture allowed the determination of the sign and magnitude of nonlinear absorption [149]. Labview software was used to collect data and automate experiments.

Qualitative Description of Ideal Z-scan Traces

Figures 10.4 and 10.5 show high-quality, normalized closed and open-aperture z-scan traces for a sample exhibiting negative diffractive nonlinearity and saturation of absorption.

When the sample is far from the focus, the intensity experienced by the sample is low, and hence no transmittance change is recorded in the closed-aperture trace. As

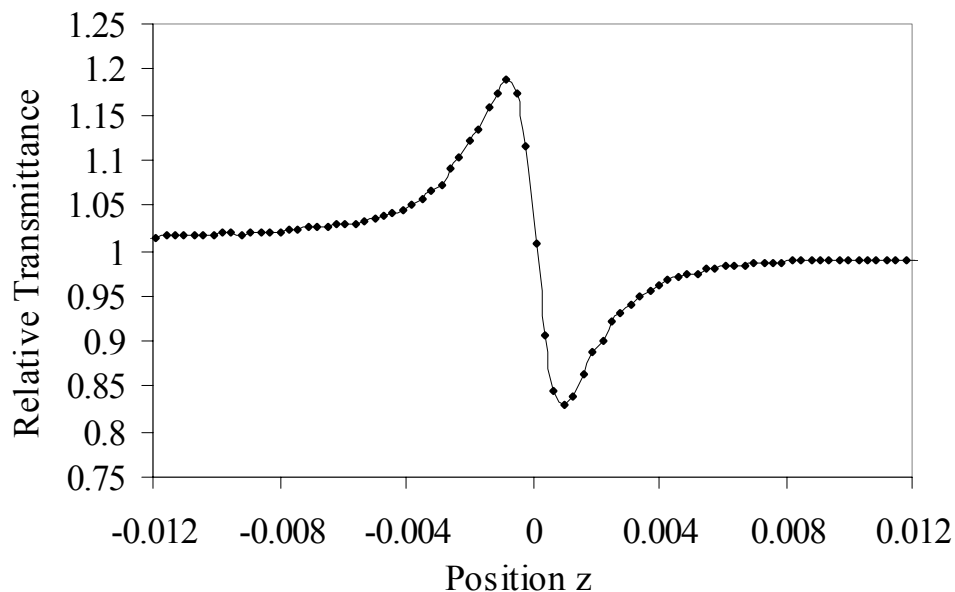


Figure 10.4: Ideal normalized closed-aperture z-scan trace for the sample with a negative refractive nonlinearity.

the sample is translated towards the focal point, the level of illumination experienced by the sample increases and the sample starts acting as a nonlinear defocusing lens. This shifts the effective focal point away from the sample, making the size of the transmitted laser beam at a closed-aperture detector smaller than the initial radius. An increased transmittance is recorded by the closed-aperture detector, manifested by the peak in the closed-aperture z-scan trace. As the sample moves closer towards the focus, there is less space between the sample and focal point to shift the effective focal point, and hence the closed-aperture transmittance decreases. When the sample is exactly at the focus the closed-aperture transmittance is equal to the initial transmittance. As the sample is translated past the focus the opposite response is recorded by the closed-aperture detector. The sample defocuses again, increasing the size of the transmitted beam at the

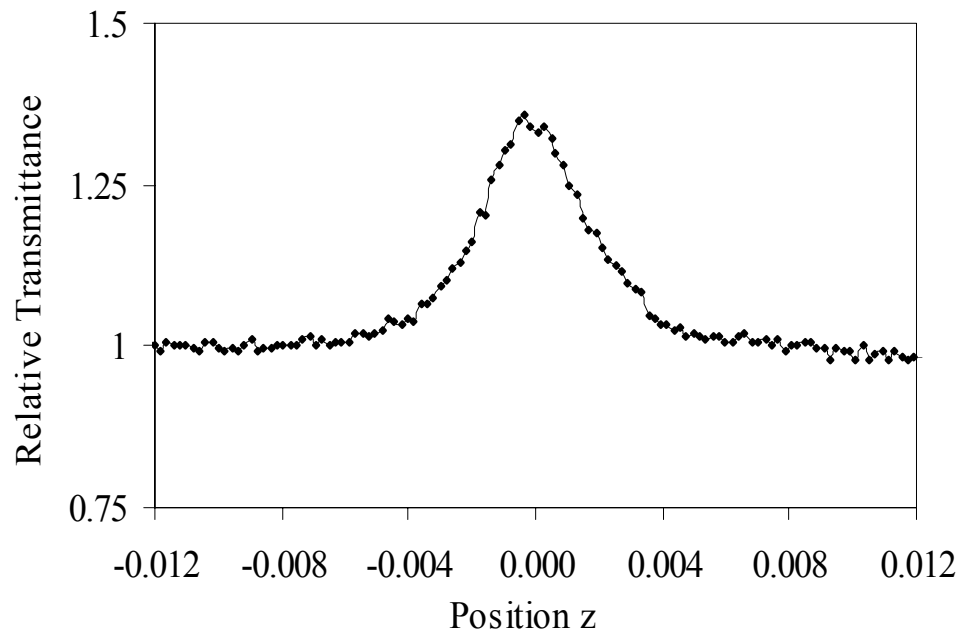


Figure 10.5: Ideal normalized open-aperture z-scan trace for the sample exhibiting saturation of absorption.

closed-aperture detector and hence decreasing the nonlinear transmittance. When the sample is moved away from the focus, the transmittance descends to its initial value.

If the material exhibits positive nonlinearity, then the closed-aperture trace is opposite to the one shown in Figure 10.4, i.e. it has valley-peak, rather than peak-valley characteristics.

Unlike the closed-aperture measurement, the open-aperture measurement of a z-scan experiment records changes in the absolute illumination-dependent transmittance (Figure 10.5). It provides information as to how much light is transmitted through the sample depending on the proximity of the sample to the focal point. The open-aperture scan provides information about the absorbing, rather than refracting, properties of the sample analyzed. Regardless of the sample position, the open-aperture detector encom-

passes the full transverse extent of the beam. Therefore the shape of the open-aperture transmittance curve is symmetrical.

If the material exhibits saturation of absorption, then the open-aperture trace is a symmetric peak (Figure 10.5). Multiphoton absorption manifests itself with a valley centered at the focal point in the open-aperture z-scan trace.

Experimental Challenges Associated with the Z-scan Technique

There are many experimental challenges associated with obtaining z-scan traces of the high quality shown in Figures 10.4 and 10.5. Apart from the requirements of the sample scanned being nonlinear, there are additional experimental problems associated with: the alignment of the experimental set up, the quality of the laser beam, and the quality of the sample.

The z-scan measurement of the refractive nonlinearity using a closed-aperture detector places very strict requirements on the collinearity and alignment of the optical components in the path of the beam. Especially, the closed-aperture detector has to collect the exactly central part of the beam transmitted through the sample. Unless the aperture is well centered on the transmitted beam, the closed-aperture shape will look distorted and results will be inconclusive.

As the beam is focused and defocused by the nonlinear sample, the size of the beam on the open-aperture detector changes. It has to be ensured that, regardless of the position of the sample during the experiment, the energy across the full transverse extent of the beam is encompassed by the open-aperture detector. This may require additional focusing in front of an open-aperture detector.

The quality of the laser beam used for z-scan experiments has to be high. Meaningful interpretation of z-scan traces requires that the experiment be performed with the beam whose transverse profile is either Gaussian or has a top-hat shape.

The stability in time and direction of the laser beam is also very important. Despite

the presence of the reference detector in the z-scan set up, the power fluctuations of the laser have to be significantly lower than the changes in the transmittance that are induced by the nonlinear response. Spatial instability leads to different sections of the sample being illuminated at various stages during the experiment, and destroys the collinearity of the set up.

The OPA laser system often used throughout the work presented in this thesis in the z-scan experiments produces light via harmonic generation and sum-frequency mixing within certain spectral ranges. As is common in such systems, the transverse shape of the beam is often distorted, and the temporal and pointing stability of laser beam are often low. The beam spatial filtering and frequent system optimization are commonly required.

The samples used in the z-scan experiment have to be of a high optical quality. Surface roughness, compositional inhomogeneity, and non-parallelism of the facets are most common problems associated with the sample quality. Roughness on the order of the optical wavelength leads to scattering of the beam and destroys the coherent phase transformation induced by the refractive nonlinear effect. The inhomogeneity of the sample places very strict requirement on the pointing stability of the laser beam and on the collinearity of the laser system. In addition, it decreases the reproducibility of the experimental results. Non-parallel facets steer the beam away from the initially centered closed-aperture detector.

If the problems associated with the sample quality are not too severe the techniques of dividing high-power by low-power scans, or subtraction of normalized low-intensity background from the normalized z-scan signal can be used to increase the quality of the measured data prior to analysis.

There are specific problems associated with each type of sample analyzed in this work.

The highest quality samples were obtained by dissolving a nonlinear agent in an optically linear solvent and placing the resulting liquid in a cuvette. In this case it had

to be ensured that the solution was well dissolved and no aggregation took place.

Thin films of organic materials spin-coated on glass substrates often suffer from inhomogeneity and surface roughness. The preparation of sufficiently high-quality samples requires careful control of the spin coating acceleration, speed, and duration, and appropriate choice of solvent viscosity.

Inorganic crystalline samples grown by molecular beam epitaxy resulted in very well ordered layers with perfect top-surface quality. However, the back facet had to be polished to eliminate phase distortion of the transmitted beam.

Thick samples of organic materials were fabricated with the press method. The nonlinear solid state materials were inserted between two flat glass slides, melted, pressed, and then cooled down. Inhomogeneity and non-parallelism of the facets were most common problems associated with samples fabricated using this technique.

Interpretation of Results

To determine nonlinear coefficients from measured z-scan traces, the closed- and open-aperture traces are normalized to their low-intensity value. Since the closed-aperture traces are influenced both by the nonlinear refraction and nonlinear absorption, the normalized closed-aperture traces are divided by the normalized open-aperture traces to yield purely refractive signature.

For the case of illumination with Gaussian pulses, the Kerr coefficient n_2 can be obtained from the divided trace using the following formula:

$$n_2 = \frac{1}{0.406} \frac{\alpha_0 \lambda}{2\pi I} \frac{1}{1 - e^{-\alpha_0 L}} \frac{1}{(1 - S)^{0.25}} \Delta T_{p-v} \quad (10.1)$$

where α_0 is the linear absorption, n_0 is the linear index of refraction, I is the intensity at the focus, L is the thickness of the sample, S is the transmittance of aperture when the sample is far from the focus and ΔT_{p-v} is the change in transmittance between the two peak-valley extrema of the divided normalized closed-aperture trace [149].

In some nonlinear measurements the refractive nonlinearity is not a purely third-order nonlinear effect, but a combination of nonlinear processes of various orders. In this case it is more appropriate to estimate nonlinear index change Δn , rather than n_2 from:

$$\Delta n = \frac{1}{0.406} \frac{\alpha_0 \lambda}{2\pi} \frac{1}{1 - e^{\alpha_0 L}} \frac{1}{(1 - S)^{0.25}} \Delta T_{p-v} \quad (10.2)$$

To obtain the nonlinear absorption coefficient β from the open-aperture trace the following formula is used:

$$\beta = \frac{\alpha_0}{I(1 - e^{-\alpha_0 L})} (6.592T_{min(max)}^2 - 15.791T_{min(max)} + 9.213) \quad (10.3)$$

where the $T_{min(max)}$ is the lowest (highest) normalized transmittance in the open-aperture trace of the sample exhibiting multiphoton absorption (saturation of absorption).

Again, it is often more appropriate to estimate the change in the absorption $\Delta\alpha = \beta I$, rather than the purely electronic coefficient β . The following formula should then be used:

$$\Delta\alpha = \frac{\alpha_0}{1 - e^{-\alpha_0 L}} (6.592T_{min(max)}^2 - 15.791T_{min(max)} + 9.213) \quad (10.4)$$

Expressions (10.3) and (10.4) provide correct estimates of nonlinear absorption if the change in the open-aperture transmittance is less than 10%. Otherwise a different approach is necessary to calculate the change in the absorption from the experimental data.

In some of the results presented in this chapter the transmittance changes were substantially larger than 10%. In such cases, in extracting nonlinear absorption from the data, the fluence across the sample was assumed to decay according to $\frac{dP}{dz} = -\alpha_0 P + \beta P^2$. The change in the absorption was obtained from the change in the open-aperture transmittance according to:

$$\Delta\alpha = \frac{(1 - T_{min(max)})e^{-\alpha_0 L}\alpha_0}{(e^{\alpha_0 L} - 1)T_{min(max)}} \quad (10.5)$$

Elimination of Cumulative Effects

If the relaxation time of the nonlinearity is shorter than the temporal pulse spacing the nonlinear effect will accumulate in time. Such cumulative nonlinearities are usually caused by the thermal effects and a relatively long time of heat dissipation. In most of the experiments presented in this section it was desired to measure the influence of the pulse on its own propagation rather than the cumulative effect.

Because the cumulative thermal nonlinear effects have long response time, their influence increases with the repetition-rate of the laser source. In order to eliminate the heating effects during measurements with the 76 MHz repetition rate Mira, a Pockels cell was used to reduce the repetition rate to 5 kHz.

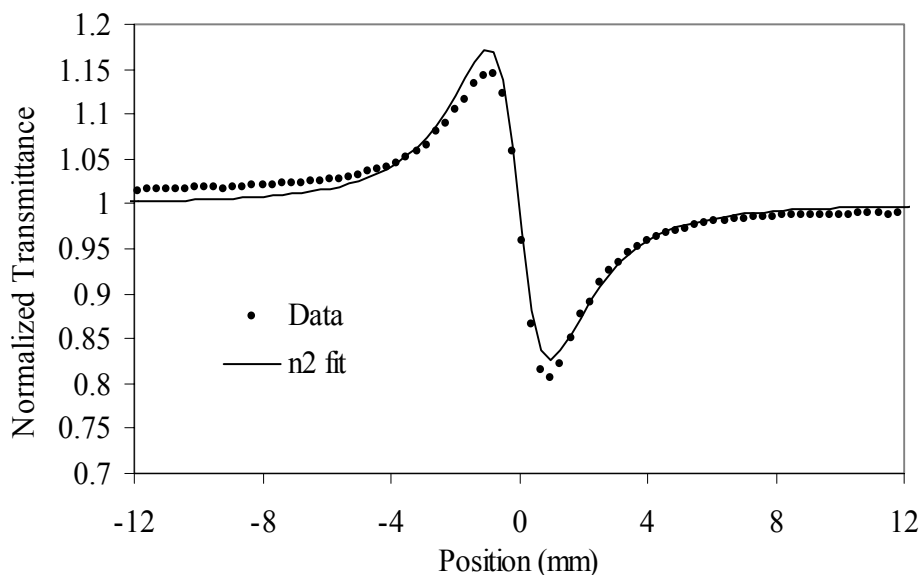


Figure 10.6: Normalized closed-aperture z-scan trace showing a negative nonlinear thermal response of CS_2 at a repetition rate of 76 MHz. The line corresponds to the nonlinear refraction fit.

Figures 10.6 and 10.7 prove that this technique was successful. These two plots show

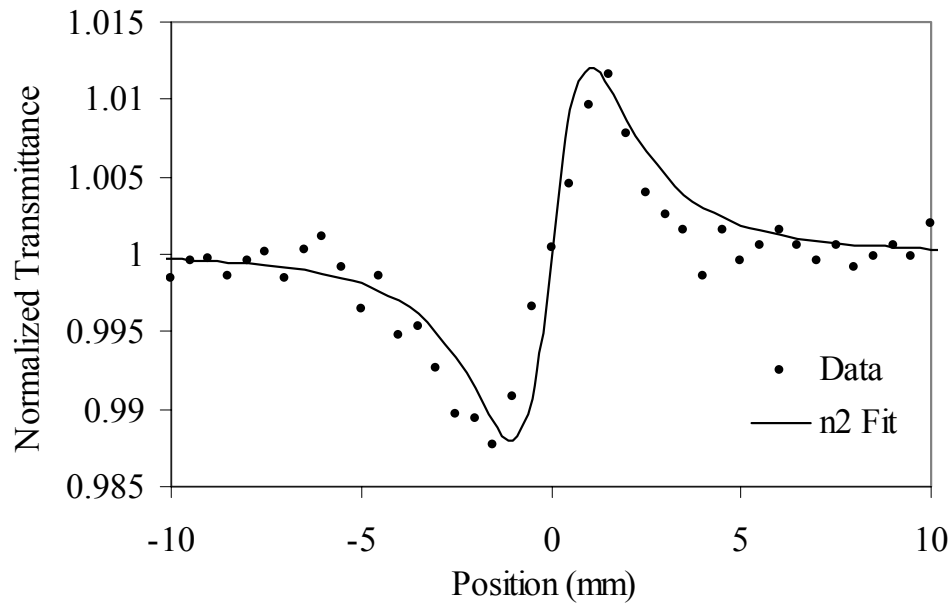


Figure 10.7: Normalized closed-aperture z-scan trace showing ultrafast positive index change of CS_2 at a repetition rate of 5 kHz.

normalized closed-aperture z-scan traces of measurements taken on carbon disulphide (CS_2) at repetition rates of 76 MHz and 5 KHz. The nonlinear signature from the high repetition rate scan results in a negative thermal refractive nonlinearity, while at the low repetition rate the ultrafast refractive nonlinearity has a positive sign.

In general, the absence of measurable cumulative effect at a given repetition rate can be verified by performing another experiment under identical experimental conditions with the exception of different repetition rates. In the absence of cumulative effects the normalized z-scan traces should be identical for the two repetition rates. All results presented herein have been verified not to depend on the repetition rate, and hence are of nonthermal origin.

Having introduced the laser sources and experimental technique used for nonlinear

measurements throughout this work, the rest of this chapter will present the results from the nonlinear measurements on a variety of materials.

This sections will follow how the research reported in this work has advanced the field of nonlinear optical materials. Section 10.2 will describe the results from the measurements of non-resonant nonlinearites. Section 10.3 will describe measured resonant nonlinear response of selected materials.

10.2 Non-resonant Response of Nonlinear Materials

Because of the prospect of ultrafast nonabsorbing nonlinearities, the search for materials throughout this work has initially concentrated on determining the applicability of non-resonant nonlinear response to optical signal processing using nonlinear periodic structures. The real and imaginary parts of the nonlinear response of various material systems were measured and the corresponding nonlinear figures of merit were computed.

10.2.1 Non-resonant Nonlinear Response of Azobenzene Dye Disperse Red 1

Based on the published reports, it was determined that pseudo-stilbene type azobenzene dyes represent one particularly promising group of nonlinear materials.

The structure of the pseudo-stilbene type azobenzene molecule is depicted in Figure 10.8. It consists of an azo group $-N=N-$ between two benzene rings, and push-pull donor and acceptor groups on the opposite sides of the benzene rings [152, 153]. For simplicity, from here on the pseudo-stilbene type azobenzenes will simply be referred to as *azobenzenes*. As shown in Figure 10.9 azobenzenes exhibit a fundamental absorption maximum between 400 and 500 nm.

The measurement of the nonlinear properties of azobenzenes was initially performed at the illumination wavelength of 760 nm on 2%, 5%, and 10% weight by weight solutions of



Figure 10.8: The molecular structure of pseudo-stilbene type azobenzene molecule: the azo group, two benzene rings, donor and acceptor groups.

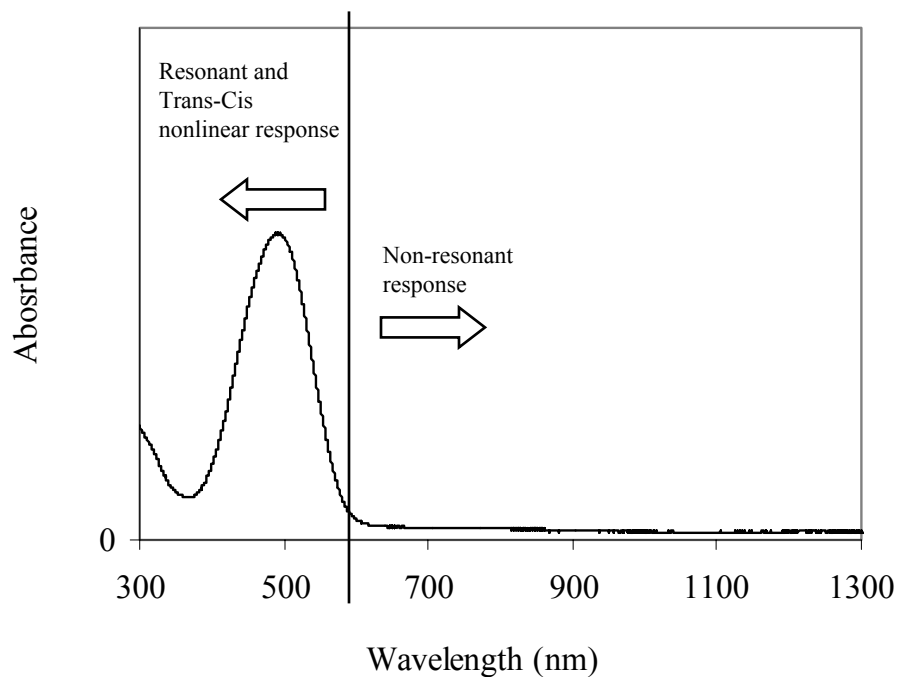


Figure 10.9: Absorption spectra of Azobenzene Dye Disperse Red 1. The absorption peaks at 490 nm.

azobenzene dye Disperse Red 1 (DR1) dissolved in THF. DR1 was synthesized by Chantal Paquet from the Chemistry Department at the University of Toronto. The results are presented in Figure 10.10. The values of Kerr coefficient n_2 , nonlinear absorption β , and

Stegeman W and T figures of merit are shown.

The values of nonlinear index of refraction range from $-1.5 \times 10^{-15} \text{ cm}^2/\text{W}$ to $-1.3 \times 10^{-14} \text{ cm}^2/\text{W}$. β coefficients range from $0.7 \times 10^{-11} \text{ cm}/\text{W}$ to $3.7 \times 10^{-11} \text{ cm}/\text{W}$. Both n_2 and β increase with increasing concentration pretty linearly. This takes place since the concentrations of the solutions are low enough that the molecules remain essentially noninteracting.

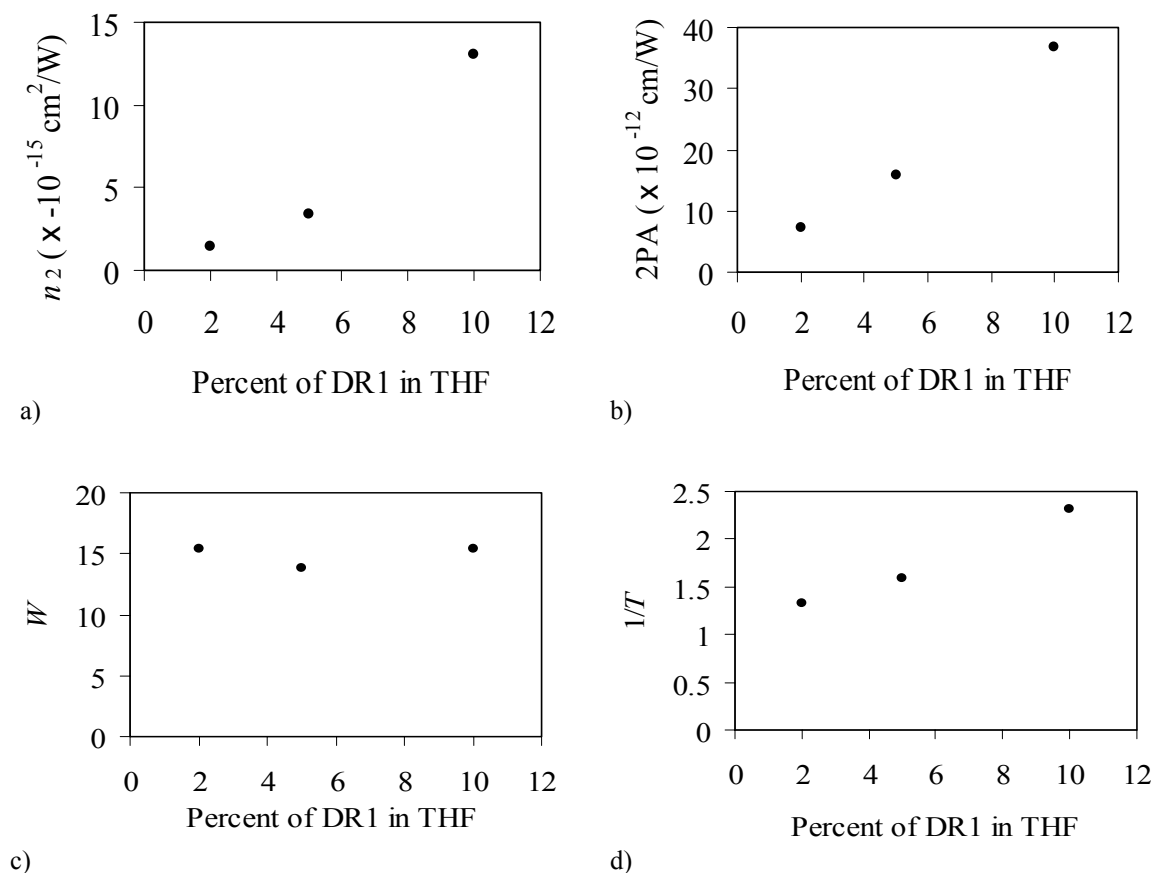


Figure 10.10: Results from the measurement of nonlinear properties at a laser wavelength of 760 nm of the solution of azobenzene dye Disperse Red 1 in THF at concentrations of 2%, 5%, and 10%. a) Kerr coefficients; b) two-photon absorption coefficients; c) W figure of merit; d) $1/T$ figure of merit.

Since at 760 nm the DR1 is transparent the linear figure of merit, W , is very good (W

of at least unity is considered good) . The nonlinear figure of merit, T , is also acceptable ($1/T$ larger than 1 is considered good).

10.2.2 Non-resonant Nonlinear Response of MEH-PPV/PMMA

Another material whose non-resonant nonlinear properties were examined was a polymer blend of MEH-PPV (poly(2-methoxy, 5-(2'-(ethyl)hexyloxy)-*p*-phenylene vinylene) within a PMMA (polymethyl methacrylate) host.

Poly(*p*-phenylene vinylene) (PPV) and its derivatives have been demonstrated to exhibit appreciable ultrafast optical nonlinearities [154, 155]. However, PPV is insoluble and hence is not easily processable. To allow processability into solid-state samples, PPV or one of its derivatives must be embedded within a soluble host.

In this work this was achieved by attaching MEH-PPV — a soluble derivative of PPV — to the PMMA host. PMMA is a good candidate for the host material since it is amorphous, has good optical transparency, and is readily processable into thin and thick films. The thickness of the sample prepared by blade casting was 0.2 mm. The weight ratio of MEH-PPV to PMMA was 0.2. A 0.2 mm sample of PMMA was also prepared to allow the comparison of the its nonlinear response to that of the MEH-PPV composite.

The MEH-PPV was synthesized by Jiguang Zhang from the Chemistry Department at the University of Toronto, while the film was prepared and nonlinear measurements were taken by the author of this thesis and by Yunakun Lin from the Department of Electrical and Computer Engineering at the University of Toronto.

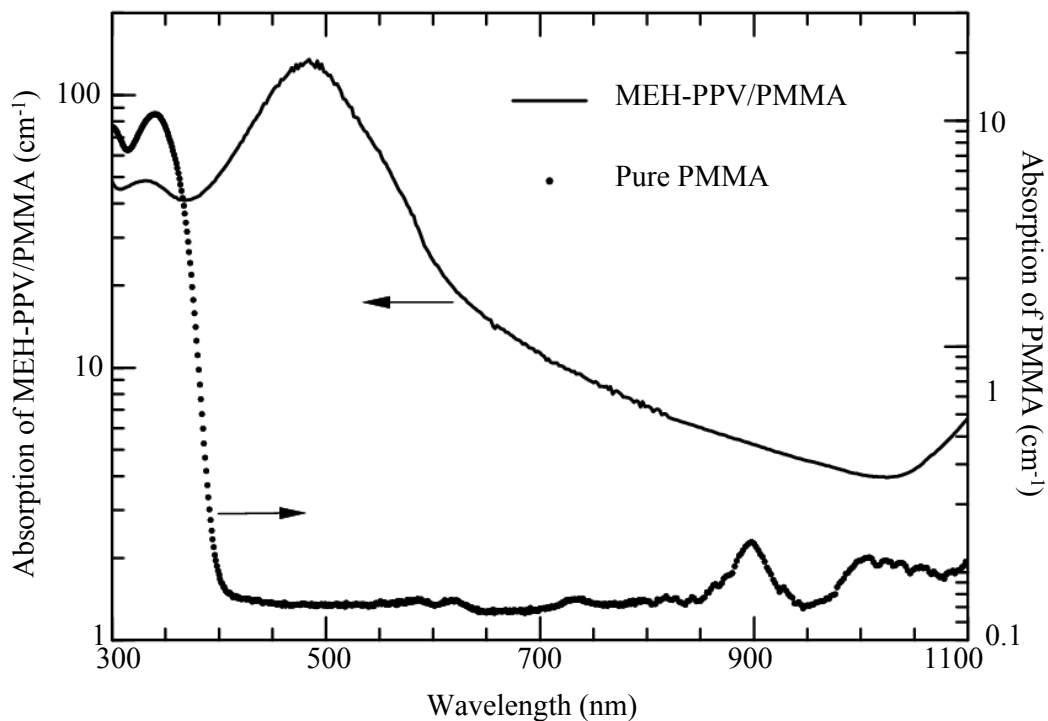


Figure 10.11: Linear absorption spectra of pure PMMA (dotted line) and MEH-PPV/PMMA composite (solid line).

The linear optical losses, including absorption and scattering, are shown in Figure 10.11 for both MEH-PPV/PMMA composite and pure PMMA. For the composite, the absorption peak is evident near 485 nm with the maximum absorption value of 135 cm^{-1} . Above 600 nm, the optical loss gradually decreases to a minimum near 1050 nm. At the wavelength of 840 nm, at which nonlinear experiments were carried out, the linear loss was found to be 6.2 cm^{-1} . Pure PMMA is essentially transparent from 380 to 1100 nm.

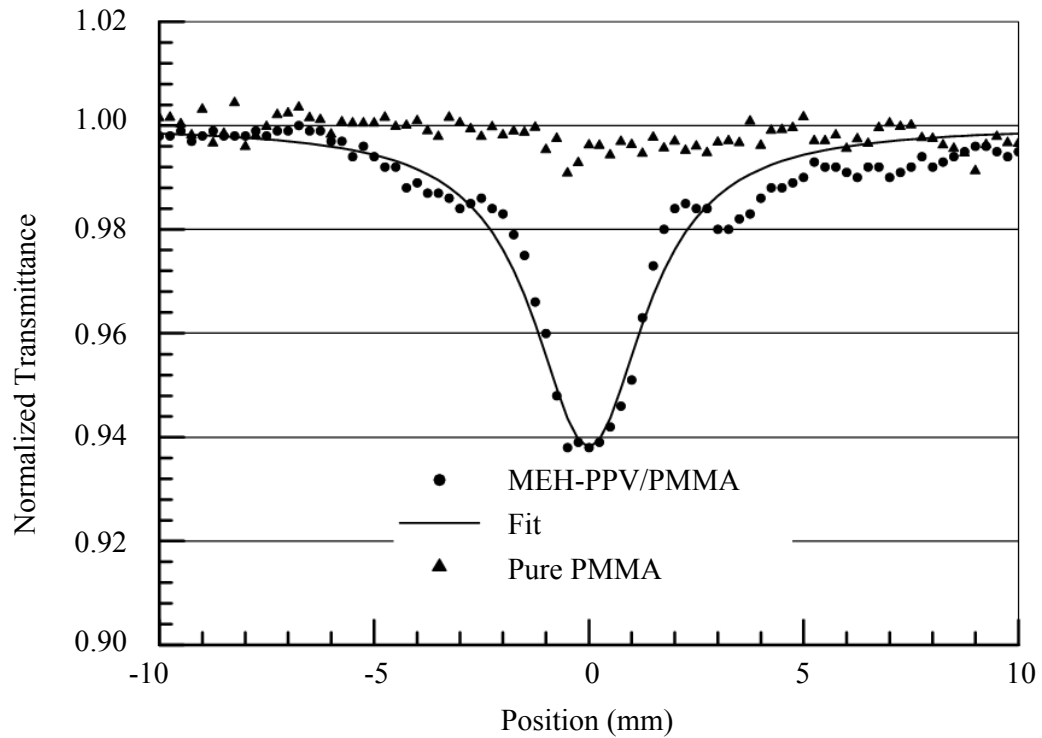


Figure 10.12: Normalized open-aperture z-scan transmittance traces of MEH-PPV/PMMA (circle) and pure PMMA (triangle) film samples using 100 femtosecond pulses at $\lambda=840$ nm. The solid line is a theoretical fit to the open-aperture trace of MEH-PPV/PMMA.

Figure 10.12 shows the results of the open-aperture z-scan measurement at 840 nm for MEH-PPV/PMMA composite and for pure PMMA. The dip in a normalized transmittance from MEH-PPV/PMMA suggests that MEH-PPV/PMMA exhibits two-photon absorption with a calculated value of $\beta=1.5\pm 0.2$ cm/GW. Multiphoton absorption from pure PMMA is not observed.

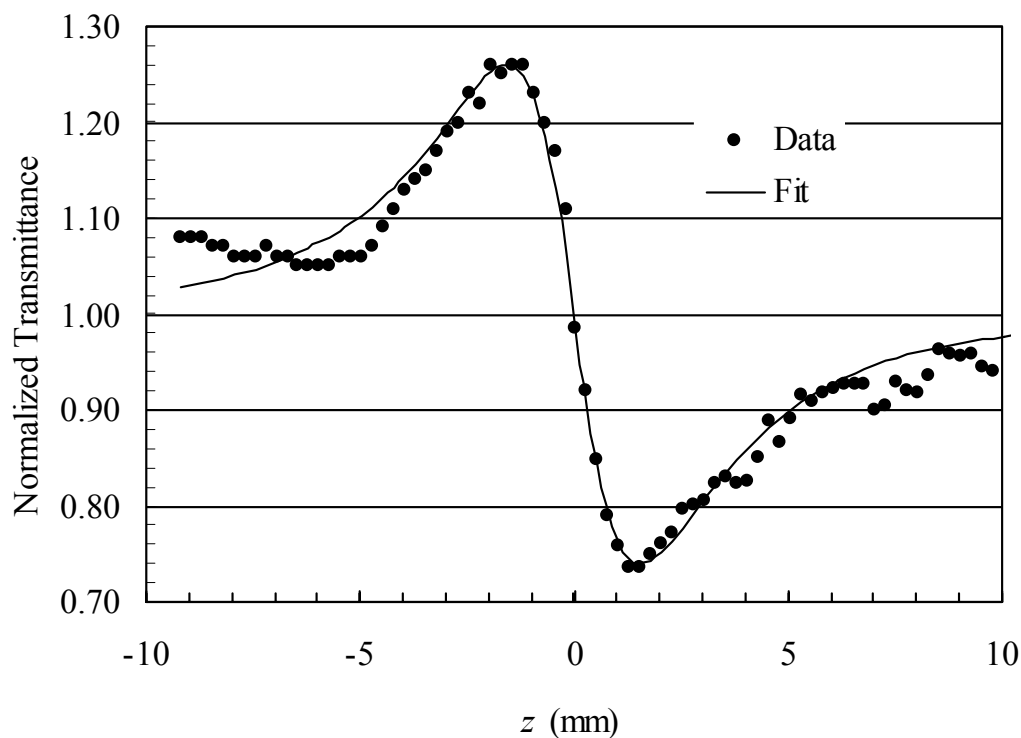


Figure 10.13: Normalized closed-aperture z -scan transmittance trace of MEH-PPV/PMMA composite. The solid line is a theoretical fitting.

The nonlinear refractive index n_2 was obtained from closed-aperture z -scan measurements shown in Figure 10.13. The value of the Kerr coefficient was calculated to be $n_2 = -2.1 \pm 0.2 \times 10^{-13} \text{ cm}^2/\text{W}$ with the maximum measured index change of $\Delta n = -9.02 \times 10^{-4}$ at intensity of $6.1 \text{ GW}/\text{cm}^2$. Together with the value of β and linear absorption measurements this indicates that the 0.2 MEH-PPV/PMMA composite has figures of merit $W = 1.7$ and $1/T = 0.83$ at 840 nm for 119 fs-wide pulses at the 5 kHz repetition rate used in this experiment.

10.2.3 Thermal Response of Organic Nonlinear Materials

While cumulative thermal nonlinearities are not at the focus of this work, the thermal nonlinearities of various compounds were also examined to determine their strength relative to the ultrafast nonlinearities. Results from the high-repetition rate z-scan measurements on the two solid state samples are described below.

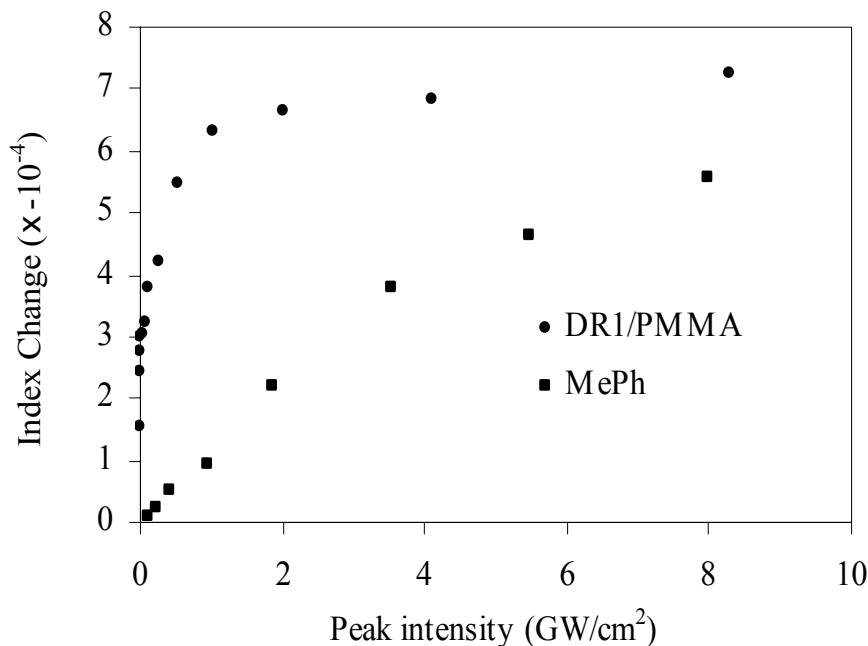


Figure 10.14: Thermal nonlinear index change of solid samples of DR1/PMMA and MePh as a function of intensity.

The two samples analyzed were: 2% DR1 attached to PMMA and metallorganic compound poly(methylphenylferrocenylsilane) (MePh). The measurements were taken with the Mira Ti:Saph oscillator at a repetition rate of 76 MHz at 840 nm. At this wavelength both materials are transparent. The solid state samples were fabricated using the press method by Chantal Paquet and were 1 mm thick. The results are summarized in Figure 10.14.

Both materials exhibited negative nonlinear index changes that saturate at $|\Delta n| <$

0.001 at intensities on the order of few GW/cm^2 . Thus, the thermal nonlinear index changes measured at high-repetition rates are comparable to the ultrafast nonlinear index changes measured at lower repetition rates. As the repetition rate was reduced to values below 10 kHz, no cumulative nonlinearities were measured.

In summary, section 10.2, using selected examples, has proven that non-resonant nonlinearities can provide index changes $|\Delta n| < 0.001$ with good figures of merit, when illuminated with light at pulse intensities of the order of $10 \text{ GW}/\text{cm}^2$.

10.3 Resonant Nonlinearities

Simultaneously with the measurements of the non-resonant nonlinear response experimental research was carried out on the incorporation of nonlinear materials into periodic structures. It was discovered that the fabrication of high-quality one- and three-dimensional samples with more than few 10s of layers would be more involved than anticipated initially. A relatively low number of layers, in turn, increases the magnitude of the required induced Δn that must be obtained in order for nonlinear grating response to become observable.

Additionally since this work deals with the dynamic observable movement and change of shape of the stopband, rather than with solitonic effects, new constraints arise on the material coefficients. In order for the change in the nonlinear stopband to be observable, the magnitude of Δn_{nl} has to be comparable to the magnitude of the built-in linear index difference. This again translates into a requirement of large nonlinear index changes.

Throughout this work, the search for nonlinear materials that could be successfully incorporated into periodic structures has moved away from small-index-change non-resonant response towards resonant nonlinearities where index changes on the order of $\Delta n > 0.1$ are achievable.

Results of measurements of resonant nonlinear refractive and absorptive index changes in two different sets of inorganic crystalline semiconductor MQWs and in strongly-confined PbS nanocrystals are reported in this section.

10.3.1 Bandedge Saturation of Absorption in GaAs/AlGaAs Multi-Quantum-Wells

As discussed in chapter 3 it has been previously predicted and in some cases demonstrated at isolated wavelengths in the vicinity of 800 nm and 1.5 μm , that bandedge nonlinearities in inorganic crystalline bulk and MQW semiconductors result in strong saturation of absorption and large nonlinear index changes. Thus, it was decided to measure the nonlinear index changes directly to fully assess the applicability of the semiconductor bandedge nonlinearities to optical switching. Nonlinear properties of two kinds of semiconductor MQWs ($\text{In}_{0.530}\text{Al}_{0.141}\text{Ga}_{0.329}\text{As}/\text{In}_{0.530}\text{Ga}_{0.470}\text{As}$ and $\text{GaAs}/\text{Al}_{0.28}\text{Ga}_{0.72}\text{As}$) were measured. Both sets of samples were grown by Anthony SpringThorpe and Marcius Extavour at Nortel Networks. In this subsection the measurements of the saturation of absorption in $\text{GaAs}/\text{Al}_{0.28}\text{Ga}_{0.72}\text{As}$ MQWs are reported over the wavelength range from 785 nm to 874 nm.

The samples analyzed here were grown using molecular beam epitaxy on a single-side polished Si-doped 3" GaAs 001 wafer. A high degree of crystalline perfection within the layers and uniform thickness of the layers within the sample were confirmed with a double-crystal x-ray diffraction measurement. The cross-section of the samples is shown in Figure 10.15.

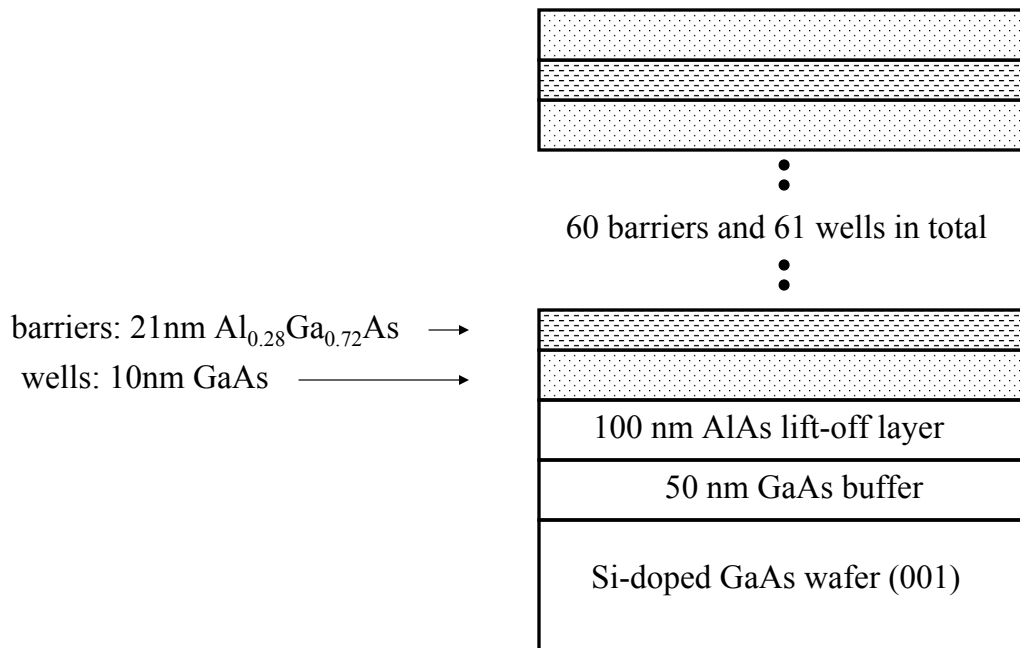


Figure 10.15: Cross-section of the GaAs/AlGaAs MQWs sample analyzed. Sixty-one 10 nm GaAs wells and sixty 21 nm $\text{Al}_{0.28}\text{Ga}_{0.72}\text{As}$ barriers were grown on on Si-doped 001 GaAs 3" substrate.

The samples were made out of sixty-one 10 nm GaAs wells and sixty 21 nm $\text{Al}_{0.28}\text{Ga}_{0.72}\text{As}$ barriers. The total thickness of the sample was $1.87 \mu\text{m}$. The structure was finished off with a GaAs well rather than with a $\text{Al}_{0.28}\text{Ga}_{0.72}\text{As}$ barrier in order to avoid the oxidation of aluminum. Figure 10.16 shows that photoluminescence spectra of the sample analyzed peaked at 850 nm.

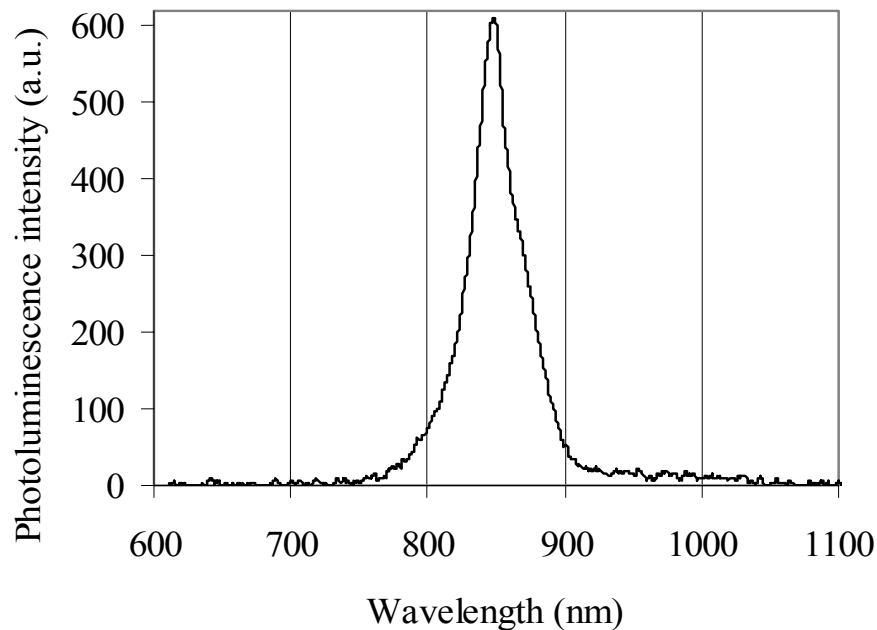


Figure 10.16: Photoluminescence intensity of the Al_{0.28}Ga_{0.72}As/GaAs MQWs sample.

The bandgap of the Al_{0.28}Ga_{0.72}As/GaAs MQWs samples analyzed is larger than the bandgap of the GaAs substrate on which the sample was grown. The sample had to be separated from the wafer to allow transmission measurements. A 100 nm AlAs lift-off layer was grown between the wafer and the sample. Because of its high aluminum content, the lift-off layer allowed selective etching.

Following growth, the sample was cleaved and ground on a SiC paper to about 120 μm total thickness. The sample was then bonded to the glass slide using clear wax with the MQWs side facing the slide. The bonded sample was immersed in a 4:1 citric acid/hydrogen peroxide solution at a room temperature. Citric acid was prepared in a 1:1 mass ratio with H₂O and citric acid powder (C₆H₈O₇+H₂O). The etch was complete when the back of the sample regained a near-specular finish and the sample became translucent. A typical etch took about 7 hours.

The linear absorption spectrum of the sample analyzed is shown in Figure 10.17.

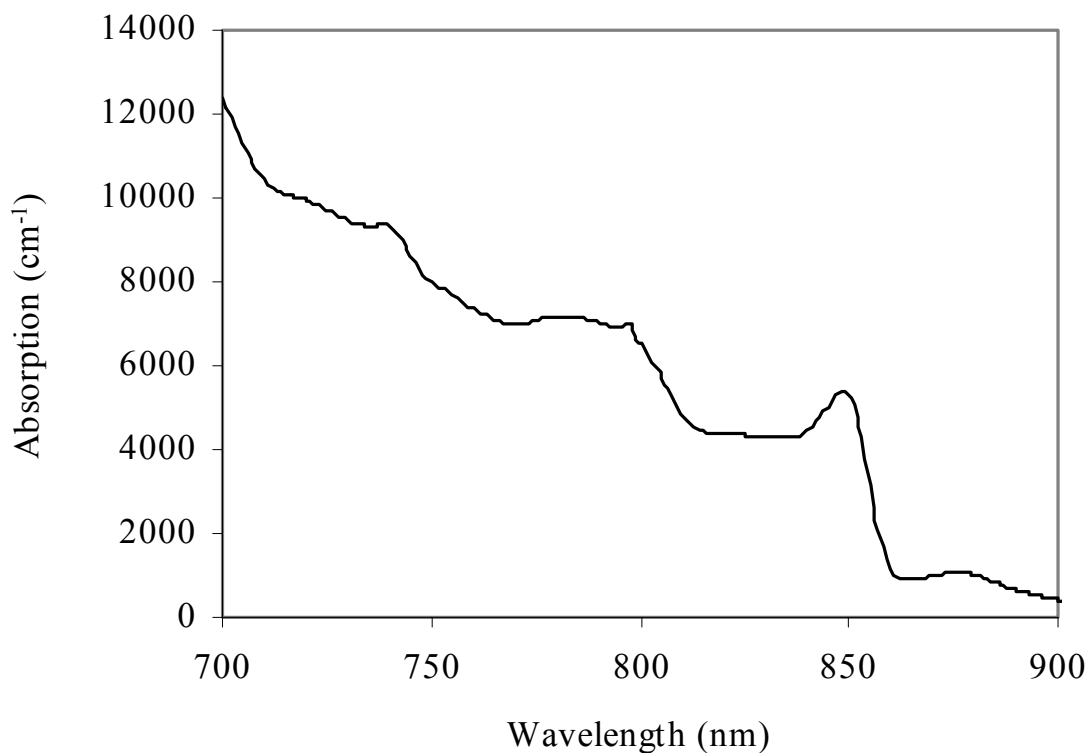


Figure 10.17: Absorption spectrum of the GaAs/Al_{0.28}Ga_{0.72}As MQWs sample.

Several excitonic steps are visible, with the first one around the photon wavelength of 850 nm being the most distinct. The nonlinear absorbing properties were measured in the spectral region around the first two excitonic peaks.

The nonlinear absorption measurements were made using the z-scan technique with the Mira Ti:Saph oscillator whose repetition rate was reduced to 5 kHz using the Pockels cell. In Figure 10.18 the results of the measurements are shown. The nonlinear absorption is shown as a function of fluence for wavelengths of 785, 800, 820, 844, 848, 855, and 874 nm.

At each wavelength analyzed, absorption decreases with increasing fluence, with most drastic changes taking place at the shortest wavelengths. At wavelengths of 844 and

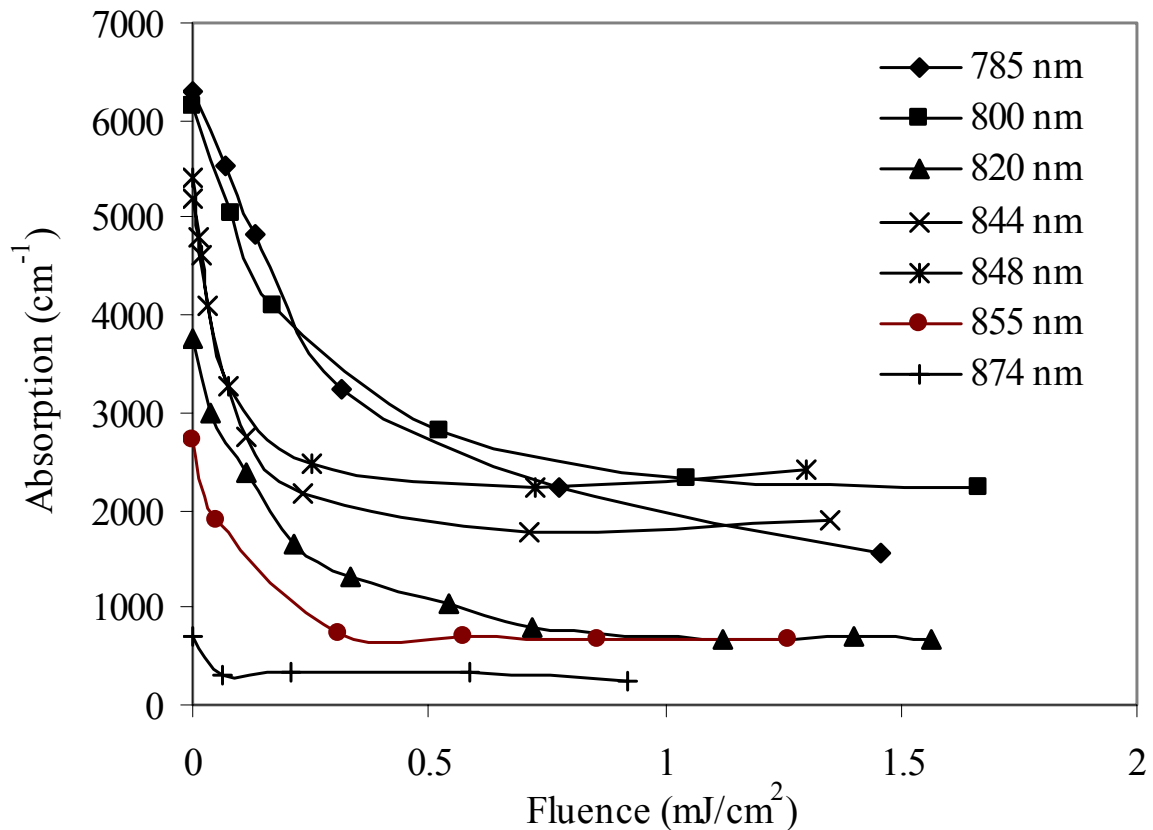


Figure 10.18: Change in the absorption in the bandedge region of GaAs/AlGaAs MQWs samples at wavelengths of 785, 800, 820, 844, 848, 855, and 874 nm.

848 nm, which are near the exciton peak, the threshold fluence for the onset of the saturation of the absorption is the lowest.

In Figure 10.19 the saturation fluences, defined here as the fluence above which no noticeable change in the transmission/absorption takes place, are shown. The saturation fluences decrease with increasing wavelength. The curve deviates from the general trend around the first excitonic peak. There the saturation fluences are larger than if they would be following the monotonic dependence on the wavelength observed at other wavelengths.

The results presented above have provided information about the saturation of absorption in a broad wavelength range around the first two excitonic peaks of semiconductor

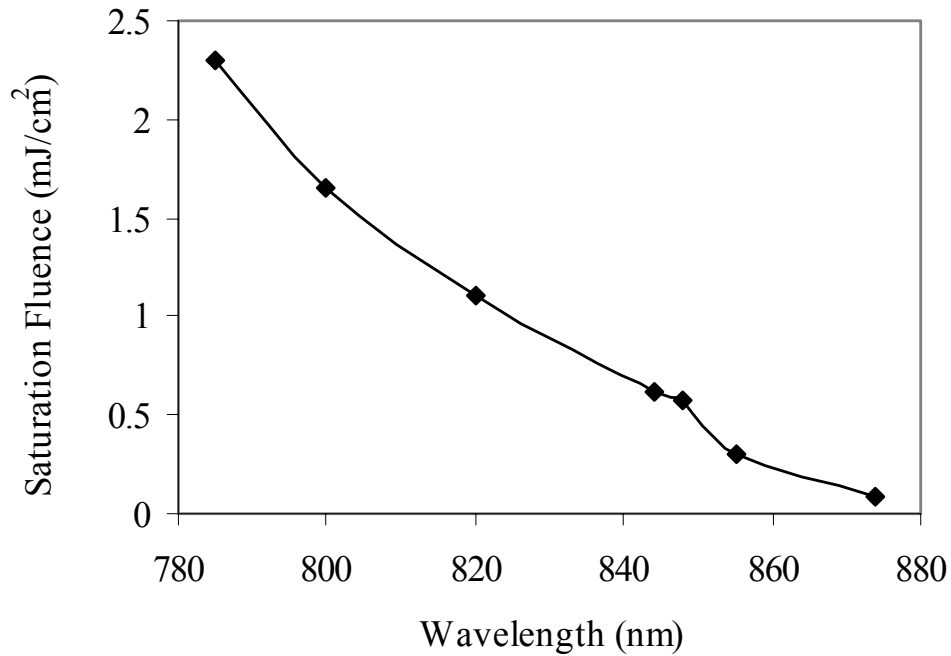


Figure 10.19: Saturation fluences of the GaAs/AlGaAs MQWs sample.

GaAs/AlGaAs MQWs analyzed. In addition, the measurements were taken using a single wavelength-tunable beam, rather than using a pump broadband-probe arrangement as in previous reports.

To determine the usefulness of the GaAs/AlGaAs samples analyzed for nonlinear switching using periodic structures it was also necessary to determine the real, refractive parts of the nonlinear response. However, the surface quality of the lifted-off sample was insufficient to allow meaningful interpretation and reproducibility of closed-aperture z-scan measurements. Thus, it was necessary to look for an alternative material system.

10.3.2 Resonant Nonlinear Properties of InGaAs/InAlGaAs Multi-Quantum-Wells

Following the measurement of saturation of absorption in AlGaAs/GaAs MQWs samples another semiconductor MQW sample was examined. This subsection describes the results of the characterization of refractive and absorptive nonlinear response of $\text{In}_{0.530}\text{Al}_{0.141}\text{Ga}_{0.329}\text{As}/\text{In}_{0.530}\text{Ga}_{0.470}\text{As}$ MQWs. This material offered two major advantages as compared to GaAs/AlGaAs samples analyzed in previous section: the spectral region where the sample was expected to display the desirable nonlinear response overlapped with the telecommunication region, and the sample did not require surface-damaging lift-off process.

No lift-off was necessary since the bandgap of the sample was smaller than the bandgap of the wafer. As such, the wafer was nonabsorbing in the bandgap region of the sample, and transmission measurements through the combined wafer-sample systems were feasible. Because the nonlinear response of sample is orders of magnitude stronger than that of the wafer, the interpretation of the results was not complicated by the presence of the wafer. All of the measurements were carried out at illumination levels at which the two-photon absorption of the wafer was negligible. This was validated experimentally.

Throughout the measurement of the nonlinear response of the InAlGaAs/InGaAs samples it was sought to determine how large nonlinear index changes can be obtained and what are the associated figures of merit.

The cross-section of the InAlGaAs/InGaAs sample analyzed is shown in Figure 10.20. Using molecular beam epitaxy, one hundred and twenty-one 10 nm $\text{In}_{0.530}\text{Al}_{0.141}\text{Ga}_{0.329}\text{As}$ barriers and one hundred and twenty 5 nm $\text{In}_{0.530}\text{Ga}_{0.47}\text{As}$ wells were grown on an S-doped (001) 400 μ thick InP 2" substrate, resulting in a total thickness of the nonlinear sample of 1.81 μm . Following the growth, the back side of the wafer was polished to allow transmittance measurements.

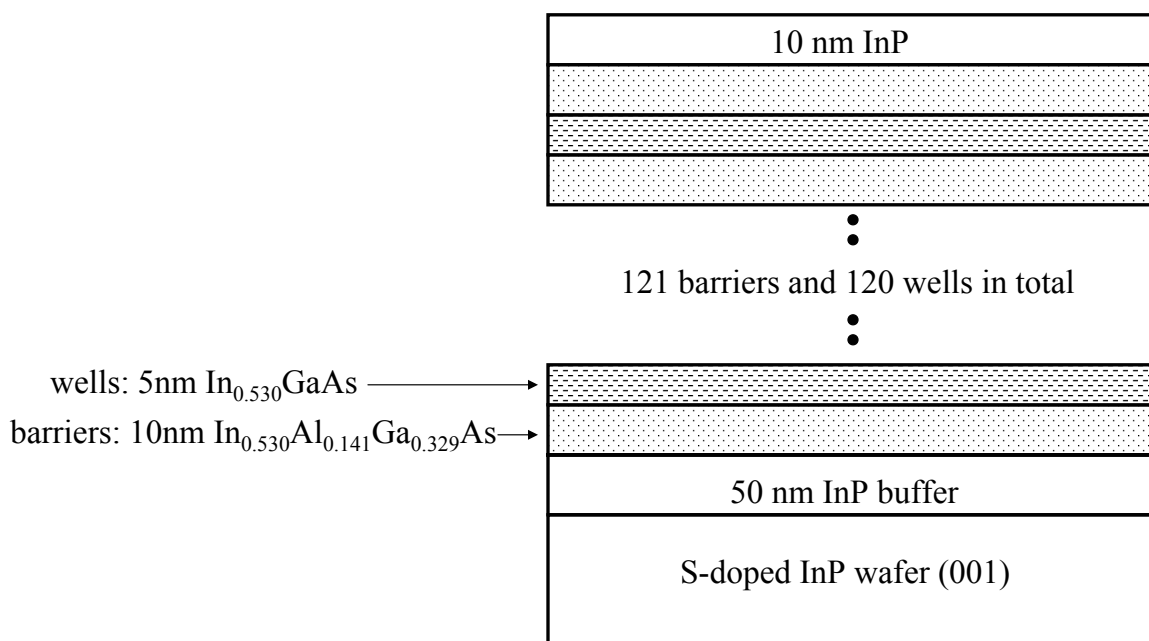


Figure 10.20: Cross-section of sample. One hundred and twenty-one 10 nm $\text{In}_{0.530}\text{Al}_{0.141}\text{Ga}_{0.329}\text{As}$ barriers and one hundred and twenty 5 nm $\text{In}_{0.530}\text{Ga}_{0.47}\text{As}$ wells were grown on on S-doped 001 InP " substrate.

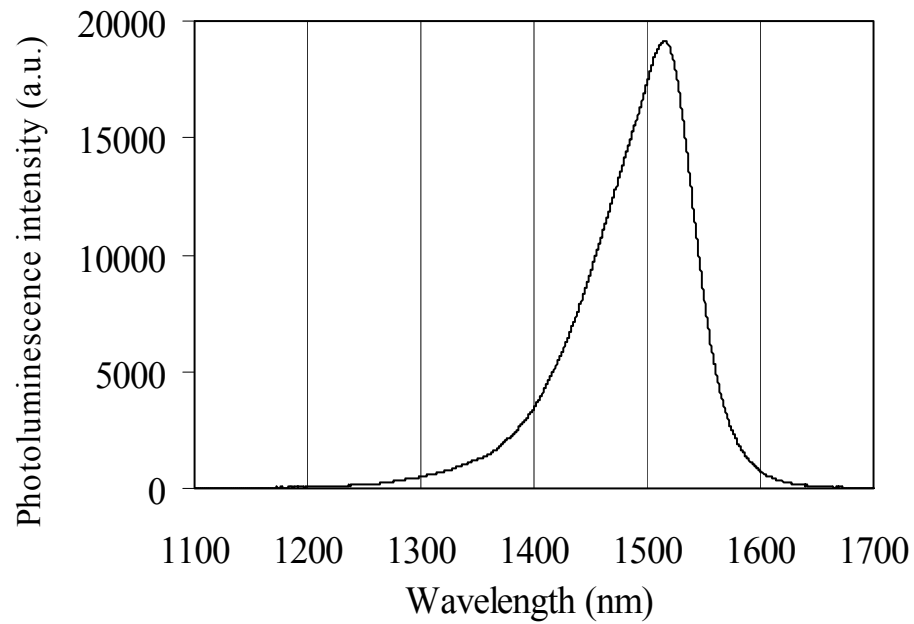


Figure 10.21: Photoluminescence spectra of the $\text{In}_{0.530}\text{Al}_{0.141}\text{Ga}_{0.329}\text{As}/\text{In}_{0.530}\text{Ga}_{0.47}\text{As}$ sample.

In the Figure 10.21 the photoluminescence spectrum of the sample with a peak at 1516 nm is shown. High sample quality and periodicity of the nanolayers were confirmed by the double crystal x-ray diffraction measurements.

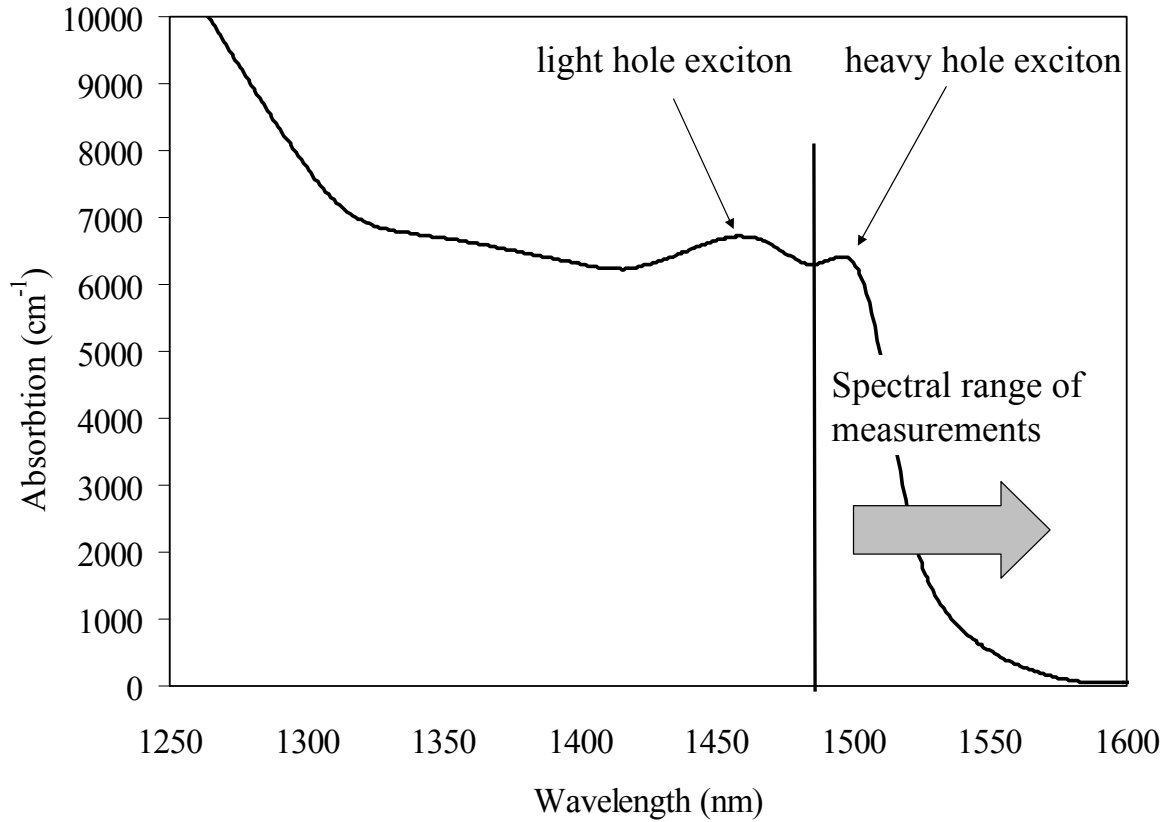


Figure 10.22: Linear absorption spectra of the $\text{In}_{0.530}\text{Al}_{0.141}\text{Ga}_{0.329}\text{As}/\text{In}_{0.530}\text{Ga}_{0.47}\text{As}$ sample.

The linear absorption spectrum of the sample analyzed is shown in Figure 10.22. Both the light hole exciton at 1453 nm and a heavy hole exciton at 1493 nm are clearly visible. The nonlinear measurements were carried out near the heavy hole exciton and bandedge spectral region 1480 to 1600 nm.

Figure 10.23 shows the saturation of absorption at a room temperature in the sample analyzed over the spectral range from 1480 to 1550 nm. The values of the nonlinear absorption were extracted from Z-scans carried out at fluences of $46 \mu\text{J}/\text{cm}^2$, $69 \mu\text{J}/\text{cm}^2$, $92 \mu\text{J}/\text{cm}^2$, and $116 \mu\text{J}/\text{cm}^2$.

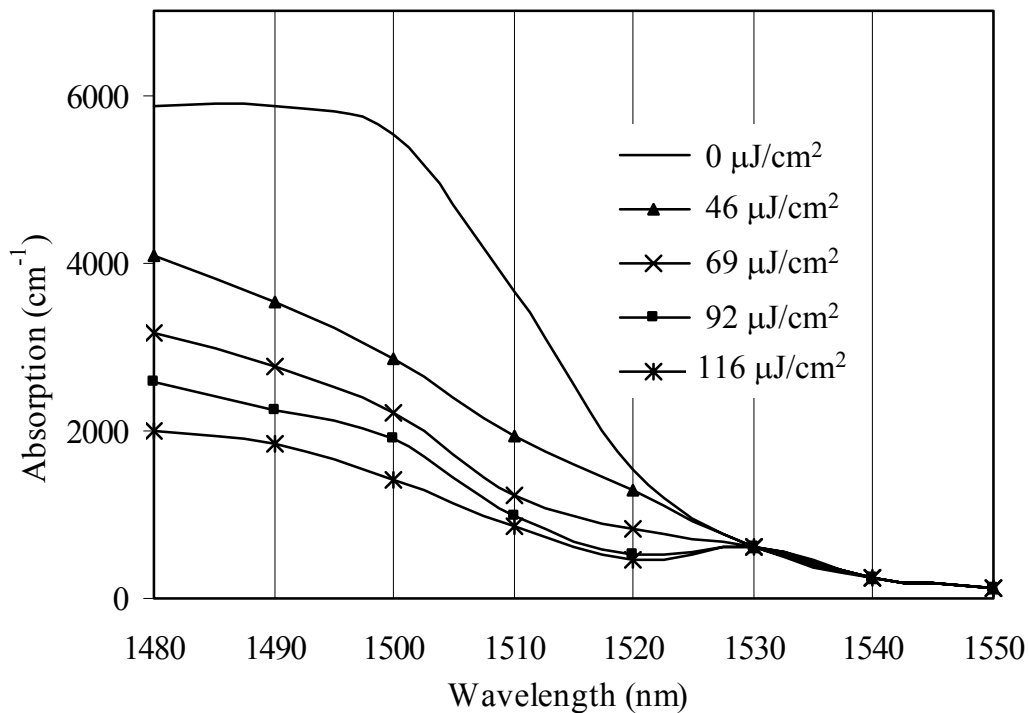


Figure 10.23: Saturation of absorption in $\text{In}_{0.530}\text{Al}_{0.141}\text{Ga}_{0.329}\text{As}/\text{In}_{0.530}\text{Ga}_{0.470}\text{As}$ MQWs at room temperature in the spectral range 1480–1550 nm at fluences of $46 \mu\text{J}/\text{cm}^2$, $69 \mu\text{J}/\text{cm}^2$, $92 \mu\text{J}/\text{cm}^2$, and $116 \mu\text{J}/\text{cm}^2$.

MQWs exhibit very strong absorption saturation in the vicinity of the bandedge caused by the bandfilling effect. The excitonic step around 1490 nm is washed out at higher fluences and the absorption decreases more than threefold throughout most of the spectral range studied.

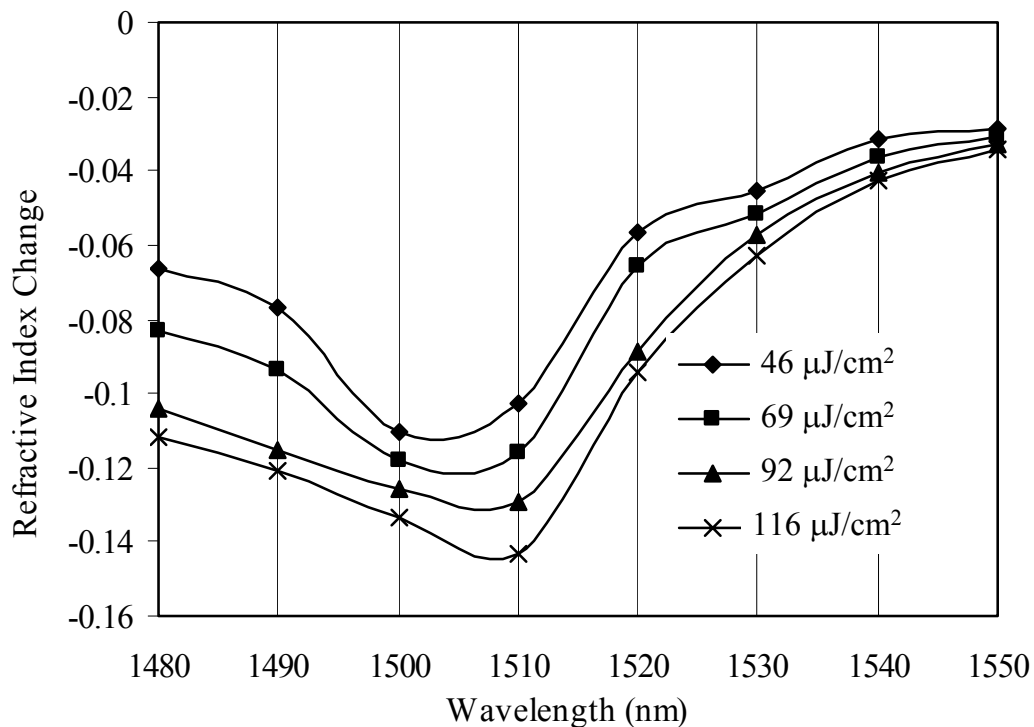


Figure 10.24: Nonlinear index change in the $\text{In}_{0.530}\text{Al}_{0.141}\text{Ga}_{0.329}\text{As}/\text{In}_{0.530}\text{Ga}_{0.470}\text{As}$ MQWs at the same experimental conditions as in Figure 10.23.

Figure 10.24 shows the nonlinear index change at the same fluences and wavelengths as in Figure 10.23.

Direct measurements reveal negative nonlinear index changes with magnitudes larger than 0.03 over the entire range studied. The largest value recorded is $|\Delta n|=0.14$ obtained at 1510 nm at a fluence of 116 mJ/cm^2 . As the signal wavelength was increased beyond the bandedge, the refractive index and absorption changes decreased.

Figure 10.25 shows the figures of merit calculated based on the results shown in Figures 10.23 and 10.24.

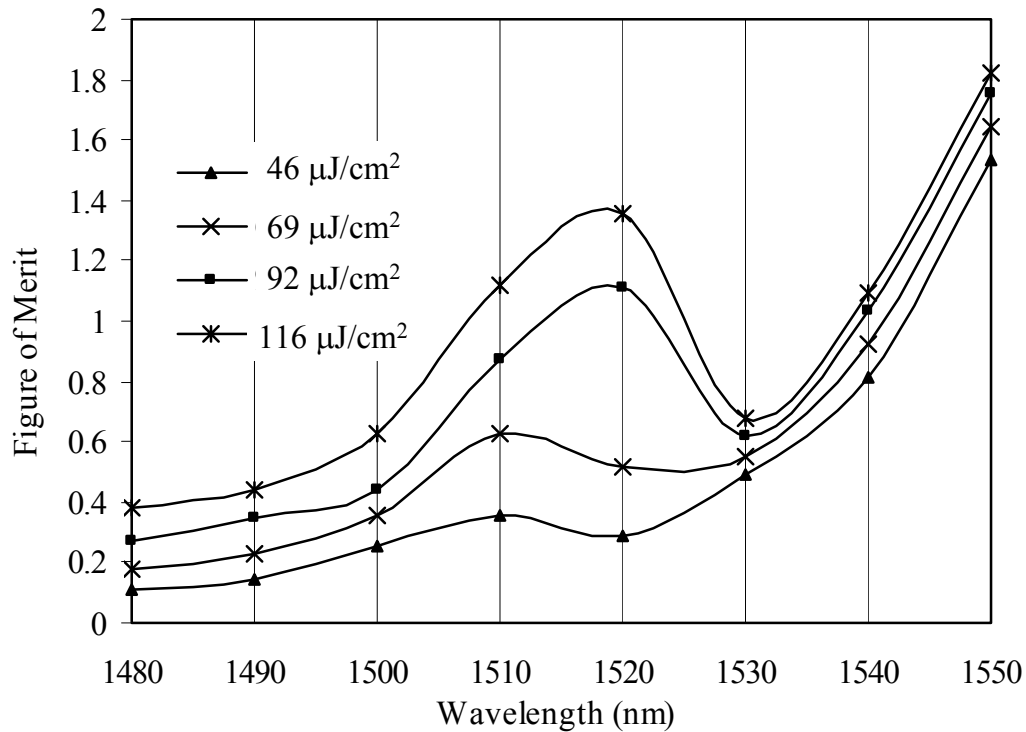


Figure 10.25: Figures of merit under the same experimental conditions as in Figures 10.23 and 10.24.

Band filling shifts the onset of absorption to higher energies. This shifts the real-valued dielectric constant dispersion curve to higher energies. In the region 1480 to 1500 nm, moderate saturation of absorption and Δn results in a comparatively poor F . Both the linear refractive index and the absorption peak locally near the excitonic feature (wavelengths 1500 nm - 1530 nm). A strong saturation of absorption in this spectral region results in a large nonlinear index change, giving large F . In the 1510 nm - 1520 nm region index changes well in excess of 0.1, with F in excess of 1 are measured. In the spectral region 1530 nm - 1550 nm, absorption is effectively washed out at increasing fluences. This combined with moderate Δn produced large F . At 1550 nm an index

change of 0.04 with a very good F was measured.

The figures of merit presented in Figure 10.25 have been calculated according to Eq. (5.7). As such, the figures of merit quantify the applicability of a given nonlinear material to nonlinear optical switching in terms of the total transmitted fluence. During the experiment the shape of the pulse would get distorted — the leading part of the pulse would saturate the absorption of the materials, increasing the transmittance of the trailing part of the pulse.

The strong saturation of absorption and large nonlinear index change reported in this section are comparable in magnitude to effects previously reported in Refs. [33, 156, 157] and predicted [30, 45, 112, 158–161] in other bulk and MQWs semiconductor materials. The nonlinear index changes predicted in continuous-wave experiment of Ref. [45] are calculated to be $\Delta n \leq -0.05$. The figures of merit as implied by the results in Ref. [45] are higher than in the sample analyzed here, since Ref. [45] reports full saturation of absorption. Measurements reported in Ref. [158] were taken at low intensity, when absorption was still high and nonlinear index change was low. The nonlinear figures of merit presented in this subsection cannot be directly compared with those estimated from the measurements in Refs. [30, 33, 156, 161]: the nonlinear pump-probe measurements and corresponding analysis based on the nonlinear Kramers-Kronig transformation predict how a strong beam at one wavelength influences weak signal at a different wavelength, but do not provide direct information how the strong signal would influence its own propagation.

The nonlinear response of samples analyzed in this section satisfies the requirements necessary to become one of the constituents of a nonlinear periodic structures: the figures of merit of large nonlinear index changes measured are satisfactory. The decay time of the nonlinearities was not measured but is expected to be on the order of several nanoseconds. It could be drastically decreased using doping techniques [31]. The semiconductor $\text{In}_{0.530}\text{Al}_{0.141}\text{Ga}_{0.329}\text{As}/\text{In}_{0.530}\text{Ga}_{0.470}\text{As}$ MQWs examined in this subsection

will constitute one of the components of nonlinear periodic structures whose response will be presented in the next chapter.

10.3.3 Resonant Nonlinear Response of PbS nanocrystals

In addition to studying the nonlinear resonant response of inorganic crystalline semiconductor MQWs, the resonant nonlinearities of another system — strongly-confined PbS nanocrystals — were characterized.

Semiconductor nanocrystals were identified as an interesting material system to study since, as discussed in chapter 3, they combine potentially strong nonlinear response and spectral tunability of linear and nonlinear properties with polymer-like processability. As such, they could be incorporated into multilayer structures or colloidal crystals.

Ultrafast Nonlinearities of Commonly Used Organic Solvents

Since the nonlinear response of PbS nanocrystals was studied in solution, the nonlinear properties of the solvents were first measured to permit correct interpretation of the measurements of the solutions in which PbS was suspended.

To date, only scarce data existed describing the nonlinear properties of organic solvents. The measurements reported were taken with nanosecond pulses at either the fundamental (1064 nm) or Raman converted (1910 nm) wavelengths of the Nd:YAG laser, or by using continuous-wave illumination at 633 nm [24, 162–165].

This subsection presents the results of direct measurement of the linear and nonlinear properties over a broad wavelength range from 1300 to 1580 nm of four commonly used organic solvents: toluene, THF, chloroform, and cyclohexane.

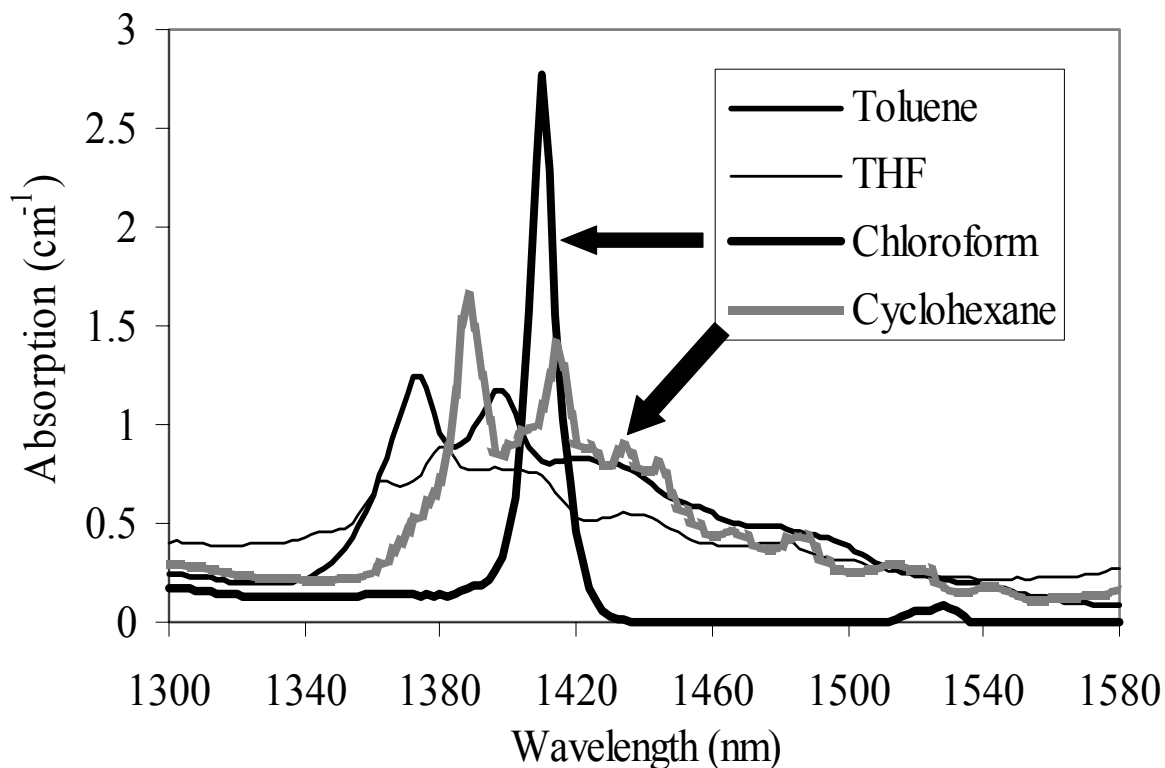


Figure 10.26: The linear absorption spectra of toluene, THF, chloroform, cyclohexane in the 1300 – 1580 nm spectral range.

Figure 10.26 shows the linear absorption spectra of the organic solvents analyzed in the wavelength range from 1300 nm to 1580 nm. The solvents exhibit absorption resonances due to vibrational overtones. THF, toluene, and cyclohexane have broad, complex absorption traces extending from about 1350 to 1500 nm. Over this spectral range the measured linear absorption exceeds 0.5 cm^{-1} . Chloroform has only one sharp absorption peak from 1390 nm to 1430 nm with a maximum absorption value of 2.8 cm^{-1} .

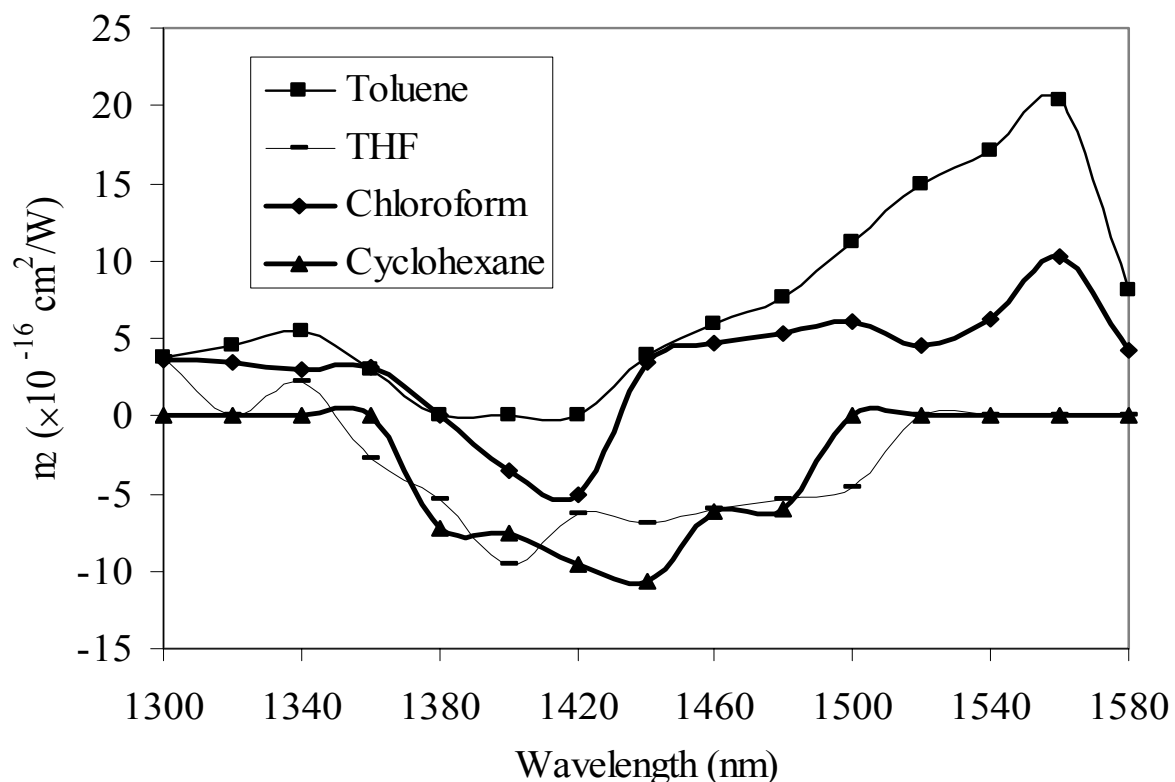


Figure 10.27: The third order nonlinear Kerr coefficients of the compounds of Figure 10.26. The measurements were taken using picosecond pulses with intensity of $75 \text{ GW}/\text{cm}^2$.

Figure 10.27 presents the nonlinear coefficients of toluene, THF, chloroform, and cyclohexane over the same wavelength range as in Figure 10.26. The measurements were taken using the z-scan method at the intensity of $I = 75 \text{ GW}/\text{cm}^2$ at a 1 kHz repetition rate.

The nonlinear Kerr coefficients of the solvents analyzed did not exceed $n_2 \leq 2 \times 10^{-15} \text{ cm}^2/\text{W}$, and for most of the spectrum analyzed were below $n_2 < 1 \times 10^{-15} \text{ cm}^2/\text{W}$. The Kerr coefficient of the toluene was always positive, while n_2 of cyclohexane was always negative. Chloroform and THF had shown n_2 of both signs at various wavelengths in the

spectral range studied. In general, toluene displays the strongest nonlinear properties while THF the weakest. Around the 1310 nm and 1550 nm telecommunication wavelengths THF and cyclohexane displayed the nonlinear n_2 coefficient below 1×10^{-16} cm^2/W .

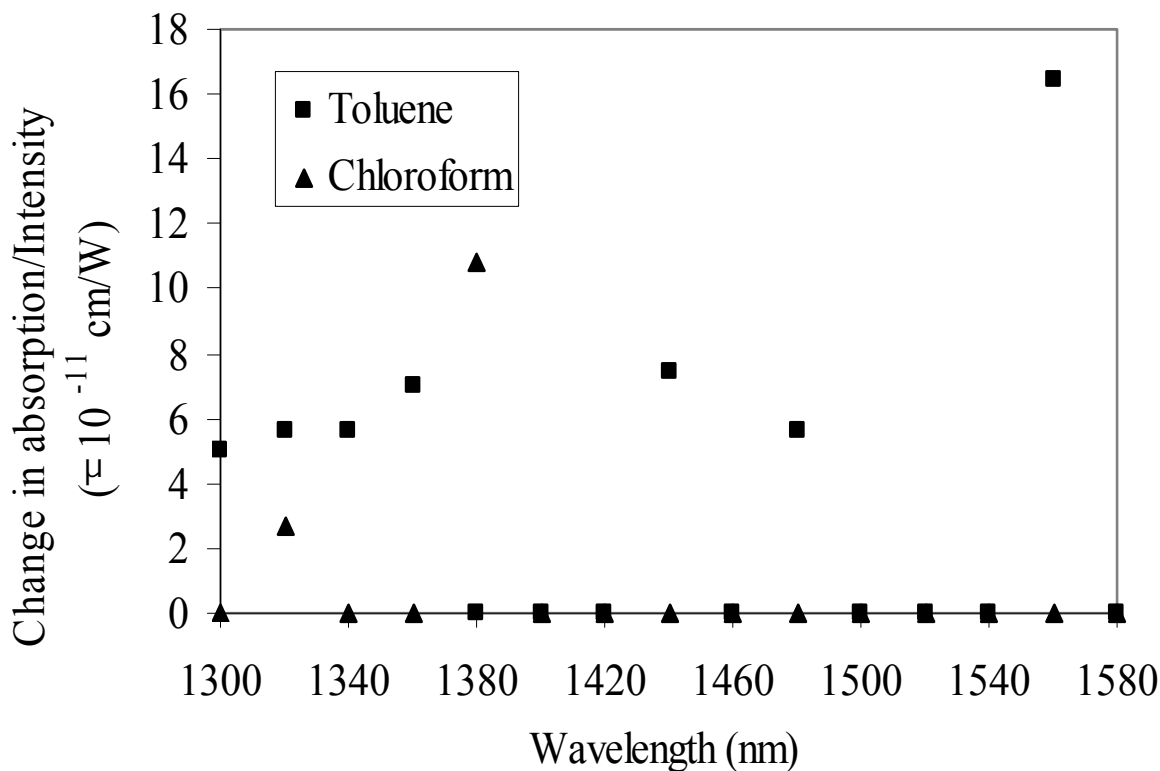


Figure 10.28: The nonlinear absorption coefficients under the same conditions as in Figure 10.28.

Figure 10.28 shows the results of the measurements of the nonlinear absorption of chloroform and toluene. The nonlinear absorption of chloroform was measurable only at wavelengths of 1320 nm and 1380 nm, with the values of $\Delta\alpha/I = 2.8 \times 10^{-11}$ cm/W and $\Delta\alpha/I = 11 \times 10^{-11}$ cm/W respectively. The nonlinear absorption of toluene was larger than 5×10^{-11} cm/W in the spectral range from 1300 nm to 1360 nm, and at

1440 nm and 1480 nm. At 1560 nm toluene exhibited the largest measured value of $\Delta\alpha/I = 16.8 \times 10^{-11}$ cm/W. THF and cyclohexane displayed nonlinear absorption below 1×10^{-11} cm/W.

Since the nonlinear response of the organic solvents studied was low, these were considered to be good candidates for use as solvents for nonlinear measurements of the solutions in which PbS nanocrystals were suspended.

Resonant Nonlinear Index Change, Saturation of Absorption, and Figures of Merit of PbS Quantum Dots

This subsection reports results of the direct picosecond measurements of the saturation of absorption and resonant nonlinear refractive index change in strongly-confined PbS nanocrystals solution in chloroform.

The nanocrystals studied were synthesized by Margaret Hines from the Chemistry Department, and by Larissa Levina from the Department of Electrical and Computer Engineering, both at the University of Toronto. The details of the synthesis are presented in Ref. [61]. The size of the quantum dots was tunable by variations in reaction parameters and growth conditions. Following the synthesis the solution in chloroform was prepared at a concentration of 22 mg/mL. The solution was placed in a 1 mm thick cuvette. The various samples of nanocrystals studied had mean diameters ranging between 4.8 ± 0.5 nm and 5.8 ± 0.5 nm. Since such dimensions are less than both the exciton radius in PbS of 20 nm, and electron and hole wavefunctions radii of 9 nm, the carriers in nanocrystals studied are strongly-confined.

Figure 10.29 shows the saturation of absorption in the nanocrystals with mean radii of 5.5 ± 0.5 nm. The measurements were taken at room temperature at three different fluences: 1 mJ/cm², 2 mJ/cm² and 3 mJ/cm².

The absorption of the sample analyzed shows a very distinct peak at 1390 nm corresponding to the first allowed electronic transition. With increasing fluence, the filling of

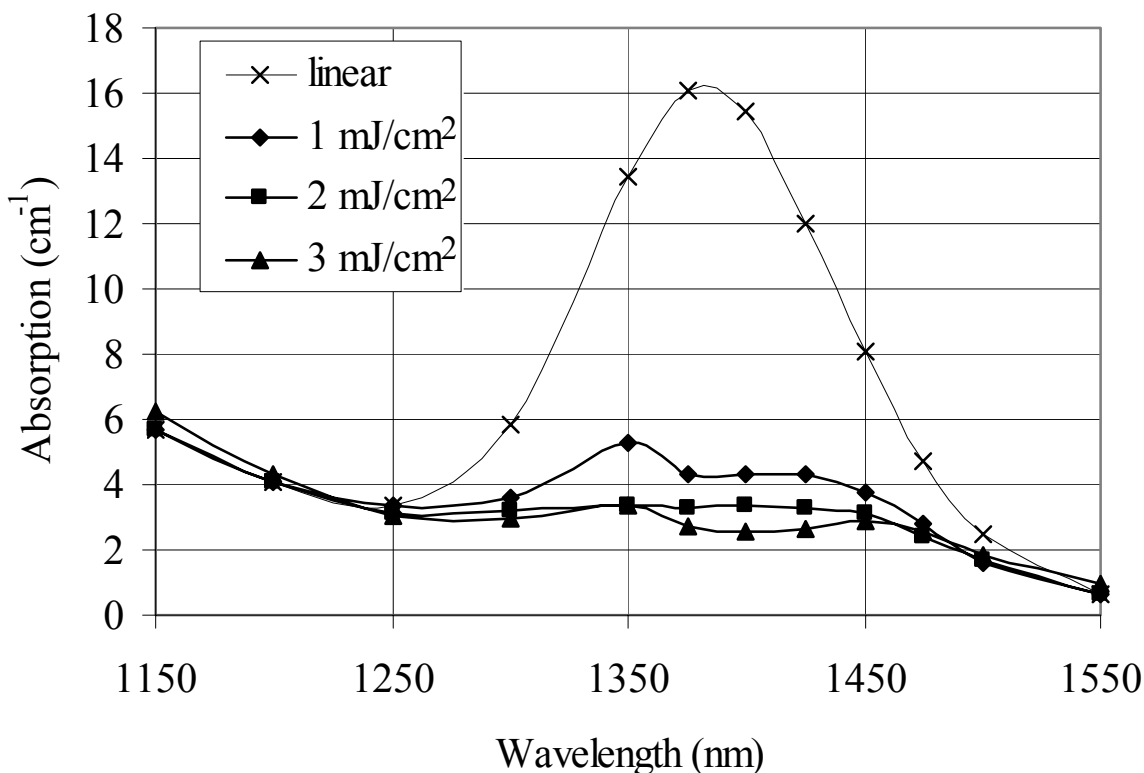


Figure 10.29: The saturation of absorption in the 5.5 ± 0.5 nm PbS nanocrystals in the wavelength range from 1150 to 1550 nm at fluences of 1 mJ/cm^2 , 2 mJ/cm^2 and 3 mJ/cm^2 .

states (quantum confined to the nanocrystals) washes out the absorption. The saturated absorption has a plateau with no residue of the excitonic peak. Compared to similar measurements performed on semiconductor multi-quantum-wells, the saturation of absorption in nanocrystals is more extreme (ratio of 5.5:1 between initial and saturated absorption) and takes place over a broader wavelength range [39, 142].

Figure 10.30 shows the nonlinear index change under the same conditions as in Figure 10.29. A strong negative nonlinear refractive response was observed in the vicinity of the absorption peak. It was attributed to the effects of saturation of absorption. As the

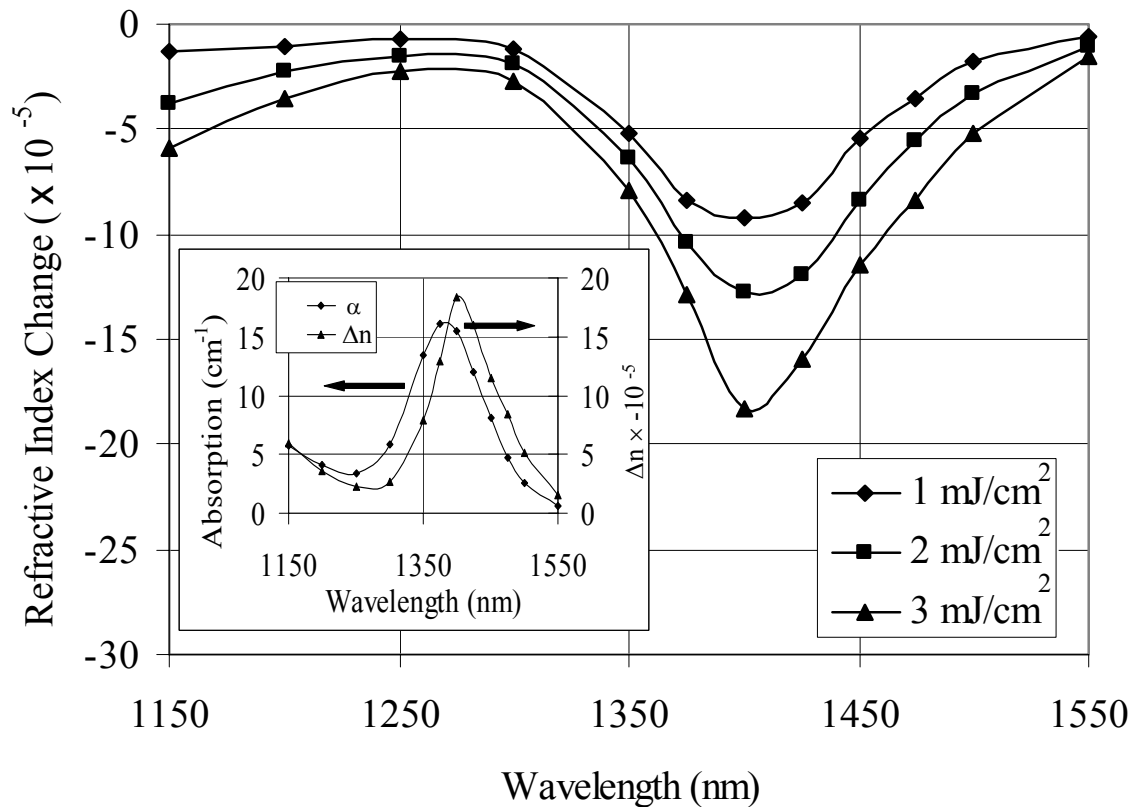


Figure 10.30: Nonlinear index change of PbS nanocrystals under the same conditions as in Figure 10.29. The inset compares the linear absorption spectrum with spectral position of the refractive index change measured at a fluence of 3 mJ/cm^2 .

laser wavelength was tuned towards 1550 nm or towards the valley around 1250 nm, the refractive index and absorption changes decreased. For wavelengths below the 1250 nm the increase in the absorption, saturation of absorption, and nonlinear Δn corresponding to the edge the second confined state were again recorded. The inset of Figure 10.30 compares the spectral positions of Δn measured at 3 mJ/cm^2 and the shape of the linear absorption. The shape of $|\Delta n|$ is very similar to that of the absorption, but is shifted towards longer wavelengths by about 10 nm.

Because of the low concentration of solution, the nonlinear refractive index changes

were all below $|\Delta n| < 2 \times 10^{-4}$. Using the approach presented in Refs. [166] and [167] the nonlinear index change within a given nanocrystal was estimated. The nonlinear index change of the nanocrystals, Δn_{NC} , is related to index change measured in solution, Δn , by $\Delta n = f_v f^4 \Delta n_{NC}$, where f_v is the volume fraction and f is the local field factor. The values were calculated to be $f = 0.64$ and $f_v = 2.9 \times 10^{-3}$ for the sample analyzed. The linear index of PbS was taken to be $n_{PbS} = 2.37$, the linear index of chloroform $n_{chloroform} = 1.446$, and mass density of PbS $\rho_{PbS} = 7.61 \text{ g/cm}^3$ [168]. For the sample analyzed, these values would give $\Delta n_{NC} \sim 0.4$ at 1400 nm. Since these calculations were made based on the refractive index of bulk PbS rather than that of quantum-confined nanocrystals, they should be treated only as an order of magnitude estimate. In addition, such record values for Δn are not realizable for macroscopic samples. They would require a concentration of nanocrystals approaching unity and the surrounding host with the same linear refractive index as the PbS. More realistically, a volume fraction of $f_v = 0.1$ would theoretically ensure that all nanocrystals are separated by at least one nanocrystal diameter from their nearest neighbors, and hence have noninteracting excitonic wavefunctions. Based on such more realistic estimated parameters, nonlinear index changes of 0.01 or more may be predicted.

The figures of merit, F , presented in Figure 10.31 were calculated from data presented in Figures 10.29 and 10.30. The best figures of merit, $0.2 < F < 0.3$, were recorded for wavelengths longer than the wavelength corresponding to the excitonic peak. In this range, strong saturation of absorption causes relatively large Δn . As shown in the inset of Figure 10.31, for wavelengths shorter than 1400 nm the dispersion in F traces shape of the absorption spectrum but is shifted towards the longer wavelengths.

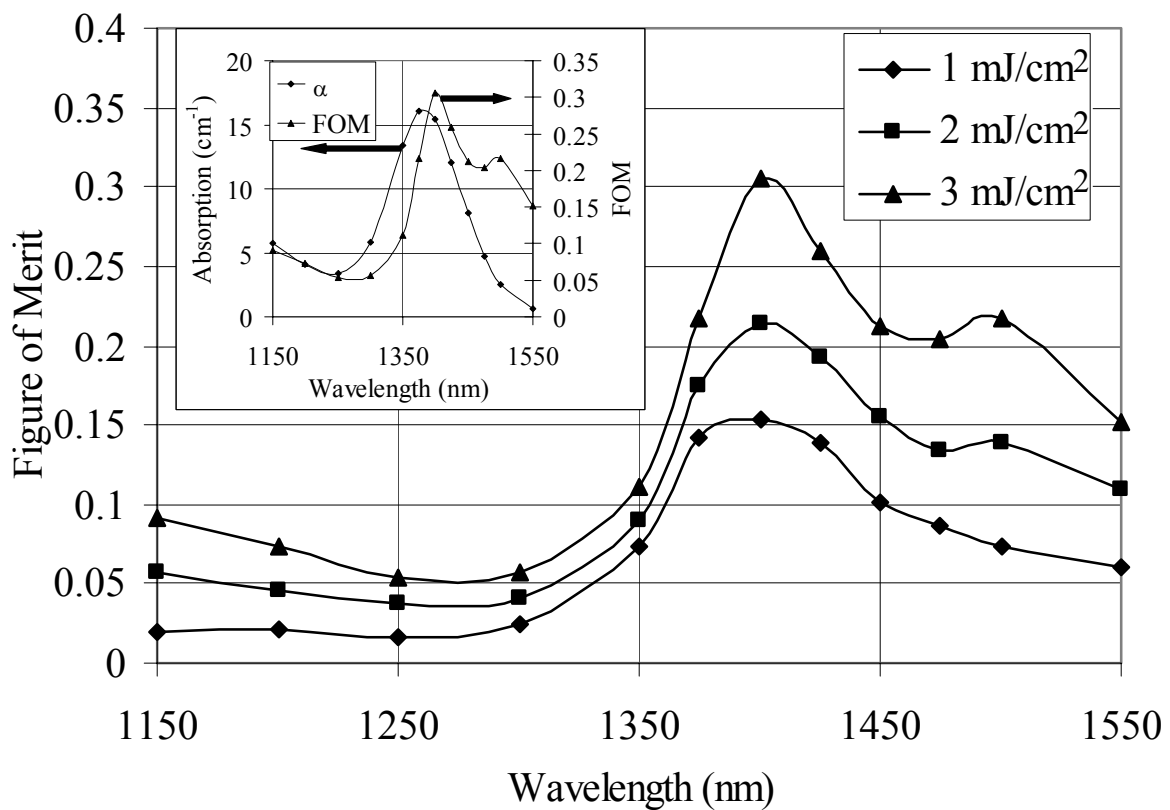


Figure 10.31: Nonlinear figures of merit (FOM) of PbS nanocrystals under the same conditions as in Figures 10.29 and 10.30. The inset displays the figures of merit recorded at a fluence of 3 mJ/cm² vs. the linear absorption spectrum.

Following nonlinear measurements of the 5.5 ± 0.5 nm PbS nanocrystals, a study of size dependence of the nonlinear properties was carried out. The results are presented and discussed below.

The nonlinear response of two additional PbS samples was compared with the response of the sample with the mean diameter of 5.5 ± 0.5 nm discussed above. These samples had mean diameters of 4.8 ± 0.5 nm and 5.8 ± 0.5 nm. A concentration of 22 mg/mL PbS in chloroform was used in all cases.

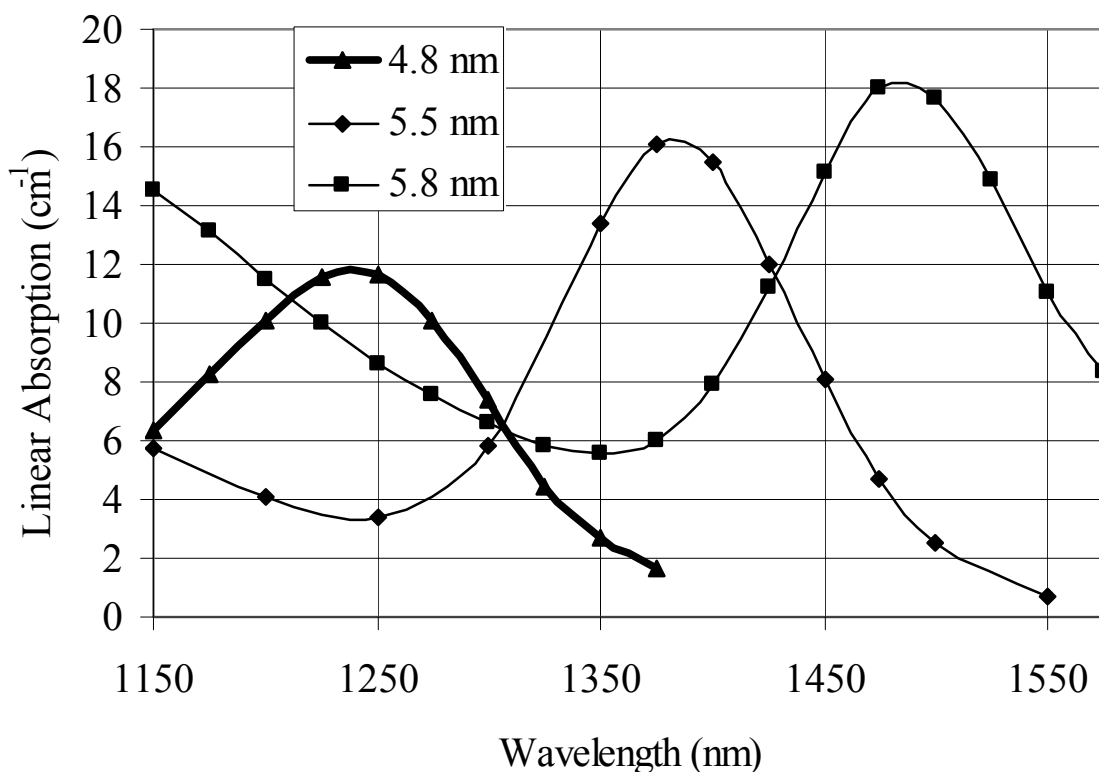


Figure 10.32: Linear absorption spectra of the 22 mg/mL PbS nanocrystals in chloroform solution for the samples with mean diameters of 4.8 ± 0.5 nm, 5.5 ± 0.5 nm, and 5.8 ± 0.5 nm.

Figure 10.32 compares the linear absorption spectra of the three samples. The exci-

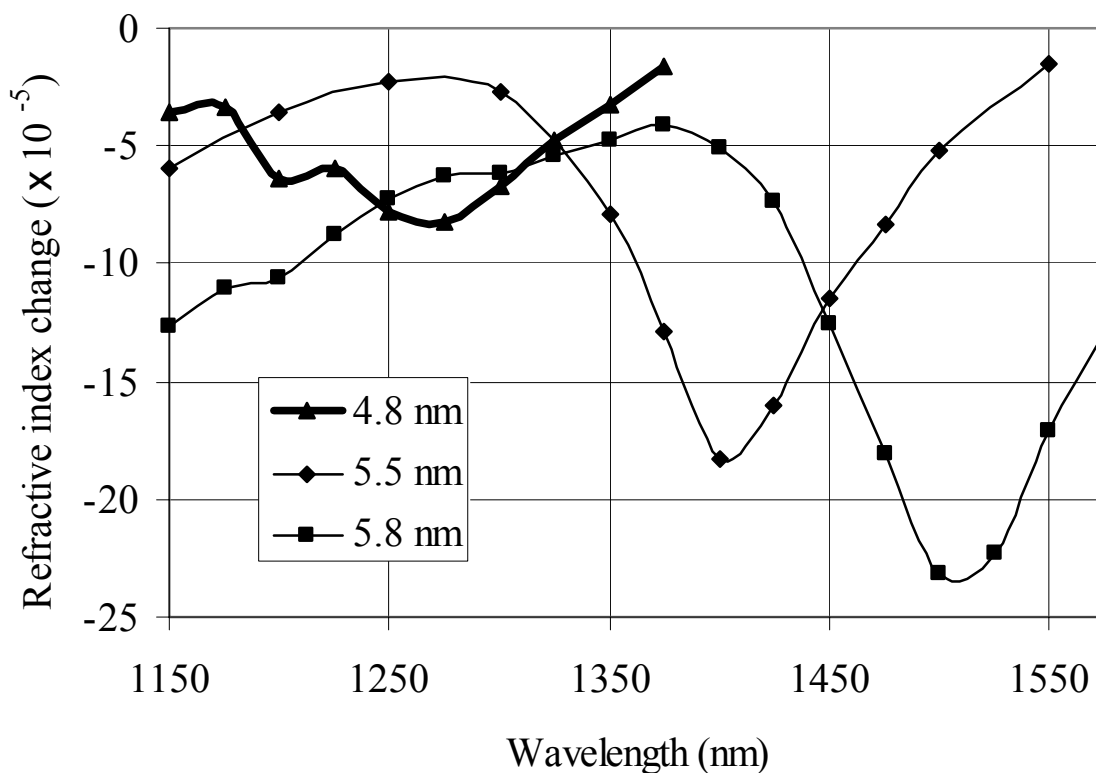


Figure 10.33: Nonlinear index change for the same samples as in Figure 10.32 as measured at a fluence of 3 mJ/cm^2 .

tonic peaks of the three samples are at 1235, 1380, and 1480 nm. The strength of the maximum absorption increases with the size of the nanocrystals. Similar widths of the absorption peaks in the three samples suggest comparable polydispersity.

The nonlinear refractive index change measured at a fluence of 3 mJ/cm^2 is shown in Figure 10.33. For all samples analyzed, the maximum nonlinear index change takes place at wavelengths about 25 nm longer than the wavelength corresponding to the absorption peak. The magnitude of the maximum nonlinear index change increases with increasing size of nanocrystals for the solutions in the same concentration: from -6×10^{-5} for the nanocrystals with $4.8 \pm 0.5 \text{ nm}$ mean diameter to -23×10^{-5} for the nanocrystals with

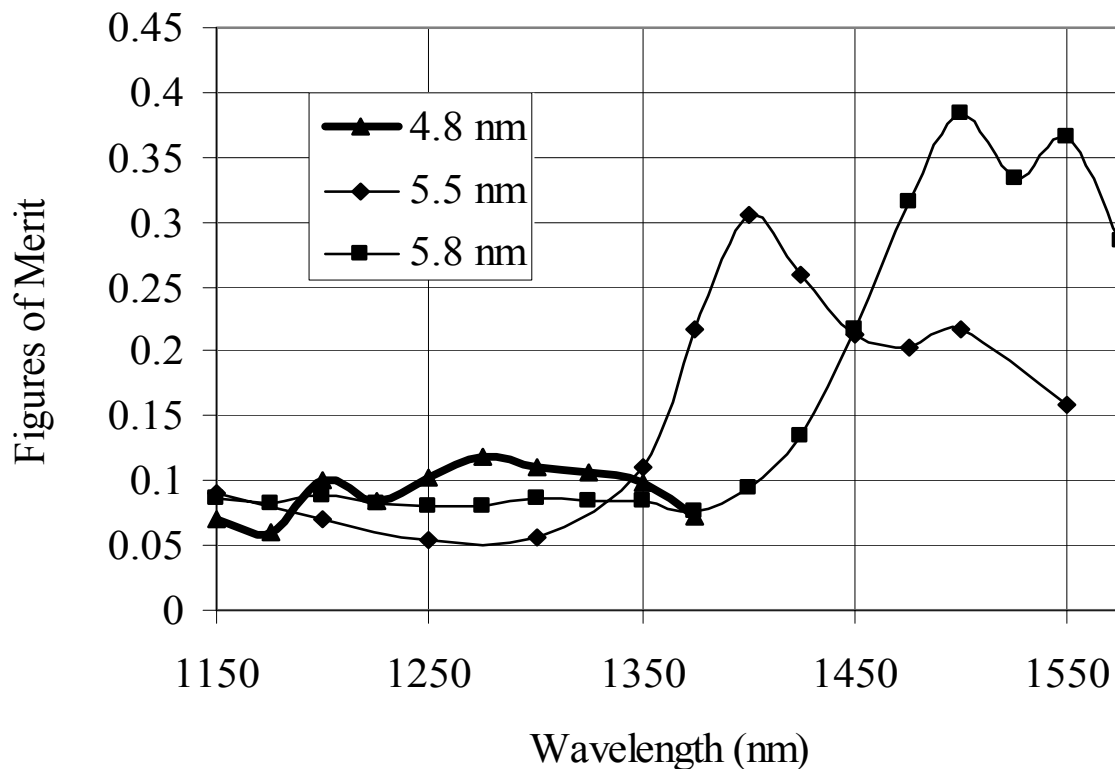


Figure 10.34: Nonlinear figures for merit of the three nanocrystal samples studied under the same conditions as in Figure 10.33.

5.8 ± 0.5 nm mean diameter.

Figure 10.34 compares the figures of merit for the three nanocrystal samples analyzed. A drastic decrease in the maximum figures of merit is observed with increasing size of the nanocrystals for samples illuminated using a fixed fluence. The figures of merit of the smallest nanocrystals analyzed do not exceed 0.13, while those of the 5.8 ± 0.5 nm mean diameter approach 0.4.

Thus, both the magnitude of nonlinear response of strongly-confined nanocrystals and the associated figures of merit were found to increase with increasing size of nanocrystals. The physical origins of the size dependence of nonlinear response are not currently

understood.

10.3.4 Resonant Nonlinear Response of DR1

Measurements of resonant nonlinear properties of the azobenzene dye Disperse Red 1 were not carried out in this work. However, based on the promising results published in one report [57] DR1 was singled out as the nonlinear dopant for the three-dimensional colloidal crystals whose nonlinear response is briefly described in the concluding chapter of this work. Hence, a brief description of the resonant nonlinear response of DR1 is necessary.

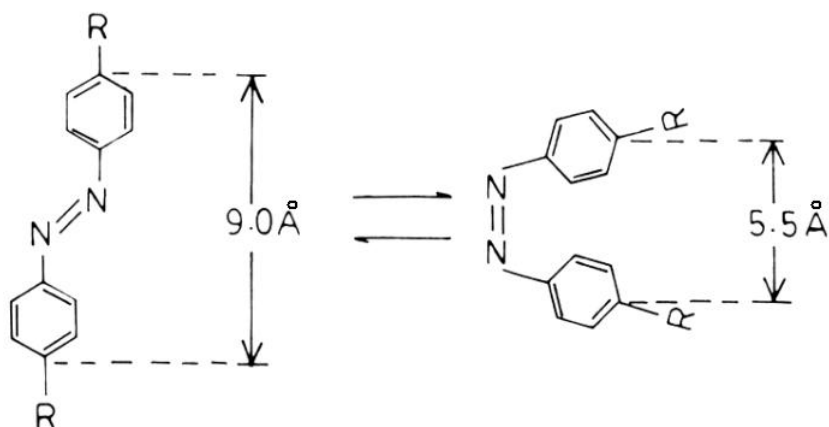


Figure 10.35: Trans-cis photoisomerization. Following resonant absorption, the azobenzene molecule changes its configuration, resulting in a decreased dipole moment.

Nonlinear index changes in excess of $|\Delta n| = 0.1$ in solid state samples of DR1 are obtained in the $\lambda < 590$ nm spectral region in which the photochemical process of trans-cis photoisomerization is triggered by absorption of photons. As illustrated in Figure 10.35, light near the main absorption resonance causes the azobenzene molecule to change from the *trans* to the *cis* configuration. During this process, the distance between the two carbons from which the acceptor and donor groups extend reduces from about 9.0 Å to 5.5 Å. This results in a drastic reduction in the molecule's dipole

moment, which reduces material's polarizability, providing a large negative nonlinearity with nonlinear index changes reaching $\Delta n_{max} = 0.12$ under an illumination with 20 ps pulses [57].

10.4 Conclusions

At the beginning of this thesis, the insufficient knowledge about efficient nonlinear materials was identified as one of the major obstacles on the road towards successful implementation of nonlinear periodic optical signal processing devices. This chapter strived to address this issue by reporting measurements of the refractive and absorption nonlinear properties of a variety of material systems.

It was demonstrated that while non-resonant nonlinear response can be characterized by good figures of merit, the achievable nonlinear refractive index changes are insufficient for the type of the devices proposed in the earlier chapters. Resonant response, on the other hand, can result in sufficiently large index changes, with the tradeoff of significant optical losses due to absorption. This was proven by reporting the results from the direct measurements of the bandedge nonlinearities of the inorganic crystalline semiconductor MQWs, and of the excitonic nonlinearities in strongly-confined PbS nanocrystals. These measurements were carried out over much broader spectral region than previously reported [42, 44, 45, 159]. In addition, in contrast to previously reported results the data presented in this chapter permits calculation of the figures of merit [33, 63, 64]

The InAlGaAs/InGaAs MQWs analyzed in this work have displayed very large nonlinear index changes, $\Delta n_{max} = 0.14$ with figures of merit exceeding unity. Based on the nonlinear measurements of the PbS nanocrystal solution it was predicted that at high concentration index changes on the order of few percent can be obtained. The resonant figures of merit of PbS nanocrystals did not exceed 0.38.

Among the materials analyzed in this chapter, InAlGaAs/InGaAs MQWs were singled

out as the most promising candidates for the fabrication of nonlinear periodic structures.

Chapter 11

Measurement of the Transfer Characteristics of Nonlinear Semiconductor Bragg Gratings

Throughout this thesis it was argued that optical signal processing functionality of nonlinear periodic structures should be increased by the introduction of new structural and material designs; the direct characterization of nonlinear materials that exhibit large nonlinear index changes accompanied by acceptable losses; and the fabrication of nonlinear periodic structures in configurations that enable increased functionality.

The preceding chapters of this thesis introduced elements and systems capable of performing complex signal processing functions and discussed characterization of various material systems. This chapter presents the concluding contributions of this work — it discusses the illumination-dependent response of nonlinear periodic structures operating at 1.5μ fabricated from the most promising materials analyzed in chapter 10.

The work presented in this chapter was published in Refs. [169] and [170].

11.1 Experiments

11.1.1 Devices

The optical elements investigated in this chapter were grown using molecular beam epitaxy by Anthony SpringThorpe and Marcius Extavour of Nortel Networks.

The devices considered in this chapter, labelled sample A, optical element B, and optical element C, are shown in Figures 11.1, 11.2, and 11.3. The structures were grown on S-doped (001) InP 2" single-side polished InP substrates. 10 nm protective InP layers were grown on top of all of the samples. Following growth, multilayer anti-reflection coatings were deposited on the front surfaces of B and C, and the back sides of A, B, and C were polished to allow transmittance measurements without scattering. High sample quality and periodicity of the superlattice layers were confirmed by double crystal x-ray diffraction measurements.

Sample A is made out of one hundred and twenty-one 10 nm $\text{In}_{0.530}\text{Al}_{0.141}\text{Ga}_{0.329}\text{As}$ barriers and one hundred and twenty 5 nm $\text{In}_{0.530}\text{Ga}_{0.47}\text{As}$ wells, resulting in a total thickness of the nonlinear sample of 1.81 μm . It is the same sample whose nonlinear response was discussed in section 10.3.2.

Optical elements B and C are both made out of two different sets of MQWs each. In this chapter a pair of adjacent MQWs sets will be referred to as one Bragg period.

It was sought to meet two criteria in designing B and C. The periodicity of B and C were chosen so that the constituent pairs of MQWs form a Bragg grating with spectral resonance in the vicinity of 1.5 μm in both optical elements. Moreover, in order to approximate matching of linear indices between the adjacent layers in the optical elements B and C the average compositions of MQWs type 1, type 2, and type 3 of which the layers made were chosen to be similar.

B is made out of MQWs type 1 and MQWs type 2 and consists of eight and a half Bragg periods. MQW type 1 consists of eight 10 nm $\text{In}_{0.530}\text{Al}_{0.141}\text{Ga}_{0.329}\text{As}$ barriers

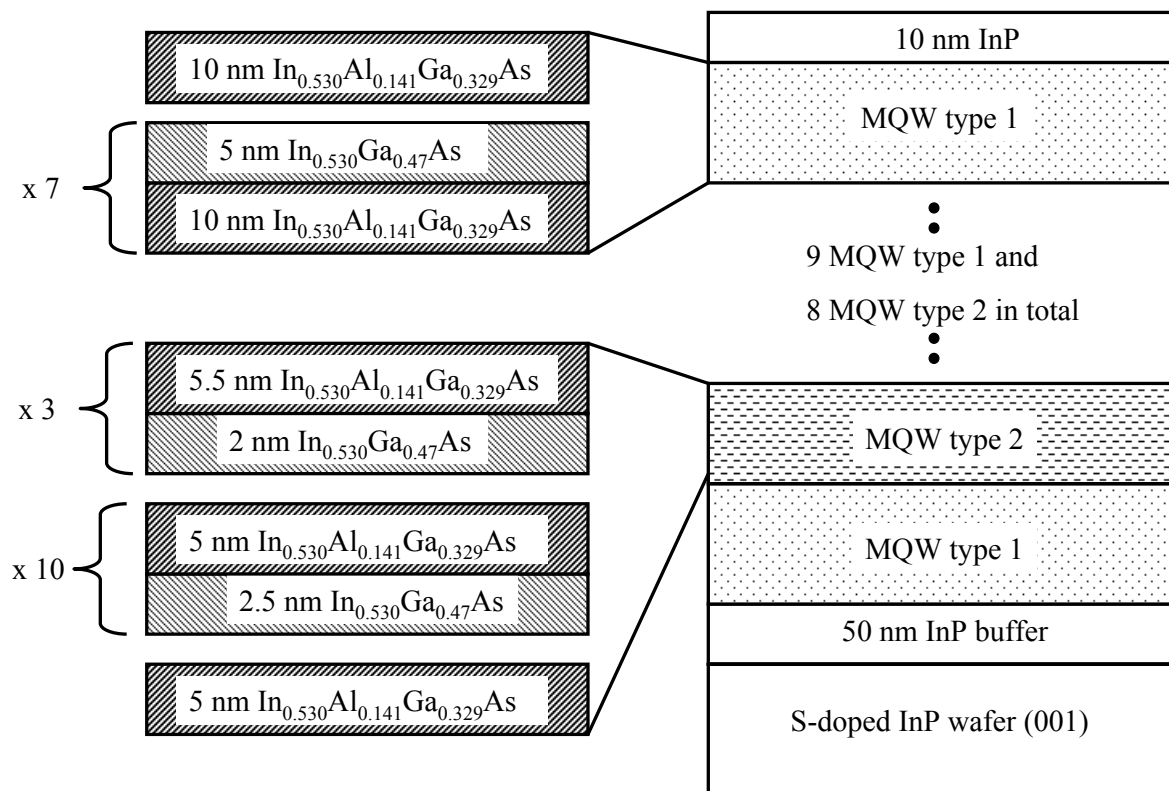


Figure 11.2: The cross-section of optical element B. B is made out of MQWs type 1 and MQWs type 2.

Samples B and C were designed with layers of similar average composition and Bragg periodicity so that they would contain hidden gratings. The reflectivity of these gratings should increase through illumination-dependent changes in the effective refractive indices of the constituent MQWs.

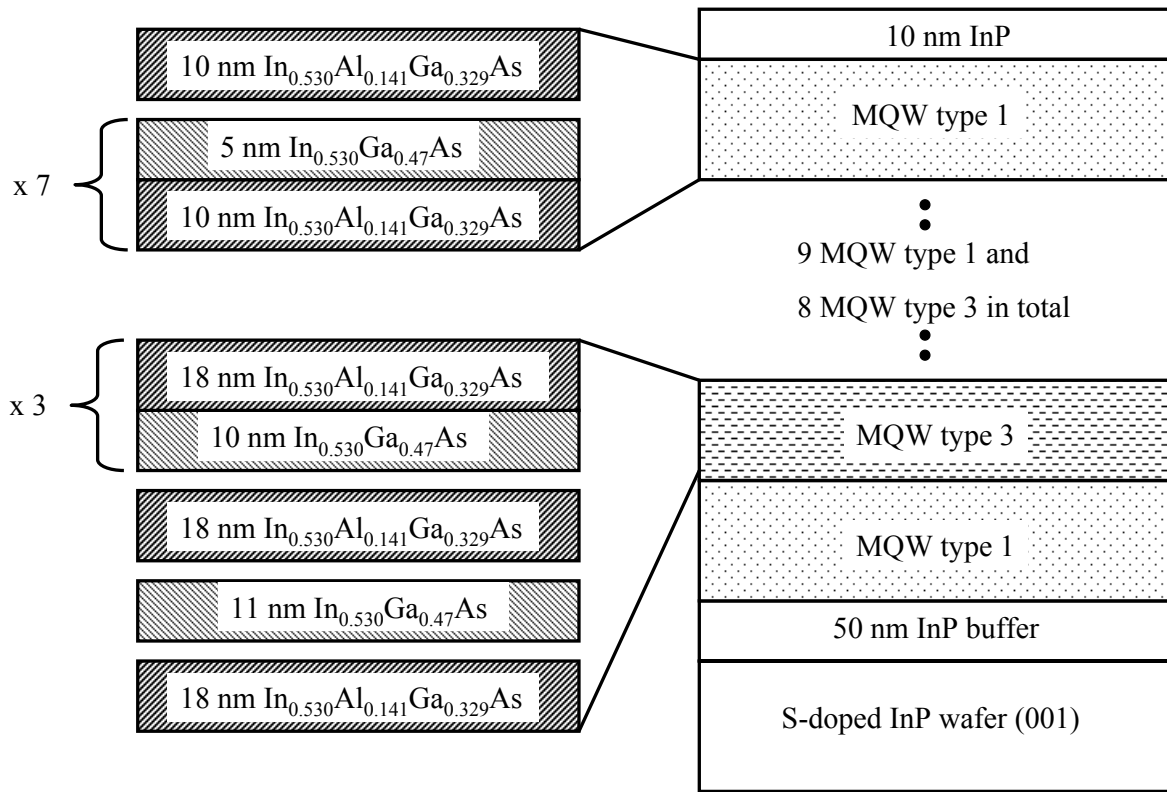


Figure 11.3: The cross-section of optical element C. C is made out of MQWs type 1 and MQWs type 3.

11.1.2 Linear Optical Properties

The PL and linear transmittance spectra of A, B, and C, are shown in Figures 11.4 and 11.5. As demonstrated in chapter 11, MQW semiconductor samples experience strong nonlinear response near PL peaks. Sample A has a PL peak and a strong excitonic feature in transmittance at 1517 nm corresponding to the first allowed optical transition in the constituent MQWs. In B there are two closely-spaced peaks, one at A's peak wavelength of 1517, and the other at 1493. The PL spectrum of C shows two PL peaks and excitonic steps in transmittance: the lower-wavelength feature at 1517 nm due to MQWs type 1 and the longer-wavelength feature at 1600 nm corresponding to the lowest transition of the second set of MQWs type 3.

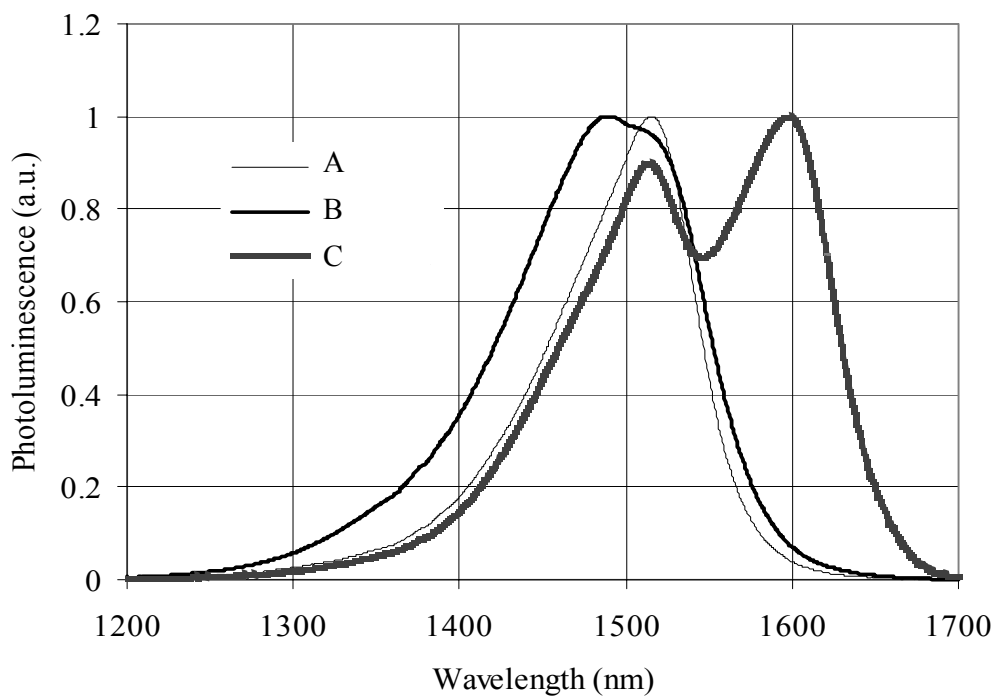


Figure 11.4: The photoluminescence spectra of semiconductor samples A, B, and C.

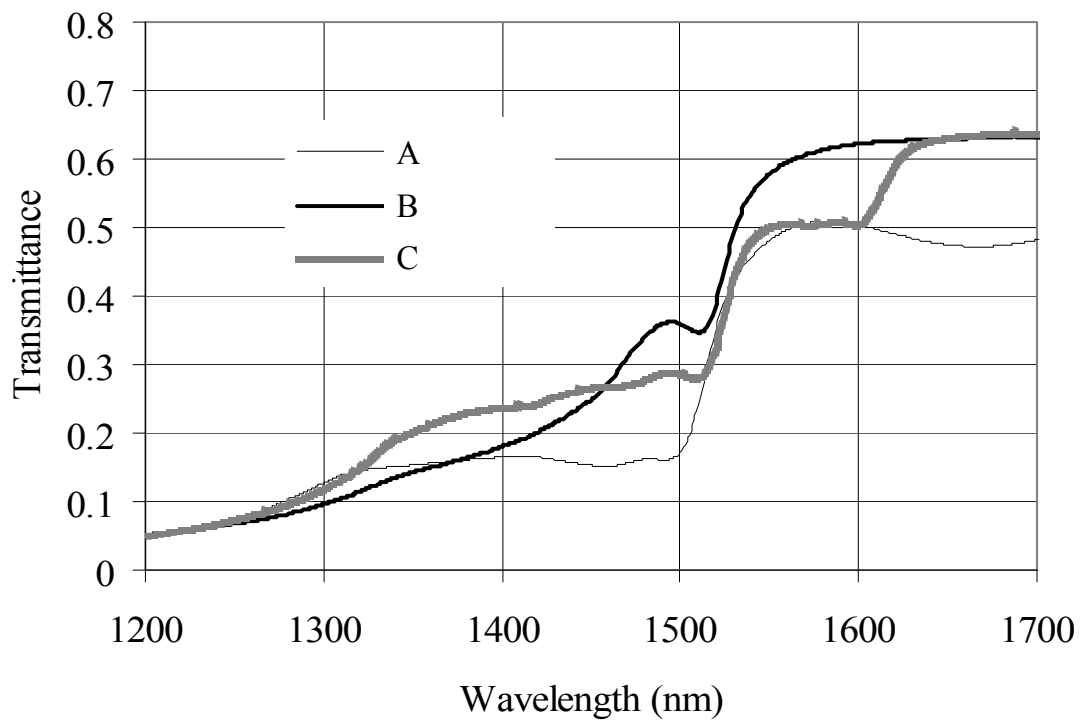


Figure 11.5: The linear transmittance spectra of semiconductor samples A, B, and C.

11.1.3 Experimental Apparatus

The experimental apparatus used in nonlinear reflectance and transmittance measurements is shown in Figure 11.6. The laser beam was focused using a lens with a 55 cm focal length onto samples placed perpendicular to the beam. The radius of the beam waist at the focus, measured at the $\frac{1}{e^2}$ of the transverse beam intensity profile, ranged from 91 μm at a wavelength of 1300 nm to 112 μm at 1600 nm. In order to monitor incident power, a portion of the incident beam was sampled using a wedged beamsplitter. This beamsplitter was also used to deflect a portion of the beam reflected from the sample. The power transmitted through the sample, as well as a fraction of the reflected power, were recorded as the incident power was varied. From this, the power-dependent transmittance and reflectance of each structure were obtained.

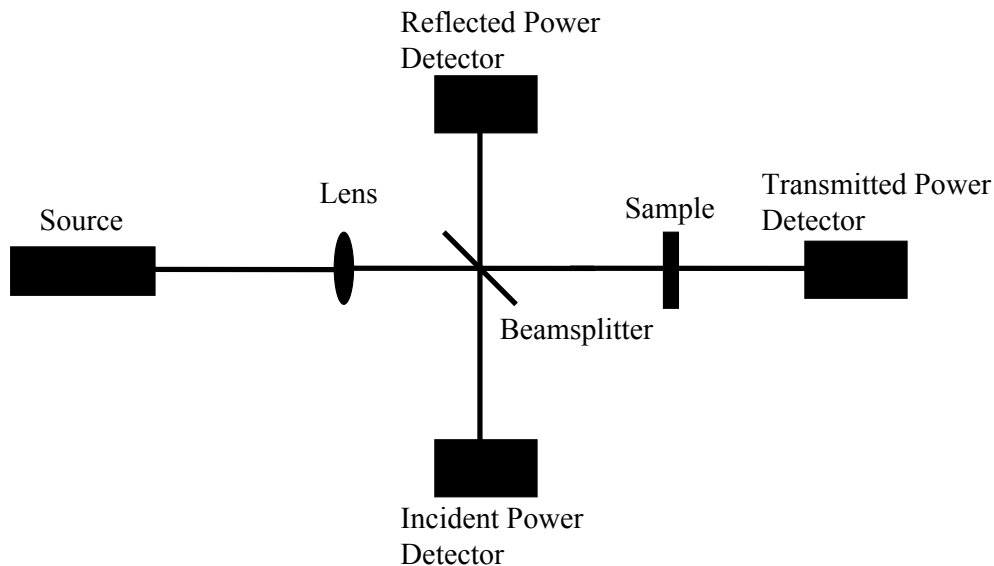


Figure 11.6: The experimental set up used in the nonlinear transmittance and reflectance measurement.

11.2 Results and Discussion

The nonlinear transmittance (T) and reflectance (R) of the three structures A, B, and C were measured in the wavelength range from 1300 nm to 1600 nm, at average incident powers ranging from 0.3 μW to 100 μW . This corresponds to pulse energies between 300 pJ and 100 nJ and fluences ranging 1 $\mu\text{J}/\text{cm}^2$ from to 320 $\mu\text{J}/\text{cm}^2$. The results are shown in Figures 11.7 – 11.14.

11.2.1 Nonlinear Response of Sample A

Figures 11.7 and 11.8 show the change in the transmittance (defined as $T - T_{initial}$) and reflectance (defined as $R - R_{initial}$) of sample A. The insets show the intensity-dependent evolution of T and R at two representative wavelengths 1420 nm and 1500 nm. At a given wavelength, as the incident fluence increases, the absorption of the sample saturates due to bandfilling. With decreasing absorption, T increases and the power reflected from the back side of the wafer rises, increasing the total R . The time required for the free carriers excited by the laser pulse to relax back to the valence band is at least a few hundreds of picoseconds, which is much longer than the roundtrip of the pulse in the sample of few ps. As a result the contribution to R from back reflection off of the wafer-air interface varies as T^2 . The shapes of the illumination-dependent transmittance and reflectance spectra of Figures 11.7 and 11.8 follow the same trends which suggests that the only contribution to the change in R is from the change in back reflection at the wafer-air interface. The change in total R from the nonlinear reflectivity changes of the sample-air and sample-wafer interfaces are negligible.

The largest changes in T and R of sample A are observed around the excitonic peak of MQW type 1 in the vicinity of 1.5 μm . Here the threshold for the saturation of absorption is the lowest. The number of unoccupied carrier states needed to be saturated increases with decreasing wavelength. As a consequence, the change in R and T is decreased for

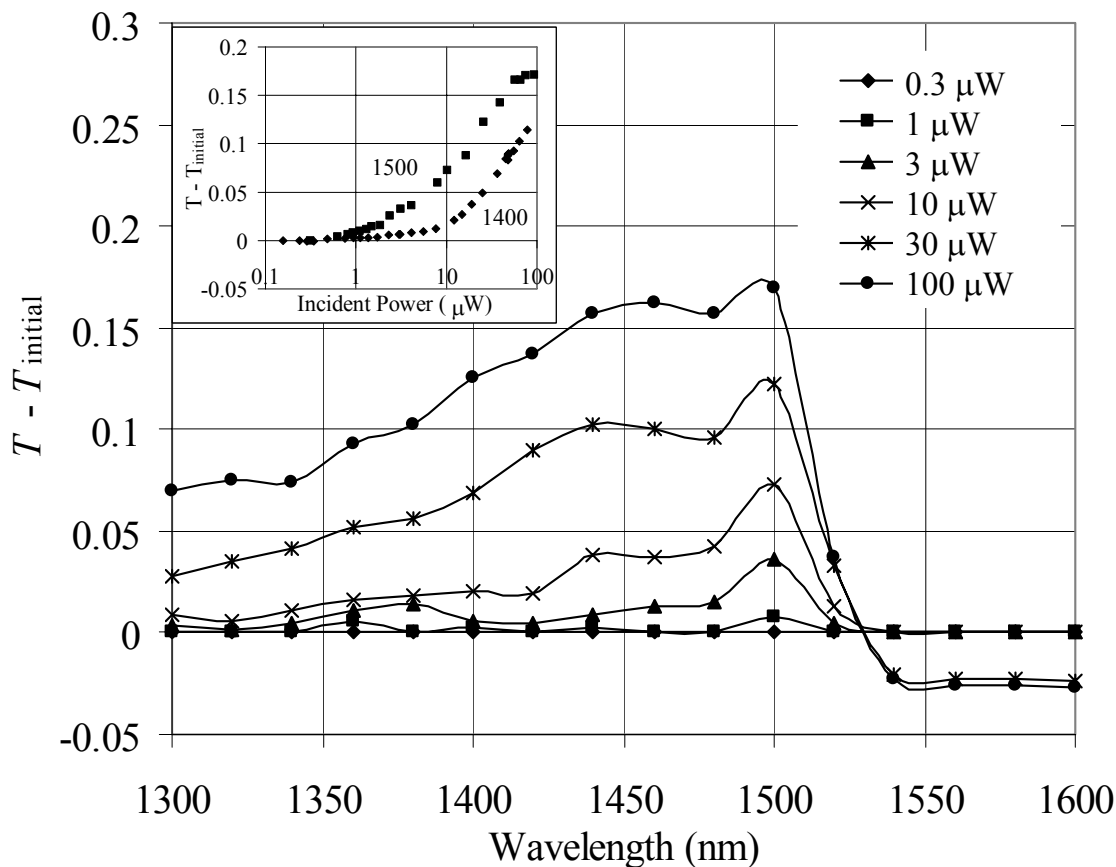


Figure 11.7: The change in the absolute transmittance of sample A in the spectral range 1300 nm to 1600 nm, at incident powers of $0.3 \mu\text{W}$, $1 \mu\text{W}$, $3 \mu\text{W}$, $10 \mu\text{W}$, $30 \mu\text{W}$, and $100 \mu\text{W}$.

a fixed incident power. For wavelengths longer than the wavelength corresponding to the bandgap ($\lambda > 1520 \text{ nm}$) there is a small negative change in T and R due to two photon absorption in the InP substrate. As has been verified experimentally, two photon absorption is a much weaker nonlinear effect than saturation of resonant absorption in sample A and under the conditions reported: it requires a higher *fluence* \times *length* product to be observed. Near 1525 nm the effect of saturation of absorption in sample A and two photon absorption in the substrate cancel each other almost exactly. As a result the change in both T and R of sample A is negligible at this

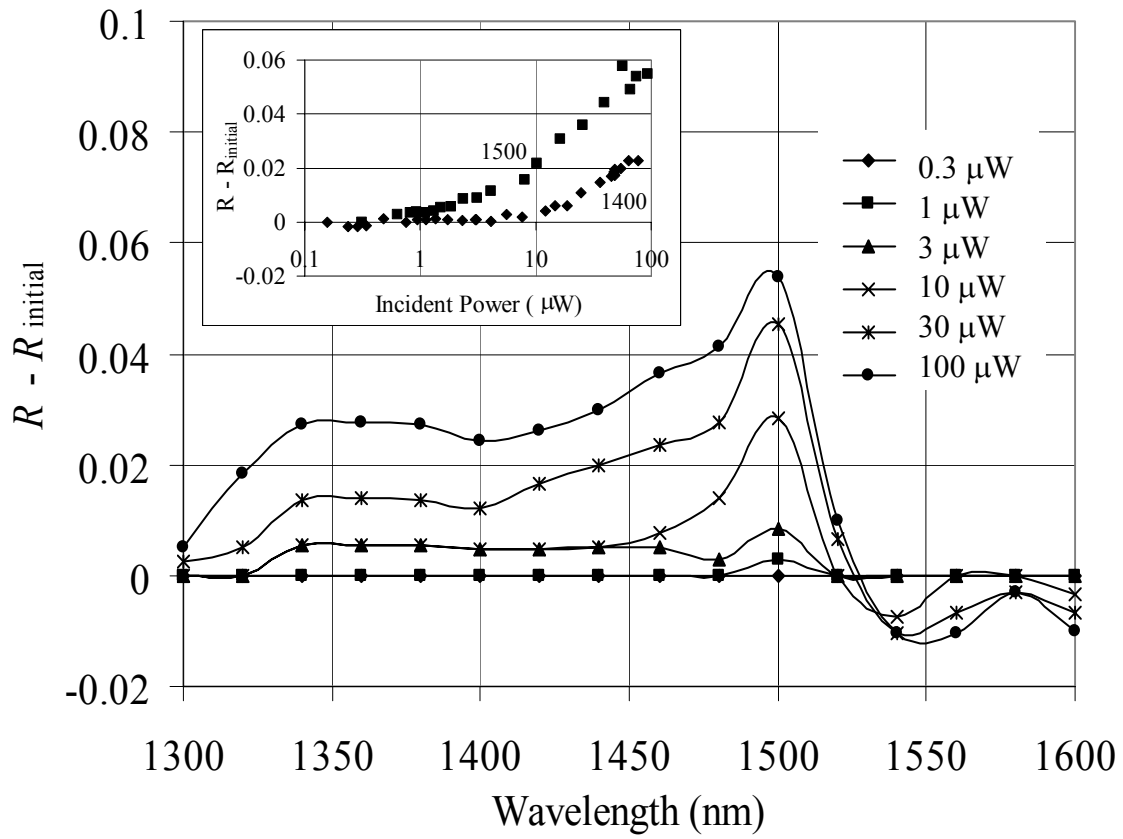


Figure 11.8: The change in absolute reflectance of sample A under the same conditions as in 11.7.

wavelength.

11.2.2 Nonlinear Response of Optical Element B

The nonlinear reflectance and transmittance spectra of optical element B are shown in Figures 11.9 and 11.10. The nonlinear response of B in the absorbing region ($\lambda < 1540$ nm) is similar to that of sample A: T and R increase with increasing incident power. Thus, the major nonlinear effect in B is again saturation of absorption. However, at some spectral ranges the corresponding $R - R_{initial}$ and $T - T_{initial}$ curves do not resemble each other as closely as in sample A. In fact, at some wavelengths the responses of R and T show opposite trends.

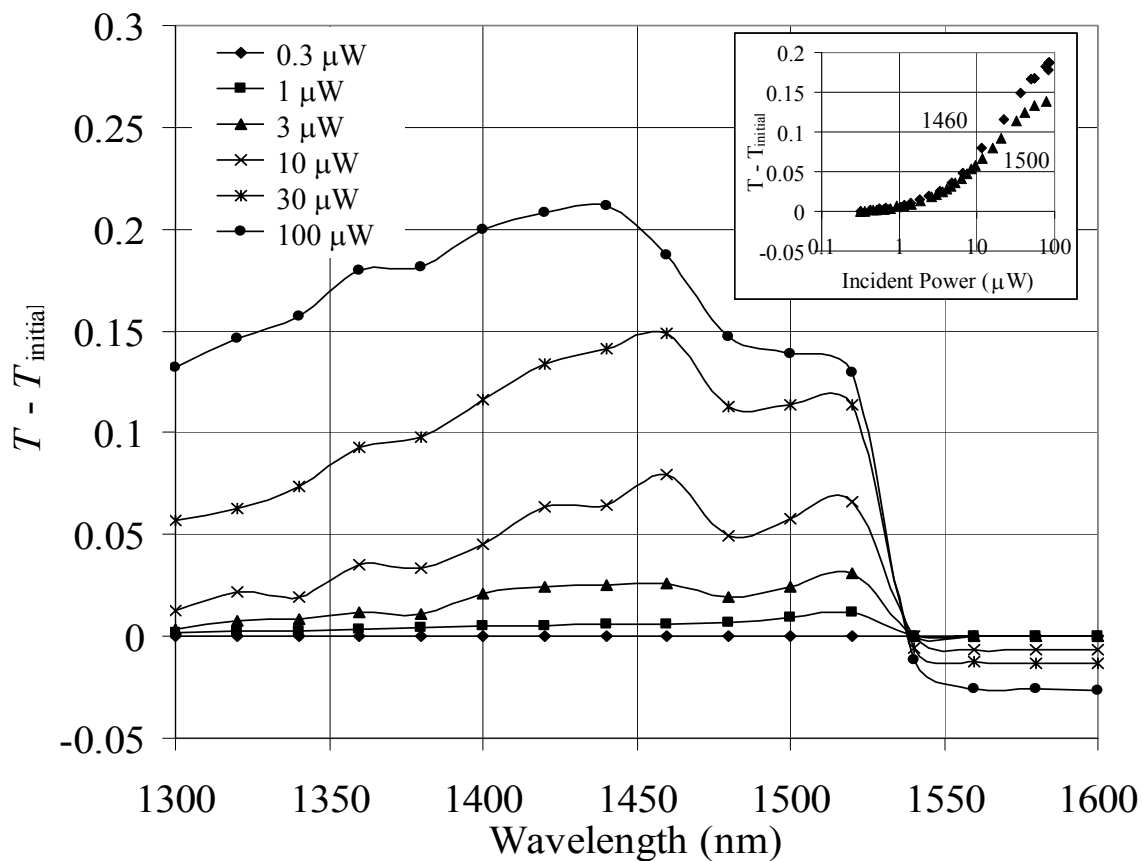


Figure 11.9: The nonlinear transmittance response of the optical element B under the same conditions as in Figure 11.7.

At high incident powers the change in T around the excitonic peak of $1.5 \mu\text{m}$ is

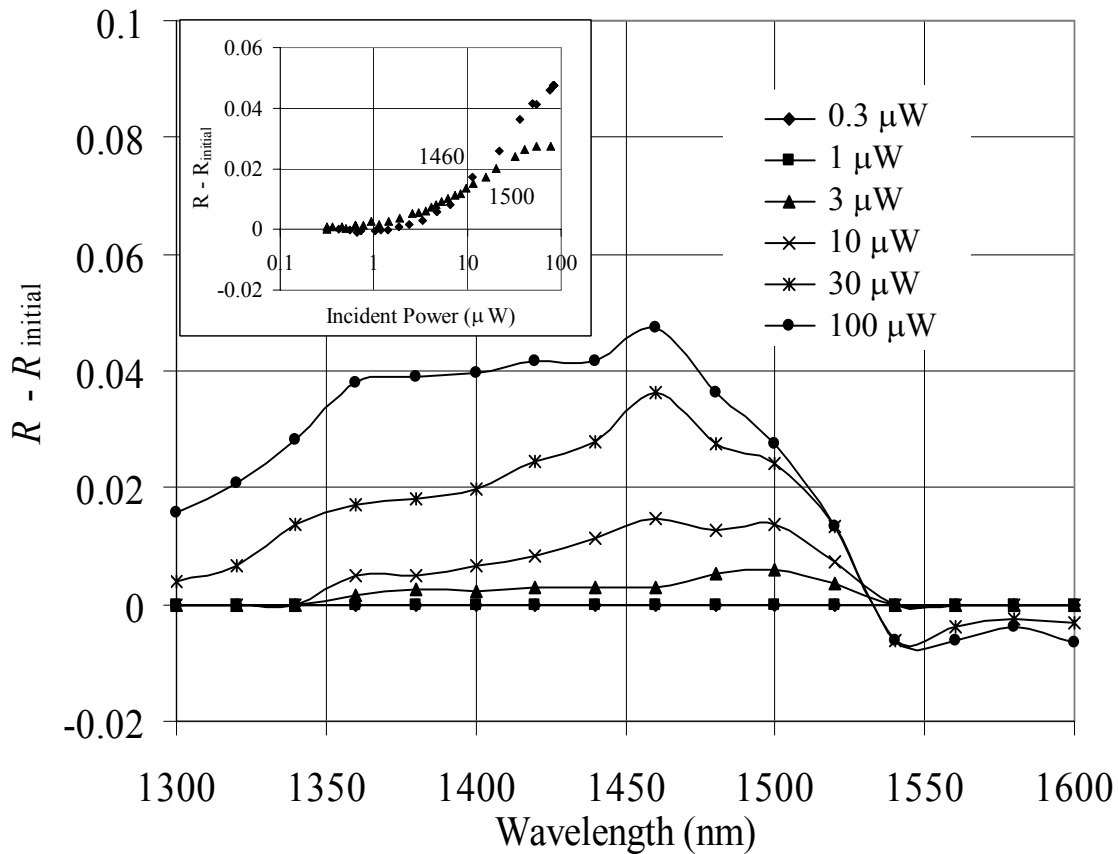


Figure 11.10: The nonlinear reflectance response of the optical element B under the same conditions as in Figure 11.7.

diminished with respect to the change in T at other wavelengths above the bandgap. This behaviour is opposite to that observed in sample A, where the change in T was the most pronounced around the bandgap. The largest change in R of B is near 1500 nm at low incident powers and around 1460 nm at high incident powers. 1460 nm is a significantly shorter wavelength than the absorption onset of MQWs type 1 of B which takes place around 1520 nm. Also, in Figure 11.9, for moderate powers (1 μW , 10 μW , 30 μW) there is a dip around 1480 nm which becomes a plateau in the range from 1480 nm to 1520 nm at 100 μW . This is again in contrast to the behaviour seen in Figure 11.10, in which there is no dip around 1480 nm. For powers of 30 μW and 100 μW the change

in R is very distinctly peaked at 1460 nm.

The insets of Figures 11.9 and 11.10 show the change in R and T as function of the incident power for 1460 nm and 1500 nm. As is also evident from the spectral plot, the change in R at 1460 nm is initially lower than the change in R at 1500 nm, but then becomes higher for incident powers larger than $10 \mu\text{W}$. In contrast the change in T of B at 1460 nm is always greater than or equal to the change in T at 1500 nm.

Similarly to the response seen in sample A for wavelengths longer than the lowest transition level of MQWs type 1, the two photon absorption of the InP substrate is the only measurable nonlinear effect. Again, near 1520 nm the effect on the nonlinear change in R and T of the saturation of absorption and two photon absorption cancel each other out.

11.2.3 Nonlinear Response of Optical Element C

In Figures 11.11 and 11.12 the nonlinear T and R response of the optical element C is shown. Saturation of absorption is again the dominant nonlinear effect. Similarly to B, the R and T change curves show opposite trends in certain spectral regions.

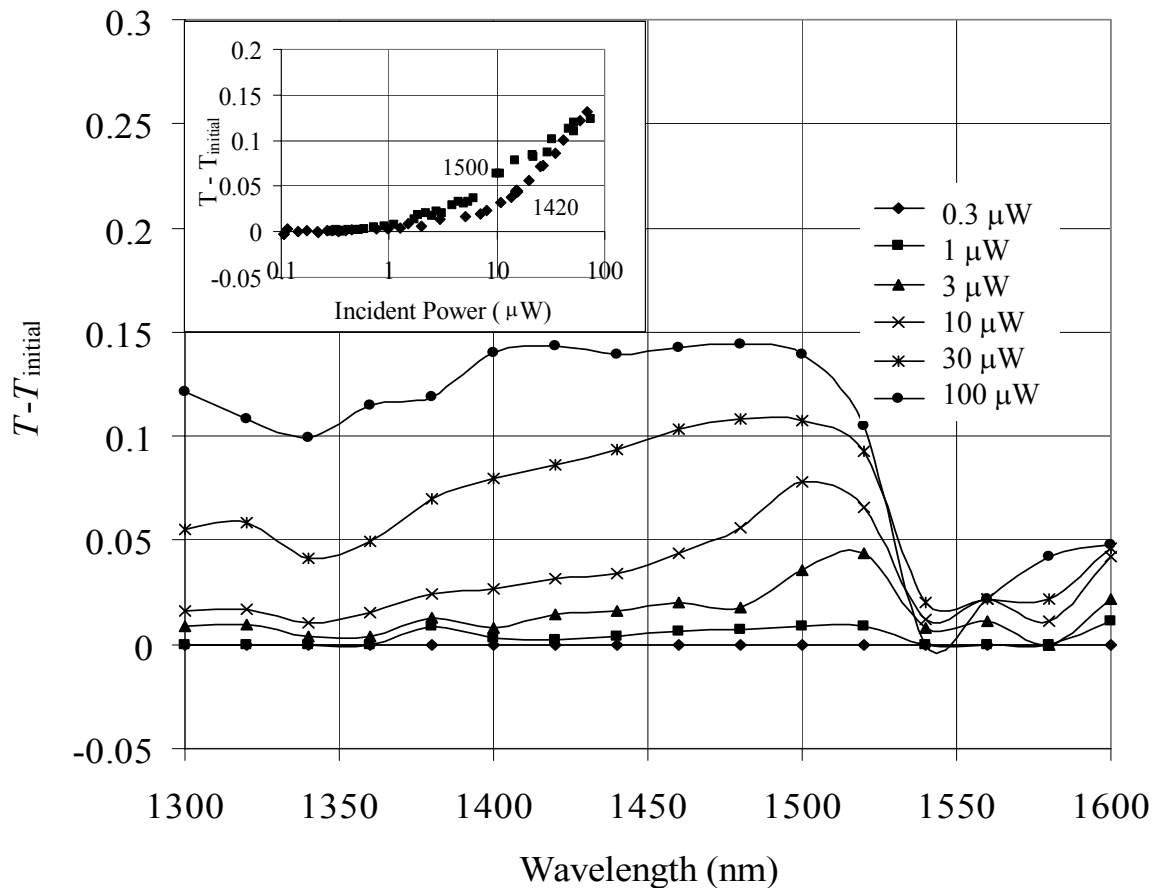


Figure 11.11: The nonlinear transmittance response of the optical element C under the same conditions as in Figure 11.7.

The change in T is peaked near the exciton at 1500 nm for incident powers of $3 \mu\text{W}$ and $10 \mu\text{W}$ and then becomes increasingly flat in the range from 1400 nm to 1500 nm. This is in contrast to the behaviour in Figure 11.12 - change in R is peaked at 1500 nm for all incident powers.

The insets in Figures 11.11 and 11.12 confirm the different response of R and T .

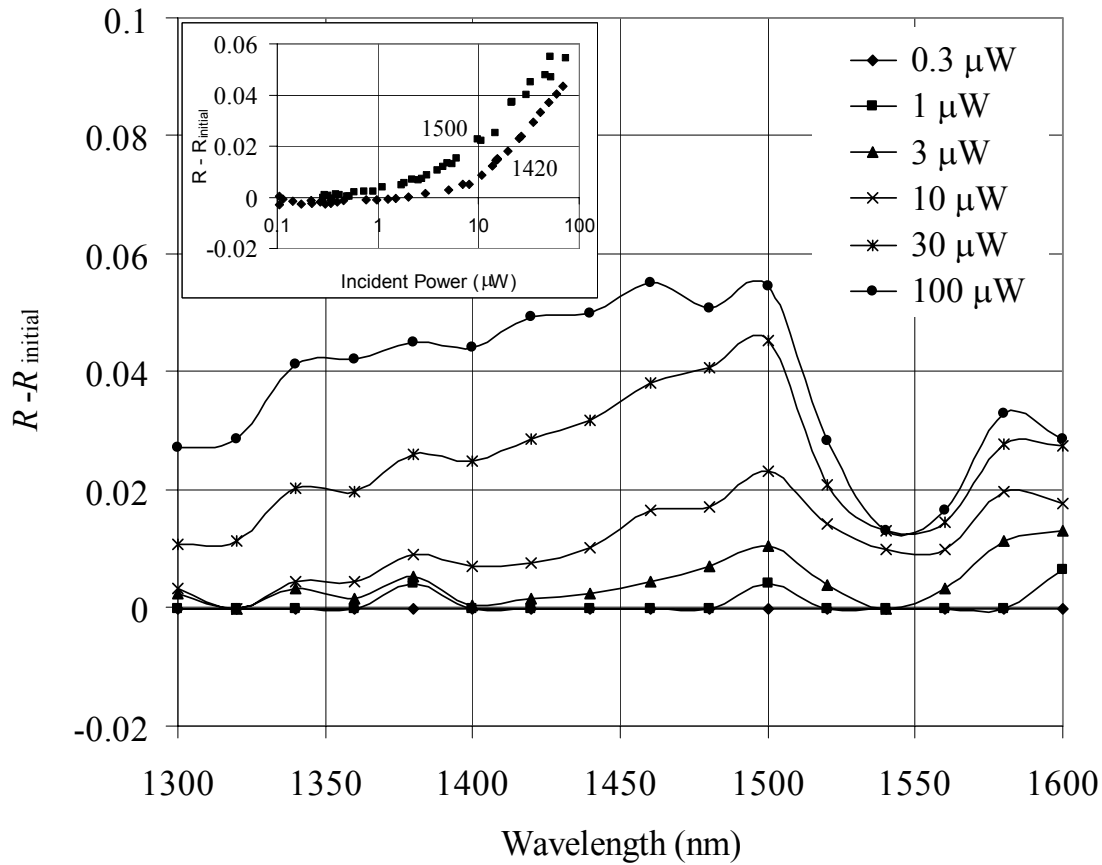


Figure 11.12: The nonlinear reflectance response of the optical element C under the same conditions as in Figure 11.7.

Whereas the change in T at 1500 nm is initially larger than or equal to the change in T at 1420 nm, the change in R at 1500 nm is always larger than the change of R at 1420 nm.

Since the optical element C absorbs beyond 1600 nm, 2PA from the wafer is not observable – the saturation of absorption dominates across the entire spectrum analyzed.

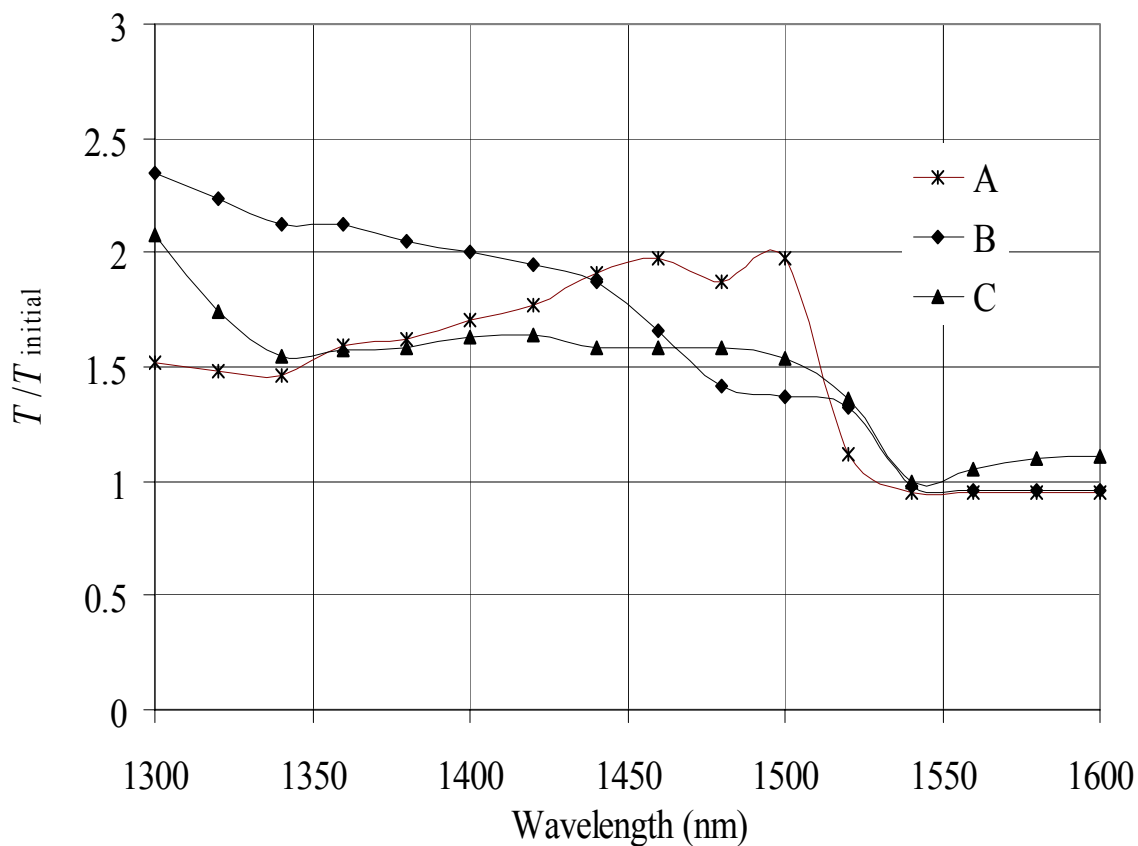


Figure 11.13: The nonlinear changes in the relative transmittance in A, B, and C.

The differences in the nonlinear response of the three samples analyzed are further displayed in Figures 11.13 and 11.14, where the relative changes in transmittance $T_{rel} = \frac{T}{T_{initial}}$ and $R_{rel} = \frac{R}{R_{initial}}$ of A, B, and C are shown. These results correspond to the maximum recorded changes, measured at $100 \mu\text{W}$. The three samples show T_{rel} between 1.5 and 2 for the spectral region $\lambda < 1500 \text{ nm}$. The T_{rel} of sample A is the largest near the excitonic peak of 1500 nm. T_{rel} of B is diminished around 1500 nm, while T_{rel} of C is flat in the region $1350 \text{ nm} < \lambda < 1500 \text{ nm}$.

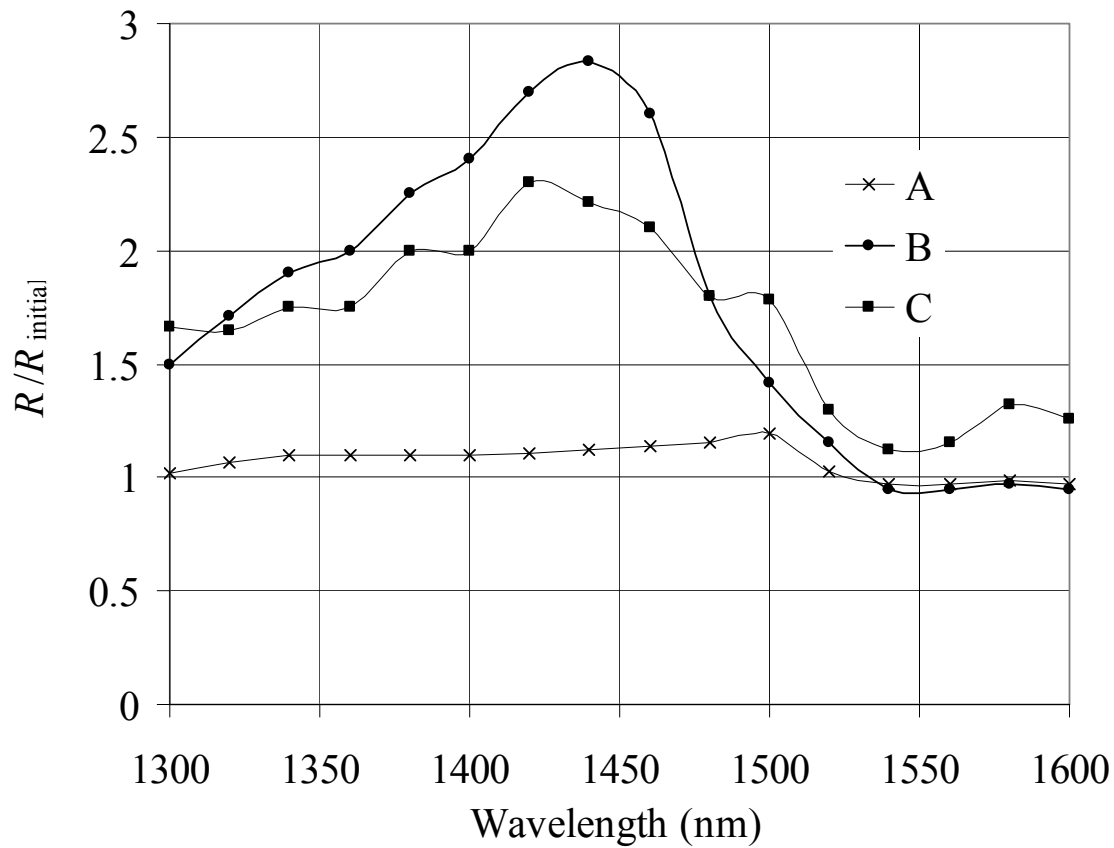


Figure 11.14: The nonlinear changes in the relative reflectance in A, B, and C.

The R_{rel} of B and C peaks around 1450 nm, while R_{rel} of sample A peaks again around 1500 nm. The large difference in the maximum R_{rel} , of sample A (≈ 1.25) and R_{rel} of B and C (≈ 2.8 and ≈ 2.3 , respectively) is because only B and C have antireflection coatings and much lower initial reflectance.

11.3 Analysis of Experimental Results Using the Models Developed in Chapters 4-9

The results of section 11.2 are strongly influenced by the saturation of absorption. Because the structures were designed with nonlinear Bragg reflection in mind, it is of interest to identify trends which would give evidence of nonlinear contradirectional coupling, the mechanism central to this work. This section will use a modified theoretical model from chapters 4 – 9 to interpret the experimental results from section 10.2 and to isolate various nonlinear contributions to the response observed.

The nonlinear steady-state transfer matrix model discussed in detail in section 4.3.5. was extended to account for absorption, saturation of absorption, and saturation of the nonlinear index change. Instead of Eq. (4.7) the following expression was substituted for the complex effective index of refraction of an m^{th} layer:

$$n_m = n_{m0} + \frac{n_{2m}P}{1 + \frac{P}{P_{satm}}} + i \frac{\kappa_{0m}}{1 + \frac{P}{P_{satm}}} \quad (11.1)$$

where n_{0m} is the linear refractive index, n_{2m} is the nonlinear coefficient, κ_{0m} is related to the linear absorption by $\kappa_{0m} = \frac{\alpha_{0m}\lambda}{4\pi}$, P is local average power, and P_{satm} is the saturation power. The n_2 used in Eq. (11.1) is not an ultrafast Kerr coefficient (expressed in units of inverse intensity), but a nonlinear coefficient that has units of inverse power. Resonant nonlinearities give rise to index changes proportional to power (or fluence) rather than to the instantaneous peak intensity.

As an effect of the changes in the expression for the refractive index, the idealized non-absorbing response predicted in chapters 4 – 9 is not observed in the simulation results that follow. It is found in what follows that the dominant effect is the saturation of absorption and the effect of nonlinear Bragg scattering is relatively weak.

The results of the simulations are shown in Figures 11.15 and 11.16. The change in the transmittance and reflectance with increasing incident power was computed for two structures illuminated at a wavelength of $1.5 \mu\text{m}$.

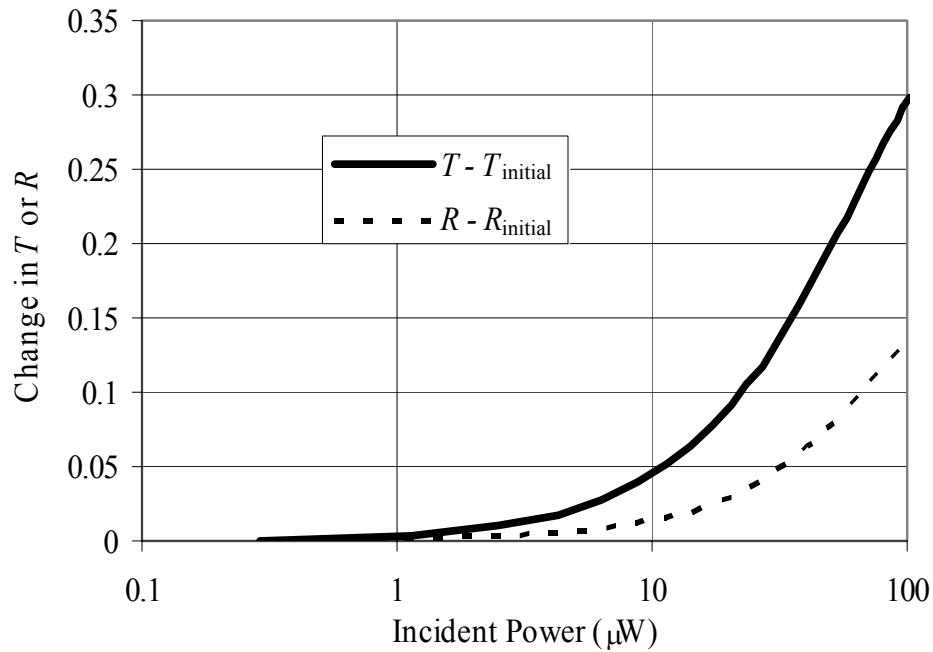


Figure 11.15: Simulated results of a change in the absolute transmittance and reflectance of a sample of uniform nonlinear absorbing material.

Figure 11.15 shows the predicted response of the structure made out of eight and a half Bragg periods of a single layer structure — a sample that, like the sample A from section 10.2, has no linear or nonlinear index contrast. In agreement with the previous measurements with the same laser source presented in section 10.3.2, the coefficients of the constituent material were taken to be $\alpha_0 = 6000 \text{ cm}^{-1}$ and $n_2 = -6 \times 10^{-9} \text{ W}^{-1}$. This gave a maximum induced nonlinear index change of $\Delta n = -0.14$ at the correct intensity. According to ellipsometric measurements, the linear index of refraction of the constituent MQWs is $n_0 = 3.47$. Saturation power was estimated to be $100 \mu\text{W}$. A constant reflection at the back facet-air interface of $R_{\text{back-air}} = 0.28$ was assumed, while the front facet of the simulated samples was taken to be anti-reflection coated.

The response displayed in Figure 11.15 has the same character as the response of sample A demonstrated in the Figures 11.7 and 11.8, the illumination-dependent changes in R and T shown in Figure 11.15 are of a similar shape. With increasing intensity the absorption saturates. Since no nonlinear Bragg scattering is present, both T and R increase monotonically.

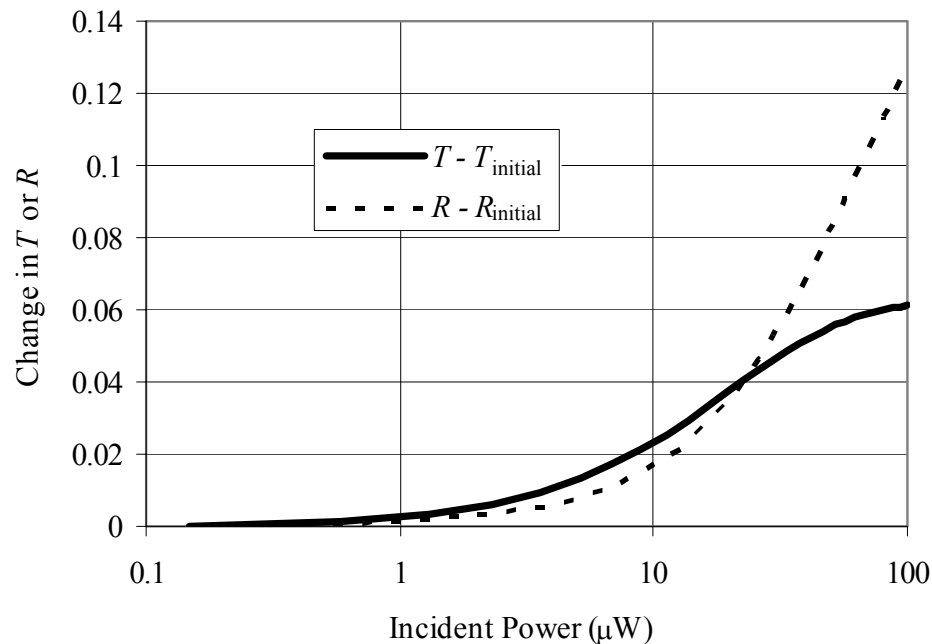


Figure 11.16: Simulated results of a change in the absolute transmittance and reflectance of a sample with a pop-up Bragg grating.

Figure 11.16 shows the modelled nonlinear response of the structure analogous to B and C in the spectral ranges 1480 – 1520 nm (sample B) and around 1500 nm (sample C). The structure analyzed is assumed to be made out of eight and a half Bragg periods in which one of the constituent materials has the properties of the material in Figure 11.15, while the other material is nonabsorbing and linear ($\alpha_0 = 0$ and $n_2 = 0$). The materials are assumed to have matched linear indices ($n_{01} = n_{02} = 3.47$). Again, the dominant feature in the simulated nonlinear response is the saturation of the absorption which

results in the initially increasing R and T . However, for higher incident power the effect of the growing Bragg grating becomes evident: as the reflectance continues to increase, the transmittance saturates.

As discussed in section 11.1 and proposed for the optical limiters and switches considered in chapters 5, 6, 8 and 9, the optical element B is made out of two sets of MQWs whose linear indices are initially closely matched. As the intensity increases absorption of MQWs type 1 becomes saturated, at the same time changing its effective refractive index. A Bragg grating appears in the vicinity of $1.5 \mu\text{m}$. As the simulation results presented in Figure 11.16 confirm, this dynamic Bragg grating enhances R and diminishes T in the range 1480 nm to 1520 nm. Since only one set of layers in optical element B exhibits nonlinearity, the nonlinear response observed falls within the multistable regime discussed in chapter 8.

A similar reasoning explains the response of the optical element C around the wavelength of 1500 nm. The enhanced change in R and diminished change in T around this spectral region suggest a growing photonic stopband around 1500 nm. In C, both sets of MQWs exhibit saturation of absorption and refractive nonlinearity. However, the expected nonlinear index change of MQWs type 1 is much larger than that of MQWs type 3, and hence a net index contrast emerges.

The numerical simulations presented in this section combined with the experimental measurements of previous section of this chapter confirm the hypothesis of an emerging photonic stopband.

11.4 Conclusions

Following the theoretical part of this thesis and the search for suitable nonlinear materials described in chapter 10, this chapter discussed the fabrication and characterization of nonlinear periodic elements with an emerging photonic stopband.

An illumination-dependent response of nonlinear periodic structures was demonstrated. Measurements of nonlinear transmittance and reflectance of semiconductor one-dimensional structures were reported. The first MQWs sample showed strong saturation of absorption, which was mostly visible around the excitonic peak. Two of the structures analyzed had a built-in periodicity which gave rise to a power-dependent Bragg grating with a resonance near $1.5 \mu\text{m}$. The nonlinear response of these two Bragg periodic samples was influenced by both nonlinear absorption and nonlinear contradirectional coupling. The effect of the nonlinear pop-up grating and the effect of saturation of the absorption were distinguished from each other by a comparison of the behaviour of nonlinear periodic structures with that of a pure MQWs.

In analogy to the theory of chapters 5, 6, 8 and 9, the Bragg grating of the nonlinear periodic elements analyzed was hidden at low levels of illumination and emerged at increased incident powers. However, in contrast to the optical limiters and switches modelled in the theoretical chapters, only one set of layers was nonlinear, the structures were absorbing, and the saturation of absorption was the dominant effect. The following concluding chapter will discuss potential venues to overcome these experimental and theoretical challenges.

Chapter 12

Summary, Original Contributions, Future Prospects

12.1 Perspective and Approach Taken During this Work

Prior to this work, the regimes of optical stability and multistability of nonlinear periodic structures had not been systematically explored. The optical response of this rich physical system, and promising applied system, had not been mapped out in full through theory and experiment. This work has developed and explored comprehensively the theory of the optical signal processing functionality of nonlinear periodic structures that are stable within the intensity domain. A nonlinear response within one interesting nonlinear periodic regime was demonstrated experimentally.

This thesis proposed a number of all-optical devices that employ an illumination-dependent dynamic photonic stopband. It was desired that these devices be capable of supporting novel signal processing functions, complementary to previously demonstrated bistable and solitonic systems.

This investigation began with a simple numerical and analytical model that was

formulated to demonstrate the most important aspects of the underlying theory. This simple model was then expanded to enable analysis of more elaborate nonlinear periodic devices and systems permitting more involved optical signal processing operations in the steady-state and in the time domain.

The next research step was a systematic search for appropriate materials that could serve as building blocks for the devices proposed. Throughout this work, the experimental analysis of materials concentrated on finding organic and inorganic materials with large refractive index change and good figures of merit. Additional work was carried out to allow the incorporation of the nonlinear materials into inorganic and organic structures that were periodic in one and three dimensions.

12.2 Original Contributions of this Work

The original contributions of this thesis can be divided into theoretical and experimental contributions.

12.2.1 Theoretical Contributions

This work developed comprehensive generalized theory of stable nonlinear periodic structures. It was demonstrated theoretically that by optimizing material and structural parameters of nonlinear periodic devices, a wide array of optical signal processing functions could be obtained.

An all-optical limiter was proposed that clamps the output level below a design-specific limiting intensity. This was followed by a theoretical demonstration of the applicability of the structures proposed to all-optical switching. The intensity- and spectral-dependencies of the proposed all-optical nonlinear periodic switches were analyzed. It was shown that a signal can control its transmittance depending on its intensity and wavelength, or, alternatively, a pump beam can be used to control the transmittance of

the signal.

This work predicted through theory that the introduction of a controlled degree of disorder into structures that are periodic on average increases the effective operational bandwidth of the proposed limiting and switching devices. The formation of stationary gap solitons and localization of light in weakly disordered structures was analyzed with respect to the degree of disorder, structural and material parameters, and optical frequency.

The theory of stable limiting and switching in nonlinear periodic structures was extended to account for additional signal processing functions. It was shown that modifications to the structure of the periodic devices proposed can allow all-optical hard-limiting, analog-to-digital conversion, and logic gating.

In addition to comprehensive numerical simulations, analytical and empirical expressions were derived that describe the response of the proposed all-optical limiter, switch, hard-limiter, logic gates, and analog-to-digital converter.

Following the demonstration of potential applicability to optical signal processing of the optically stable devices proposed in chapters 4 – 7, it was desired to develop a generalized stability analysis. This was accomplished in chapter 8, which presented a comprehensive analytical and numerical study of the phenomena of intensity-domain optical stability and multistability of nonlinear periodic structures. Regimes in which periodic structures exhibit different kinds of optical response were quantified for the first time in terms of material and structural parameters.

The analysis of the response to pulsed illumination of the devices proposed followed. It was shown that the lack or presence of an initial built-in out-of-phase linear refractive index grating leads to phenomena of pulse intensity limiting and pulse compression.

In summary, by elaborating the analytical and numerical models, the theoretical part of this work proposed and comprehensively contextualized an array of applications for nonlinear periodic structures.

12.2.2 Experimental Contributions

The second part of this thesis dealt with experimental investigation of nonlinear materials and nonlinear periodic structures. It was sought to find and characterize directly nonlinear materials that exhibited large nonlinear index changes with good figures of merit and to incorporate them into nonlinear periodic structures.

A number of nonlinear material systems were analyzed with respect to their applicability to nonlinear switching. This thesis presented and discussed the results of the measurements of resonant, ultrafast, and thermal illumination-dependent refraction and absorption in inorganic crystalline semiconductors, strongly-confined nanocrystals, and organic materials. The primary concern of the material research part of this work was to obtain materials with large nonlinear index change while preserving acceptable figure of merit. Two classes of materials, InGaAs/InAlGaAs multi-quantum-wells and strongly-confined semiconductor PbS nanocrystals, were characterized and were proven to demonstrate the most promising nonlinear characteristics in their bandgap and excitonic spectral regions.

Nonlinear periodic optical elements were fabricated and analyzed. Experimental nonlinear transmission and reflection measurements of one-dimensional semiconductor nonlinear periodic structures supported by numerical analyses enabled the isolation of the contributions of nonlinear absorption and refraction. A Bragg grating that remained hidden at low levels of irradiation was seen to emerge with increasing incident fluence.

The significance of the this work is evidenced by publications in scientific and engineering journals [6–8,39,126,136,138,139,145–147,169,171] and presentations at international conferences [122, 124, 125, 127–130, 137, 140, 142–144, 148, 170].

12.3 Future Prospects

Many challenges remain on the road towards further realization and optimization of the nonlinear periodic devices proposed in this work.

12.3.1 Further Search for Suitable Nonlinear Materials

There remains a substantial uncertainty regarding which nonlinear materials are the best candidates for nonlinear periodic devices. Various research groups have used different approaches and conventions while measuring and interpreting nonlinear data. There is a lack of systematic broadband measurements of large nonlinear index changes and, most importantly, associated figures of merit in different classes of nonlinear materials. Most of the experimental reports lack sufficient data to estimate the nonlinear figures of merit.

While this work selectively addressed many of these points, the number of degrees of freedom in materials research is enormous. The results presented in this thesis suggest that the best figures of merit associated with large index change are exhibited by the bulk and MQW direct-bandgap semiconductors. The figures of merit of the PbS nanocrystals characterized throughout this thesis are about a third of the measured figures of merit of InGaAs/InAlGaAs MQWs. However, an increase in the nanocrystal figures of merit was noticed with increasing nanocrystal size and decreasing polydispersity. To compare fairly the figures of merit of nanocrystals with those of bulk and MQWs semiconductors, further research is needed. New classes of nanocrystals of various sizes should be characterized. If nanocrystals would prove to have figures of merit exceeding unity then, given their size-tunability and processability in organic hosts, they would constitute a very attractive group of nonlinear materials.

Organic materials also need to be characterized more thoroughly. The measured resonant figures of merit of organic materials are about an order of magnitude lower than those of bulk and MQWs semiconductors. Such figures of merit are insufficient for nonlin-

ear optical switching. However, organic materials provide a broad possibility of structural modification so that their nonlinear properties could potentially be enhanced. As will be shown in the next section of this chapter, organic materials are natural candidates for the constituents of three-dimensional nonlinear periodic structures.

In addition to finding materials with good figures of merit, further work is needed to maximize the speed of their nonlinear response. Well-established growth and doping techniques exist that enable drastic reduction in the relaxation times of bulk and MQWs semiconductors. No such techniques have been introduced for semiconductor nanocrystals or organic materials. Particularly in the case of semiconductor nanocrystals, multiple experimentally-controllable degrees of freedom – nanocrystal composition, diameter and doping; surface properties and interface with the surrounding organic and polymer matrix; nanocrystal concentration – provide multiple avenues to engineering the recovery time of resonant nonlinear materials based on quantum dots.

More research is needed in order to demonstrate experimentally the existence of nonlinear materials with refractive nonlinearities of both signs. To date, there has been no direct experimental demonstration of large positive refractive nonlinearity in semiconductors. Based on the nonlinear Kramers-Kronig relations, bulk and MQWs semiconductors have been predicted to exhibit positive nonlinearities for wavelengths shorter than the wavelengths corresponding to the first excitonic step. This, however remains to be directly verified experimentally.

Recently, there has been one report of direct observation of large positive nonlinear refractive index in organic material [172]. Similar to the behaviour predicted in semiconductors, this positive index change has been observed for wavelengths shorter than the main resonance. The measurement was performed in the visible spectral range and is not directly applicable to switching at telecommunication wavelengths.

The search for nonlinear materials with large index changes of both signs, good figures of merit, and fast response would greatly benefit from theoretical work carried out

in parallel. A comprehensive theory is needed: to understand various complex nonlinear processes exhibited by different classes of nonlinear materials; to predict the sign and strength of nonlinear response; and to determine the upper bounds of nonlinear coefficients and figures of merit.

12.3.2 Incorporation of Nonlinear Materials into Periodic Structures

To fabricate nonlinear periodic devices, the appropriate nonlinear materials have to be incorporated into periodic structures.

Epitaxial techniques permit fabrication of planar bulk and MQW semiconductor one-dimensional nonlinear periodic structures. Established etching techniques also allow fabrication of corrugated semiconductor waveguides.

Recent advances in the fabrication of colloidal crystals permit the preparation of three-dimensional nonlinear periodic structures from organic materials and nanocrystals incorporated in organic and glass hosts. Infiltration techniques and composite core-shell colloidal crystals provide additional degrees of freedom in modifying the nonlinear response. Nonlinear colloidal crystals can be deposited on semiconductor and organic waveguides to provide effective nonlinear coupling into and out of the waveguide, or to provide a nonlinear Bragg reflection within the waveguide.

Throughout this work, dye-doped three-dimensional nonlinear periodic structures have been fabricated and characterized in addition to the one-dimensional semiconductor Bragg gratings discussed in chapter 11. Preliminary testing of these colloidal crystals has been carried out and the results are reported below.

The three-dimensional colloidal crystals analyzed were prepared in three steps. First, a nonlinear monomer was synthesized. The monomer was then polymerized forming spherical colloids. Finally, the colloids were deposited on a glass substrate in an ordered, periodic form. The spheres were 260 nm in diameter and the samples were 21 periods

thick on average. These steps were carried out by Chantal Paquet from the Chemistry Department at the University of Toronto [173].

Disperse Red 1 azobenzene dye was chosen as the nonlinear dopant since DR1 was previously demonstrated to exhibit a strong refractive nonlinearity in the absorbing spectral range 490 – 590 nm [57]. This nonlinear response of DR1 was discussed at the end of chapter 10.

The nonlinear reflection measurements were taken with the same experimental set up as described in chapter 11 in Figure 11.6.

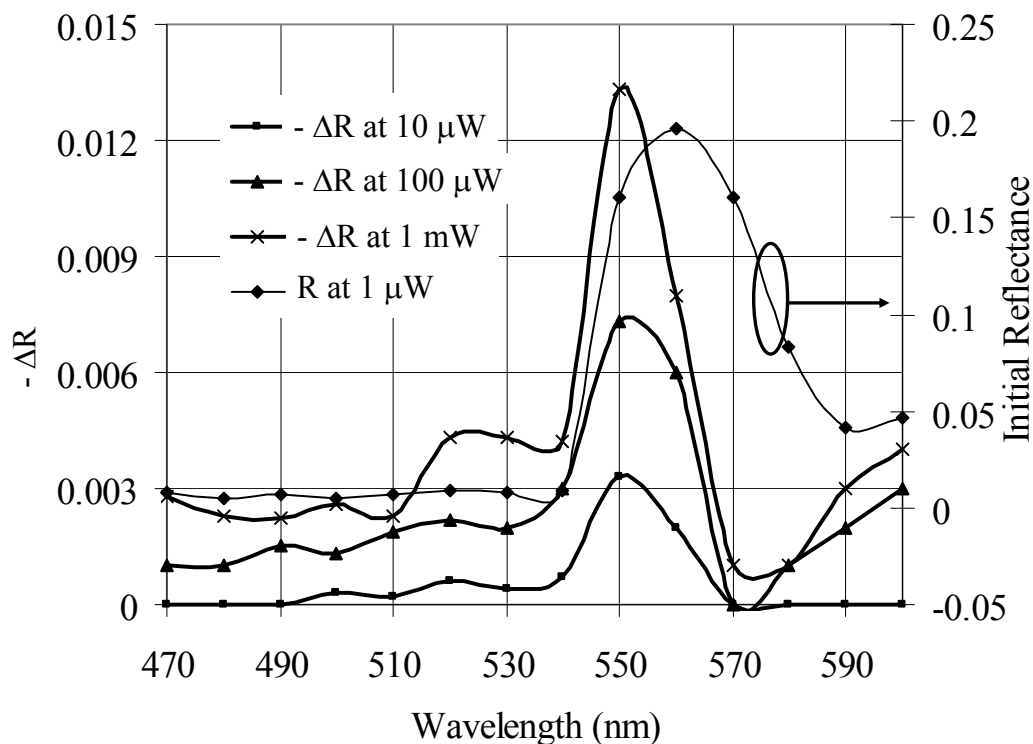


Figure 12.1: Differential nonlinear reflectance from colloidal crystal 1 compared to its initial reflectance.

Figure 12.1 shows the movement of the stopband by showing the change in reflectance at increased incident powers. Measurements were taken in the spectral range 470 nm to 600 nm at average incident powers ranging from 1 μ W to 1 mW corresponding to

fluences ranging from $3 \mu\text{J}/\text{cm}^2$ to $3 \text{mJ}/\text{cm}^2$. For comparison, the linear reflectance of the colloidal crystal analyzed is shown as well. The change in the reflectance is most dramatic around the blue edge of the stopband while it is most strongly diminished near its red edge. To first order, the change in the reflectance is proportional to the derivative of the reflectance spectra taken with respect to the average refractive index. A nonlinear decrease in the reflectance near the left side of the top of the stopband observed in Figure 12.1 indicates that the stopband moves towards the lower wavelengths.

This behaviour is anticipated given the expected refractive negative nonlinearity of the DR1 dye in the spectral range analyzed. However, the magnitude of the effect is lower than expected. Index changes as large as $\Delta n = 0.1$ have been predicted around the wavelength 570 nm [57]. Such large index changes should cause a change in the position of the center of the stopband in the vicinity of 10% and a strong decrease in the amplitude of reflectance inside the stopband. As will be discussed below, the weaker than expected nonlinear response is attributed to a strong disorder present in the sample and to nonlinear response of DR1 smaller than previously reported [57].

The changes in the reflectance outside of the stopband are attributed to the saturation of absorption of DR1 combined with back reflection from the glass slide – air interface.

A number of other samples were prepared and characterized in the same way as colloidal crystal 1.

In Figure 12.2 the nonlinear response of colloidal crystal 2 is shown. Unlike in colloidal crystal 1, the response of colloidal crystal 2 is characterized by a strong decrease in the stopband. As demonstrated in the inset of Figure 12.2, at the center of the stopband (570 nm) the reflectance decreases from 0.56 to 0.35 when the incident power is increased from $3 \mu\text{W}$ to 3mW . Moreover, no shift in the central position of the stopband is observed. For wavelengths shorter than 530 nm the reflectance increases with increasing incident power. The saturation of absorption is again the dominant nonlinear response in this spectral region.

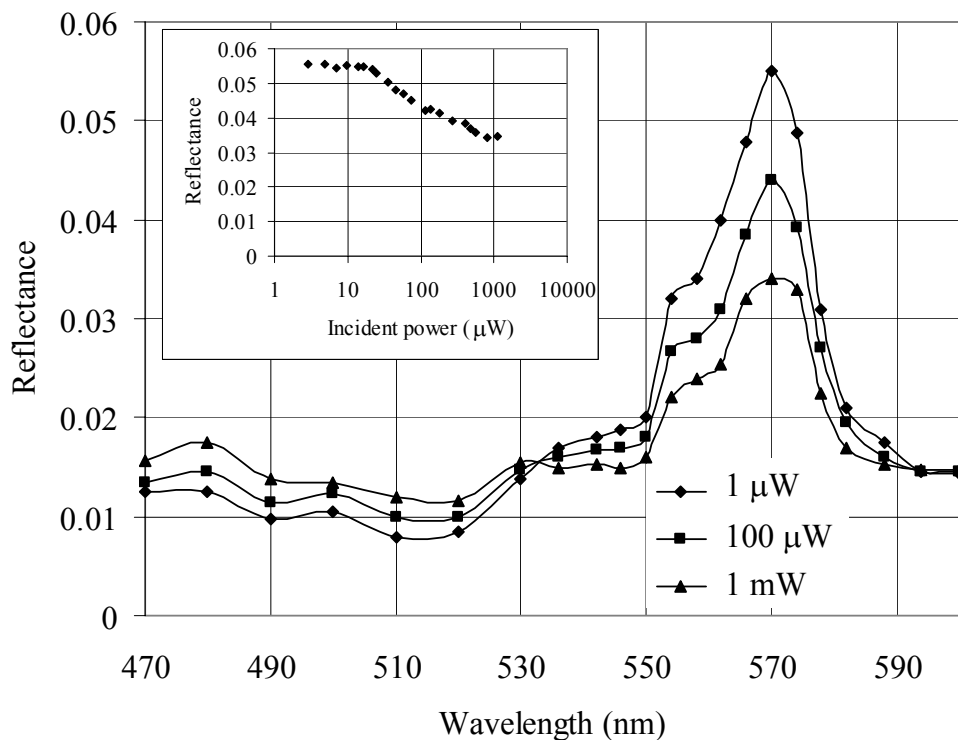


Figure 12.2: Nonlinear reflectance from colloidal crystal 2. The inset demonstrates how the reflectance at 570 nm decreases with increasing incident power

The discrepancies between results obtained from the two colloidal crystals characterized above were attributed to the fabrication imperfections and weaker than predicted nonlinearity of the constituent materials. The weaker nonlinearity measured can be caused by the fact that the 1 ps pulses used in this work were 20 times shorter than those used in Ref. [57] while the time required for the trans-cis photoisomerization of azobenzenes embedded in a solid can be longer than subpicosecond as measured in solution [174, 175].

12.3.3 Extension of Theoretical Models

In addition to the search for better nonlinear materials and the quest to devise and optimize the fabrication of periodic structures, there is a need for more comprehensive theoretical analysis. New theoretical models should allow the simulation of propagation of light in nonlinear periodic structures while fully accounting for time-dependent refractive and absorptive linear and nonlinear material parameters. Waveguiding and multi-dimensional periodic structures should also be theoretically analyzed beyond the planar one-dimensional configuration, to predict and understand the response of the devices. Such multi-dimensional devices can provide additional angular degrees of freedom that should increase the optical signal processing functionality of nonlinear periodic structures.

12.4 Final Comments

This work has advanced the field of optical signal processing using nonlinear periodic structures. New signal processing devices and systems were proposed, nonlinear optical materials were characterized, and nonlinear periodic structures were fabricated and analyzed.

At present there remain many obstacles on the road towards wider implementation of nonlinear periodic structures. However, the available structural and material degrees of freedom offer an enormous opportunity for improvement. This work has pointed out and demonstrated new ways for increasing the optical signal processing functionality of nonlinear periodic structures.

Bibliography

- [1] E. Cotter, J. K. Lucek, and D. D. Marcenac, “Ultra-high-bit-rate networking: From the transcontinental backbone to the desktop,” *IEEE Communications Magazine*, vol. 34, pp. 90–95, 1997.
- [2] P. P. Mitra and J. B. Stark, “Nonlinear limits to the information capacity of optical fiber communications,” *Nature*, vol. 411, p. 1027, 2001.
- [3] P. W. Smith, “On the physical limits of digital optical switching and logic elements,” *The Bell System Technical Journal*, vol. 61, pp. 1975–1983, 1982.
- [4] R. Ramaswami and K. N. Sivarajan, *Optical Networks, A Practical Prespective*. Morgan Kaufmann Publishers Inc., 1998.
- [5] D. Greenfield, *The Essential Guide to Optical Networks*. Prentice Hall, 2002.
- [6] L. Brzozowski and E. H. Sargent, “Nonlinear distributed-feedback structures as passive optical limiters,” *Journal of the Optical Society of America B*, vol. 17, pp. 1360–1365, 2000.
- [7] L. Brzozowski and E. H. Sargent, “Optical signal processing using nonlinear distributed feedback structures,” *IEEE Journal of Quantum Electronics*, vol. 36, pp. 550–555, 2000.

- [8] L. Brzozowski and E. H. Sargent, "Nonlinear disordered media for broad-band optical limiting," *IEEE Journal of Quantum Electronics*, vol. 36, pp. 1237–1242, 2000.
- [9] P. W. Smith, I. P. Kaminov, P. J. Maloney, and L. W. Stulz, "Self-contained integrated bistable optical devices," *Applied Physics Letters*, vol. 34, pp. 62–65, 1979.
- [10] P. W. Smith and E. H. Turner, "A bistable Farby-Perot resonator," *Applied Physics Letters*, vol. 30, pp. 280–281, 1977.
- [11] B. E. A. Saleh and M. C. Teich, *Fundamentals of Photonics*. New York: Wiley, 1991.
- [12] P. W. E. Smith and L. Qian, "Switching to optical for a faster tomorrow," *IEEE Circuits and Devices Magazine*, vol. 15, pp. 28–33, 1999.
- [13] P. W. E. Smith, "All-optical devices: materials requirements," in *Nonlinear Optical Properties of Advanced Materials*, vol. 1852, pp. 2–9, SPIE, 1993.
- [14] G. I. Stegeman, "All-optical devices: materials requirements," in *Nonlinear Optical Properties of Advanced Materials*, vol. 1852, pp. 75–89, SPIE, 1993.
- [15] I. C. Khoo, M. Wood, and B. D. Guenther, "Nonlinear liquid crystal optical fiber array for all-optical switching/limiting," in *LEOS '96 9th Annual Meeting*, vol. 2, pp. 211–212, IEEE, 1996.
- [16] G. L. Wood, W. W. Clark III, M. J. Miller, G. J. Salamo, and E. J. Sharp, "Evaluation of passive optical limiters and switches," in *Materials for Optical Switches, Isolators, and Limiters*, vol. 1105, pp. 154–181, SPIE, 1989.
- [17] R. Bozio, M. Meneghetti, R. Signorini, M. Maggini, G. Scorrano, M. Prato, G. Brusatin, and M. Guglielmi, "Optical limiting of fullerene derivatives embedded

- in sol-gel materials,” in *Photoactive Organic Materials. Science and Applications. Proceedings of the NATO Advanced Research Workshop*, vol. 572, pp. 159–174, Kluwer, 1996.
- [18] J. A. Hermann, P. B. Chapple, J. Staromlynska, and P. Wilson, “Design criteria for optical power limiters,” in *Nonlinear Optical Materials for Switching and Limiting*, vol. 2229, pp. 167–178, SPIE, 1994.
- [19] R. W. Boyd, *Nonlinear Optics*. Academic Press, 1992.
- [20] M. G. Kuzyk and C. W. Dirk, *Characterization Techniques and Tabulations for Organic Nonlinear Optical Materials*. Marcel Dekker, Inc., 1998.
- [21] D. L. Mills, *Nonlinear Optics: Basic Concepts*. Springer, 1998.
- [22] P. Gunter, *Nonlinear Optical Effects and Materials*. Springer, 2000.
- [23] P. N. Prasad and D. J. Williams, *Introduction to Nonlinear Optical Effects in Molecules and Polymers*. John Wiley & Sons, Inc., 1991.
- [24] R. L. Sutherland, *Handbook of Nonlinear Optics*. Marcel Dekker, Inc., 1996.
- [25] E. Garmire, “Resonant optical nonlinearities in semiconductors,” *IEEE Journal on Selected Topics in Quantum Electronics*, vol. 6, pp. 1094–1110, 2000.
- [26] P. Yeh, *Optical Waves in Layered Media*. John Wiley & Sons, 1988.
- [27] S. John, *The Localization of Light*. New York: Plenum Press, 1993.
- [28] E. W. Van Stryland, M. A. Woodall, H. Vanherzeele, and M. J. Soileau, “Energy band-gap dependence of two-photon absorption,” *Optics Letters*, vol. 10, pp. 490–492, 1985.

- [29] M. Sheik-Bahae, D. C. Hutchings, D. J. Hagan, and E. W. Van Stryland, "Dispersion of bound electronic nonlinear refraction in solids," *IEEE Journal of Quantum Electronics*, vol. 27, pp. 1296–1309, 1991.
- [30] S. H. Park, J. F. Morhange, A. D. Jeffery, R. A. Morgan, A. Chevez-Pirson, H. M. Gibbs, S. W. Koch, N. Peyghambarian, M. Derstine, A. C. Gossard, J. H. English, and W. Weigmann, "Measurements of room-temperature band-gap-resonant optical nonlinearities of GaAs/AlGaAs multiple quantum wells and bulk GaAs," *Applied Physics Letters*, vol. 52, pp. 1201–1203, 1988.
- [31] L. Qian, S. D. Benjamin, P. W. E. Smith, H. Pinkney, B. J. Robinson, and D. A. Thompson, "Picosecond carrier lifetime and large optical nonlinearities in InGaAsP grown by helium-plasma-assisted molecular beam epitaxy," *Optics Letters*, vol. 22, pp. 108–110, 1997.
- [32] H. S. Loka, S. D. Benjamin, and P. W. E. Smith, "Optical characterization of low-temperature-grown GaAs for ultrafast switching devices," *IEEE Journal of Quantum Electronics*, vol. 34, pp. 1426–1437, 1998.
- [33] M. Kawase, E. Garmire, H. C. Lee, and P. D. Dapkus, "Single-pulse pump-probe measurement of optical properties in GaAs/AlGaAs multiple quantum wells," *IEEE Journal of Quantum Electronics*, vol. 30, pp. 981–988, 1994.
- [34] S. Gupta, M. Y. Frankel, J. A. Valdmanis, J. F. Whitaker, G. A. Mourou, F. W. Smith, and A. R. Calawa, "Subpicosecond carrier lifetime in GaAs grown by molecular beam epitaxy at low temperatures," *Applied Physics Letters*, vol. 59, pp. 3276–3278, 1991.
- [35] E. S. Harmon, M. R. Melloch, J. W. Woodall, D. D. Nolte, N. Olsuka, and C. L. Chang, "Carrier lifetime versus anneal in low temperature growth GaAs," *Applied Physics Letters*, vol. 63, pp. 2248–2250, 1993.

- [36] S. D. Benjamin, A. Othonos, and P. W. E. Smith, "Large ultrafast optical nonlinearities in As-rich GaAs," *Electronics Letters*, vol. 30, pp. 1704–1706, 1994.
- [37] P. W. E. Smith, S. D. Benjamin, and H. S. Loka, "Tailoring of trap-related carrier dynamics in low-temperature-grown GaAs," *Applied Physics Letters*, vol. 71, pp. 1156–1158, 1997.
- [38] H. Pinkney, D. A. Thompson, B. J. Robinson, L. Qian, S. D. Benjamin, and P. W. E. Smith, "Growth of novel InP-based materials by He-plasma-assisted epitaxy," *Journal of Crystal Growth*, vol. 209, pp. 237–241, 2000.
- [39] L. Brzozowski, E. H. Sargent, A. SpringThorpe, and M. Extavour, "Direct measurement of large near-bandedge nonlinear index change from 1.48 - 1.55 μm in InGaAs/InAlGaAs multi-quantum-wells," *Applied Physics Letters*, vol. 82, pp. 4429–4431, 2003.
- [40] D. A. B. Miller, D. S. Chemla, D. J. Eilenberger, P. W. Smith, A. C. Gossard, and W. T. Tsang, "Large room-temperature optical nonlinearity in GaAs/Ga_{1-x}Al_xAs multiple quantum well structures," *Applied Physics Letters*, vol. 41, pp. 679–681, 1982.
- [41] S. Schmitt-Rink, D. S. Chemla, and D. A. B. Miller, "Theory of transient excitonic optical nonlinearities in semiconductor quantum-well structures," *Physical Review B*, vol. 32, pp. 6601–6609, 1985.
- [42] Y. H. Lee, A. Chavez-Pirson, S. W. Koch, H. M. Gibbs, S. H. Park, J. Morchange, A. Jeffery, N. Peyghambarian, J. Banyai, A. C. Gossard, and W. Wiegmann, "Room temperature optical nonlinearities in GaAs," *Physical Review Letters*, vol. 57, pp. 2446–2449, 1986.
- [43] F. Stern, "Dispersion of the index of refraction near the absorption edge of semiconductors," *Physical Review*, vol. 133, pp. A1653–A1664, 1964.

- [44] A. M. Fox, A. C. Maciel, J. F. Ryan, and M. D. Scott, "Nonlinear excitonic optical absorption in GaInAs/InP quantum wells,"
- [45] A. M. Fox, A. C. Maciel, M. G. Shorthose, J. F. Ryan, M. D. Scott, J. I. Davies, and J. R. Riffat, "Nonlinear excitonic optical absorption in GaInAs/InP quantum wells,"
- [46] P. W. Joudawlkis, D. T. McInturff, and S. E. Ralph, "Ultrafast carrier dynamics and optical nonlinearities of low-temperature-grown InGaAs/InAlAs multiple quantum wells," *Applied Physics Letters*, vol. 69, pp. 4062–4064, 1996.
- [47] R. V. Penty, H. K. Tsang, I. H. White, R. S. Grant, W. Sibert, and J. E. A. Whiteaway, "Repression and speed improvement of photogenerated carrier induced refractive nonlinearity in InGaAs/InGaAsP quantum well waveguide," *Electronics Letters*, vol. 27, pp. 1447–1449, 1991.
- [48] I. E. Day, P. A. Snow, R. V. Penty, I. H. White, R. S. Grant, G. T. Kennedy, W. Sibbett, D. A. O. Davies, M. A. Fisher, and M. J. Adams, "Bias dependent recovery time of all-optical resonant nonlinearity in and InGaAsP/InGaAsP multi-quantum well waveguide," *Applied Physics Letters*, vol. 65, pp. 2657–2659, 1994.
- [49] M. A. Fisher, H. Wickes, G. T. Kennedy, R. S. Grant, and W. Sibbett, "Ultrafast nonlinear refraction in an active MQW waveguide," *Electronics Letters*, vol. 29, pp. 1185–1186, 1993.
- [50] D. A. O. Davies, M. A. Fisher, D. J. Elton, S. D. Perrin, M. J. Adams, G. T. Kennedy, R. S. Grant, P. D. Roberts, and W. Sibbett, "Nonlinear switching in InGaAsP laser amplifier directional couplers biased at transparency," *Electronics Letters*, vol. 29, pp. 1710–1711, 1993.

- [51] C. Aversa, J. E. Sipe, M. Sheik-Bahae, and E. W. V. Stryland, "Third-order optical nonlinearities in semiconductors: Two-band model," *Physical Review B*, vol. 24, pp. 18073–18082, 1994.
- [52] M. J. Shaw and M. Jaros, "Anomalous optical nonlinearity in semiconductor superlattices," *Physical Review B*, vol. 47, pp. 1620–1623, 1993.
- [53] K. S. Bindra and A. K. Kar, "Role of femtosecond pulses in distinguishing third- and fifth-order nonlinearity for semiconductor-doped glasses," *Applied Physics Letters*, vol. 79, pp. 3761–3763, 2001.
- [54] M. Sheik-Bahae, D. J. Hagan, and E. W. Van Stryland, "Dispersion and band-gap scaling of the electronic Kerr effect in solids associated with two-photon absorption," *Physical Review Letters*, vol. 65, pp. 96–99, 1990.
- [55] N. J. Long, "Organometallic compounds for nonlinear optics — The search for en-light-enment!," *Angewandte Chemie, International Edition (english)*, vol. 34, pp. 21–38, 1995.
- [56] I. Liakatas, C. Cai, M. Bösch, C. B. M. Jäger, and P. Günter, "Importance of intermolecular interactions in the nonlinear optical properties of poled polymer," *Applied Physics Letters*, vol. 76, pp. 1368–1370, 2000.
- [57] R. Rangel-Rojo, S. Yamada, H. Matsuda, and D. Yankelevicg, "Large near-resonance third-order nonlinearity in an azobenzene-functionalized polymer film," *Applied Physics Letters*, vol. 72, pp. 1021–1023, 1998.
- [58] F. W. Wise, "Lead salt quantum dots: The limit of strong confinement," *Accounts of Chemical Research*, vol. 33, pp. 773–780, 2000.
- [59] L. Banyai and S. W. Koch, "Absorption blue shift in laser-excited semiconductor microspheres," *Physical Review Letters*, vol. 57, pp. 2722–2724, 1986.

- [60] S. Schmitt-Rink, D. A. B. Miller, and D. S. Chemla, “Theory of the linear and nonlinear optical properties of semiconductor microcrystallites,” *Physical Review B*, vol. 35, pp. 8113–8125, 1987.
- [61] M. A. Hines and G. D. Scholes, “Synthesis of colloidal PbS nanocrystals with size-tunable NIR emissions,” *submitted*.
- [62] G. Wang and K. Guo, “Excitonic effects on the third-order nonlinear optical susceptibility in parabolic quantum dots,” *Physica B*, vol. 315, pp. 234–239, 2001.
- [63] P. T. Guerreiro, S. Ten, N. F. Borrelli, J. Butty, G. E. Jabbour, and N. Peyghambarian, “PbS quantum-dot doped glasses as saturable absorbers for mode locking of Cr:forsterite laser,” *Applied Physics Letters*, vol. 71, pp. 1595–1597, 1997.
- [64] K. Wundke, S. Pötting, J. Auxier, A. Schülzgen, N. Peyghambarian, and N. F. Borrelli, “Pbs quantum-dot doped glasses for ultrashort pulse generation,” *Applied Physics Letters*, vol. 76, pp. 10–12, 2000.
- [65] D. Cotter, M. C. Burt, and R. J. Manning, “Below-band gap third-order optical nonlinearity of nanometer-size semiconductors crystallines,” *Physical Review Letters*, vol. 68, pp. 1200–1203, 1992.
- [66] D. Cotter, M. C. Burt, and R. J. Manning, “Below-band gap third-order optical nonlinearity of nanometer-size semiconductors crystallines,” *Physical Review Letters*, vol. 68, pp. 1200–1203, 1992.
- [67] T. D. Krauss and F. W. Wise, “Femtosecond measurement of nonlinear absorption and reflection in CdS, ZnSe, and ZnS,” *Applied Physics Letters*, vol. 65, pp. 1739–1741, 1994.
- [68] W. W. Lam, *Dispersion of Optical Nonlinearity in Bulk GaAs, CdSe Nanocrystals, and PbS Nanocrystals*. Masters’ Thesis, University of Toronto, 2003.

- [69] L. Yang, K. Becker, F. M. Smith, R. H. Magruder III, R. F. Haglund Jr., L. Yang, R. Dorsinville, R. R. Alfano, and R. A. Zuhr, "Size dependence of the third-order susceptibility of copper nanocrystals investigated by four-wave mixing,"
- [70] K. Uchida, S. Kaneko, S. Omi, C. Hata, H. Tanji, Y. Asahara, A. J. Ikushima, T. Tokizaki, and A. Nakamura, "Optical nonlinearities of a high concentration of small metal particles dispersed in glass: copper and silver particles," *Journal of the Optical Society of America*, vol. 11, pp. 1236–1243, 1994.
- [71] H. Inouye, K. Tanaka, I. Tanahashi, T. Hattori, and H. Nakatsuka, "Ultrafast optical switching in a silver nanoparticle system," *Japanese Journal of Applied Physics*, vol. 39, pp. 5132–5133, 2000.
- [72] D. Ricard, P. Roussignol, and C. Flytanis, "Surface-mediated enhancement of optical phase conjugation in metal colloids," *Optics Letters*, vol. 10, pp. 511–513, 1985.
- [73] D. V. Petrov, "Nonlinear phase shift by cascaded quasi-phase-matched second harmonic generation," *Optics Communications*, vol. 13, pp. 102–106, 1996.
- [74] C. Bosshard, "Cascading of second-order nonlinearities in polar materials," *Advanced Materials*, vol. 5, pp. 385–397, 1996.
- [75] G. I. Stegeman, D. J. Hagan, and L. Torner, " $\chi^{(2)}$ cascading phenomena and their applications to all-optical signal processing, mode-locking, pulse compression and solitons," *Optical and Quantum Electronics*, vol. 28, pp. 1691–1740, 1996.
- [76] P. W. Smith, E. H. Turner, and B. B. Mumford, "Nonlinear electro-optic Fabry-Perot devices using reflected-light feedback," *Optics Letters*, vol. 2, pp. 53–57, 1978.
- [77] P. W. Smith, I. P. Kaminov, P. J. Maloney, and L. W. Stulz, "Integrated bistable optical devices," *Applied Physics Letters*, vol. 33, pp. 24–26, 1978.

- [78] H. M. Gibbs, S. L. McCall, T. N. C. Venkatesan, A. C. Gossard, A. Passner, and W. Wiegmann, "Optical bistability in semiconductors," *Applied Physics Letters*, vol. 35, pp. 451–453, 1979.
- [79] P. W. Smith, A. Ashkin, J. E. Bjorkholm, and D. J. Eilenberger, "Studies of self-focusing bistable devices using liquid suspensions of dielectric particles," *Optics Letters*, vol. 10, pp. 131–133, 1978.
- [80] H. M. Gibbs, S. S. Tang, J. L. Jewell, D. A. Winberger, K. Tai, A. C. Gossard, S. L. McCall, and A. Passner, "Room temperature excitonic optical bistability in a GaAs-GaAlAs superlattice etalon," *Applied Physics Letters*, vol. 41, pp. 221–222, 1982.
- [81] N. Peyghambarian and H. M. Gibbs, "Optical nonlinearity, bistability, and signal processing in semiconductors," *Journal of the Optical Society of America B*, vol. 2, pp. 1215–1227, 1985.
- [82] H. M. Gibbs, *Optical Bistability: Controlling Light with Light*. Academic Press, 1985.
- [83] H. G. Winful, J. H. Marburger, and E. Garmire, "Theory of bistability in nonlinear distributed feedback structures," *Applied Physics Letters*, vol. 35, pp. 379–381, 1979.
- [84] A. Empsten and I. Veretennicoff, "Optical bistability in an NLDFB device showing absorption: Comparison of feedback efficiencies for different grating profiles and study of the behavior of aperiodic and nonperfect grating profiles," *IEEE Journal of Quantum Electronics*, vol. 26, pp. 1089–1097, 1990.
- [85] J. He and M. Cada, "Optical bistability in semiconductor periodic structures," *IEEE Journal of Quantum Electronics*, vol. 27, pp. 1182–1188, 1991.

- [86] J. He and M. Cada, “Combined distributed feedback and Fabry-Perot structures with a phase-matching layer for optical bistable devices,” *Applied Physics Letters*, vol. 61, pp. 2150–2152, 1992.
- [87] C.-X. Shi, “Optical bistability in reflective fiber gratings,” *IEEE Journal of Quantum Electronics*, vol. 31, pp. 2037–2043, 1995.
- [88] J. He, M. Cada, B. Acklin, M. Proctor, D. Martin, F. Morier-Genoud, M. A. Dupertuis, and J. M. Glinski, “All-optical reflectivity tuning and logic gating in a GaAs/AlAs periodic layered structure,” *Applied Physics Letters*, vol. 60, pp. 404–406, 1992.
- [89] C. J. Herbert and M. S. Malcuit, “Optical bistability in nonlinear periodic structures,” *Optics Letters*, vol. 21, pp. 1783–1785, 1993.
- [90] Q. Li, C. T. Chen, K. M. Ho, and C. M. Soukoulis, “Wave propagation in nonlinear photonic band-gap materials,” *Physical Review B*, vol. 57, pp. 15577–15585, 1996.
- [91] E. Lidorikis, Q. Li, and C. M. Soukoulis, “Optical bistability in colloidal crystals,” *Applied Physics Letters*, vol. 55, pp. 3613–3618, 1997.
- [92] C. M. de Sterke and J. E. Sipe, “Gap solitons,” *Progress in Optics*, vol. 33, pp. 203–260, 1994.
- [93] W. Chen and D. L. Mills, “Gap solitons and the nonlinear optical response of superlattices,” *Physical Review Letters*, vol. 58, pp. 160–163, 1987.
- [94] D. L. Mills and S. E. Trullinger, “Gap solitons in nonlinear periodic structures,” *Physical Review B*, vol. 36, pp. 947–952, 1987.
- [95] S. John, “Strong localization of photons in certain disordered dielectric superlattices,” *Physical Review Letters*, vol. 58, pp. 2486–2489, 1987.

- [96] A. Kondilis and P. Tzanetakis, “Numerical calculations on optical localization in multilayer structures with random-thickness layers,” *Physical Review B*, vol. 46, pp. 15426–15431, 1992.
- [97] A. R. McGurn, K. T. Christensen, F. M. Mueller, and A. A. Maradudin, “Anderson localization in one-dimensional randomly disordered optical systems that are periodic on average,” *Physical Review B*, vol. 47, pp. 13120–13125, 1993.
- [98] A. A. Bulgakov, S. A. Bulgakov, and M. Nieto-Vasperinas, “Inhomogeneous waves and energy localization in dielectric superlattices,” *Physical Review B*, vol. 58, pp. 4438–4448, 2000.
- [99] M. Rusek, A. Orłowski, and J. Mostowski, “Localization of light in three-dimensional random dielectric media,” *Physical Review E*, vol. 53, pp. 4122–4130, 1996.
- [100] M. Rusek and A. Orłowski, “Example of self-averaging in three-dimensions: Anderson localization of electromagnetic waves in random distributions of pointlike scatterers,” *Physical Review E*, vol. 56, pp. 6090–6094, 1997.
- [101] M. Rusek and A. Orłowski, “Anderson localization of electromagnetic waves in confined dielectric media,” *Physical Review E*, vol. 59, pp. 3655–3660, 1999.
- [102] P. Devillard and B. Souillard, “Polynomially decaying transmission for the nonlinear Schrödinger equation in a random medium,” *Journal of Statistical Physics*, vol. 43, pp. 423–428, 1986.
- [103] B. Doucot and R. Rammal, “On Anderson localization in nonlinear random media,” *Europhysics Letters*, vol. 3, pp. 969–972, 1987.

- [104] Q. Li, C. M. Soukoulis, S. Pnevmatikos, and E. N. Economou, “Scattering properties of solitons in nonlinear disordered chains,” *Physical Review B*, vol. 57, pp. R12673–R12676, 1998.
- [105] J. E. Sipe and H. G. Winful, “Nonlinear Schrödinger solitons in a periodic structure,” *Optics Letters*, vol. 13, pp. 132–133, 1988.
- [106] H. G. Winful, “Pulse compression in optical fiber filters,” *Applied Physics Letters*, vol. 46, pp. 528–530, 1985.
- [107] C. M. de Sterke and J. E. Sipe, “Envelope-function approach for the electrodynamics of nonlinear periodic structures,” *Physical Review A*, vol. 38, pp. 5149–5165, 1988.
- [108] D. N. Christodoulides and R. I. Joseph, “Slow Bragg solitons in nonlinear periodic structures,” *Physical Review Letters*, vol. 62, pp. 1746–1749, 1989.
- [109] A. B. Aceves and S. Wabnitz, “Self-induced transparency solitons in nonlinear refractive periodic media,” *Physical Letters A*, vol. 141, pp. 37–42, 1989.
- [110] B. J. Eggleton, R. E. Slusher, C. M. de Sterke, P. A. Krug, and J. E. Sipe, “Bragg grating solitons,” *Physical Review Letters*, vol. 76, pp. 1627–1630, 1996.
- [111] N. D. Sankey, D. F. Prelewitz, and T. G. Brown, “All-optical switching in a nonlinear periodic-waveguide structure,” *Applied Physics Letters*, vol. 60, pp. 1427–1429, 1992.
- [112] P. Miller, R. M. De La Rue, T. F. Krauss, J. S. Aitchison, N. G. R. Broderick, and D. J. Richardson, “Nonlinear propagation effects in an AlGaAs Bragg grating filter,” *Optics Letters*, vol. 24, pp. 685–687, 1999.

- [113] N. G. R. Broderick, D. Taverner, D. J. Richardson, M. Ibsen, and R. I. Laming, "Optical pulse compression in fiber Bragg gratings," *Physical Review Letters*, vol. 79, pp. 4566–4569, 1997.
- [114] N. G. R. Broderick, D. Taverner, D. J. Richardson, M. Ibsen, and R. I. Laming, "Experimental observation of nonlinear pulse compression in nonuniform Bragg gratings," *Optics Letters*, vol. 22, pp. 1837–1839, 1997.
- [115] M. Scalora, J. P. Dowling, C. M. Bowden, and J. M. Bloemer, "Optical limiting and switching of ultrashort pulses in nonlinear photonic band gap materials," *Physical Review Letters*, vol. 73, pp. 1368–1371, 1994.
- [116] G. Pan, R. Kesavamoorthy, and A. Asher, "Optically nonlinear Bragg diffracting nanosecond optical switching," *Physical Review Letters*, vol. 58, pp. 3860–3863, 1997.
- [117] P. Tran, "All-optical switching with a nonlinear chiral photonic bandgap structure," *Journal of the Optical Society of America B*, vol. 16, pp. 70–73, 1999.
- [118] J. S. Shirk, R. G. S. Pong, S. R. Flonn, A. Hiltner, and E. Baer, "Nonlinear nanolayer polymers: 1D photonic materials with applications to optical limiting," *LEOS 2001*, pp. 83–84, 2001.
- [119] S. R. Flonn, S. R. Carlo, J. S. Shirk, R. G. S. Pong, A. Hiltner, and E. Baer, "Nanostructured polymeric optical limiter materials," *LEOS 2002*, pp. 570–572, 2002.
- [120] S. W. Leonard, H. M. van Driel, J. Schilling, and R. B. Werhspohn, "Ultrafast band-edge tuning of two-dimensional silicon photonic crystal via free-carrier injection," *Physical Review B*, vol. 66, pp. 16102(1–4), 2002.
- [121] A. Yariv and P. Yeh, *Optical Waves in Crystals*. John Wiley & Sons, 1984.

- [122] L. Brzozowski and E. H. Sargent, "Nonlinear distributed feedback structures for optical sensor protection," in *AERO Sense 2000*, vol. 4037, pp. 64–71, SPIE, 2000.
- [123] H. R. Lin, R. J. Tonucci, and A. J. Campillo, "Two-dimensional photonic bandgap optical limiters in the visible," *Optics Letters*, vol. 23, pp. 94–96, 1998.
- [124] L. Brzozowski and E. H. Sargent, "Photonic crystals for integrated optical computing," in *OSA's Optical Computing 2000*, pp. W3–4, 2000.
- [125] L. Brzozowski and E. H. Sargent, "Photonic crystals for spectrally and angularly broadband all-optical limiting," in *International Workshop on Photonic and Electromagnetic Crystal Structures*, vol. 4089, pp. 786–796, SPIE, 2000.
- [126] L. Brzozowski and E. H. Sargent, "All-optical analog-to-digital converters, hardlimiters, and logic gates," *IEEE Journal of Lightwave Technologies*, vol. 19, pp. 114–119, 2000.
- [127] E. H. Sargent, E. Istrate, M. Allard, and L. Brzozowski, "Integrable, low cost all-optical WDM processing: Narrowband hard limiters and analog-to-digital converters," in *Contemporary Photonic Technologies*, 2000.
- [128] L. Brzozowski and E. H. Sargent, "All-optical analog-to-digital converter for photonic networks using multilevel signaling," in *IEEE International Conference on Transparent Optical Networks*, pp. 203–206, IEEE, 2000.
- [129] E. Johnson, L. Brzozowski, and E. H. Sargent, "All-optical time-domain IP router using optical limiters," in *LEOS 2000*, pp. 33–34, IEEE, 2000.
- [130] L. Brzozowski, E. V. Johnson, W. Ye, and E. H. Sargent, "Nonlinear periodic structures as building blocks of all-optical signal processing devices and systems," in *Canada France Conference on Molecular Photonics and Electronics*, 2001.

- [131] T. Ohtsuki, K. Sato, I. Sasase, and S. Mori, "Direct-detection CDMA systems with double optical hard-limiters using modified prime sequence codes," *IEEE Journal on Selected Areas in Communication*, vol. 14, pp. 1879–1887, 1996.
- [132] T. Ohtsuki, "Performance analysis of direct-detection optical asynchronous CDMA systems with double optical hard-limiters," *IEEE Journal of Lightwave Technology*, vol. 14, pp. 452–457, 1997.
- [133] S. Trillo and S. Wabnitz, "Nonlinear nonreciprocity in a coherent mismatched directional coupler," *Applied Physics Letters*, vol. 49, pp. 752–754, 1986.
- [134] M. S. Whalen and T. H. Wood, "Effectively nonreciprocal evanescent-wave optical-fiber directional coupler," *Electronics Letters*, vol. 21, pp. 175–176, 1985.
- [135] B. P. Lathi, *Modern Digital and Analog Communication Systems*. Dyden, 1989.
- [136] D. Pelinovsky, L. Brzozowski, and E. H. Sargent, "Transmission regimes of periodic nonlinear optical structures," *Physical Review E*, vol. 60, pp. R4536–R4539, 2000.
- [137] L. Brzozowski and E. H. Sargent, "Stability of periodic nonlinear optical structures for limiting and logic," in *CLEO Europe*, p. CthE49, IEEE, 2000.
- [138] D. Pelinovsky, J. Sears, L. Brzozowski, and E. H. Sargent, "Stable all-optical limiting in nonlinear periodic structures. I. Analysis.," *Journal of the Optical Society of America B*, vol. 19, pp. 45–53, 2002.
- [139] W. N. Ye, L. Brzozowski, E. H. Sargent, and D. Pelinovsky, "Stable all-optical limiting in nonlinear periodic structures III: Non-Solitonic pulse propagation," *Journal of the Optical Society of America B*, vol. 20, pp. 695–705, 2003.
- [140] W. N. Ye, L. Brzozowski, E. H. Sargent, and D. Pelinovsky, "Nonlinear propagation of ultrashort pulses in nonlinear periodic materials with oppositely-signed Kerr

- coefficients,” in *IEEE LEOS Annual General Meeting Proceedings*, pp. 441–442, IEEE, 2001.
- [141] L. Brzozowski, W. N. Ye, and E. H. Sargent, “Pulse switching and compression in out-of-phase superimposed linear-nonlinear grating,” in *LEOS 2003 Summer Topical Meeting*, p. MA4.4, 2003.
- [142] L. Brzozowski, E. H. Sargent, A. SpringThorpe, and M. Extavour, “Measurement of large near-bandedge nonlinearities in InGaAs/InAlGaAs multi-quantum-wells in 1.48 - 1.55 μm spectral range,” in *CLEO 2003*, p. CThT2, 2003.
- [143] Y. Lin, J. Zhang, L. Brzozowski, C. Paquet, E. Kumacheva, and E. H. Sargent, “Processible nonlinear polymers: Engineering Kerr coefficient sign, strength, and figure-of-merit,” in *Workshop on Organics for Photonics and Electronics*, p. 31, 2001.
- [144] Q. Chen, Y. Lin, L. Brzozowski, E. H. Sargent, P. W. E. Smith, J. Zhang, C. Paquet, E. Kumacheva, X. Feng, and Z. Lu, “Nonlinear and luminescent molecular materials for photonic applications,” in *Canada France Conference on Molecular Photonics and Electronics*, 2001.
- [145] L. Brzozowski and E. H. Sargent, “Azobenzenes for photonic network applications: Third order nonlinear optical properties,” *Journal of Materials Science: Materials in Electronics*, vol. 12, pp. 483–489, 2001.
- [146] Y. Lin, J. Zhang, L. Brzozowski, E. Kumacheva, and E. H. Sargent, “Nonlinear optical figures of merit of highly processible MEH-PPV/PMMA composite,” *Journal of Applied Physics*, vol. 91, pp. 522–525, 2002.
- [147] L. Brzozowski, E. H. Sargent, and M. A. Hines, “Measurement of the resonant third-order nonlinearities in strongly-confined PbS nanocrystals in the 1150 nm to 1550 nm range,” *in preparation*.

- [148] L. Brzozowski, E. H. Sargent, and M. A. Hines, "Resonant nonlinearities and figures of merit of strongly-confined 5.5 nm PbS nanocrystals in the 1150 nm to 1550 nm wavelength range," in *to be presented at CLEO Pacific Rim 2003*.
- [149] M. Sheik-Bahae, A. A. Said, T.-H. Wei, D. J. Hagan, and E. W. Van Stryland, "Sensitive measurements of optical nonlinearities using a single beam," *IEEE Journal of Quantum Electronics*, vol. 26, pp. 760–769, 1990.
- [150] M. Sheik-Bahae, A. A. Said, and E. W. Van Stryland, "High-sensitivity, single-beam n_2 measurement," *Optics Letters*, vol. 14, pp. 955–957, 1989.
- [151] D.-S. Fournier, *Broadband Characterization of the Kerr Third-Order Nonlinear Optical Properties of a Polymer-Based Organic Azobenzene Dye: DR1-PMMA*. University of Toronto Masters' Thesis, 2002.
- [152] S. Kumar, *Azo Functional Polymers*. Technomic Publishing Co. Inc., 1992.
- [153] H. Rau, "Photoisomerization of azobenzenes," in *Photochemistry and Photophysics*, vol. 2, pp. 120–141, CRC Press, 1990.
- [154] M. Samoc, A. Samoc, B. Luther-Davies, Z. Bao, L. Yu, B. Hsieh, and U. Scherf, "Femtosecond z-scan and degenerate four-wave mixing measurements of real and imaginary parts of the third-order nonlinearity of soluble conjugated polymers," *Journal of the Optical Society B*, vol. 15, pp. 817–825, 1998.
- [155] S. J. Martin, D. D. C. Bradley, P. A. Lane, H. Mellor, and P. L. Burn, "Linear and nonlinear optical properties of the conjugated polymers PPV and MEH-PPV," *Physical Review B*, vol. 59, pp. 15133–15142, 1999.
- [156] M. N. Islam, E. P. Ippon, E. G. Burkardt, and T. J. Bridges, "Picosecond nonlinear absorption and four-wave mixing in GaInAsP," *Applied Physics Letters*, vol. 47, pp. 1042–1044, 1985.

- [157] K. Tai, J. L. Jewll, W. T. Tsand, H. Temkin, M. Panish, and Y. Twu, "1.55- μ m optical logic talon with picojoule switching energy made of InGaAs/InP multiple quantum wells," *Applied Physics Letters*, vol. 50, pp. 795–797, 1987.
- [158] D. A. B. Miller, C. T. Seaton, M. E. Prise, and S. D. Smith, "Band-gap resonant nonlinear refraction in III-V semiconductors," *Physical Review Letters*, vol. 47, pp. 197–200, 1981.
- [159] H.-C. Lee, A. Kost, M. Kawase, A. Hariz, and P. Daniel Dapkus, "Nonlinear absorption properties of AlGaAs/GaAs multiple quantum wells grown by metalorganic chemical vapor deposition," *IEEE Journal of Quantum Electronics*, vol. 24, pp. 1581–1592, 1988.
- [160] J. S. Weiner, D. B. Pearson, D. A. B. Miller, D. S. Chemla, D. Sivco, and A. Y. Cho, "Nonlinear spectroscopy of InGaAs/InAlAs multiple quantum well structures," *Applied Physics Letters*, vol. 49, pp. 531–533, 1986.
- [161] R. Jin, K. Okada, G. Khitrova, H. M. Gibbs, M. Pereira, S. W. Koch, and N. Peyghambarian, "Optical nonlinearities in strained-layer InGaAs/GaAs multiple quantum wells," *Applied Physics Letters*, vol. 61, pp. 1745–1747, 1992.
- [162] F. Kajzar and J. Messier, "Third-harmonic generation in liquids," *Physical Review A*, vol. 32, pp. 2352–2363, 1985.
- [163] G. R. Meredith, B. Buchalter, and C. Hanzlik, "Third-order susceptibility determination by third harmonic generation. I," *Journal of Chemical Physics*, vol. 78, pp. 1533–1542, 1983.
- [164] G. R. Meredith, B. Buchalter, and C. Hanzlik, "Third-order susceptibility determination by third harmonic generation. II," *Journal of Chemical Physics*, vol. 78, pp. 1543–1551, 1983.

- [165] N. Prasad, P. E. Permin, and M. Samoc, "A coupled anaharmonic oscillator model for optical nonlinearities of conjugated organic structures," *Journal of Chemical Physics*, vol. 91, pp. 2360–2365, 1989.
- [166] L. Banyai, Y. Z. Hu, M. Lindberg, and S. W. Koch, "Third-order optical nonlinearities in semiconductor microstructures," *Physical Review B*, vol. 38, pp. 8142–8153, 1988.
- [167] G. P. Banfi, V. Degiorgio, M. Ghigliazza, H. M. Tan, and A. Tomaselli, "Two-photon absorption in semiconductor nanocrystals," *Physical Review B*, vol. 50, pp. 5699–5702, 1994.
- [168] *CRC Handbook of Chemistry and Physics*. CRC Press, eighty-second edition, 2001.
- [169] L. Brzozowski, V. Sukhovatkin, E. H. Sargent, A. SpringThorpe, and M. Extavour, "Intensity-dependent reflectance and transmittance of semiconductor periodic structures," *IEEE Journal of Quantum Electronics*, vol. 39, pp. 924–930, 2003.
- [170] L. Brzozowski, V. Sukhovatkin, E. H. Sargent, A. SpringThorpe, and M. Extavour, "Nonlinear reflectance and transmittance of semiconductor periodic structures between 1.3 and 1.6 μm ," in *CLEO 2003*, p. CTuM19.
- [171] T. K. L. Wong, L. Brzozowski, and E. H. Sargent, "Design of optical signal processing devices using a modified fourier transfer method," *Applied Optics*, vol. 41, pp. 6763–6767, 2002.
- [172] R. Rangel-Rojo, S. Yamada, H. Matsuda, H. Kasai, Y. Komai, S. Okada, H. Oikawa, and H. Nakanishi, "Refractive third-order nonlinearity in vanadium oxide phthalocyanine micro-crystals," *Japanese Journal of Applied Physics*, vol. 38, pp. 69–73, 1999.

- [173] C. Paquet, *Optical Characterization of Polyferrocenes and Colloid Crystals*. University of Toronto Masters' Thesis, 2002.
- [174] I. K. Ledneve, T. Ye, R. E. Hester, and J. N. Moore, "Femtosecond time-resolved UV-visible absorption spectroscopy of trans-azobenzene in solution," *Journal of Physical Chemistry*, vol. 100, pp. 13338–13341, 1996.
- [175] T. Nagele, R. Hoche, W. Zinth, and J. Wachtveitl, "Femtosecond photoisomerization of cis-azobenzene," *Chemical Physics Letters*, vol. 272, pp. 489–495, 1997.